

UNIVERSIDADE DE LISBOA
FACULDADE DE CIÊNCIAS
DEPARTAMENTO DE ENGENHARIA GEOGRÁFICA,
GEOFÍSICA E ENERGIA



**USING MIDDLE-INFRARED
REFLECTANCE FOR BURNED AREA
DETECTION**

RENATA LIBONATI DOS SANTOS

DOUTORAMENTO EM CIÊNCIAS GEOFÍSICAS E DA
GEOINFORMAÇÃO
(METEOROLOGIA)

2010

UNIVERSIDADE DE LISBOA
FACULDADE DE CIÊNCIAS
DEPARTAMENTO DE ENGENHARIA GEOGRÁFICA,
GEOFÍSICA E ENERGIA



**USING MIDDLE-INFRARED
REFLECTANCE FOR BURNED AREA
DETECTION**

RENATA LIBONATI DOS SANTOS

DOUTORAMENTO EM CIÊNCIAS GEOFÍSICAS E DA
GEOINFORMAÇÃO
(METEOROLOGIA)

Tese orientada pelos Professores Doutores
Carlos da Camara e José Miguel Cardoso Pereira

2010

to Leonardo and Maria Carolina

*É o tempo da travessia: e, se não ousarmos fazê-la,
teremos ficado, para sempre, à margem de nós mesmos.*

Fernando Pessoa

Acknowledgements

First and foremost I offer my sincerest gratitude to my supervisor, Prof. Carlos da Camara, who has supported me throughout my thesis with his patience and knowledge whilst allowing me to work in my own way. I attribute the level of my PhD degree to his encouragement and effort and without him this thesis would not have been completed.

I also wish to thank Prof. José Miguel Cardoso Pereira for his assistance, dedication and inspired ideas. The supervision and support that he gave truly help the progression of this work.

I am especially indebted to Dr. Alberto Setzer to whom I thank the support, suggestions; and fruitful discussions, which helped overcoming a lot of difficulties. Moreover I wish to thank him to be responsible for my long stay in the Satellite Division from the Brazilian National Institute for Space Research (DSA/INPE).

I am grateful to DSA/INPE where I have partially developed this thesis, for providing satellite data and giving access to all the related information, as well as for supporting my participation in some scientific conferences and workshops where I have presented scientific

results from this research. A word of acknowledgment is also due to all my colleagues at DSA/INPE who have assisted me one way or another, especially in challenging me with alternative views. Their friendship and professional collaboration meant a great deal to me. In particular I would like to thank Dr. Fabiano Morelli, whom I have contributed in a fundamental way to my understanding of geographic information system.

I am very thankful to my colleagues at CGUL, in particular Dr. Teresa Calado, Dr. Célia Gouveia, Dr. Joana Freire, and Dr. Ricardo Trigo for their friendship, motivation, support, and suggestions that eased and made this work more pleasant. To Célia and Teresa a special thanks, more than ever, at the final stage of this work.

I am indebted to Dr. Wilfrid Schroeder (NOAA) who kindly provided the fire scars from LANDSAT sensor, to Jurandir Ventura (DSA/INPE) for making available some MODIS data, to José Carlos dos Santos (LCP/INPE) for collecting the samples of charcoal in Alta Floresta, to Dr. Simon Hook (JPL/NASA) for performing the charcoal emissivity measurements, to Dr. Alexandre Correia (USP) and Dr. Karla Longo (INPE) for kindly clarify my doubts concerning aerosols.

I can not forget my friends Liliana Madeira, Raquel Marujo and Sónia Domingos for their friendship and constant support during my stay in Portugal.

Last, but not the least, a very special word of acknowledgement to my family, family-in-law and close friends for their understanding and help provided during this long path. To my brother and my parents, for all the motivation, encouragement, support they have always provided and for every bit of their love and patient; without it this work would have been impossible. A very special thought towards my mom and my dad, who always believe on me.

To my husband, Leonardo, who has always accompany me along this journey, and whom made me believe that nothing is out of reach, I wish to thank for all his patient, help and unconditional love without which all this effort would never make sense. Moreover I would like to thank all his scientific support and suggestions; that without them this work would not have ever ended.

Finally, to Maria Carolina, who was born during this thesis and who cannot understand yet why mummy has to work so much, I want to thanks for all the happiness she brought to my life and for being my mainly inspiration during this work.

This work was supported by the Portuguese Foundation of Science and Technology (FCT) (Grant No. SFRH/BD/21650/2005).

Abstract

A strategy is presented that allows deriving a new index for burned area discrimination over the Amazon and Cerrado regions of Brazil. The index is based on information from the near-infrared (NIR) and middle-infrared (MIR) channels of the Moderate Resolution Imaging Spectroradiometer (MODIS). A thorough review is undertaken of existing methods for retrieving MIR reflectance and an assessment is performed, using simulated and real data, about the added value obtained when using the radiative transfer equation (RTE) instead of the simplified algorithm (KR94) developed by Kaufman and Remer (1994), the most used in the context of burned area studies. It is shown that use of KR94 in tropical environments to retrieve vegetation reflectance may lead to errors that are at least of the same order of magnitude of the reflectance to be retrieved and considerably higher for large values of land surface temperature (LST) and solar zenith angle (SZA). Use of the RTE approach leads to better estimates in virtually all cases, with the exception of high values of LST and SZA, where results from KR94 are also not usable. A transformation is finally defined on the MIR/NIR reflectance space aiming to enhance the spectral information such that vegetated and burned surfaces may be effectively discriminated. The transformation is based on the difference between MIR and NIR in conjunction with the distance from a convergence point in the MIR/NIR space, representative of a totally burnt surface. The

transformation allows defining a system of coordinates, one coordinate having a small scatter for pixels associated to vegetation, burned surfaces and soils containing organic matter and the other coordinate covering a wide range of values, from green and dry/stressed vegetation to burned surfaces. The new set of coordinates opens interesting perspectives to applications like drought monitoring and burned area discrimination using remote-sensed information.

Key-words: Middle-infrared; Burned area; Remote sensing; Spectral index; MODIS

Resumo

O coberto vegetal da superfície da Terra tem vindo a sofrer mudanças, por vezes drásticas, que conduzem a alterações tanto na rugosidade da superfície terrestre como no seu albedo, afectando directamente as trocas de calor sensível e latente e de dióxido de carbono entre a superfície terrestre e a atmosfera (Sellers et al., 1996). Neste contexto, as queimadas assumem um papel de extremo relevo (Nobre et al., 1991; O'Brien, 1996; Xue, 1996) na medida em que constituem uma das mais importantes fontes de alteração do coberto vegetal, resultando na destruição de florestas e de recursos naturais, libertando carbono da superfície continental para a atmosfera (Sellers et al., 1995) e perturbando as interações biosfera-atmosfera (Levine et al., 1995; Scholes, 1995) através de mudanças na rugosidade do solo, na área foliar e noutros parâmetros biofísicos associados ao coberto vegetal. Ora, neste particular, a Amazónia Brasileira constitui um exemplo notável de mudanças no uso da terra e do coberto vegetal nas últimas décadas, como resultado da desflorestação induzida pelo homem bem como por causas naturais (Gedney e Valdes, 2000; Houghton, 2000; Houghton et al., 2000; Lucas et al., 2000), estimando-se que as

regiões tropicais sejam responsáveis por cerca de 32% da emissão global de carbono para a atmosfera (Andreae, 1991). Neste contexto, a disponibilidade de informações pormenorizadas e actualizadas sobre as distribuições espacial e temporal de queimadas e de áreas ardidadas em regiões tropicais afigura-se crucial, não só para uma melhor gestão dos recursos naturais, mas também para estudos da química da atmosfera e de mudanças climáticas (Zhan et al., 2002).

A detecção remota constitui, neste âmbito, uma ferramenta indispensável na medida em que permite uma monitorização em tempo quase real, a qual se revela especialmente útil em áreas extensas e/ou de difícil acesso afectadas pelo fogo (Pereira et al., 1997). Diversos instrumentos, tais como o *Land Remote Sensing Satellite/Thematic Mapper* (LANDSAT/TM) e o *National Oceanic and Atmospheric Administration/Advanced Very High Resolution Radiometer* (NOAA/AVHRR) têm vindo a ser extensivamente utilizados na gestão dos fogos florestais, em particular aos níveis da detecção de focos de incêndio e da monitorização de áreas queimadas. Mais recentemente, o instrumento VEGETATION a bordo do *Satellite Pour l'Observation de la Terre* (SPOT) tem vindo a ser utilizado com sucesso na monitorização de fogos. Finalmente, são de referir os sensores da série *Along Track Scanning Radiometer* (ATSR) para os quais têm vindo a ser desenvolvidos algoritmos de identificação de focos de incêndio, e ainda o sensor *Moderate Resolution Imaging Spectroradiometer* (MODIS) que tem vindo a demonstrar capacidades óptimas no que respeita à observação global de fogos, plumas e áreas queimadas.

Neste contexto, os métodos actuais de detecção de áreas ardidadas através da detecção remota têm vindo a dar prioridade à utilização das regiões do vermelho (0.64 μm) e infravermelho-próximo (0.84 μm) do espectro eletromagnético. No entanto, tanto a região do vermelho quanto a do infravermelho-próximo apresentam a desvantagem de serem sensíveis à presença de aerossóis na atmosfera (Fraser e Kaufman, 1985; Holben et al., 1986). Desta forma, em regiões tropicais como a Amazónia, onde existem grandes camadas de fumo devido à queima de biomassa, a utilização destas duas regiões do espectro

eletromagnético torna-se insatisfatória para a detecção de áreas áridas. Por outro lado, a região do infravermelho médio (3.7 – 3.9 μm) tem a vantagem de não ser sensível à presença da maior parte dos aerossóis, exceptuando a poeira (Kaufman e Remer, 1994) mostrando-se, ao mesmo tempo, sensível a mudanças na vegetação devido à absorção de água líquida.

Com efeito, estudos acerca dos efeitos do vapor de água na atenuação do espectro eletromagnético demonstraram que a região do infravermelho médio é uma das únicas regiões com relativamente pouca atenuação (Kerber e Schut, 1986). Acresce que a região do infravermelho médio apresenta uma baixa variação da irradiância solar (Lean, 1991), tendo-se ainda que a influência das incertezas da emissividade na estimativa da temperatura da superfície é pequena quando comparada com outras regiões térmicas tais como as de 10.5 e 11.5 μm (Salisbury e D'Aria, 1994).

A utilização da radiância medida através de satélites na região do infravermelho médio é, no entanto, dificultada pelo facto de esta ser afectada tanto pelo fluxo térmico quanto pelo fluxo solar, contendo, desta forma, duas componentes, uma emitida e outra reflectida, tendo-se que a componente reflectiva contém os fluxos térmico e solar reflectidos pela atmosfera e pela superfície enquanto que as emissões térmicas são oriundas da atmosfera e da superfície. Ora, a componente solar reflectida é de especial interesse para a detecção de áreas áridas pelo que se torna necessário isolá-la do sinal total medido pelo sensor. Devido à ambiguidade deste sinal, a distinção dos efeitos da reflectância e da temperatura torna-se uma tarefa muito complexa, verificando-se que os métodos em que se não assume nenhuma simplificação, levando-se, portanto, em consideração todos os constituintes do sinal do infravermelho médio se tornam complexos e difíceis de serem aplicados na prática, na medida em que requerem dados auxiliares (e.g. perfis atmosféricos) e ferramentas computacionais (e.g. modelos de transferência radiativa). Kaufman e Remer (1994) desenvolveram um método simples para estimar a reflectância do infravermelho médio o qual assenta em diversas hipóteses simplificadoras. Apesar do objectivo primário

que levou ao desenvolvimento do método ser a identificação de áreas cobertas por vegetação densa e escura em regiões temperadas, este método tem sido largamente utilizado nos estudos acerca da discriminação de áreas queimadas, algumas das vezes em regiões tropicais (Roy et al., 1999; Barbosa et al., 1999; Pereira, 1999). Na literatura não existe, no entanto, nenhum estudo acerca da exactidão e precisão deste método quando aplicado com o objectivo de detectar áreas ardidas, em especial em regiões tropicais. Neste sentido, no presente trabalho procedeu-se a um estudo de viabilidade do método proposto por Kaufman e Remer (1994) em simultâneo com a análise da equação de transferência radiativa na região do infravermelho médio, tendo sido realizados testes de sensibilidade dos algoritmos em relação aos erros nos perfis atmosféricos, ruído do sensor e erros nas estimativas da temperatura da superfície. Para tal recorreu-se ao modelo de transferência radiativa *Moderate Spectral Resolution Atmospheric Transmittance and Radiance Code* (MODTRAN), dando-se especial atenção ao caso do sensor MODIS. Os resultados demonstraram que a utilização do método proposto por Kaufman e Remer (1994) em regiões tropicais para a estimativa da reflectância no infravermelho médio, leva a erros que são pelo menos da mesma ordem de magnitude do parâmetro estimado e, em alguns casos, muito maior, quando ocorre a combinação de altas temperaturas da superfície terrestre com baixos ângulos zenitais solares. A utilização da equação de transferência radiativa mostrou-se uma boa alternativa, desde que estejam disponíveis dados acerca da temperatura da superfície terrestre assim como dos perfis atmosféricos. Entretanto, nas regiões onde ocorrem altos valores de temperatura da superfície terrestre e baixos ângulos zenitais solares, quaisquer dos dois métodos se mostra pouco utilizável, já que nesta região a estimativa da reflectância constitui um problema mal-posto.

Em paralelo, utilizaram-se informações sobre aerossóis de queimada para efectuar simulações do MODTRAN que permitiram avaliar a resposta do canal do infravermelho-médio à este tipo de perturbação do sinal, muito comum na Amazónia Brasileira. A fim de tornar o estudo o mais realístico possível, procedeu-se à coleta de material resultante de queimadas

na região Amazônica, mais especificamente em Alta Floresta, Mato Grosso, Brasil. Estes resultados foram então integrados nos estudos em questão, possibilitando a caracterização espectral das áreas ardidas.

Com base nos resultados obtido definiu-se uma transformação no espaço do infravermelho próximo e médio com o objetivo de maximizar a informação espectral de forma a que as superfícies vegetadas pudessem ser efetivamente discriminadas e as áreas ardidas identificadas. A transformação baseia-se na diferença entre a reflectância nos infravermelhos próximo e médio, em conjunto com a distância a um ponto de convergência no espaço espectral dos infravermelhos próximo e médio, ponto esse representativo de uma área completamente ardida. A transformação permitiu a definição de um novo sistema de coordenadas, o qual provou ser bastante útil no que diz respeito à identificação de áreas ardidas. Este novo espaço de coordenadas constitui uma inovação na área dos estudos de queimadas, já que permite ao mesmo tempo definir dois tipos de índices, o primeiro dos quais identifica superfícies que contém ou não biomassa e o segundo identifica, de entre as superfícies que contêm biomassa, a quantidade de água presente, podendo variar de vegetação verde (abundância de água) até áreas ardidas (ausência de água). Além de distinguir áreas ardidas, os índices desenvolvidos podem ainda ser aplicados em outros casos como, por exemplo, estudos de estresse hídrico e secas.

Contents

Acknowledgements	i
Abstract	v
Resumo	vii
Contents	xiii
List of Figures	xvii
List of Tables	xxv
Acronyms	xxvii
Chapter 1. Introduction	1
1.1. Motivation	1
1.2. The Problem	6
1.3. Main Contributions	8
1.4. Publications	9
1.5. Thesis Organization	11
Chapter 2. Theoretical background	13
2.1. Fundamentals of Radiation in MIR	13
2.1.1. Blackbody concept	13

2.1.2. Radiative transfer equation in MIR	15
2.1.3. Channel equivalent quantities	19
2.2. Retrieval of MIR reflectance	21
2.3. Usage of MIR reflectance for burned area identification	26
Chapter 3. Sensors, datasets and radiative transfer code	37
3.1. Satellite sensors characteristics	37
3.1.1. MODIS coarser resolution sensor	37
3.1.2. ETM+ high resolution sensor	40
3.2. Datasets	41
3.2.1. Satellite data	41
3.2.1.1. MODIS data	41
3.2.1.2. Landsat data	44
3.2.2. Laboratory spectral data on reflectance	46
3.2.2.1. Spectral library data	46
3.2.2.2. Charcoal data	51
3.2.3. Auxiliary information	55
3.2.3.1. AERONET	55
3.2.3.2. Hot spots	56
3.3. MODTRAN radiative transfer code and atmospheric characterization	56
Chapter 4. Retrieving MIR reflectance for burned area mapping in tropical regions	61
4.1. Introduction	61
4.2. Data and methods	63
4.2.1. Theoretical background	63
4.2.2. Retrieval of MIR reflectance	64
4.2.3. Radiative transfer simulations	68
4.3. Analysis and results	72

4.3.1. MODTRAN-4 simulations	72
4.3.2. Case study	79
4.4. Concluding remarks	86
Chapter 5. Retrieval of middle-infrared reflectance using the Radiative Transfer Equation	89
5.1. Introduction	89
5.2. Method and data	91
5.2.1. Radiative Transfer Simulations	91
5.2.2. Sources of errors in the retrieval of MIR reflectance	92
5.2.2.1. Radiometric Noise of MODIS channel 20	93
5.2.2.2. Atmospheric Profiles	94
5.2.2.3. Uncertainty in Surface Temperature	98
5.3. Analysis and Results	99
5.3.1. Error-free case	99
5.3.2. Error case	104
5.3.3. Total MIR Reflectance Error	110
5.4. Concluding remarks	116
Chapter 6. On a new coordinate system for optimal discrimination of vegetation and burned areas using MIR/NIR information	121
6.1. Introduction	121
6.2. Data	124
6.3. Methods	125
6.3.1. Rationale	125
6.3.2. The η/ξ space	129
6.3.3. The V/W coordinate system	135
6.4. Results and discussion	143
6.4.1. Supervised validation	143

6.4.2. Unsupervised validation	146
6.5. Concluding remarks	150
Chapter 7. Concluding remarks	153
References	159
Annex. Papers in Refereed Journals	181

List of Figures

- Figure 1.1. Spectrum of emission from the Sun and the Earth highlighting the contributions of both sources of radiation in the MIR domain. Adapted from <http://aerial.evsc.virginia.edu/~jlm8h/class/>. 7
- Figure 2.1. Radiative transfer at a middle-infrared wavelength λ . 17
- Figure 2.2. Spectral signatures of burned material sample (solid curves), green vegetation (dot curve) and dry vegetation (dashed curve). Gray boxes delimit the VISIBLE (between 0.4 and 0.7), NIR (around 0.8) and SWIR (between 1.0 and 2.0 μm) spectral regions in order to emphasize their contrast. Charcoal signatures were obtained from the USGS Digital Spectral Library as well as from samples provide by the author, whereas vegetation signatures were obtained from the MODIS-UCSB spectral library (see Chapter 3). 29
- Figure 2.3. Spectral signatures of four charcoal samples (solid curves) and of three vegetation samples (dot-dashed curves). Gray boxes delimit the SWIR (between 2.0 and 2.5 μm) and MIR (between 3.5 and 4 μm) spectral regions in order to emphasize their contrast. Charcoal and vegetation signatures were respectively obtained from samples of fire residues from Alta Floresta (see next Chapter), state of Mato Grosso,

Brazil and from the Advanced Spaceborne Thermal Emission and Reflection Radiometer (ASTER) spectral library (Baldrige et al., 2009).	30
Figure 2.4. Histograms of the burned and unburned classes for MODIS channels.	31
Figure 2.5. Atmospheric transmittance attenuation [%] on MODIS VIS to MIR channels for three different levels of smoke contamination due to biomass burning. $\tau_a(0.55)$ indicates the AOD at 0.55 μm and α denotes the Ångstrom parameter, which characterizes aerosol particle size distribution.	33
Figure 2.6. Comparison between MIR (left panel) and TIR (right panel) regions concerning the attenuation by water vapor content throughout the three atmospheric profiles (MLS, MLW and TRO) stored at MODTRAN-4 (see Chapter 3 for details).	33
Figure 3.1. Spectral response function of MODIS channels.	38
Figure 3.2. Spectral response functions of MODIS MIR channels.	44
Figure 3.3. IBAMA general biomes classification map for Brazil and the location of the 16 Landsat ETM+ scenes listed in Table 3.3.	45
Figure 3.4. Spectral signature of vegetation from ASTER spectral library in (A) the 0.25-2.5 μm and (B) the 2-15 μm spectral ranges.	49
Figure 3.5. As in Figure 3.4, but respecting to soils.	49
Figure 3.6. As in Figure 3.4, but respecting to water.	49
Figure 3.7. Spectral signature of vegetation from MODIS-UCSB spectral library.	50
Figure 3.8. Spectral signature of the five charcoal samples.	53
Figure 3.9. Burned area stored at the USGS Digital Spectral Library. Adapted from http://speclab.cr.usgs.gov/spectral-lib.html	54
Figure 3.10. Computed reflectance values in channels 20 (MIR) and 2 (NIR) for samples belonging to vegetation, water and soil classes as stored in the JHU directory at ASTER spectral library, as well as based on samples of burned materials.	54
Figure 3.11. Pressure, temperature and humidity profiles of the six standard model atmospheres prescribed in MODTRAN.	58

Figure 3.12. Standard deviation (SD) of the MODIS and the three ECMWF (TRO, MLS and MLW) SD profiles of mass mixing ratio (solid curves) and temperature (dashed curves). 59

Figure 4.1. Contribution to the MIR signal due to surface emission (SE), surface reflection (SR), atmospheric emission (AE) and atmospheric scattering (AS) for TRO atmospheric profile, considering all simulations. 64

Figure 4.2. Monthly values of P75 of LST during August, 2008 over Brazil. Data were retrieved from METEOSAT-8/SEVIRI data. 70

Figure 4.3. Monthly values of P75 of SZA as obtained from samples of Aqua/MODIS and Terra/MODIS imagery along the year of 2007 over Brazil. The threshold of 40° for SZA is highlighted by the dotted horizontal line. Dotted vertical lines delimit the fire season in Amazonia (June to October). 71

Figure 4.4. Relative error [%] on MIR reflectance in the case of MLW for charcoal (left panel) and vegetation (right panel). Solid (dotted) curves indicate positive (negative) errors and the thick curve highlights the no-error line. 75

Figure 4.5. As in Figure 4.4 but in the case of MLS. 75

Figure 4.6. As in Figure 4.4 but in the case of TRO. 75

Figure 4.7. Plot of the ratio L_e/L_{MIR} [%] as a function of LST in the case of MLW (left panel) and TRO (right panel). Square (circle) symbols denotes charcoal (vegetation) surface whereas open (black) symbols characterizes SZA of 0° (60°). 77

Figure 4.8. Diagram of values of reflectance for vegetation and charcoal surfaces for different atmospheric profiles, LST and SZA; a) the two surfaces with prescribed constant values of 0.03 and 0.24 for vegetation (green) and charcoal (orange); b) to d) retrieved values of reflectance using Eq. (4.11) as a function of SZA and LST for MLW, MLS and TRO profiles. 78

Figure 4.9. Location of the Ilha Grande National Park, between the states of Paraná and Mato Grosso do Sul (upper right panel) in southwestern Brazil (upper left panel) and

- Landsat TM image (RGB 543) of the National park before the fire episode, on April 26, 2006 (lower left panel) and after the fire episode on May 12, 2006 (lower right panel). The outline of the National Park is shown in red. 81
- Figure 4.10 MODIS mean profiles (bold curves) of temperature (left panel) and humidity (right panel) over Ilha Grande National Park on May 12, 2006. The TRO profile stored at MODTRAN-4 is also represented (thin curves). 82
- Figure 4.11. Retrieved values of surface MIR reflectance (left panel) and LST (right panel) over the Ilha Grande National Park on May 12, 2006. 83
- Figure 4.12. Histograms of MIR reflectance for burned (black) and unburned (gray) classes as retrieved by means of Eq. (4.11) for May-12 (upper panel), TRO (middle panel) and TRO-HOT (lower panel) environments. 85
- Figure 5.1. Sensitivity of MODIS channel 20 to small changes in temperature. The dashed line indicates the values of $NE\Delta T$ and $NE\Delta L$. 93
- Figure 5.2. Frequency histogram of the satellite radiance perturbations for MODIS channel 20. 94
- Figure 5.3. Comparison between the perturbed profiles (black curves) and respective reference profile (white curve) of water vapor mass mixing ratio (upper panel) and temperature (lower panel). Adapted from Peres and DaCamara (2004). 96
- Figure 5.4. Distributions of the perturbed atmospheric parameters, namely one-way total atmospheric transmittance, two-way total atmospheric transmittance, atmospheric upward radiance and atmospheric downward radiance, respecting to MODIS channel 20 for TRO standard atmosphere. 97
- Figure 5.5. As in Figure 5.4 but for MLS standard atmosphere. 97
- Figure 5.6. As in Figure 5.4 but for MLW standard atmosphere. 98
- Figure 5.7. Frequency histogram of the errors in LST. 99

- Figure 5.8. Accuracy in the retrieval of MIR reflectance using Eq. (4.2), for TRO, MLS and MLW, three view angles, three solar zenith angles and for charcoal (full lines) and pine tree (dashed lines). 101
- Figure 5.9. Dependence of the logarithm of retrieval error on LST and SZA for TRO profile. 102
- Figure 5.10. Dependence of land surface temperature of errors in the retrieval of MIR reflectance of charcoal for TRO, MLS and MLW for nadir view and four solar zenith angles. 102
- Figure 5.11. Dependence on LST of the different terms of Eq. (4.2). 104
- Figure 5.12. Error in MIR reflectance using Eq. (4.2) as obtained from each set of imposed perturbations on TRO profile as a function of four solar zenith angles (0° , 30° , 45° and 60°) and three view zenith angles (0° , 30° and 60°) in the case of a charcoal surface. 106
- Figure 5.13. As in Figure 5.12 but for a vegetated surface. 106
- Figure 5.14. As in Figure 5.12 but for the MLS profile. 107
- Figure 5.15. As in Figure 5.13 but for the MLS profile. 107
- Figure 5.16. As in Figure 5.12 but for the MLW profile. 108
- Figure 5.17. As in Figure 5.13 but for the MLW profile. 108
- Figure 5.18. As in Figure 5.9, but for an offset of +1 K in LST. 109
- Figure 5.19. As in Figure 5.18, but for the MLW atmosphere. 110
- Figure 5.20. Comparison between the total errors when using KR94 (labeled as KFE) and RTE in the case of TRO. 113
- Figure 5.21. As in Figure 5.20 but in the case of MLS. 114
- Figure 5.22. As in Figure 5.20 but in the case of MLW. 115
- Figure 5.23. MODIS images (02/28/2001) over Los llanos, Venezuela/Colombia, South America: a) MODIS channel 20 radiance; b) MODIS LST product cloud mask; c) RGB

- from MODIS channels 7, 2 and 1; d), e) and f) zooms of a burned scar (red square) of a), b) and c), respectively. Black pixels denote NaN. 118
- Figure 6.1. MIR and NIR reflectance bi-spectral space showing the reflectance convergence point of recently burned areas samples extracted from MODIS imagery covering the north, northwest and midwest of Brazil. Dashed-dot lines delimit the upper and lower bounds in MIR and NIR and their intersection is the convergence point. 128
- Figure 6.2. Pre- (open symbols) and post-fire (black symbols) mean values of MIR and NIR over 12 selected scars in the Amazon (circles) and Cerrado (squares). Displacement vectors and contour lines of ξ (left panel) and η (right panel) are represented by solid and dotted lines, respectively. 129
- Figure 6.3. The unit square U in the x - y space and the kite domain U' in the η/ξ space, together with a set of points in U and the respective images in U' . 132
- Figure 6.4. Location in the η/ξ space of laboratory measurements respecting to five types of materials. 134
- Figure 6.5. Images in the space η/ξ of the points shown in Figure 6.2. 135
- Figure 6.6. Coordinate lines $V=\text{const}$ (from -1 to 1 with intervals of 0.2) and $W=\text{const}$ (from 0 to 1 with intervals of 0.2) over the kite domain U' . 139
- Figure 6.7. The spider web (V, W) in the MIR/NIR space. Contour lines of V from -1 to 1 (with intervals of 0.2) and contour lines of W from 0 to 1 (with intervals of 0.1). 139
- Figure 6.8. As in Figure 6.4 (left panel) and in Figure 3.10 (right panel) but with representation of coordinate curves of V (thin lines) and of W (thick lines) on spaces η/ξ and MIR/NIR, respectively. Laboratory measurements include discrimination among soil types. 141
- Figure 6.9. As in Figure 6.8 but respecting to pre- and post-fire pixels as shown in Figure 6.5 (left panel) and in Figure 6.2 (right panel). 141
- Figure 6.10. Comparison between RGB (721) from MODIS showing scene number 3 and two false color images respectively from V and W coordinates. 143

Figure 6.11. Scatter plot (gray points) of MODIS pixels corresponding to scene 3 in the R/NIR space (left panel), in the MIR/NIR space (middle panel) and in the η/ξ space and respective coordinate lines of V and W (right panel). Selected pixels corresponding to burned surfaces, soil, vegetation and clouds are respectively represented by red, yellow, green and cyan crosses. 145

Figure 6.12. As in Figure 6.11 but corresponding to scene 4. Selected pixels representative of burned surfaces, soil, vegetation and water are respectively represented by red yellow, green and blue crosses. 145

Figure 6.13. As in Figure 6.11 but respecting to scene 6. Selected pixels corresponding to burned surfaces, soil, vegetation, sparse vegetation and cloud shadows are respectively represented by red yellow, green brown and black crosses. 146

Figure 6.14. As in Figure 6.11 but corresponding to scene 8. Selected pixels representative of burned surfaces, soil and vegetation are respectively represented by red, yellow, and green crosses. 146

Figure 6.15. Comparison of results of k-means corresponding to scene 3 in the η/ξ (left panel) and the geographical (central panel) spaces with the RGB (543) of the corresponding high resolution ETM+ image (right panel). See main text for color codes of clusters. 148

Figure 6.16. As in Figure 6.15, but corresponding to scene 4. 149

List of Tables

Table 3.1. MODIS channels specifications.	39
Table 3.2. ETM+ channels specifications.	41
Table 3.3. The 16 Landsat ETM+ images used for validation and respective biomes and locations.	46
Table 3.4. ASTER spectral library – vegetation.	47
Table 3.5. ASTER spectral library – soil.	47
Table 3.6. ASTER spectral library – water.	48
Table 3.7. MODIS spectral library – vegetation.	51
Table 3.8. Description of the five charcoal samples.	52
Table 3.9. Air temperature at the first boundary and total water vapour contents of the six standard model atmosphere stored at MODTRAN-4.	57
Table 4.1. Typical values of the different terms of Eq. (4.2) in the case of nadir view and for three different SZA considering a MLW atmospheric profile and a surface temperature equal to 290 K.	66
Table 4.2. Effects of water vapor content [$\text{g}\cdot\text{cm}^{-2}$] on atmospheric terms for the three profiles analyzed, considering nadir view and a SZA of 0° .	73

Table 4.3. Mean values, μ_u (μ_b), and standard deviation, σ_u (σ_b), of unburned (burned) surfaces and discrimination indices, M, for retrieved values of surface reflectance in the case of May-12, TRO and TRO-HOT environments.	86
Table 6.1. Coordinates (x,y) of the considered points in Figure 6.3 (upper panel) and coordinates (η , ξ) of the respective images (lower panel).	133
Table 6.2. Centroids of clusters as obtained from applying k-means to coordinates V and W of the 16 scenes described in Table 3.3.	149
Table 7.1. Comparison of the discriminating ability between burned and unburned surfaces (M index) by means of traditional indices and using the new proposed (V,W) index for three regions over Amazon and Cerrado (see Table 3.3).	156

Acronyms

AE	Atmospheric Emission
AERONET	Aerosol Robotic Network
AFRL	Air Force Research Lab
AOD	Aerosol Optical Depth
ARM	Atmospheric Radiation Measurement
ARPEGE	Action de Recherche Petit Echelle Grande Echelle
AS	Atmospheric Scattering
ASTER	Advanced Spaceborne Thermal Emission and Reflection Radiometer
ATBD	Algorithm Theoretical Basis Document
ATSR	Along Track Scanning Radiometer
AVHRR	Advanced Very High Resolution Radiometer
BAI	Burned Area Index
BRDF	Bidirectional Reflectance Distribution Function
DGI	Divisão de Geração de Imagens
DISORT	Discrete Ordinates Radiative Transfer Program for a Multi- Layered Plane-Parallel Medium

DSA	Divisão de Satélites e Sistemas Ambientais
ECMWF	European Centre for Medium-Range Weather Forecast
ENVI	Environment for Visualizing Images
EOS	Earth Observing System
ETM+	Enhanced Thematic Mapper Plus
ETM	Enhanced Thematic Mapper
FAPAR	Fraction of Absorbed Photosynthetically Active Radiation
FGV	Fraction of Green Vegetation
FOVs	Field of Views
FTP	File Transfer Protocol
GEMI	Global Environmental Monitoring Index
GOES	Geostationary Satellite Server
HDF	Hierarchical Data Format
IBAMA	Instituto Brasileiro do Meio Ambiente e dos Recursos Naturais Renováveis
INPE	Brazilian National Institute for Space Research
ITPP	International TOVS Processing Package
JHU	John Hopkins University
JPL	JET Propulsion Laboratory
KR94	Kaufman and Remer (1994)
LANDSAT	Land Remote Sensing Satellite
LCP	Laboratório de Combustão
LSE	Land Surface Emissivity
LST	Land Surface Temperature
LTE	Local Thermodynamic Equilibrium
MIR	Middle-Infrared
MLS	Mid-Latitude Summer

MLW	Mid-Latitude Winter
MODIS	Moderate Resolution Imaging Spectroradiometer
MODTRAN	Moderate Spectral Resolution Atmospheric Transmittance and Radiance Code
MOD01	MODIS/Terra Level 1A Sensor
MOD07	MODIS/Terra Atmospheric Profiles Product
MOD021	MODIS/Terra S Level 1B 1 km V5 product,
MOD35_L2	MODIS/Terra Cloud Mask Level 2
MYD07_L2	MODIS/Aqua Atmosphere Profile Level 2.0 product
MYD11_L2	MODIS/Aqua LST/E 5-Minute L2 Swath 1 km data set
NASA	National Aeronautics and Space Administration
NCEP	National Center for Environmental Prediction
NDVI	Normalized Difference Vegetation Index
NE Δ L	Noise-Equivalent Radiance Difference
NE Δ T	Noise-Equivalent Temperature Difference
NIR	Near-Infrared
NOAA	National Oceanic and Atmospheric Administration
NWP	Numeric Weather Prediction
PVI	Perpendicular Vegetation Index
P75	Third Quartile
R	Red
RGB	Red Green Blue
RTE	Radiative Transfer Equation
SAS	Sub-Arctic Summer
SAVI	Soil-Adjusted Vegetation Index
SAW	Sub-Arctic Winter
SD	Standard Deviation

SE	Surface Emission
SEVIRI	Spinning Enhanced Visible and Infra-Red Imager
SGP	Southern Great Plains
SNR	Signal-to-Noise Ratio
SPOT	Satellite Pour l'Observation de la Terre
SR	Surface Reflection
SST	Sea Surface Temperature
STD	1976 US Standard
SWIR	Short-Wave Infrared
SZA	Solar Zenith Angle
TE	Thermodynamic Equilibrium
TIR	Thermal Infrared
TISI	Temperature Independent Spectral Index
TM	Thematic Mapper
TOA	Top of the Atmosphere
TOVS	TIROS Operational Vertical Sounder
TRO	Tropical
UCSB	University of California, Santa Barbara
USGS	U.S. Geological Survey
VI	Vegetation Index
VIS	Visible
VSBT	Space Vehicles Directorate
VZA	View Zenith Angle

Chapter 1

Introduction

1.1. Motivation

Over the last decade continuous monitoring of vegetation fires from space has greatly contributed to an increased recognition of the major role played by biomass burning in climate change. In fact, biomass burning is a global source of greenhouse gases (e.g. CO₂ and CH₄) as well as of CO, NO₂, NO_x, CH₃Br and hydrocarbons involved in the formation of acid rain, in the photochemical production of tropospheric ozone and in the destruction of stratospheric ozone (e.g. Crutzen and Andreae, 1990; Penner et al., 1992). High concentrations of aerosol particles in the atmosphere due to biomass burning decrease the amount of global photosynthetic radiation at canopy levels, affecting sensible and latent heat fluxes at the surface (Eck et al., 1998; Schafer et al., 2002; Procopio et al., 2004). At the regional level, biomass burning may induce changes in atmospheric stability and associated vertical motions, leading to alterations of the hydrologic cycle with significant impacts on

regional climate (e.g. Rosenfeld, 1999; Menon et al., 2002; Koren et al., 2004). Teleconnection processes may also take place, inducing changes e.g. of rainfall and surface temperature patterns across distant parts of the world (Chase et al., 2000; Zhao et al., 2001; Pielke et al., 2002). In particular, the study by Evangelista et al. (2007) suggests that almost half of the aerosol black carbon in the South-West Atlantic may derive from South American biomass burning. In addition, vegetation fires are one of the most important causes of land use/cover dynamics (Lambin and Geist, 2006), destroying and altering vegetation structure and depositing charcoal and ash on the surface. Such changes may, in turn, lead to modifications in the ratio of latent to sensible heat flux, the transfer of momentum from the atmosphere and the flux of moisture through evaporation and transpiration (Sellers et al., 1996; Jin and Roy, 2005).

Accordingly, a considerable number of environmental studies and Earth resources management activities require an accurate identification of burned areas. In addition, the apparent global increase in the incidence, extent, and severity of uncontrolled burning have lead to calls for international environmental policies concerning fire (Stocks et al., 2001). Such concerns support the need to provide reliable fire information to policymakers, scientists, and resource managers. However, due to the very broad spatial extent and the limited accessibility of some of the largest areas affected by fire, instruments on-board satellites are currently the only available operational systems capable to collect cost-effective burned area information at adequate spatial and temporal resolutions (Pereira, 1999). Several studies have been carried out using remote sensing images for burned land mapping, covering a variety of techniques based on different spatial, spectral and temporal resolutions. However an accurate algorithm to detect surface changes caused by fire is still hampered by the complexity of the processes involved, the spectral signature of burned areas depending on the type of vegetation that burns, the completeness of the burn, the post fire evolution and regeneration of the vegetation, and the rate of charcoal and ash dissipation. Even if the persistence of the signal is longer for burned areas, the detection of

active fires benefits from the fact that active fires have a spectral signature strongly contrasting with the environmental context (Eva and Lambin, 1998). Besides, there is another essential aspect of the problem which relates to two different post-fire signals, both commonly designated by fire scar (Robinson, 1991); first, the deposition of charcoal and ash on surface and second the alteration of vegetation structure/abundance. The first type of signal is a unique consequence of vegetation combustion, but has relatively short duration and tends to be almost completely erased by wind and rainfall in a few weeks or months after the fire. The second signal is more stable, although its persistence may vary from 2-3 weeks in tropical grasslands to several years in boreal forest ecosystems. However, the second type of signal is less appropriate to discriminate fire effects, since partial or complete removal of plant canopies may also be due to other factors such as cutting, grazing, wind throw, water stress, or the action of insects and pathogens (Pereira et al., 1994).

In such context, reliable detection of burned vegetation from remote sensing requires the use of spectral bands that are sensitive to changes in radiance in response to burning (Trigg and Flasse, 2000). In this particular, most efforts have relied on spectral channels from coarse resolution sensors such as the National Oceanic and Atmospheric Administration/Advanced Very High Resolution Radiometer (NOAA/AVHRR) (Fraser et al., 2000; Martín and Chuvieco, 1993; Pereira, 1999), Satellite Pour l'Observation de la Terre (SPOT/VEGETATION) (Gregoire et al., 2003; Stroppiana et al., 2002), the Along Track Scanning Radiometer (ATSR) data (Eva and Lambin, 1998) and more recently, the Moderate Resolution Imaging Spectroradiometer (MODIS) (Roy et al., 2002; Chuvieco et al., 2008). A large number of such studies have been undertaken using vegetation indices, in particular those based on the AVHRR sensor (Pereira et al., 1994; Caetano et al., 1996; Frederiksen et al., 1990; Malingreau, 1990; Kasischke et al., 1993; Martín and Chuvieco, 1993; Kasischke et al., 1995). Although the AVHRR sensor has been widely applied for burned area mapping, a number of limitations were identified which make AVHRR a less ideal tool for monitoring fire-effects (Barbosa et al., 1999; Martín and Chuvieco, 1995; Pereira, 1999). In contrast, the

MODIS sensor was designed to enhance fire-mapping capabilities and its spectral bands in near-infrared (NIR) wavelengths provide a better spectral discrimination among burned and unburned surfaces (Loboda et al., 2007). Moreover, MODIS produces full global coverage everyday, with a repeat cycle of approximately 1-2 days which is especially relevant for burned area detection in cloudy and smoky regions since it provides further alternative days for analysis.

Current methods for detecting burned areas mainly rely on information in the red (R) and the NIR regions of the electromagnetic spectrum. In fact, the NIR region appears as especially adequate for burned area detection, since the contrast between healthy vegetation (which are highly reflective) and charred surfaces (which are highly absorbent) tends to be very sharp in NIR region. On the other hand, several studies have shown that the visible (VIS) range is not very effective for discriminating burned surfaces (López and Caselles, 1991; Pereira and Setzer, 1993; Razafimpanilo et al., 1995; Pereira, 1999). and have pointed out a number of reasons for such impairment; 1) several common land cover types, namely water bodies and wetlands, some forest types, especially the dense coniferous ones, and many soil types are as dark in the VIS as recent burns, reducing the usefulness of the VIS range to discriminate burns; 2) since Earth observation satellites were designed to image all types of surface features, ranging from the very bright, such as clouds, snow, and deserts, to the very dark ones, such as water, the dynamic range available for discriminating between different types of surfaces, which are dark in the VIS, is narrow; 3) the VIS domain is especially sensitive to aerosol and water vapor scattering and absorption in the atmosphere and therefore its usage for burned area detection may bring unsatisfactory results, in particular because of the presence of heavy smoke layers due to the biomass burning and as well as in case of very moist atmospheres. It is also worth mentioning that the short-wave infrared (SWIR) domain, from 1.2 to 2.5 μm , has also been widely used for burned area detection, with reasonably good results (Pereira and Setzer, 1993; Trigg and Flasse, 2001; Martin et al., 2006).

More recently the middle-infrared (MIR) spectral domain (around 3.75 – 3.9 μm) has been applied for burned area discrimination, since it may contribute to solving certain ambiguities between burned and unburned surfaces which may occur, for example, when using information from other parts of the electromagnetic spectrum, namely the SWIR, especially between 2.0 and 2.5 μm (França and Setzer, 2001). As shown by Libonati et al. (2010) the increase in reflectance over burned surfaces is higher in MIR than in SWIR, allowing a better discrimination between both surfaces. In addition, the spectral response to fire in the MIR domain is similar to that observed in the VIS region, but with a larger increase in brightness and with an unequivocal reduction of sensitivity to atmospheric effects. In fact, one of the major difficulties encountered in the tropics when discriminating burned areas relates to the ephemeral character of spectral signatures, in contrast with temperate and boreal regions, where it is possible to wait until the end of the fire season to map scars from previous months (Pereira, 2003). This procedure is not feasible in tropical savannas, where combustion products are easily scattered by wind, and the charcoal spectral signal quickly fades out. Burning of converted tropical forest produces a short-lived signal, since fire in this region is closely related to pasture and agriculture practices, which disturb the soil surface. In tropical regions, mapping burned areas with remote sensing data has, therefore, to be performed during the dry season, i.e. simultaneously with the fire episodes. Accordingly, results will be, largely affected by smoke aerosols, which contaminate surface observation and reduce the spectral contrast between distinct land cover types. As pointed out by Kaufman (1995), most of these particles may remain in the atmosphere for around a week. In addition, from July to October, i.e. during the Amazon fire season, a large high pressure system tends to dominate the region, inhibiting precipitation and reducing relative humidity due to the subsidence of dry air from the upper levels of the atmosphere (Nobre et al., 1998).

The associated atmospheric circulation favors the retention over a large horizontal area of smoke emitted by fires, reducing visibility to the point of closing airports during, even up to two or three weeks after the end of the fire season (Reinhardt et al., 2001). Under such

circumstances, the MIR spectral band appears especially adequate for monitoring the land surface during fire episodes, because it is largely unaffected by the presence of most aerosols, a highly desired characteristic in remote sensing.

1.2. The Problem

As mentioned above, the MIR spectral domain potentially appears as an optimal way to mitigate the aerosol effects associated to biomass burning, since it is also affected by vegetation changes but is not sensitive to the presence of most aerosols. Pereira (1999) found that the increase in reflectance over burnt surfaces is higher in the MIR than in the VIS and thus considered the NIR/MIR bi-spectral space as more appropriate for burned area discrimination than the classical VIS/NIR space used in remote sensing of vegetation. However usage of the MIR radiation brings up the difficult problem of distinguishing, in a single measurement, between a diversity of radiance sources, namely the thermal emission and the solar reflection from the atmosphere and the surface, as shown in Figure 1.1.

Boyd and Duane (2001) have pointed out that the use of MIR radiation for studying the Earth's surface properties at and beyond the regional scale may be unreliable. At such scales, the emitted radiation component of the signal may be subject to additional confounding variables, rather than representing the intrinsic properties of the surface itself (Kaufman and Remer, 1994). Considering the tropical forest environment, emitted radiation, though related to forest canopy properties, may also be influenced by varying localized atmospheric conditions such as wind speed and air vapour conductance (Price, 1989), site-specific factors such as topography and aspect (Florinsky et al., 1994), and soil moisture conditions (Luvall and Holbo, 1991; Nemani et al., 1993). Indeed, such factors have been more strongly related to emitted radiation from tropical forest canopies than to forest properties such as basal area and tree density (Luvall et al., 1990; Wong, 1993; Nichol,

1995). It may be preferable, therefore, to use only the reflected component of the MIR radiation in the study of tropical forests at regional to global scales.

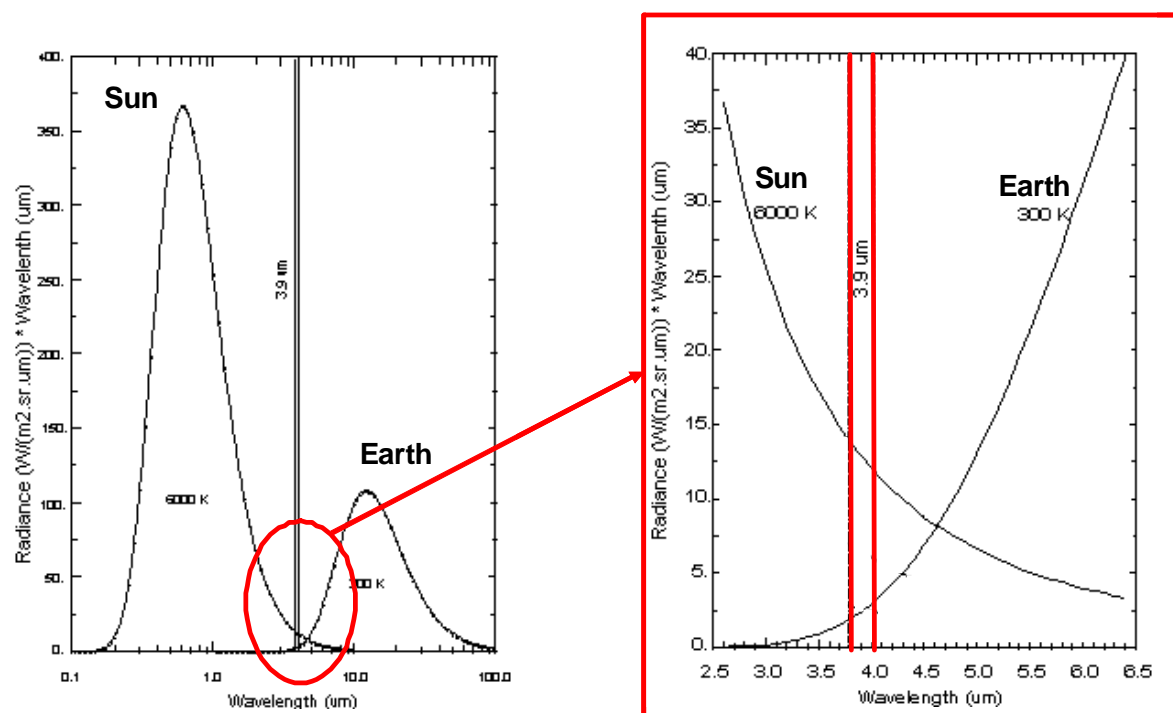


Figure 1.1. Spectrum of emission from the Sun and the Earth highlighting the contributions of both sources of radiation in the MIR domain. Adapted from <http://aerial.evsc.virginia.edu/~jlm8h/class/>.

Methods that take into account the major components of the MIR signal have to rely on information from auxiliary datasets (e.g. atmospheric profiles) and require large computational means (e.g. for radiative transfer computations). Other methods like those proposed by Li and Becker (1993), Nerry et al. (1998) and Petitcolin and Vermote (2002) also require auxiliary datasets and heavy numerical computations. The methodology proposed by Goita and Royer (1997) shows promising potential but need further validation. Schutt and Holben (1991) and Roger and Vermote (1998) proposed the retrieval of MIR reflectance using data provided by the five AVHRR channels but results have significant bias when the surface emissivity in MIR and in thermal infrared (TIR) is not close to unity.

A simple method was proposed by Kaufman and Remer in 1994 where different assumptions are made to separate the thermal and solar components of the MIR signal. This method does not require heavy numerical computations and present the major advantage of avoiding the use of auxiliary datasets. It was first designed to identify dense, dark vegetation areas in mid-latitude environments and has been widely used in burned area discrimination (Roy et al., 1999; Barbosa et al., 1999; Pereira, 1999). However, to the best of our knowledge, no assessment has been made on the required accuracy of the MIR reflectance retrievals to adequately identify burnt areas in tropical environments.

1.3. Main Contributions

Taking into account the issues discussed in the previous sections, the work developed in the present thesis was organized into the following four main contributions and to the best of our knowledge the last three may be regarded as innovative:

1. To perform, for a wide range of atmospheric, geometric and surface conditions, a quality assessment of MIR reflectance data when retrieved using i) the algorithm proposed by Kaufman and Remer (1994) and ii) the complete radiative transfer equation (RTE);
2. To understand the adequacy and limitations of the above mentioned algorithms when applied to burned area discrimination, in particular in the Amazon and Cerrado regions. Special attention will be devoted to the MODIS sensor;

3. To define a strategy that allows achieving an acceptable accuracy in retrieved MIR reflectances for a wide range of atmospheric and surface conditions occurring within the Amazon and Cerrado regions;
4. To develop a bi-spectral index, based on NIR and MIR information, which allows an optimal discrimination of burned areas.

1.4. Publications

Several parts of the results found in the present thesis were published both in conferences and journals with referee. These papers are listed below:

I. Papers published in journals with referees

- 1) Libonati, R.; DaCamara, C. C.; Pereira, J. M. C.; Peres, L. F. (2010). Retrieving middle-infrared reflectance for burned area mapping in tropical environments using MODIS. *Remote Sensing of Environment*, v. 114, p. 831-843, 2010. <http://dx.doi.org/10.1016/j.rse.2009.11.018>.
- 2) Chuvieco, E.; Opazo, S.; Sione, W.; Valle, h.; Anaya, J.; Bella, C.; Cruz, I.; Manzo, L.; Lopez, G.; Mari, N.; Gonzalez-Alonso, F.; Morelli, F., Setzer, A.; Csiszar, I.; Kanpandegi, J. A., Bastarrika, A., and Libonati, R. (2008). Global burned land estimation in Latin America using MODIS composite data. *Ecological Applications*, v. 18, p. 64-79, 2008.

II. Papers submitted to journals with referees

- 1) Libonati, R.; DaCamara, C. C.; Pereira, J. M. C.; Peres, L. F. (2010). On a new coordinate system for optimal discrimination of vegetation and burned areas using MIR/NIR information. *Remote Sensing of Environment*.
- 2) Libonati, R.; DaCamara, C. C.; Pereira, J. M. C.; Peres, L. F. (2010). Retrieval of middle-infrared reflectance using the Radiative Transfer Equation. *IEEE Transactions on Geoscience and Remote Sensing*.

III. Papers in conferences

- 1) Libonati, R., DaCamara, C. C., Pereira, J. M. C., Setzer, A., and Peres, L. F. (2009). Developing an optimal spectral index for burnt scars identification. *2009 EUMETSAT Meteorological Satellite Conference*.
- 2) Libonati, R., DaCamara, C. C., Pereira, J. M. C., Setzer, A., and Peres, L. F. (2009). Retrieval of middle-infrared reflectance using remote sensing data: the tropical point of view. XIV Simpósio Brasileiro de Sensoriamento Remoto.
- 3) Libonati, R., DaCamara, C. C., Pereira, J. M. C., Setzer, A., and Peres, L. F. (2008). On the use of MIR reflectance for burned area identification. 2008 EUMETSAT Meteorological Satellite Conference.
- 4) Libonati, R., DaCamara, C. C., Pereira, J. M. C., Setzer, A., and Peres, L. F. (2008). Effects of the geometry of illumination on the retrieval of MIR reflectance. XV Congresso Brasileiro de Meteorologia.

- 5) Morelli, F., Libonati, R. and Setzer, A. (2007). Refinamento de um método de área queimada, e validação utilizando imagens CBERS no norte de Mato Grosso, Brasil. Simpósio Brasileiro de Sensoriamento Remoto 2007.
- 6) Libonati, R, DaCamara, C. C., Pereira, J. M. C., Setzer, A., and Morelli, F. (2007). A new optimal index for burnt area discrimination. Satellite Imagery. 2007 EUMETSAT Meteorological Satellite Conference and the 15th Satellite Meteorology & Oceanography Conference of the American Meteorological Society.
- 7) Libonati, R., Morelli, F., Setzer, A., DaCamara, C. e Pereira, J.M.C. (2006). Assinatura espectral de áreas queimadas em produtos MODIS. XIV Congresso Brasileiro de Meteorologia.

IV. Abstracts in conferences

- 1) Libonati, R., DaCamara, C. C., Pereira, J. M. C., Setzer, A., and Peres, L. F., (2008). On the use of MIR reflectance for burned area identification. International Radiation Symposium 2008.
- 2) Libonati, R., DaCamara, C. C., Pereira, J. M. C., Setzer, A., and Peres, L. F.,(2008). On the usage of MIR reflectance to detect burnt areas in tropical regions. EUMETSAT 3rd Training Workshop.
- 3) Libonati, R., Morelli, F., Setzer, A., DaCamara, C., e Pereira, J.M.C. (2006). Análise da assinatura espectral de áreas queimadas em produtos MODIS. XII Simposio SELPER.

- 4) Morelli, F., Libonati, R., e Setzer, A. (2006). Avaliação da resposta espectral dos canais 20 e NDVI do MODIS/AQUA na área queimada do parque nacional de Ilha Grande – PR – Brasil. XII Simposio SELPER.

1.5. Thesis Organization

Including the present Introduction, the thesis is organized in seven Chapters. Chapter 2 presents an overview of the fundamentals of radiometric theory in the middle infrared spectral region, as well as of the currently proposed methods aiming to the retrieval of MIR reflectance. The usage of MIR reflectance for burned area discrimination is also discussed in this Chapter. Chapter 3 provides a thorough description of the satellite datasets, sensors used and auxiliary data, and gives a brief overview of the Moderate Spectral Resolution Atmospheric Transmittance and Radiance code (MODTRAN). Chapter 4 deals with the problem of retrieving MIR reflectance by means of the Kaufman and Remer (1994) methodology, and provides an assessment of its advantages and disadvantages for burned area detection. Chapter 5 addresses the problem of inverting the MIR radiative transfer equation and a strategy is defined that allows achieving an adequate accuracy in MIR reflectance retrieval for a wide range of atmospheric and surface conditions occurring within Amazon and Cerrado regions. In this respect, a comparison between RTE and KR94 approaches was carried out, taking into account the performance, the need for auxiliary data and also the required computing resources. The development of a new coordinate system aiming burned area discrimination is presented in Chapter 6 together with its validation over the study area. Finally, Chapter 7 provides a critical review of the results obtained in this work, focusing on the limitations of the proposed index and pointing out some of the possible directions of future research.

Chapter 2

Theoretical background

2.1. Fundamentals of Radiation in MIR

2.1.1. Blackbody concept

A blackbody is defined as an ideal perfectly opaque material that absorbs all the incident radiation at any wavelength and reflects none. When in thermodynamic equilibrium (TE), the emitted radiance of a blackbody is isotropic and is determined by its temperature, T , according to Planck's function given by:

$$B(\lambda, T) = \frac{2hc^2}{\lambda^5 (e^{hc/\lambda T} - 1)} = \frac{C_1}{\lambda^5 (e^{C_2/\lambda T} - 1)} \quad (2.1)$$

where $B(\lambda, T)$ is the spectral blackbody radiance at a given wavelength λ , K is the Boltzmann's constant ($1.381 \times 10^{-23} \text{ J} \cdot \text{K}^{-1}$), h is the Planck constant ($6.626 \times 10^{-34} \text{ J} \cdot \text{s}$), c represents the speed of light in the vacuum ($2.998 \times 10^8 \text{ m} \cdot \text{s}^{-1}$) and T is the absolute temperature of the blackbody. $C_1 = 2hc^2$ is given by ($1.191 \times 10^8 \text{ W} \cdot \text{m}^2 \cdot \mu\text{m}^4 \cdot \text{sr}^{-1}$) and $C_2 = hc/K$ is given by ($1.438 \times 10^4 \mu\text{m} \cdot \text{K}$).

A blackbody emits more than any other body in TE at the same temperature. A blackbody is therefore a perfect emitter as well as a perfect absorber. The radiance emitted by a non-blackbody object at a given wavelength from a surface at thermodynamic temperature T_s is given by multiplying the Planck function by the so-called spectral emissivity $\varepsilon(\lambda)$:

$$L(\lambda, T) = \varepsilon(\lambda)B(\lambda, T_s). \quad (2.2)$$

The atmosphere is not strictly in TE, but below about 70 km a bulk volume of air behaves approximately as a blackbody, so that its radiant emission may be considered as depending only on the respective local temperature. In fact, some of the energy absorbed by every molecule of each chemical species in that volume of air is transferred by the collisional exchange with nearby molecules during the lifetime of the excited molecular in its vibrational or rotational state. If the mean time between molecular collisions is much shorter than the lifetime of the excited molecular state and diffusion time, then a single kinetic temperature characterizes the emission of the gas, to a good approximation. This condition is referred to as local thermodynamic equilibrium (LTE) and prevails up to height of about 70 km at the wavelength of the infrared radiation (Goody, 1964). The concept of LTE plays a fundamental role in radiative transfer studies since the main radiation laws discussed below, which are strictly valid in TE, may be extended to LTE.

2.1.2. Radiative transfer equation in MIR

The atmosphere plays an important role both along the Sun-to-target and target-to-sensor paths and as a source of thermal emission. First the atmosphere may reduce the radiance of the beam throughout absorption as well as by scattering. On the other hand, atmosphere may increase the radiance of the beam by emission plus multiple scattering from all other directions into the direction of its propagation (Liou, 1980). Therefore, under clear-sky conditions, absorption, scattering and emission of radiation by atmospheric constituents (gaseous and aerosols) have also to be taken into account.

Contributions to the total MIR radiation measured by a sensor are illustrated in Figure 2.1. Surface thermal emission [1] is expressed by Eq. (2.2) and depends on the temperature and emissivity, on the wavelength and on the view zenith angle. As the Earth's surface is not a blackbody, the downward radiance emitted by the atmosphere [2] may be reflected by it and propagated up to the sensor together with the downward solar diffuse radiance [3]. During day time, in the MIR spectral domain, part of the direct solar irradiance that reaches the surface is then reflected by it towards the sensor [4]. The other part of the radiance emitted and scattered by the atmosphere that reaches the sensor is represented by the atmospheric upward emitted radiance [5] and by the scattering of solar radiation [6]. The surface emission [1], the downward atmospheric radiance [2], the downward solar diffuse radiance [3] and the reflected direct solar irradiance [4], penetrate the atmosphere and part of them reach the sensor after atmospheric absorption and scattering. Therefore, in clear sky conditions and for an atmosphere in LTE, the top of the atmosphere (TOA) radiance, $L(\lambda, \mu)$ as measured by a sensor in the wavelength λ , is given by:

$$\begin{aligned}
L(\lambda, \mu) &= \tau(\lambda, \mu)\varepsilon(\lambda, \mu)B(\lambda, T_s) + L_{\text{atm}} \uparrow (\lambda, \mu) + L_s(\lambda, \mu, \mu_0, \phi_0) \\
&+ t(\lambda, \mu, \mu_0)f_r(\mu; \mu_0, \phi_0)\mu_0 E_0(\lambda) \\
&+ \int_0^{2\pi} \int_0^1 \mu' f_r(\mu; \mu_0, \phi_0) [\tau'(\lambda, \mu)L_d(\lambda, -\mu', \phi') + t'(\lambda, \mu)L_t \downarrow (\lambda, -\mu', \phi')] du' d\phi'
\end{aligned} \tag{2.3}$$

where μ is the cosine of the viewing zenith angle (θ_v), $\varepsilon(\lambda, \mu)$ is the surface spectral emissivity, $B(\lambda, T_s)$ is the radiance emitted by a blackbody at surface temperature T_s , $L_{\text{atm}} \uparrow (\lambda, \mu)$ is the atmospheric upward radiance, $L_s(\lambda, \mu, \mu_0, \phi_0)$ is the radiance resulting from scattering of solar radiation, $E_0(\lambda)$ is the spectral solar irradiance incident on the TOA (normal to the beam), μ_0 is the cosine of the solar zenith angle (θ_s), ϕ_0 is the relative azimuth between viewing direction and the solar beam direction, $f_r(\mu; \mu_0, \phi_0)$ is the Bidirectional Reflectance Distribution Function (BRDF), $L_d(\lambda, -\mu', \phi')$ is the downward solar diffuse radiance, $L_t \downarrow (\lambda, -\mu', \phi')$ is the atmospheric downward thermal radiance, their incident direction is represented by $-\mu'$ and ϕ' , and τ, τ', t, t' are transmission functions for the corresponding terms.

The wavelength λ in Eq. (2.3) is the wavelength center of a narrow wavelength interval because there is no way to measure the exact monochromatic signal as a continuous function of wavelength satellite sensors (Wan, 1999). Equation (2.3) is the form used in the thermal infrared range 8-14 μm (Wan and Dozier, 1990) generalized to a wider wavelength range of 3-14 μm .

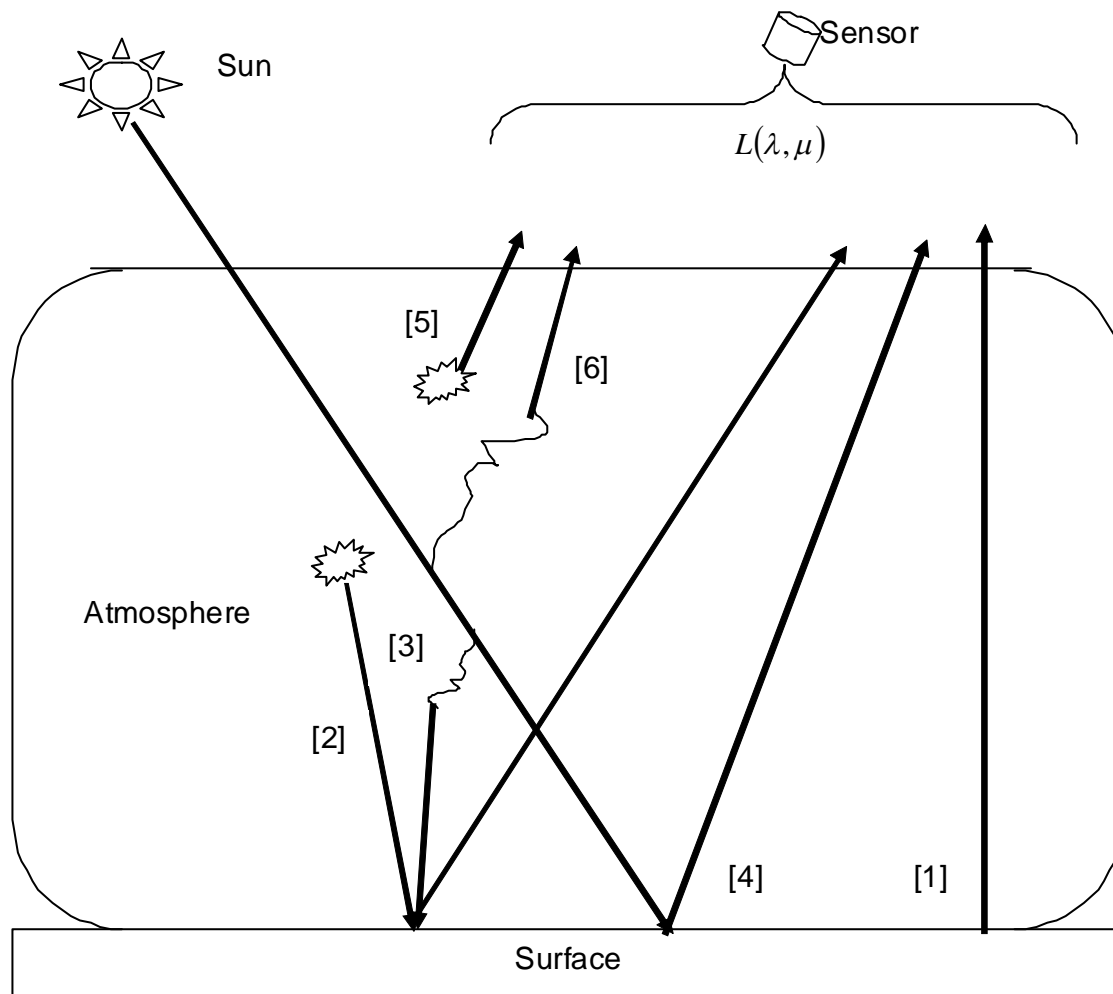


Figure 2.1. Radiative transfer at a middle-infrared wavelength λ .

In order to make practical use of multi-temporal and multi-channel data, it is necessary to simplify Eq. (2.3) by taking some realistic assumptions about the atmosphere and surface properties. First, it is assumed that $\tau(\lambda, \mu) = \tau'(\lambda, \mu)$ and that $\tau(\lambda, \mu) = t'(\lambda, \mu)$, i.e., the transmittances corresponding to the surface emittance, solar diffuse radiation and to the atmospheric downward emitted radiance are assumed to be equal and represented by $\tau(\lambda, \mu)$. This assumption is motivated by the fact that the set of simulated radiances was produced using MODTRAN-4, where these transmission functions are assumed to be equal at wavenumber intervals of 1 cm^{-1} . Second, the surface is considered to be Lambertian, i.e. the surface reflectance is assumed as isotropic. Within the $3 - 14 \text{ }\mu\text{m}$ range the Lambertian

surface approximation does not introduce a significant error in the terms concerning the surface-reflected diffuse solar and surface-reflected atmospheric downward thermal irradiances, since atmospheric radiative transfer simulations show that in clear-sky conditions the surface-reflected diffuse solar irradiance term is much smaller than the surface-reflected solar beam term, and that the surface-reflected atmospheric downward thermal irradiance term is smaller than the surface thermal emission (Wan, 1999).

However, the BRDF effects should be taken into account in the case of the reflection of the direct solar radiation ($E_0(\lambda)$). The assumption of a Lambertian surface is nevertheless often considered in the literature (Li and Becker, 1993; Goita and Royer, 1997; Roger and Vermote, 1994), mainly on practical grounds so that only one reflectivity measurement is enough to retrieve emissivity. Jiang and Li (2008) have shown that the maximum deviation in the bi-directional reflectance with solar zenith angle (from 0° to 60°) is about 0.025 with mean values around 0.02.

In the present work, the Lambertian assumption was also made for the following two reasons. On the first hand, for charcoal reflectance in MIR (around 0.24) the above-mentioned deviation around 0.02 in the bi-directional reflectance with solar zenith angle accounts for 10%, whereas for vegetation reflectance in this wavelength (around 0.03) is of the same order of magnitude. Accordingly, even in case of a high deviation in vegetation, this order of magnitude for errors will not significantly affect the distinction between charcoal and vegetated surfaces. On the second hand, MODTRAN has several parameterized BRDF representations and therefore it is necessary to accommodate angularly varying bi-directional reflectance distribution functions. However, angular dependences with this wavelength range are not available in the literature for our broad selection of cover types. Besides, incorporating any real surface BRDF would probably not change the main conclusions drawn in this study.

By taking the Lambertian assumption, the BRDF function $f_r(\mu; \mu_0, \phi_0)$ in Eq. (2.3) may be replaced by ρ/π , where ρ is the reflectance of the assumed Lambertian surface, and then linked to the surface emissivity ε , since according to Kirchhoff's law $\rho = 1 - \varepsilon$.

Based on the above assumptions, Eq. (2.3) becomes:

$$\begin{aligned}
L(\lambda, \mu) &= \tau(\lambda, \mu)\varepsilon(\lambda, \mu)B(\lambda, T_s) + L_{atm} \uparrow(\lambda, \mu) + L_s(\lambda, \mu, \mu_0, \phi_0) \\
&+ \frac{(1 - \varepsilon(\lambda, \mu))}{\pi} t(\lambda, \mu, \mu_0)\mu_0 E_0(\lambda) \\
&+ \int_0^{2\pi} \int_0^1 \mu' \frac{(1 - \varepsilon(\lambda, \mu))}{\pi} \tau(\lambda, \mu) [L_d + L_t \downarrow] d\mu' d\phi'.
\end{aligned} \tag{2.4}$$

Integrating the last term and taking into account that both the surface and the radiance are considered as isotropic:

$$\begin{aligned}
L(\lambda, \mu) &= \tau(\lambda, \mu)\varepsilon(\lambda, \mu)B(\lambda, T_s) + L_{atm} \uparrow(\lambda, \mu) + L_s(\lambda, \mu, \mu_0, \phi_0) \\
&+ \frac{(1 - \varepsilon(\lambda, \mu))}{\pi} t(\lambda, \mu, \mu_0)\mu_0 E_0(\lambda) + (1 - \varepsilon(\lambda, \mu))\tau(\lambda, \mu)\bar{L}_{atm} \downarrow
\end{aligned} \tag{2.5}$$

where $\bar{L}_{atm} \downarrow = \left(\frac{E_d + E_t}{\pi} \right)$.

2.1.3. Channel equivalent quantities

Equations (2.3), (2.4) and (2.5) represent radiance at a particular wavelength λ , however, as already pointed out, real sensors do not measure radiance at a unique wavelength, but over a finite range. Therefore, the so-called channel-average radiance,

defined as the radiance recorded in a given channel i by a sensor on-board a satellite observing the Earth's surface, is given by:

$$L_i = \int_{\lambda=\lambda_1}^{\lambda=\lambda_2} \Phi_i(\lambda) \tau_\lambda \varepsilon_\lambda B_\lambda(\lambda, T_s) d\lambda + \int_{\lambda=\lambda_1}^{\lambda=\lambda_2} \Phi_i(\lambda) L_{atm,\lambda} \uparrow d\lambda + \int_{\lambda=\lambda_1}^{\lambda=\lambda_2} \Phi_i(\lambda) L_{s,\lambda} d\lambda + \int_{\lambda=\lambda_1}^{\lambda=\lambda_2} \Phi_i(\lambda) \tau_\lambda \frac{1-\varepsilon_\lambda}{\pi} \mu_0 E_{0,\lambda} d\lambda + \int_{\lambda=\lambda_1}^{\lambda=\lambda_2} \Phi_i(\lambda) \tau_\lambda (1-\varepsilon_\lambda) \bar{L}_{atm,\lambda} \downarrow d\lambda \quad (2.6)$$

where $\Phi_i(\lambda)$ is the normalized spectral response function of the sensor in channel i (see Chapter 3), and λ_1 and λ_2 are respectively the lower and the upper limit of the channel spectral range. The channel response functions define the channel ranges and characterize the response of a given sensor to available radiance in a particular wavelength range.

In the case of channels with a narrow spectral range ($\sim 1.0 \mu\text{m}$), the radiance given by Eq. (2.6) may be expressed, without significant errors, in terms of channel-equivalent quantities, namely $\varepsilon_i, \tau_i, B_i, L_{s,i}, L_{atm,i} \uparrow, \bar{L}_{atm,i} \downarrow, E_{0,i}$, i.e.,

$$L_i = \tau_i \varepsilon_i B_i(T_s) + L_{atm,i} \uparrow + L_{s,i} + t_i \left(\frac{1-\varepsilon_i}{\pi} \right) \mu_0 E_{0,i} + \tau_i (1-\varepsilon_i) \bar{L}_{atm,i} \downarrow \quad (2.7)$$

where the channel-equivalent quantities $\varepsilon_i, \tau_i, B_i, L_{s,i}, L_{atm,i} \uparrow, \bar{L}_{atm,i} \downarrow, E_{0,i}$ are given by

$$\Omega_i = \frac{\int_{\lambda=\lambda_1}^{\lambda=\lambda_2} \Phi_i(\lambda) \Omega_\lambda d\lambda}{\int_{\lambda=\lambda_1}^{\lambda=\lambda_2} \Phi_i(\lambda) d\lambda} \quad (2.8)$$

the mute variable Ω standing for $\varepsilon_i, \tau_i, B_i, L_{s,i}, L_{atm,i} \uparrow, \bar{L}_{atm,i} \downarrow, E_{0,i}$.

It is worth noting that the symbols respecting to the view and solar angles were neglected in Eq. (2.7). The first term on the right-hand side of Eq. (2.7) represents the radiance emitted by the surface that is attenuated by the atmosphere. The second term denotes the radiance emitted by the atmosphere towards the sensor. The third term represents atmospheric scattering. The fourth term stands for the solar radiance that is attenuated by the atmosphere in its downward path, then reflected by the surface and again attenuated in its upward path to the sensor. The last term denotes the downward atmospheric radiance that is reflected by the surface and then attenuated in its upward path to the sensor.

2.2. Retrieval of MIR reflectance

As pointed out in the previous sections, the retrieval of MIR reflectance from the total radiance measured by a sensor is a very difficult task, since the total MIR radiance is a combination of an emitted and a reflected radiance. It is a non-linear and under-determined problem with three other unknowns beyond the target reflectance, namely the surface temperature, the atmospheric state and the BRDF. The latter unknown may be replaced by MIR emissivity or any relation between MIR bidirectional reflectance (Boyd and Petitcolin, 2004) but, even considering a Lambertian surface, an accurate retrieval of MIR reflectance still requires a proper characterization of the atmosphere influence and an adequate knowledge of the land surface temperature (LST). Such as in the case of the retrieval of LST, the main difficulty is that the data are non-deterministic (Gillespie et al., 1999) and therefore the algorithms differ according to the hypothesis assumed in order to generate a new equation that closes the problem and reduces it to a unique solution. In this section a thorough review will be undertaken of the current algorithms for MIR reflectance retrieval.

1) Becker and Li (1990). The so-called Temperature Independent Spectral Index (TISI) method aimed at the separation of land surface emissivity (LSE) and LST, a problem that requires retrieving the MIR reflectance. The approach is based on the fact that around 3.75 μm (e.g., AVHRR channel 3) the radiance emitted by land surface and the reflected radiance due to sun irradiation during the day, are of the same order of magnitude. The general idea behind the method is to make use of the emission at night to estimate the emissive part of the signal at daytime by means of a TISI. Using combined day/night data and TISI, the emitted part of the radiance is calculated allowing for the determination of the reflected part (Li and Becker, 1993). It may be further noted that the method relies on the Lambertian assumption.

Since the TISI method is applicable only to ground-level radiances, atmospheric correction needs first to be performed. Moreover the use of the method may be compromised by the requirement of consecutive day and night acquisitions (so that the surface conditions do not change). Other issues inherent to the method include the need for precise image geo-location and cloud cover occurrence.

2) Kaufman and Remer (1994). The method was originally designed to identify dense, dark vegetation areas in mid-latitude environments where aerosols loading can be assessed using AVHRR sensor. The proposed approach for retrieving MIR reflectance requires neither direct knowledge of atmospheric conditions, nor a radiative transfer model and considers a Lambertian surface. The approach is based on the studies of Gesell (1989) and Ruff and Gruber (1983), who pointed out the existence of a mutual compensation between attenuation and thermal emission terms, so that both atmospheric transmittances may be assumed as equal to unity, and both the atmospheric downward and upward thermal emission terms may be neglected. Kaufman and Remer (1994) introduced another approximation, which consists of using the brightness temperature, from a TIR band (10 - 12 μm) as a surrogate for the LST.

A number of assumptions are used for land emissivity and BRDF as well as for all atmospheric effects. Nevertheless, the method represents the first attempt to derive and apply MIR reflectance in a land based application.

3) Goita and Royer (1997). This method aimed at the separation of surface temperature and emissivity over land without any *a priori* knowledge of these variables. The work of Becker and Li (1990) is at the root of the method in the sense that it uses MIR reflectance as a step towards the derivation of thermal emissivity. Atmospheric contributions to the MIR signal are accounted for by using a radiative transfer code such as MODTRAN, together with a description of the atmospheric state. Placed in such configuration, the method assumes an *a priori* knowledge of the solar irradiance at ground level as well as of the atmospheric downward emission and presupposes that the ground level brightness temperature in MIR and TIR channels may be derived because upward atmospheric transmission and emission are known. The model requires two consecutive measurements in MIR and TIR channels and relies on the assumption that MIR reflectance and TISI do not change between the two records. The method is hard to reproduce operationally and computing is time consuming.

4) Nerry et al. (1998). This method aims at the operational retrieval of MIR reflectance using day- and night-time measurements of MIR and TIR radiation using AVHRR data at the regional scale. The approach is based on Li and Becker's method, incorporating minor modifications. Nerry et al. (1998) have shown that the Lambertian approximation may lead to considerable uncertainties because the reflected radiance is not small with respect to the surface-emitted radiance. In such context, they have determined the so-called angular form factor $R_i(\theta, \varphi)$, that quantifies how much the reflectance of a non-Lambertian surface differs from that of a Lambertian reflector ($R_i(\theta, \varphi) = 1$) and allows taking into account land-surface anisotropy. The method assumes that combination of MIR and TIR emissivities does not change significantly between the two measurements made at day- and night-time.

Atmospheric effects are computed using the MODTRAN radiative transfer model which is run using atmospheric data extracted from analysis fields of the global circulation model ARPEGE provided by the French meteorological service. No account is made for solar contributions to the MIR radiative signal due to scattering in the atmosphere.

The method has the advantage of not assuming a Lambertian behavior of the surface, allowing for the study of the angular variation of MIR reflectance. However, like other similar methods, there may be limitations to its application since the main assumption is that the combination of MIR and TIR emissivities does not change between day- and nighttime acquisitions. This assumption may be compromised in case of rapid changes of the surface state (e.g. surface drying, or snow melt) or when faced with two different viewing directions. The latter means that the product of MIR and TIR emissivities at specific powers is assumed to be independent of the viewing direction.

5) Roger and Vermote (1998). The method presents a formula for computation of the reflectance in MIR, in particular for AVHRR channel 3. The formulation takes into account emissivity, emitted radiation, and atmospheric transmission without the need for any ancillary data other than those provided by the five AVHRR channels. MIR reflectance is computed by subtracting the thermal contribution from the total signal and then dividing the remaining signal component by atmospheric transmission and solar irradiance. The thermal contribution is estimated by using thermal infrared channels as well as the Normalized Difference Vegetation Index (NDVI) to estimate infrared surface emissivities. The atmospheric transmission is computed with MODTRAN and uses integrated water vapor as derived from the split window technique (Wan and Dozier, 1996).

This method builds on that developed by Kaufman and Remer (1994) with attention paid to atmospheric effects on the MIR radiative signal through the use of the radiative transfer code and a simulation dataset. The retrieved MIR reflectance is successfully validated over water in the case of sun glint with comparisons made against that computed

with the Cox and Munk (1954) model. An indirect validation using the MIR land surface temperature was also conducted; however, there was a limited number range of land cover types evaluated. Assumptions made include that of Lambertian target behavior.

6) *Petitcolin and Vermote (2002)*. This study aimed at the operational retrieval of MIR reflectance in order to encourage its inclusion in the MODIS surface reflectance product. The method first requires the atmospheric correction of the middle to thermal infrared radiances. The atmospheric correction scheme is based on MODTRAN and atmospheric profiles were extracted from analysis of the global circulation model as provided by the US National Center for Environmental Prediction (NCEP). The second requirement is the construction and use of a database of night emissivity ratios. Here, two aspects of Becker and Li's (1990) method were modified according to the findings of Petitcolin et al. (2002), who demonstrated that the products of MIR and TIR emissivities, all derived from night-time observations, do not change significantly over several weeks, or at least that variations of view angle and surface state have less impact on them than instrumental noise or inaccuracies introduced by the atmospheric correction scheme. The first modification consisted on the accumulation of 16 days of night-time acquisitions at the same location in order to average the products of MIR and TIR emissivities. The second modification was the introduction of an advanced BRDF model, namely the kernel-driven BRDF model of Lucht et al. (2000), with the MIR reflectance obtained during a 16-day period. MIR hemispherical reflectance is computed with the same scheme as for MODIS reflectance in visible and near-infrared (Strahler et al., 1999) that is able to adequately represent the various BRDF shapes of natural surfaces. The BRDF model is then used to derive MIR directional emissivity. Petitcolin and Vermote (2002) validated their retrieved MIR reflectance over water for two cases; 1) in case of no sun-glint, very low MIR reflectance values were obtained and 2) when sun-glint occurred, MIR reflectance was in agreement with that of the Cox and Munk (1954) model. Assumptions made in this method are similar to those of Nerry et al. (1998).

The above-described methods clearly show that retrieving MIR reflectance from satellite data is not an easy task due to the complexity of the total MIR radiative signal, which has three sources of radiation (sun, surface and atmosphere) and three type of interactions (emission, absorption and reflection) with the two media (surface and atmosphere). The usefulness of each method depends on the simplifications and assumptions in their formulation, as well as on the nature of the data to be used (e.g. the temporal and spatial resolution and spectral characteristics), and on the available ancillary information (e.g. an accurate description of the atmosphere or a good knowledge about LST). Methods that take into account the major constituents of the MIR signal remain complex and are quite difficult to apply without the help of important auxiliary datasets and major computational requirements.

The theoretical work of Li and Becker (1993) forms the basis for a family of MIR surface reflectance retrieval methods. These methods (Nerry et al., 1998; Petitcolin and Vermote, 2002) provide the quantitative estimation of MIR reflectance with acceptable accuracy. However, they require large auxiliary datasets and heavy numerical computations for the atmospheric corrections. The method developed by Kaufman and Remer (1994) is the simplest, but relies on many assumptions that may impair an accurate estimation of MIR reflectance. This method, alike the one adopted by Roger and Vermote (1998), performs well over areas with dense vegetation, or water surfaces, because assumptions made for the estimation of MIR thermal emission have limited impact on MIR reflectance. However, they introduce significant bias when the surface emissivity in MIR and TIR is not close to unity, for instance over bare soil. Finally, the two methods proposed by Goita and Royer (1997) show promising potential but require further testing and validation.

2.3. Usage of MIR reflectance for burned area discrimination

A large number of studies have shown that use of MIR region is promising for a variety of applications which include discriminating among different vegetation types (Holben and Shimabukuro, 1993; Shimabukuro et al., 1994; Goita and Royer, 1997); estimating the total biomass and leaf biomass of several forest ecosystems (Boyd, 1999; Boyd et al., 2000); monitoring temporal changes in vegetation (França and Setzer, 1998; Boyd and Duane, 2001); and detecting deforestation processes (Amaral, 1992; Di Maio Mantovani and Setzer, 1996; 1997).

MIR reflectance has also proven to be useful when applied to burned area discrimination (e.g. Roy et al., 1999; Barbosa et al., 1999; Pereira, 1999). Healthy vegetation has low MIR reflectance, due to water absorption, and therefore the scorching or combustion of vegetation, and the soil drying caused by fire, are likely causes for the observed increase in MIR brightness. Natural materials seem to display a broader range of reflectance values in the MIR than in the visible, facilitating the discrimination of different land cover types (Figure 2.2). On the other hand, the increase in reflectance over burned surfaces is higher in MIR than in the SWIR region (Figure 2.3), allowing a better discrimination between both surfaces.

Besides, atmospheric scattering is very insignificant in this wavelength range, and therefore does not reduce spectral contrast at the surface. The better discriminant ability of the MIR, in comparison with the visible region of the spectrum, appears to be confirmed by studies that identified the MIR-NIR bi-spectral space as more adequate for burned area detection and mapping, than the classical visible-NIR space. For instance, Libonati et al. (2006, 2007) has performed an analysis on the potential of MODIS visible and MIR channels to discriminate burned areas in Cerrado regions of Brazil. MIR channel 20 was evaluated under two configurations, i.e. using the full normalized radiance of the surface (i.e. the sum of emitted and reflected components of the signal) and restricting to the reflected component of the signal. The reflected component was estimated based on the methodology proposed by Kaufman and Remer (1994). The ability of each index to discriminate between burned and

unburned surfaces was assessed by means of a discrimination index similar to the one proposed by Kaufman and Remer (1994), i.e.

$$M = \frac{(\mu_u - \mu_b)}{(\sigma_u - \sigma_b)} \quad (2.9)$$

where μ_u (μ_b) is the mean value for the unburned (burned) class and σ_u (σ_b) the standard deviation for the unburned (burned) class.

Figure 2.4 shows the histograms corresponding to the burned and unburned classes for each evaluated MODIS channel. A full description of MODIS channels is provided in Chapter 3. It may be noted that the degree of overlap between burned and unburned areas is too high for channels 3 ($M=0.10$), 7 ($M=0.24$), 4 ($M=0.40$), 1 ($M=0.51$), and 6 ($M=0.69$). Channel 5 was not considered in this study because it was totally contaminated by noise. Although some overlaps are still observed, obtained results clearly show that the burned and unburned classes are better discriminated when channel 2 ($M=1.06$), the reflected component of channel 20 ($M=0.88$) and the total radiance of channel 20 ($M=0.84$) are used. The histograms also illustrate that burnt surfaces tend to be darker than the background in R (channel 1) and NIR (channel 2), and brighter in MIR (channel 20).

In fact, in most of the studies, the MIR band is commonly used together with the NIR one to identify vegetation and detect its changes, given the strong contrast between these two bands, since green vegetation appears quite bright in the latter and quite dark in the former (Figures 2.2, 2.3 and 2.4).

Vegetation reflectance in the NIR, around $0.8 \mu\text{m}$, is affected primarily by leaf structure (Slaton et al., 2001). Green vegetation exhibits high reflectance values, as the leaf matures the cells enlarge, crowing together, and reducing the intercellular space, consequently decreasing the reflectance (Gates et al., 1965). On the other hand, the use of MIR band in vegetation indices as a surrogate of the traditional R band (around $0.6 \mu\text{m}$), is

based on the fact that MIR reflectance is well correlated to the R one, but is not sensitive to most aerosols. Several authors have pointed out this important advantage of MIR region.

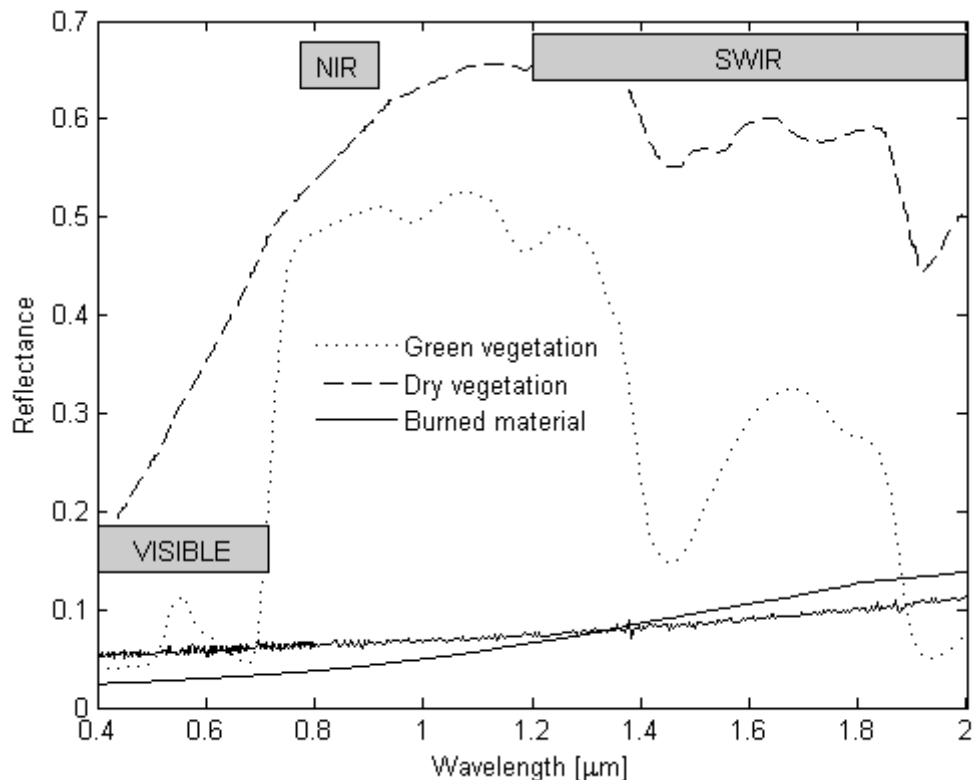


Figure 2.2. Spectral signatures of burned material sample (solid curves), green vegetation (dot curve) and dry vegetation (dashed curve). Gray boxes delimit the VISIBLE (between 0.4 and 0.7), NIR (around 0.8) and SWIR (between 1.0 and 2.0 μm) spectral regions in order to emphasize their contrast. Charcoal signatures were obtained from the USGS Digital Spectral Library as well as from samples provide by the author, whereas vegetation signatures were obtained from the MODIS-UCSB spectral library (see Chapter 3).

Kaufman and Remer (1994) showed that the Mie scattering cross-section of the typical aerosol particle (except dust) at MIR wavelengths is considerably smaller than at shorter wavelengths used in remote sensing; França and Setzer (1998) observed a lack of atmospheric effects on the viewing angle due to the little effects of smoke aerosols in AVHRR channel 3, and more recently Libonati et al. (2010) showed that MODIS MIR channel

20 is unaffected by aerosols associated to smoke from biomass burning events. This feature of MIR becomes well apparent when atmospheric transmittance attenuation is computed over the VIS to MIR bands, for different levels of smoke contamination due to biomass burning. Transmittance attenuation is defined here as the difference between the transmittance from an aerosol-free atmosphere and that from an atmosphere with a given level of smoke contamination.

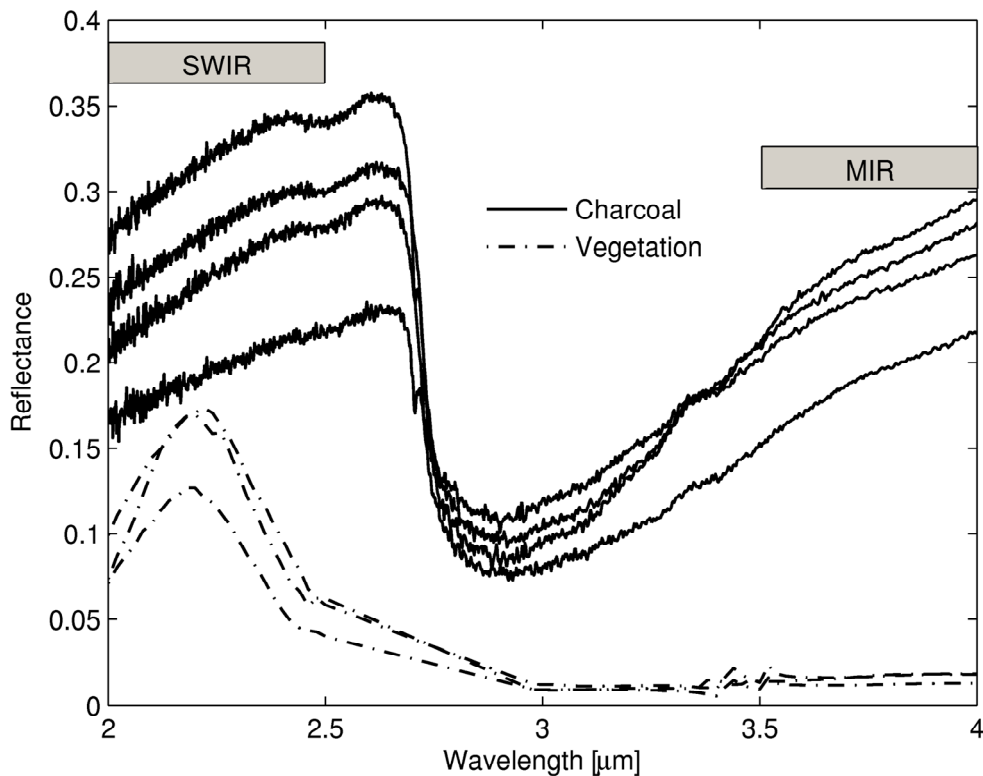


Figure 2.3. Spectral signatures of four charcoal samples (solid curves) and of three vegetation samples (dot-dashed curves). Gray boxes delimit the SWIR (between 2.0 and 2.5 μm) and MIR (between 3.5 and 4 μm) spectral regions in order to emphasize their contrast. Charcoal and vegetation signatures were respectively obtained from samples of fire residues from Alta Floresta (see next Chapter), state of Mato Grosso, Brazil and from the Advanced Spaceborne Thermal Emission and Reflection Radiometer (ASTER) spectral library (Baldrige et al., 2009).

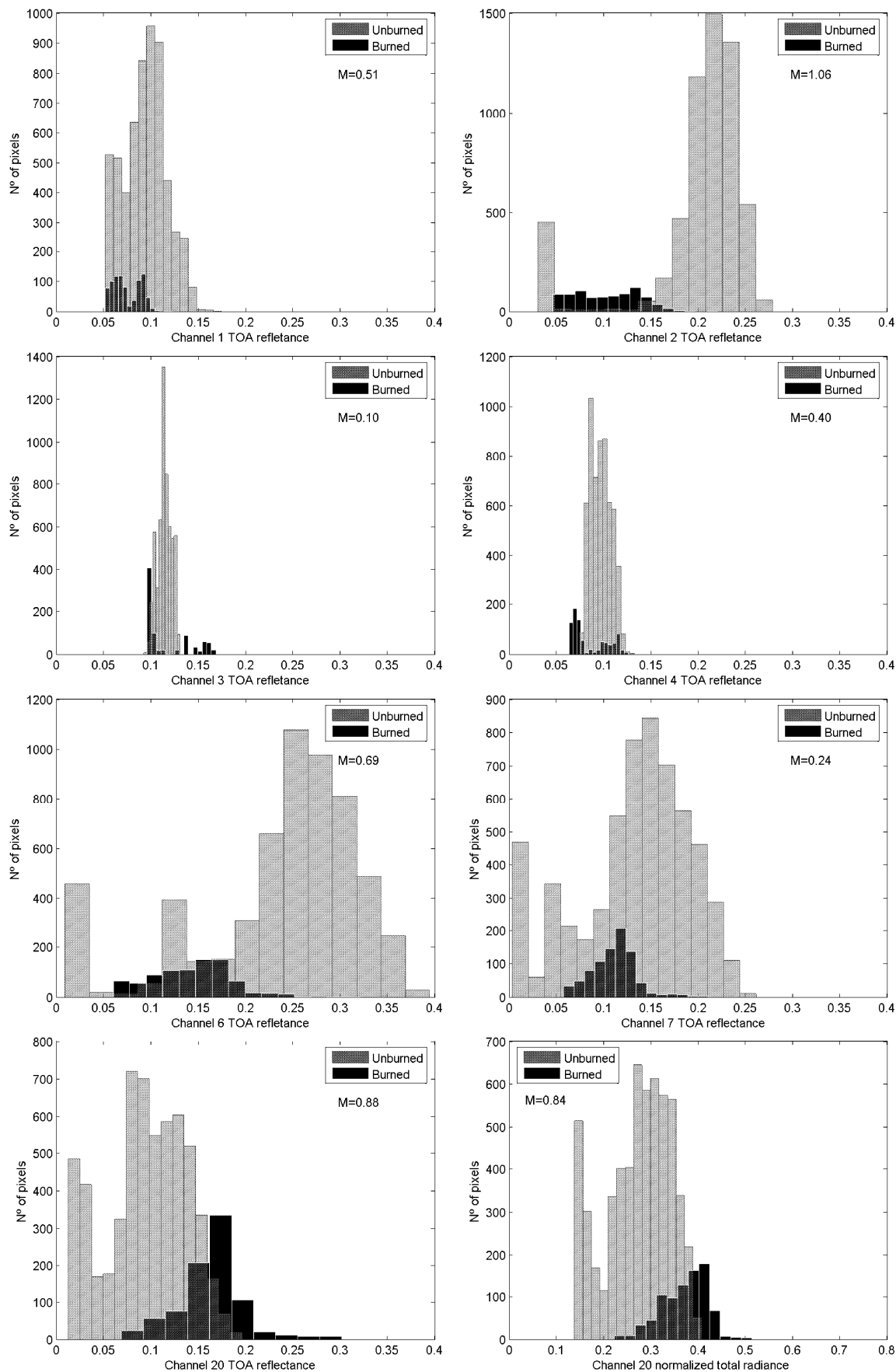


Figure 2.4. Histograms of the burned and unburned classes for MODIS channels.

Figure 2.5 shows the impact on MODIS VIS to MIR channels resulting from increasing the aerosol optical depth (AOD) associated to biomass burning. Values of transmittance attenuation were obtained from radiative transfer simulations performed with MODTRAN-4. The model was run using a Tropical atmospheric profile perturbed with aerosols associated to biomass burning, based on cloud-screened level 2.0 AOD at 550 nm ($\tau_a(0.55)$) data from the Abracos Hill station. Details about MODTRAN and perturbation of the Tropical atmospheric profile by aerosols are given in Chapter 3.

During the dry season, in an atmosphere heavily contaminated by smoke (e.g. with an AOD at 0.55 μm for about 2.73), the VIS and NIR channels (0.4 – 1.0 μm) are inadequate for surface observation. Even at lower levels of contamination by smoke (with an AOD at 0.55 μm lower than 0.72) VIS channels remain strongly affected. Although less sensitive to smoke aerosol, atmospheric transmittance in the SWIR (1.2 – 2.5 μm) spectral region is still markedly attenuated. In striking contrast, the MIR domain is practically unaffected by smoke, allowing for almost undisturbed surface observation. The atmospheric transmittance attenuation displays almost constant low values of atmospheric contamination by smoke in all three cases analyzed, including under extreme AOD conditions. This is a major reason to favor the MIR spectral domain for monitoring and mapping burned areas.

By taking into account the effects of atmospheric water on the attenuation of the electromagnetic spectrum, Bird (1984) and Kerber and Schutt (1986) have demonstrated that the MIR spectral region is one of the few regions with relatively little attenuation, requiring about 10 cm of precipitable water to reduce transmission below 90%. For instance, Figure 2.6 clearly shows the considerable impact of water vapor content in the transmittance over the TIR region in contrast with the small attenuation in MIR for three atmospheric profiles stored at MODTRAN-4.

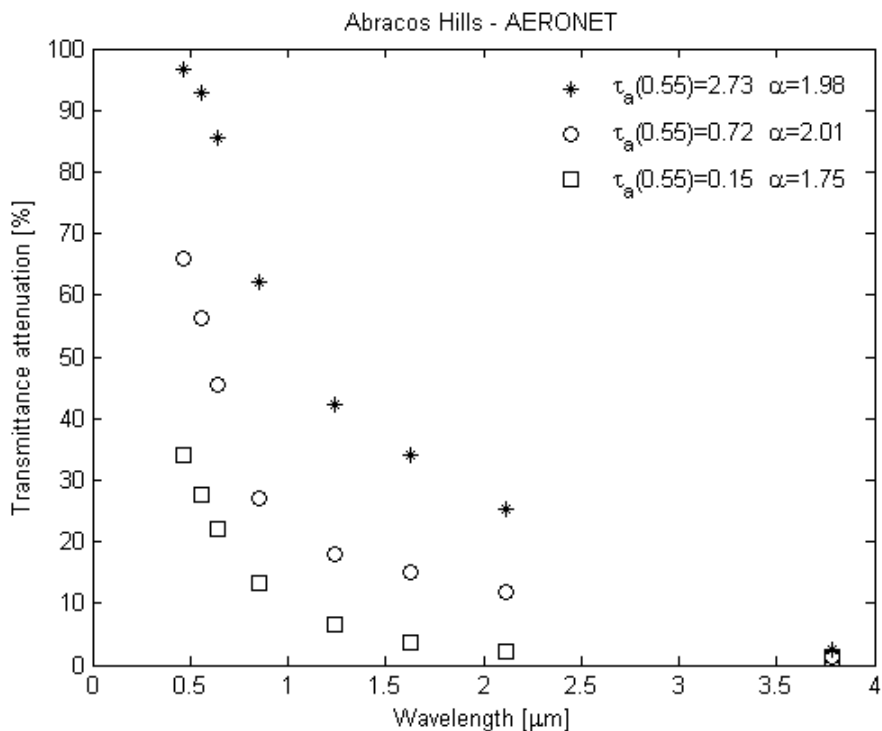


Figure 2.5. Atmospheric transmittance attenuation [%] on MODIS VIS to MIR channels for three different levels of smoke contamination due to biomass burning. $\tau_a(0.55)$ indicates the AOD at $0.55 \mu\text{m}$ and α denotes the Ångström parameter, which characterizes aerosol particle size distribution.

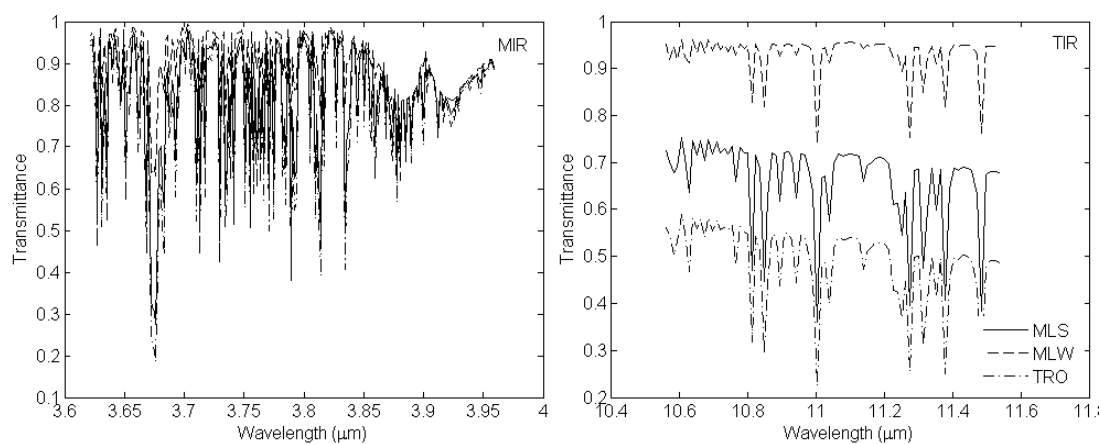


Figure 2.6. Comparison between MIR (left panel) and TIR (right panel) regions concerning the attenuation by water vapor content throughout the three atmospheric profiles (MLS, MLW and TRO) stored at MODTRAN-4 (see Chapter 3 for details).

Kaufman and Remer (1994) have shown that the correlation between MIR and R is due to the simultaneous occurrence of processes that darken the surface in these two bands. Whereas in the visible wavelengths, the pigmentation of leaves, especially by active chlorophyll, absorbs the solar radiation, reducing the reflectivity, in the MIR domain (around 3.7 - 3.9 μm) the cellular water content, present in green vegetation, causes a strong absorption, reducing the reflectance at these wavelengths (Gates, et al., 1965; Salisbury and D’Aria, 1994). As green leaves become senescent due to the decrease of the levels of chlorophyll and the decrease of water content, the absorption of solar radiation decreases in both R and MIR regions, rising the brightness of the two bands.

Regional to global monitoring of burned areas currently involves the use of spectral indices as measured from satellite remote sensors. The MIR/NIR bi-spectral space has been widely used within different vegetation indices, such as the VI3 (Kaufman and Remer, 1994) and the GEMI3 (Pereira, 1999). The VI3 is a modified version of the traditional NDVI, where the red reflectance is replaced by the reflective part of the middle-infrared signal (channel 3 from AVHRR sensor). It was firstly proposed by Kaufman and Remer (1994) aiming at the identification of dark, dense vegetation. Because of the specific characteristics of the MIR spectral region for distinguishing between burned/unburned surfaces as well as its virtual insensitivity to atmospheric effects, Pereira (1999) suggested the application of VI3 for burned scars mapping. The index is defined as following:

$$VI3 = (\rho_{NIR} - \rho_{MIR}) / (\rho_{NIR} + \rho_{MIR}), \text{ for } \rho_{NIR} \geq \rho_{RED}$$

or

$$VI3 = 0, \text{ for } \rho_{NIR} < \rho_{RED}$$
(2.10)

where ρ_{MIR} , ρ_{NIR} and ρ_{RED} are the MIR, NIR and R reflectance, respectively. The restriction that $\rho_{NIR} \geq \rho_{RED}$, protects the index from being applied to water areas where it is ill defined (Kaufman and Remer, 1994).

Pinty and Verstraete (1992) have proposed the so-called Global Environmental Monitoring Index (GEMI), which was specifically designed to minimize contamination of the vegetation signal by extraneous factors, such as the atmosphere and the soil background. Pereira (1999) explored the synergistic effects of the desirable properties of the AVHRR channel 3 reflective components for burned area mapping with the sophisticated nonlinear design of the GEMI. Therefore, the GEMI3 index is an empirical modification of the GEMI, since the values of the coefficients in the GEMI equation, which were kept unchanged, are not expected to retain their original physical interpretation. As in VI3, this decision was based on the fact that the range of reflectance values over the study area was similar for AVHRR channels 1 and 3. GEMI3 is defined as follows:

$$GEMI3 = \eta(1 - 0.25\eta) - (\rho_{MIR} - 0.125)/(1 - \rho_{MIR}) \quad (2.11a)$$

where

$$\eta = (2(\rho_{NIR}^2 - \rho_{MIR}^2) + 1.5\rho_{NIR} + 0.5\rho_{MIR}) / (\rho_{NIR} + \rho_{MIR} + 0.5). \quad (2.11b)$$

Although the above mentioned indices generally provide reasonable results, they are merely empirical in what respects to the respective design. According to the authors responsible for VI3 and GEMI3, the indices are basically based on the fact that MIR and R reflectance are strongly correlated. Moreover, they stressed out that the processes governing the reflectance in R and MIR are not expected to lead to the same value and that there are other processes that may change the reflectance in the two channels.

Taking into account the above-mentioned limitations, at least from the theoretical perspective, the present thesis represents a first attempt to fill the present lack of indices specifically designed to map burned areas. Accordingly, a new burned area index will be developed, adapted to the spectral resolutions of MODIS MIR/NIR channels, and particularly appropriate for the Amazon and Cerrado regions of Brazil. The decision lies on the following grounds:

1. On the first hand, although the AVHRR sensor has been widely applied for burned area mapping, a number of limitations have been identified which made AVHRR a less ideal tool for monitoring fire-effects (Barbosa et al., 1999; Martín and Chuvieco, 1995; Pereira, 1999). In contrast, the MODIS sensor was designed to enhance fire-mapping capabilities and its spectral bands in NIR wavelength provide the better spectral discrimination among burned and unburned surfaces (Loboda et al., 2007). Moreover, MODIS provides full global coverage everyday, with a repeat cycle of approximately 1-2 days which is especially relevant for burned area detection in cloudy and smoky regions since it provides further alternative days for analysis.
2. On the second hand, and although the Brazilian Amazonia together with the adjacent savanna (Cerrado) presents one of the highest numbers of occurrences of fire events (Prins et al., 1998), to the best of our knowledge, hardly any studies have attempted to design burned area indices specifically for these regions.

The development of an index with the above described characteristics would in fact be especially useful for operational purposes taking into account that present thesis the accuracy of burned area maps is closely related to the characteristics of the location where it is applied (e.g., pre-fire land-cover type and conditions, background soil, fire severity, post-fire processes, atmospheric conditions), and that index thresholds are often subjective and/or vary from region to region.

Chapter 3

Sensors, datasets and radiative transfer code

3.1. Satellite sensors characteristics

3.1.1. MODIS coarser resolution sensor

A major instrument for the National Aeronautics and Space Administration (NASA)'s Earth Observing System (EOS) missions, MODIS is currently operating on-board the EOS Terra and Aqua spacecraft, respectively launched on December 1999 and May 2002. Both satellites have sun-synchronous, near-polar, circular orbits at a 705 km nominal altitude and

Terra's orbit around the Earth is timed so that it passes from north to south across the equator in the morning (10:30 AM, descending), while Aqua passes south to north over the equator in the afternoon (1:30 AM, ascending). The entire Earth's surface is viewed every 1 to 2 days by Terra MODIS and Aqua MODIS, the MODIS instrument acquiring data in 36 spectral bands from the visible to the thermal infrared regions of the spectrum at the spatial resolutions of 250 m (bands 1-2), 500 m (bands 3-7) and 1 km (bands 7-36). Together, Terra and Aqua MODIS have already produced more than 10 years of global data sets which have significantly helped scientists worldwide to better understanding the Earth as an interacting system and assessing the impacts on this system due to human related activities. Figure 3.1 presents the normalized spectral response function of the MODIS channels.

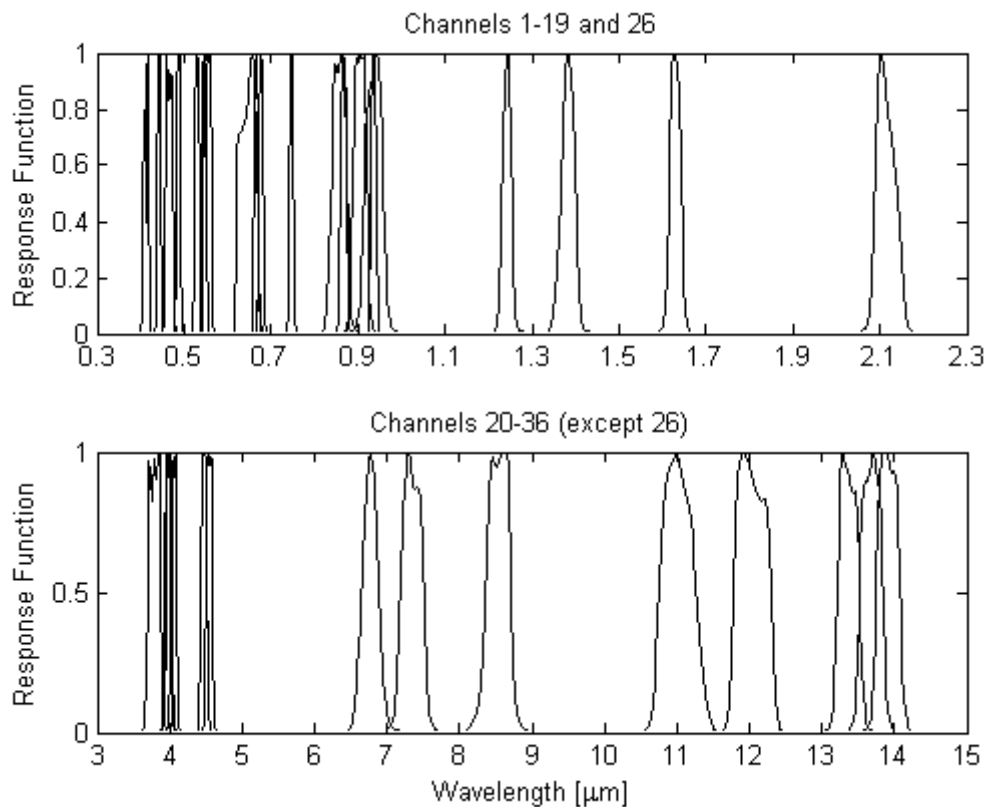


Figure 3.1. Spectral response function of MODIS channels.

Table 3.1 provides a summary of MODIS channels specifications, including the respective bandwidth, central wavelength, spectral radiance and signal-to-noise ratio (SNR) or noise equivalent temperature differences (NEAT). MODIS channels 1 – 19 and 26 with wavelengths from 0.41 to 2.2 μm are the reflective solar bands, collecting data only during daytime. In turn, bands 20 – 25 and 27 – 36 are the thermal emissive bands, making continuous measurements during day and nighttime.

Table 3.1. MODIS channels specifications.

Band	Bandwidth [nm]	Central wavelength [nm]	Spectral Radiance [$\text{W}\cdot\text{m}^{-2}\cdot\mu\text{m}^{-1}\cdot\text{sr}^{-1}$]	Required SNR
1	620 - 670	645	21.8	128
2	841 - 876	858	24.7	201
3	459 - 479	469	35.3	243
4	545 - 565	555	29.0	228
5	1230 - 1250	1240	5.4	74
6	1628 - 1652	1640	7.3	275
7	2105 - 2155	2130	1.0	110
8	405 - 420	412	44.9	880
9	438 - 448	443	41.9	838
10	483 - 493	488	32.1	802
11	526 - 536	531	27.9	754
12	546 - 556	551	21.0	750
13	662 - 672	667	9.5	910
14	673 - 683	678	8.7	1087
15	743 - 753	748	10.2	586
16	862 - 877	869	6.2	516
17	890 - 920	905	10.0	167
18	931 - 941	936	3.6	57
19	915 - 965	940	15.0	250
Band	Bandwidth [μm]	Central wavelength [μm]	Spectral Radiance [$\text{W}\cdot\text{m}^{-2}\cdot\mu\text{m}^{-1}\cdot\text{sr}^{-1}$]	Required NEAT[K]
20	3.660 - 3.840	3.75	0.45 (300 K)	0.05
21	3.929 - 3.989	3.96	2.38 (335 K)	2.00
22	3.929 - 3.989	3.96	0.67 (300 K)	0.07

23	4.020 - 4.080	4.05	0.79 (300 K)	0.07
24	4.433 - 4.498	4.47	0.17 (250 K)	0.25
25	4.482 - 4.549	4.52	0.59 (275 K)	0.25
26	1.360 - 1.390	1.375	6.00	150 (SNR)
27	6.535 - 6.895	6.72	1.16 (240 K)	0.25
28	7.175 - 7.475	7.33	2.18 (250 K)	0.25
29	8.400 - 8.700	8.55	9.58 (300 K)	0.05
30	9.580 - 9.880	9.73	3.69 (250 K)	0.25
31	10.780 - 11.280	11.03	9.55 (300 K)	0.05
32	11.770 - 12.270	12.02	8.94 (300 K)	0.05
33	13.185 - 13.485	13.34	4.52 (260 K)	0.25
34	13.485 - 13.785	13.64	3.76 (250 K)	0.25
35	13.785 - 14.085	13.94	3.11 (240 K)	0.25
36	14.085 - 14.385	14.24	2.08 (220 K)	0.35

3.1.2. ETM+ high resolution sensor

The Land Remote Sensing Satellite (Landsat) Program is a series of Earth-observing satellite missions jointly managed by NASA and the U.S. Geological Survey (USGS). Landsat 7 is the latest NASA satellite in a series that has produced an uninterrupted multispectral record of the Earth's land surface since 1972. Landsat 7's sensor - the Enhanced Thematic Mapper Plus (ETM+) is a successor of the Thematic Mapper (TM) engineered for Landsats 4 and 5, but is more closely related to the Enhanced Thematic Mapper (ETM) lost during the Landsat 6 failure. The primary performance related changes of the ETM+ over the TM's are the addition of the panchromatic band and two gain ranges (added for Landsat 6), the improved spatial resolution for the thermal band, and the addition of two solar calibrators. The ETM+ design provides for a nadir-viewing, eight-band multispectral scanning radiometer capable of providing high-resolution image information of the Earth's surface when operated from Landsat 7, a 3 axis stabilized spacecraft located in a near polar, sun-synchronous and circular orbit at a 705 km nominal altitude, with an orbit inclination of 98.2 degrees. The ETM+ is designed to collect, filter and detect radiation from

the Earth in a swath 185 km wide as it passes overhead and provides the necessary cross-track scanning motion while the spacecraft orbital motion provides an along-track scan. Approximately one quarter of the Earth's landmass is imaged every 16 days, with an equatorial crossing time at 10 AM local time (descending node). The spatial resolution varies from 15 m in the panchromatic band, to 30 m in visible bands and to 60 m in the thermal band (Table 3.2).

Table 3.2. ETM+ channels specifications.

Band	Bandwidth [μm]	Resolution [m]
1	0.45-0.515	30
2	0.525-0.605	30
3	0.63-0.69	30
4	0.75-0.90	30
5	1.55-1.75	30
6	10.4-12.5	60
7	2.09-2.35	30
8	0.52-0.9	15

3.2. Datasets

3.2.1. Satellite data

3.2.1.1. MODIS data

Currently more than 40 science data products derived from MODIS observations are routinely produced and widely distributed (Salomonson et al., 2002; Justice et al., 1998; Esaias et al., 1998; King et al., 1998). These products include LST, vegetation and land-surface cover and productivity, snow and sea-ice cover, ocean color, sea surface temperature (SST), cloud mask, aerosol concentration and optical properties, and

atmospheric profiles. The Level 1B data set contains calibrated and geolocated at-aperture radiances, in $[W \cdot m^{-2} \cdot \mu m^{-1} \cdot sr^{-1}]$, for 36 bands generated from MODIS Level 1A sensor (MOD01) counts. In addition, reflectance may be determined for the solar reflective bands (bands 1 - 19, 26) through knowledge of the solar irradiance (e.g., determined from MODIS solar-diffuser data, and from the target-illumination geometry). Additional data are provided, including quality flags, error estimates, and calibration data.

The MODIS Atmospheric Profiles product (MOD07) consists of several parameters, including total-ozone burden, atmospheric stability, temperature and moisture profiles, and atmospheric water vapor. There are two MODIS Atmosphere Profile data product files, respectively the so-called MOD07_L2, containing data collected from the Terra platform; and the so-called MYD07_L2, containing data collected from the Aqua platform. Data are produced day and night for Level 2 at 5 x 5 1-km pixel resolution when at least 9 field of views (FOVs) are cloud free. Temperature and moisture profile retrieval algorithms are adapted from the International TOVS Processing Package (ITPP), taking into account the lack of stratospheric channels and far higher horizontal resolution of MODIS. The profile retrieval algorithm requires calibrated, navigated, and coregistered 1-km FOV radiances from MODIS channels 20, 22-25, 27- 29, and 30-36. The MODIS cloud mask (MOD35_L2) is used for cloud screening. The algorithm also requires NCEP model analyses of temperature and moisture profiles as a first guess and an NCEP analysis of surface temperature and pressure.

The MODIS Land Surface Temperature and Emissivity products provide per-pixel temperature and emissivity values in a sequence of swath-based to grid-based global products. The MODIS/Aqua LST/E 5-Minute L2 Swath 1 km data set (MYD11_L2) is produced daily at 5-minute increments, and covers both daytime and nighttime acquisitions including the polar regions. The LST and Emissivity daily data are retrieved at 1-km pixels by the generalized split-window algorithm and at 6km grids by the day/night algorithm. In the split-window algorithm (Wan and Dozier, 1996), emissivities in bands 31 and 32 are

estimated from land cover types, and atmospheric column water vapor and lower boundary air surface temperature are separated into tractable sub-ranges for optimal retrieval. In the day/night algorithm (Wan and Li, 1997), daytime and nighttime LSTs and surface emissivities are retrieved from pairs of day and night MODIS observations in seven TIR bands. The product comprises LST values, quality assessment, observation time, view angles, and emissivities.

TOA values of MIR radiance, NIR reflectance and TIR brightness temperature as acquired by the MODIS instrument on-board the Terra satellite during the year of 2002 were used in this work, as well as solar and view zenith angles (respectively SZA and VZA). Data were obtained from the Terra/MODIS Level 1B 1 km V5 product, MOD021 (MCST, 2006) and respect to channels 20 (centered at 3.785 μm), 2 (centered at 0.858 μm) and 31 (centered at 11.017 μm). According to Boyd and Petitcolin (2004), when considering the three MODIS bands from which MIR reflectance can be retrieved, reflectance in band 20 appears to be less noisy than reflectance derived in band 22 (around 3.96 μm) and band 23 (around 4.06 μm). This result illustrates in fact the rapid decrease of the solar contribution to radiation at MIR wavelengths. In addition, Petitcolin and Vermote (2002) have shown that although surface reflectances in bands 20, 22 and 23 are similar, reflectances at 3.79 μm are slightly higher than those at 3.97 and 4.06 μm , with weaker angular variations. These two aspects have motivated the choice of band 20 in this work, in particular the last one, because of the assumption of a Lambertian surface, as explained in Chapter 2. Figure 3.2 presents the MODIS response functions of the four MIR channels, in particular channel 20, which was used in this work.

Data from land surface temperature and from atmospheric profiles of temperature and humidity were finally obtained using the Land Surface Temperature/Emissivity Daily 5-Min L2 Swath 1km product, MYD11_L2 (Wang, 1999) and the Atmospheric profiles were obtained from the Atmosphere Profile Level 2.0 product, MYD07_L2 (Seemann et al., 2006).

It may be noted that all MODIS products mentioned above were requested via the MODIS website and downloaded via File Transfer Protocol (FTP) server. The products are available in Hierarchical Data Format (HDF) format, and were directly imported into Environment for Visualizing Images 4.2 (ENVI) software in order to be georeferenced.

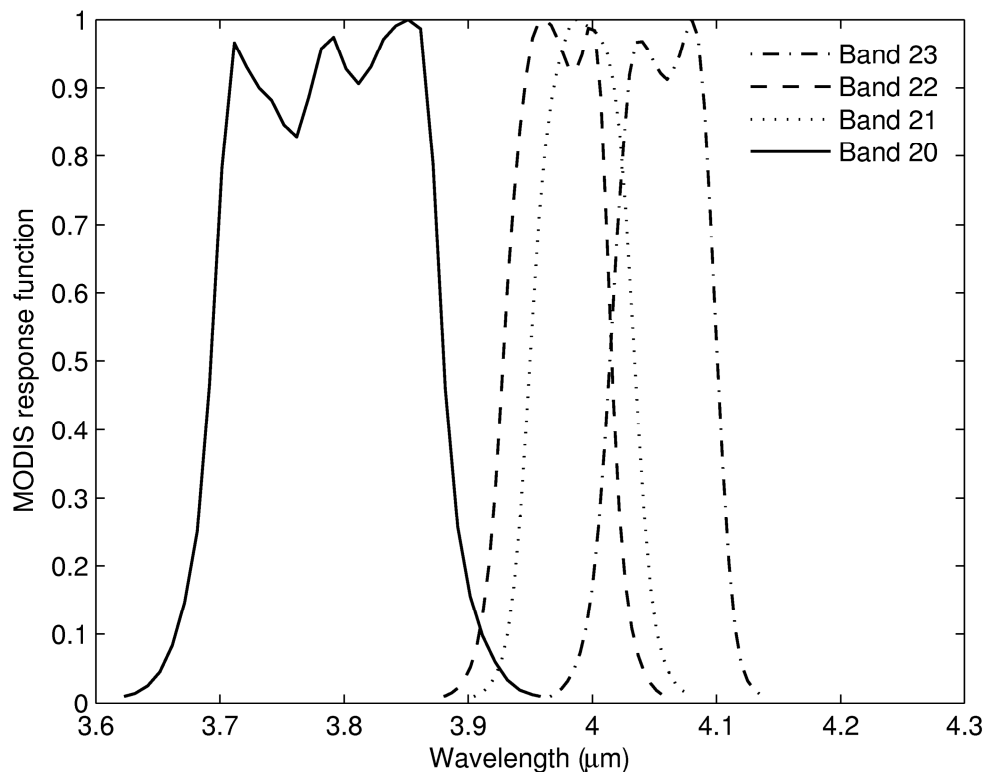


Figure 3.2. Spectral response functions of MODIS MIR channels.

3.2.1.2. Landsat data

Use of Landsat ETM+ images in this work was motivated by the need to have ground reference information for the analysis performed on MODIS images in Chapter 6. Imagery was provided by the Brazilian National Institute for Space Research (INPE) and obtained from the Image Generation Division (DGI) database (<http://www.dgi.inpe.br/CDSR/>). The

images were geometrically corrected by Dr. Wilfrid Schroeder from NOAA, who also identified recent burned area polygons based on visual classification of ETM+ images.

Selection of different classes of surface in MODIS data, namely vegetation, soil, and water, was performed based on visual comparison with high resolution ETM+ images, whereas identification of recent burned pixels in MODIS images was based on burned area polygons as derived from the above mentioned visual classification made by Dr. Wilfrid Schroeder.

A total of 16 Landsat ETM+ images were used in the present work, covering two main Brazilian biomes (accordingly to the *Instituto Brasileiro do Meio Ambiente e dos Recursos Naturais Renováveis* (IBAMA)), namely the Amazon Forest and the Cerrado, as shown in Figure 3.3. Detailed information is given in Table 3.3.

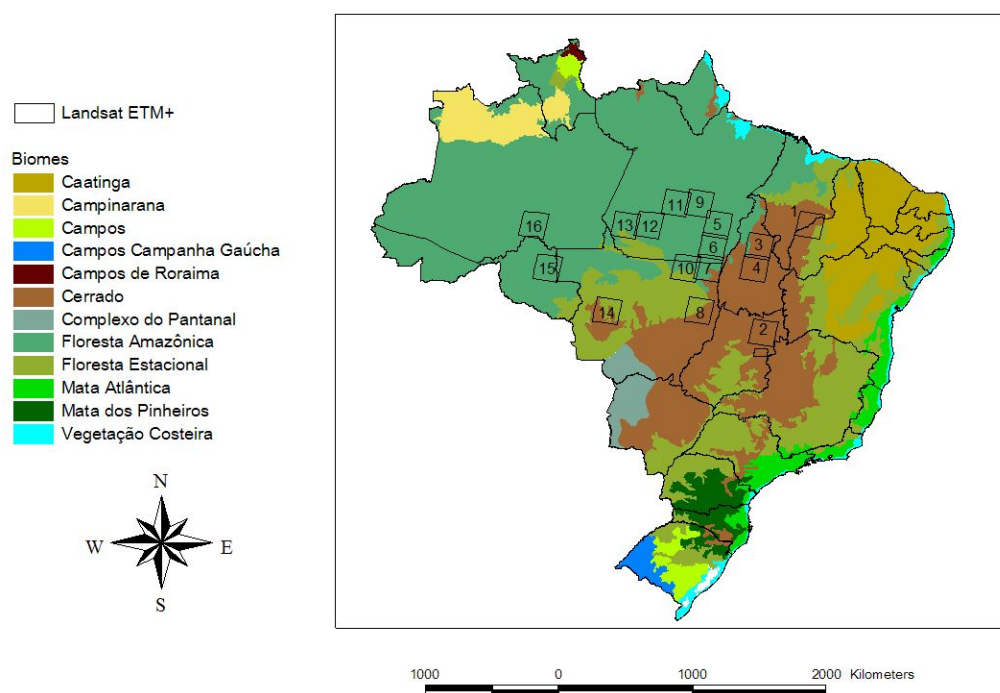


Figure 3.3. IBAMA general biomes classification map for Brazil and the location of the 16 Landsat ETM+ scenes listed in Table 3.3.

Finally, two TM images were used when testing the performance of the algorithm developed by Kaufman and Remer (1994) when applied for burned area discrimination

(Chapter 4). The two TM images respect to pre-fire (04/26/2006) and post-fire (05/12/2006) scenes of a large fire event that took place from April 30 to May 12, 2006 and affected the entire area of the Ilha Grande National Park, located between the states of Paraná and Mato Grosso do Sul, Brazil. The images were also extracted from the DGI/INPE's Database and were geographically corrected at the Satellite Division from INPE (DSA/INPE).

Table 3.3. The 16 Landsat ETM+ images used for validation and respective biomes and locations.

ETM scene number	Path/row	Date (mm/dd/yyyy)	Location	Biome
1	220/65	06/28/2002	Maranhão/Piauí	Cerrado
2	221/70	06/05/2002	Goiás	Cerrado
3	222/66	08/15/2002	Tocantins	Cerrado
4	222/67	08/15/2002	Tocantins	Cerrado
5	224/65	08/13/2002	Pará	Amazon Forest
6	224/66	08/13/2002	Pará	Amazon Forest
7	224/67	08/13/2002	Mato Grosso	Cerrado/ Amazon Forest
8	224/69	08/29/2002	Mato Grosso	Cerrado/ Deciduous Forest
9	225/64	08/20/2002	Pará	Amazon Forest
10	225/67	08/04/2002	Mato Grosso	Amazon Forest/ Deciduous Forest
11	226/64	08/11/2002	Mato Grosso	Cerrado/ Deciduous Forest
12	227/65	08/18/2002	Pará	Amazon Forest
13	228/65	08/09/2002	Pará	Amazon Forest
14	228/69	10/28/2002	Pará	Amazon Forest
15	231/67	06/11/2002	Rondonia	Amazon Forest
16	232/65	08/05/2002	Amazonas	Amazon Forest

3.2.2. Laboratory spectral data on reflectance

3.2.2.1. Spectral library data

Data on reflectance were obtained from the Johns Hopkins University (JHU) and the Jet Propulsion Laboratory (JPL) spectral libraries included in ASTER spectral library (Baldrige et al., 2009) as well as from the MODIS-University of California-Santa Barbara (MODIS-UCSB) spectral library.

The ASTER library provides a comprehensive collection of over 2300 spectra of a wide variety of materials, made available from <http://speclib.jpl.nasa.gov>. The library includes spectra of rocks, minerals, lunar soils, terrestrial soils, manmade materials, meteorites, vegetation, snow and ice covering the visible through thermal infrared wavelength region (0.4-15.4 μm). We have restricted to materials belonging to vegetation, water and terrestrial soils (Table 3.4, 3.5 and 3.6). Samples of the library spectra are shown in Figure 3.4 (vegetation), 3.5 (soils) and 3.6 (water). Figure 3.4(A), 3.5(A) and 3.6(A) show the 0.25-2.5 μm spectral range and Figure 3.4(B), 3.5(B) and 3.6(B) show the 2-15 μm spectral range.

Table 3.4. ASTER spectral library – vegetation.

Name	Class	Sub-class
Dry grass	Grasses	Dry grass
Grass	Grasses	Green grass
Conifer	Trees	Conifers
Deciduous	Trees	Deciduous

Table 3.5. ASTER spectral library – soil.

Name	Class	Sub-class
Brown to dark brown clay	Vertisol	Chromoxerert
Pale brown dry silty clay loam	Inceptisol	Ustocrept
Brown to dark brown silt loam	Entisol	Ustifluent
Pale brown silty loam	Alfisol	Fragiboralf
Brown to dark brown gravelly loam	Alfisol	Haploxeralf
Brown loamy fine sand	Alfisol	Haplustalf
Brown fine sandy loam	Alfisol	Haplustalf
Brown fine sandy loam	Alfisol	Haplustalf
Reddish brown fine sandy loam	Alfisol	Paleustalf

Reddish brown fine sandy loam	Alfisol	Paleustalf
Brown sandy loam	Alfisol	Paleustalf
Dark reddish brown fine sandy loam	Alfisol	Paleustalf
Light yellowish brown interior dry gravelly loam	Aridisol	Calciorthid
Light yellowish brown loam	Aridisol	Calciorthid
Brown silty loam	Aridisol	Camborthid
Light yellowish brown loamy sand	Aridisol	Camborthid
Very pale brown to brownish yellow interior dry gravelly silt loam	Aridisol	Gypsiorthid
Brown gravelly sandy loam	Aridisol	Haplargid
Dark brown interior moist clay loam	Aridisol	Salorthid
Light yellowish brown clay	Aridisol	Salorthid
Dark yellowish brown silty clay	Aridisol	Salorthid
Very dark grayish brown loamy sand	Aridisol	Torripsamment
Brown to dark brown sand	Entisol	Quartzipsamment
White gypsum dune sand.	Entisol	Torripsamment
Gray/dark brown extremely stoney coarse sandy	Inceptisol	Cryumbrept
Dark yellowish brown micaceous loam	Inceptisol	Dystrochrept
Dark brown fine sandy loam	Inceptisol	Haplumbrept
Brown sandy loam	Inceptisol	Haplumbrept
Very dark grayish brown silty loam	Inceptisol	Plaggept
Brown to dark brown gravelly fine sandy loam	Inceptisol	Xerumbrept
Dark grayish brown silty loam	Mollisol	Agialboll
Vary dark grayish brown loam	Mollisol	Agriudoll
Very dark grayish brown silty loam	Mollisol	Argiustoll
Black loam	Mollisol	Cryoboroll
Very dark grayish brown loam	Mollisol	Cryoboroll
Gray silty clay	Mollisol	Haplaquoll
Brown to dark brown sandy loam	Mollisol	Hapludoll
Grayish brown loam	Mollisol	Haplustall
Very dark grayish brown loam	Mollisol	Paleustoll
Dark reddish brown, organic-rich, silty loam	Spodosol	Cryohumod
Brown to dark brown loamy sand	Urtisol	Hapludult

Table 3.6. ASTER spectral library – water.

Name	Class	Sub-class
Tap water	Tap water	

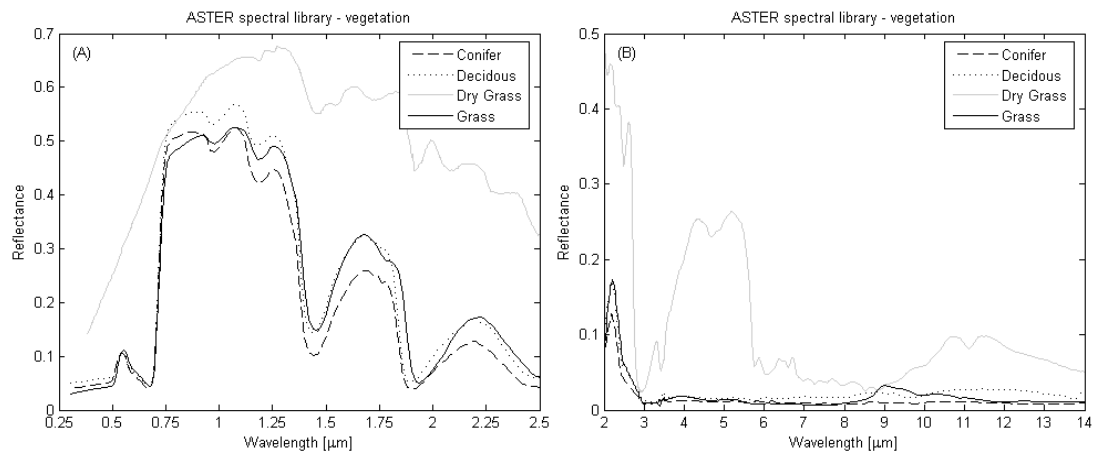


Figure 3.4. Spectral signature of vegetation from ASTER spectral library in (A) the 0.25-2.5 μm and (B) the 2-15 μm spectral ranges.

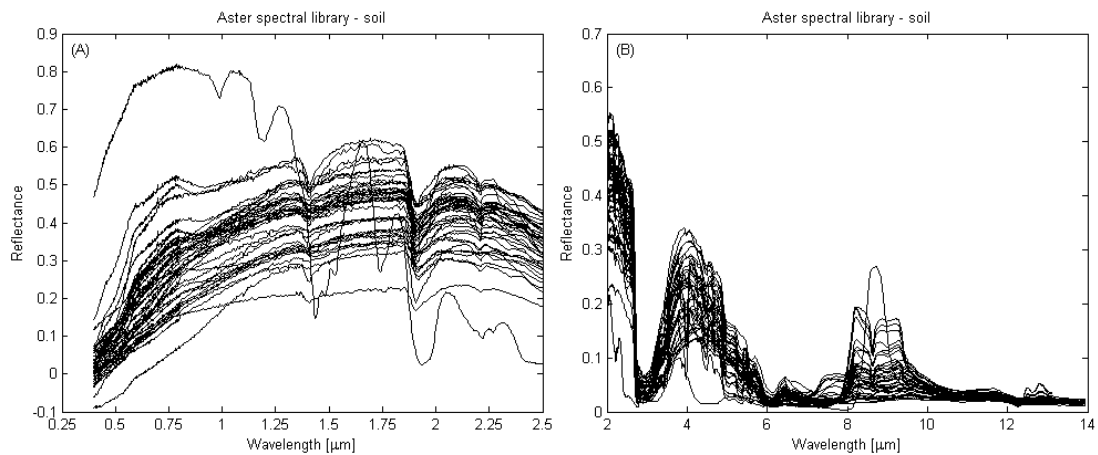


Figure 3.5. As in Figure 3.4, but respecting to soils.

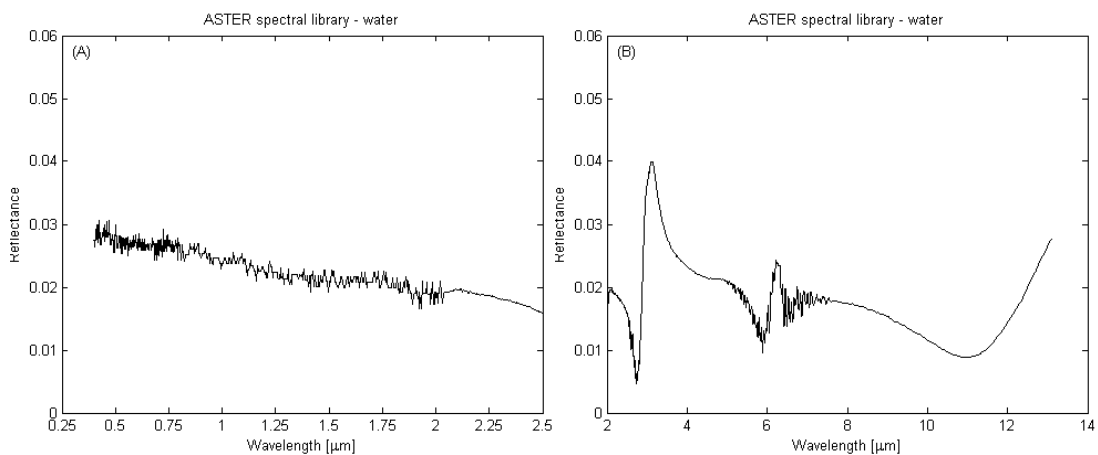


Figure 3.6. As in Figure 3.4, but respecting to water.

The MODIS-UCSB spectral library provides information of natural and manmade materials from MIR to TIR region (3 - 14 μm). Data are available at: <http://www.ices.ucsb.edu/modis/EMIS/html/em.html> and we have relied on information about vegetation, which includes most vegetation types (Salisbury and D’Aria, 1994; Peres and DaCamara, 2005), with surfaces emissivities varying from 0.96 to 0.99 in MODIS MIR channel 20. Figure 3.7 presents the spectral behavior of the vegetation samples used in the present work (Table 3.7).

It may be noted that the information from MODIS-UCSB spectral library is used in this thesis in all approaches that take only rely on MIR information, since this library does not provide information in the visible domain. On the other hand, the ASTER spectral library is used here as a surrogate for issues that take into consideration information in the visible domain. For instance, Chapters 4 and 5 rely on information from the MODIS-UCSB spectral library, since both only deal with the MIR region. In the case of Chapter 6, where the bi-spectral domain MIR/NIR is used for identification of burned areas, the ASTER spectral library is employed instead.

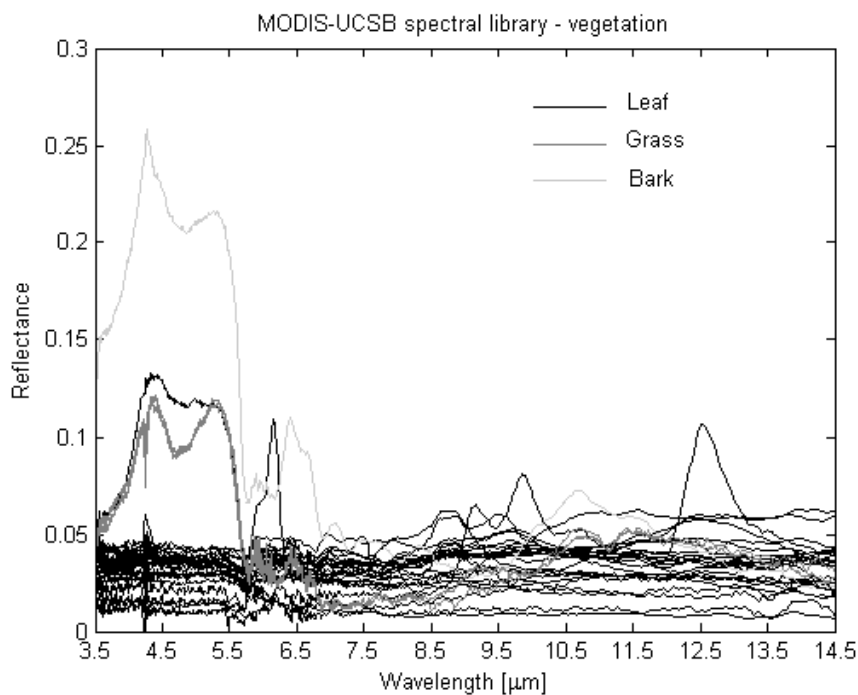


Figure 3.7. Spectral signature of vegetation from MODIS-UCSB spectral library.

Table 3.7. MODIS spectral library – vegetation.

Name	Class	Description
Algerian Ivy	Vegetation	Leaf Algerian Ivy
Bird of Paradise	Vegetation	Leaf of Bird of Paradise
Brazilian Peppertree	Vegetation	Leaf of Brazilian Peppertree
Bronze Loquat	Vegetation	Leaf of Bronze Loquat
Naked Coral	Vegetation	Leaf of Naked Coral tree
Cypress	Vegetation	Leaf of Cypress
Eucalyptus	Vegetation	Fresh Leaf of Eucalyptus Tree
Eucalyptus	Vegetation	Leaf of Eucalyptus tree
Tasmanian Blue Gum Eucalyptus	Vegetation	Leaf of Tasmanian Blue Gum Eucalyptus
Laurel	Vegetation	Leaf of Laurel Tree
India Hawthorne	Vegetation	Leaf of India Hawthorne
Arailia Japonica	Vegetation	Leaf of Arailia Japonica
Laurel	Vegetation	Leaf of Laurel tree
Laurel	Vegetation	Leaf of Laurel (Fresh)
Magnolia	Vegetation	Leaf Magnolia (1st day)
Maple	Vegetation	Leaf of Maple (Red Star)
Myoporum	Vegetation	Leaf of Myoporum
Oak	Vegetation	Leaf of Oak (Face)
Shiny Xylosma	Vegetation	Leaf of Shiny Xylosma
Evergreen Pear	Vegetation	Leaf of Evergreen Pear
Pine	Vegetation	Leaf of Pine (Old)
Pine	Vegetation	Leaf of Pine (New)
Green Spruce	Vegetation	Leaf of Green Spruce from Canada
Sweet Gum	Vegetation	Leaf of Sweet Gum
Bark	Bark	Bark of Eucalyptus Tree
Dry Grass	Grass	Dry Grass (Averaged over 9 Sets)
Dry Grass	Grass	Dry Grass (Averaged over 9 Sets)
Dry Grass	Grass	Dry Grass (Averaged over 9 Sets)

3.2.2.2. Charcoal data

Spectral libraries like ASTER and MODIS-UCSB supply reliable reflectance data for different types of materials, such as vegetation, water, soil, rocks and manmade. However, to the best of our knowledge, no reflectance measurements are currently available for charcoal, ash or any burned plant material, in the spectral region accounted for in this thesis (MIR region). Therefore, four fire residue samples were collected at Alta Floresta, state of Mato

Grosso, Brazil. The samples were kindly collected by the Combustion Laboratory from INPE (LCP/INPE). In addition, fire residues were also collected by J.M.C.P. at Portugal from samples of burned pine tree. Fire residues from Alta Floresta relies basically on charcoal, while those from Pine tree relies on a mixed of bark, charcoal and dry leaf. Both charcoal samples (from Brazil and from Portugal) were send to the NASA/JPL, where spectral signatures were measured by Dr. Simon Hook. Spectral measurements from samples of Alta Floresta were made only in the 2 - 15 μm region, due to problems in the instruments, while the pine tree sample was measured in both 0.4 - 2.5 μm and 2 - 15 μm regions.

The above-mentioned data on emissivity of charcoal in the vicinity of 3.9 μm appear therefore as the only information currently available about the behavior of burned materials in this spectral domain. Table 3.8 shows the description of the five samples of charcoal and Figure 3.8 presents the respective spectral signatures.

Table 3.8. Description of the five charcoal samples.

Name	Family	Origin
Tachi	Polygonaceae	Brazil
Quina	Rubiaceae	Brazil
Angelim	Leguminosae-apilionoideae	Brazil
Amescla	Burseraceae	Brazil
Pine	Pinaceae	Portugal

As already mentioned, the Pine tree sample of fire residues were the only ones that were measured in the visible domain. Therefore, in order to extend the spectral domain of the Brazilian trees samples to the visible domain, we have opted to rely on information from burned area as stored at the USGS Digital Spectral Library. This information corresponds to an average of 16 field spectra collected on a severely burned area, specifically of blackened ash/char coated materials on the soil surface following a wildfire in a ponderosa pine forest (Figure 3.9).

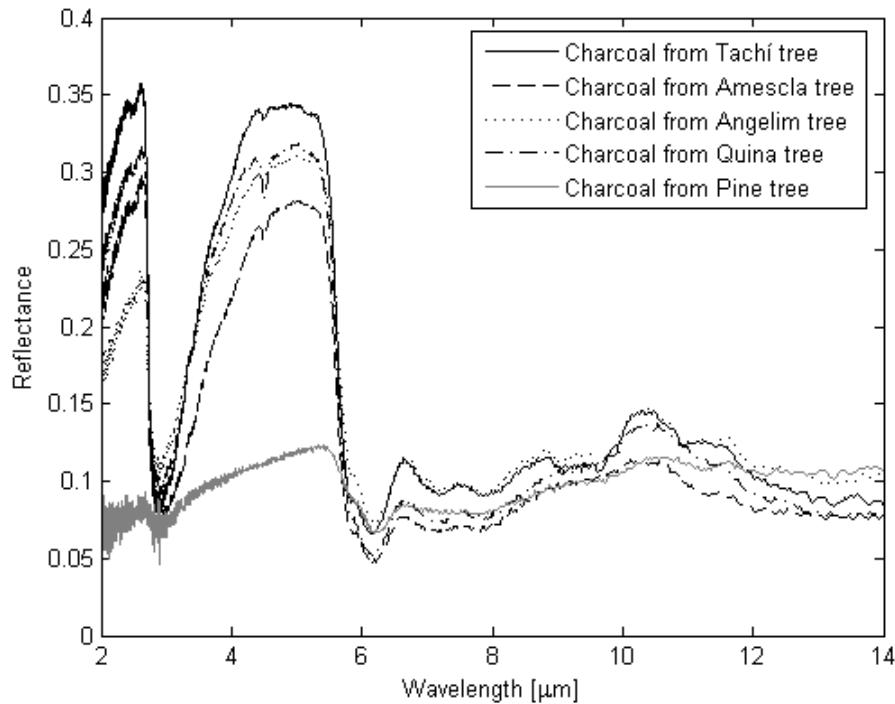


Figure 3.8. Spectral signature of the five charcoal samples.

For each laboratory spectral data described above (Section 3.2.2), the MODIS channel equivalent reflectance was estimated by convolving the laboratory measurements within the MODIS channels normalized response function according to Eq. (2.10), where Ω stands for ρ_i . Figure 3.10 depicts the computed reflectance values in MODIS channels 2 and 20 for different samples from the ASTER spectral library as well as from burned material samples. Computed values of reflectance in MODIS channels will be used in Chapters 4 and 5 to prescribe the surface reflectance as input to MODTRAN-4. The same reflectance values will be used in Chapter 6 as auxiliary information in the development of a new coordinate system aiming at an optimal discrimination of burned areas using data in the MIR and NIR domains.

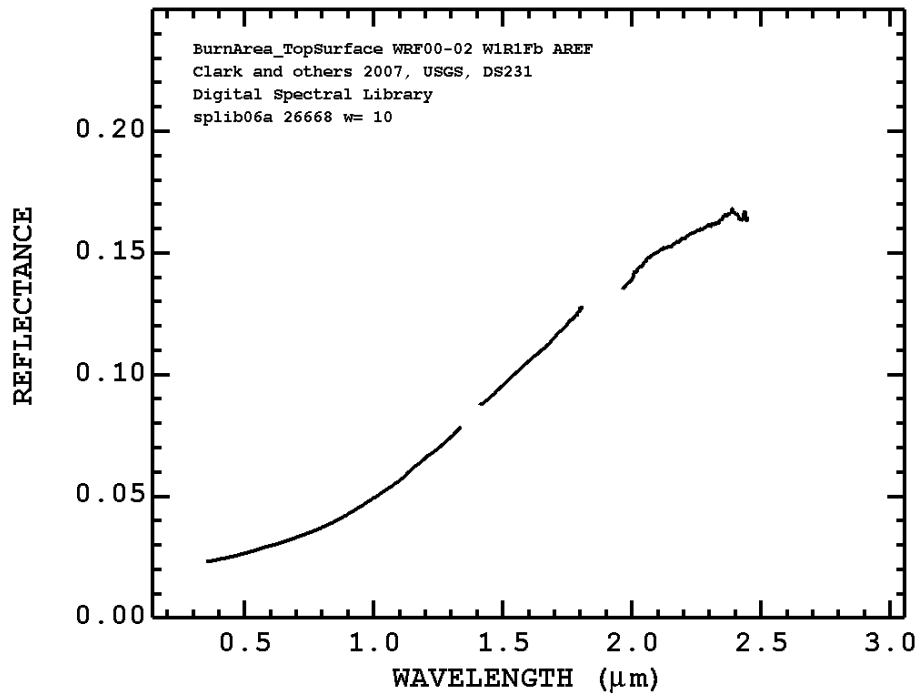


Figure 3.9. Burned area stored at the USGS Digital Spectral Library. Adapted from <http://speclab.cr.usgs.gov/spectral-lib.html>

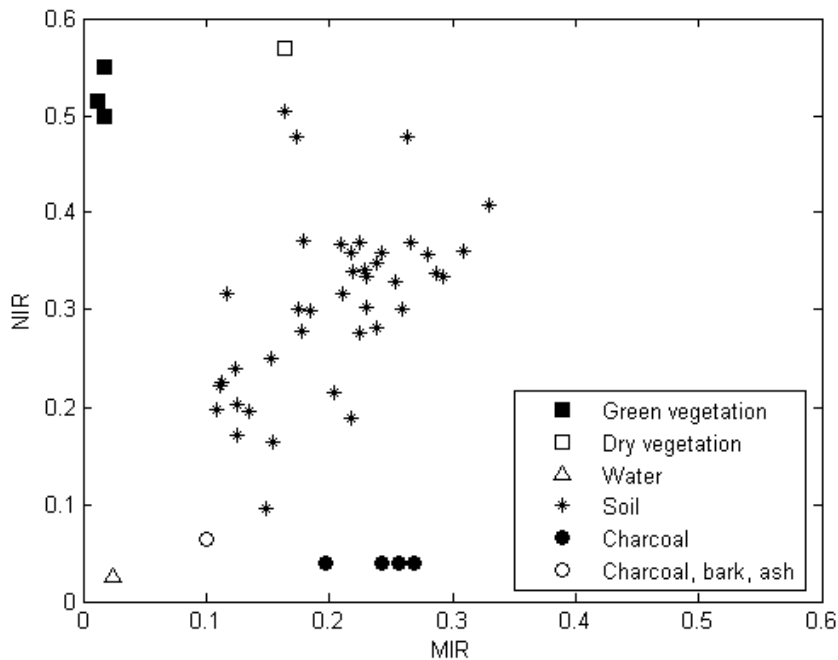


Figure 3.10. Computed reflectance values in channels 20 (MIR) and 2 (NIR) for samples belonging to vegetation, water and soil classes as stored in the JHU directory at ASTER spectral library, as well as based on samples of burned materials.

3.2.3. Auxiliary information

3.2.3.1. AERONET

The AErosol RObotic NETwork (AERONET) program provides a long-term, continuous and readily accessible public domain database of aerosol optical, microphysical and radiative properties for aerosol research and characterization, validation of satellite retrievals, and synergism with other databases. The network imposes standardization of instruments, calibration, processing and distribution (Holben et al., 1998).

In this respect, the AERONET collaboration provides globally distributed observations of spectral AOD, inversion products, and precipitable water in diverse aerosol regimes. The aerosol optical depth is computed at three data quality levels, namely Level 1.0 (unscreened), Level 1.5 (cloud-screened), and Level 2.0 (cloud-screened and quality-assured). Inversions, precipitable water, and other AOD-dependent products are derived from these levels and may implement additional quality checks. Typically the sun photometers, that are currently installed, take measurements of the direct sun radiance at eight spectral channels (340, 380, 440, 500, 670, 870, 940 and 1020 nm) with triplet observations per wavelength and diffuse sky radiances at four spectral channels (440, 670, 870 and 1020 nm).

For this study, we used data from Abracos Hill station (latitude -10.76, longitude -62.35), as obtained through the AERONET webservice (<http://aeronet.gsfc.nasa.gov>), which is located in Rondonia, Brazil, an area with high fire activity. We have selected data on the extinction coefficient at 550 nm from aerosols associated to biomass burning, based on cloud-screened level 2.0 AOD at 550 nm ($\tau_a(0.55)$), during the local dry season (August to October) from the years of 1999 to 2005. It may be further noted that level 2.0 data are pre and post field calibrated, automatically cloud cleared and manually inspected.

3.2.3.2. Hot spots

INPE makes available data on active fires using data based on information provided by Geostationary Satellite Server (GOES), NOAA, Aqua and Terra satellites (see information at <http://www.dpi.inpe.br/proarco/bdqueimadas/>). Data on active fires will be used in Chapter 4 in order to provide ground reference information for burned areas analysis.

3.3. MODTRAN radiative transfer code and atmospheric characterization

MODTRAN is a well established radiative transfer code, developed jointly by the Air Force Research Lab/Space Vehicles Directorate (AFRL/VSBT) and the Spectral Sciences, Inc. The MODTRAN code calculates atmospheric transmittance and radiance for frequencies from 0 to 50,000 cm^{-1} at moderate resolution, primarily 2 cm^{-1} (20 cm^{-1} in the ultraviolet region). The latest version, MODTRAN-4, which was used in the present research, adds some new features, e.g. two correlated-k options, an azimuth dependent DISORT option, upgraded ground surface modeling and an high-speed option that make the computations more accurate than the former version (Berk et al., 1998).

As shown in Table 3.9, MODTRAN prescribes six standard model atmospheres, namely Tropical (TRO), Mid-Latitude Summer (MLS), Mid-Latitude Winter (MLW), Sub-Arctic Summer (SAS), Sub-Arctic Winter (SAW) and 1976 US Standard (STD). Each standard atmosphere available in MODTRAN-4 is tabulated at 36 levels in terms of temperature, humidity and pressure. In the present research work, we restrict to TRO, MLS and MLW profiles and the respective pressure, temperature and humidity profiles are shown in Figure 3.11. The three standard atmospheric profiles chosen are expected to cover a wide variety of atmospheric conditions (air temperature at the first boundary from 272.2 to 299.7 K and water vapour contents from 0.85 to 4.11 $\text{g}\cdot\text{cm}^{-2}$) that are likely to be encountered within the

Amazon and Cerrado regions where both wet and dry conditions may be observed. For instance, from July to October, a large high pressure system dominates partially the North and the Center-West Regions of Brazil reducing the humidity due to subsidence of dry air from the upper levels of the atmosphere (Nobre et al., 1988).

Representative atmospheric aerosol, cloud and rain models are also provided within the MODTRAN code with options to replace them by user-modelled or measured values. In this work, we have used aerosol from biomass burning as obtained from the AERONET network.

Table 3.9. Air temperature at the first boundary and total water vapour contents of the six standard model atmosphere stored at MODTRAN-4.

Model atmosphere	Air temperature [K]	Column water vapour [g-cm⁻²]
TRO	299.7	4.11
MLS	294.2	2.92
MLW	272.2	0.85
SAS	287.2	2.08
SAW	257.2	0.42
STD	288.2	1.42

In addition to the standard model atmospheres, MODTRAN also enables users to define their own atmospheric profiles, e.g. from radiosounding, satellite sounder or numeric weather prediction (NWP) model data. A set of perturbed TRO, MLS and MLW profiles was accordingly generated to be used in Chapter 5 with the aim of assessing the effect of the atmospheric profile source of error on the retrieval of MIR reflectance. Following Peres and DaCamara (2004) the three standard profiles were perturbed with values based on the background error covariance matrix used in the assimilation schemes of the Global Circulation Model operated at the European Centre for Medium-Range Weather Forecast (ECMWF) (Fillion and Mahfouf, 2000). It may be noted that the covariance coefficients were computed statistically using the NCEP method based on 24/48-hour forecast differences of the ECMWF model And that the background refers to a short-range forecast, which has been

started from the analysis at the previous assimilation cycle and is used, in conjunction with a set of observations, to help finding the new analysis state. It may be further noted that ECMWF model prognostic variables like temperature and specific humidity are currently represented on a vertical grid with 60 levels (from the top of the atmosphere to the surface). Since the MLS, MLW and TRO standard atmospheres available in MODTRAN-4 are tabulated at 36 levels with temperature, humidity and pressure values, the temperature and humidity profiles were interpolated to the 60 pressure-level grids in order to impose the above-mentioned perturbations on the three standard atmospheres.

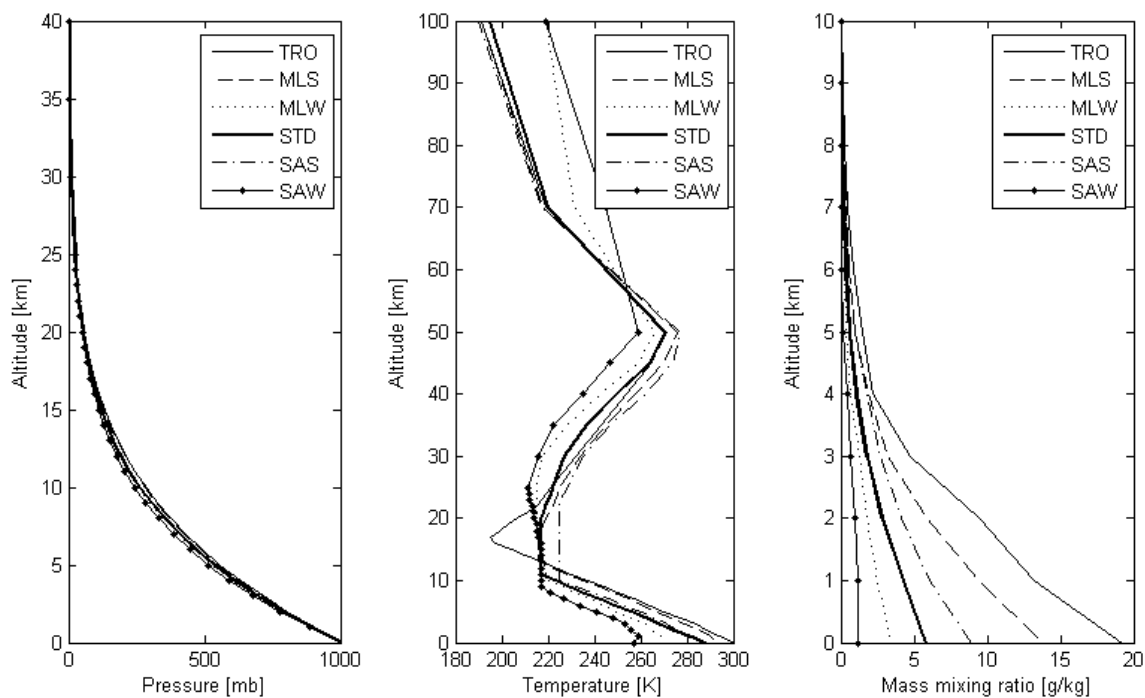


Figure 3.11. Pressure, temperature and humidity profiles of the six standard model atmospheres prescribed in MODTRAN.

Although it may seem obvious, at first sight, to adopt the error associated with the MODIS Atmospheric Profile product (since it is the main sensor used in the present study), the use of the ECMWF background error covariance matrix is preferable because it allows generating sets of perturbed profiles of temperature and humidity based on the reference

TRO, MLS and MLW profiles. The set of imposed errors due to uncertainties on atmospheric information respects therefore to a specific and pre-defined standard profile/atmospheric condition. On the other hand, the information about the accuracy of the MODIS product is based on the comparison between collocated MODIS profile retrievals and the so-called best-estimated profiles (Tobin et al., 2006) at the Southern Great Plains (SGP) Atmospheric Radiation Measurement (ARM) site for 80 clear sky Aqua cases between October 2002 and August 2005. The best estimate profiles of the atmospheric state are an ensemble of temperature and moisture profiles generated from two radiosondes launched within two hours of the Aqua satellite overpass times. The use of the ECMWF background error covariance matrix provides therefore uncertainty information that is more realistic for each standard profile than the one from the MODIS product.

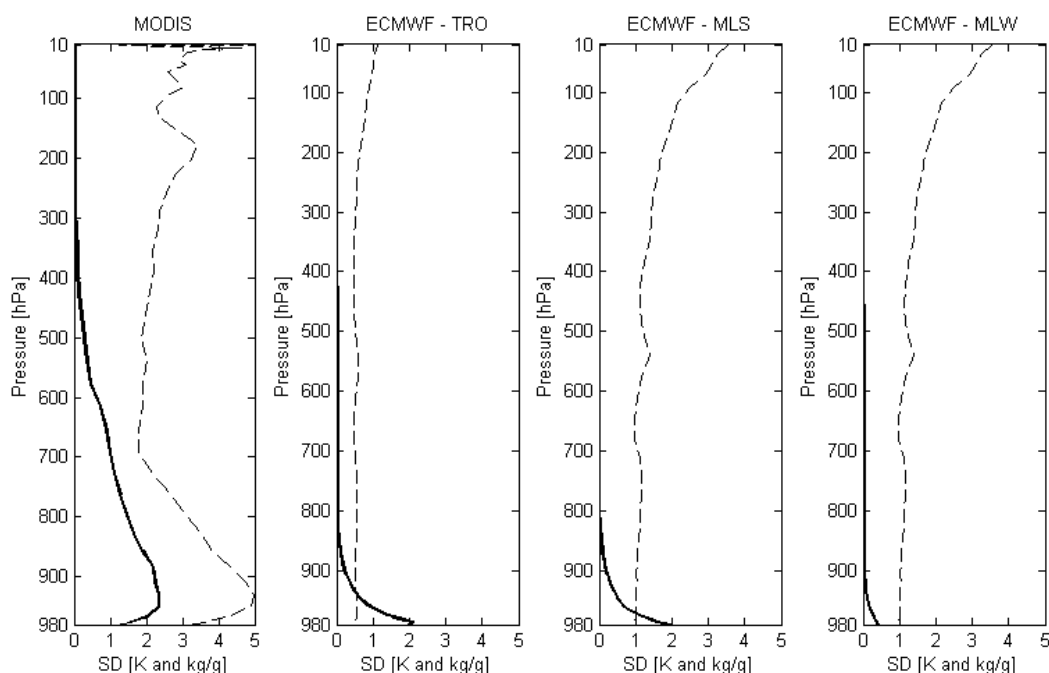


Figure 3.12. Standard deviation (SD) of the MODIS and the three ECMWF (TRO, MLS and MLW) SD profiles of mass mixing ratio (solid curves) and temperature (dashed curves).

Moreover, and as shown in Figure 3.12, the computed standard deviation (SD) of the mass mixing ratio (solid curves) and temperature (dashed curve) errors using the ECMWF

background error covariance matrix present lower values than the SD from MODIS Atmospheric Profile product. Perturbing the three standard profiles by using the former type of errors may be viewed as adopting the most favorable conditions when assessing the effect of the atmospheric profile source of error on the retrieval of MIR reflectance.

Chapter 4

Retrieving MIR reflectance for burned area mapping in tropical regions

4.1. Introduction

The ephemeral character of the radiative signal together with the presence of aerosols imposes severe limitations on the use of classical approaches, e.g. based on red and near-infrared, to discriminate between burned and unburned surfaces in tropical environments. Surface reflectance in MIR has been used to circumvent these difficulties because the signal is virtually unaffected by the presence of aerosols associated to biomass burning. Retrieval of the MIR reflected component from the total signal is, however, a difficult

problem because of the presence of a diversity of radiance sources, namely the surface reflected solar irradiance and the surface emitted radiance that may reach comparable magnitude during daytime. The method proposed by Kaufman and Remer (1994), hereafter KR94, to retrieve surface MIR reflectance presents the advantage of not requiring auxiliary datasets (e.g. atmospheric profiles) nor major computational means (e.g. for solving radiative transfer models). Nevertheless, the method was specifically designed to retrieve MIR reflectance over dense dark forests in the middle latitudes and severe problems may therefore arise when applying it beyond the range of validity, namely for burned area mapping in tropical environments. The present Chapter consists of an assessment of the performance of the method for a wide range of atmospheric, geometric and surface conditions and of the usefulness of extracted surface reflectances for burned area discrimination. Approximate solutions, like that proposed by KR94, are fast and easy to implement, but may be insufficiently accurate under specific surface and atmospheric conditions. The aim of the present Chapter is to assess the quality and limitations of the retrieved MIR reflectance by means of KR94's method when applied to discriminate burned areas in tropical environments.

Accordingly, the main objectives of the analysis are twofold:

1. To perform a quality assessment of MIR reflectance when retrieved using the algorithm proposed by KR94, for a wide range of atmospheric, geometric and surface conditions;
2. To assess the adequacy and limitations of the above mentioned algorithm when applied to burned area discrimination, in particular in the Amazon and Cerrado regions. Special attention will be devoted to the MODIS sensor, because of its widespread use in operational applications at INPE.

4.2. Data and methods

4.2.1. Theoretical background

As discussed in Chapter 2, TOA radiance measured by a sensor in the MIR region results from the contribution of the reflective and thermal emissive components. In case of clear-sky conditions, radiation balance is translated by the so-called RTE given by Eq. (2.8).

Since the Earth surface is opaque and assuming it behaves as a Lambertian emitter-reflector, surface reflectance and emissivity are related as:

$$\rho_{\text{MIR}} = 1 - \varepsilon_{\text{MIR}}. \quad (4.1)$$

Using Eq. (4.1) and neglecting the atmospheric scattering term, L_s , the solution to Eq. (2.8) is given by:

$$\rho_{\text{MIR}} = \frac{L_{\text{MIR}} - \tau_{\text{MIR}} B(\lambda_{\text{MIR}}, T_s) - L_{\text{atm, MIR}} \uparrow}{t_{\text{MIR}} \frac{E_{0\text{MIR}}}{\pi} \mu_0 - \tau_{\text{MIR}} B(\lambda_{\text{MIR}}, T_s) + \tau_{\text{MIR}} \bar{L}_{\text{atm, MIR}} \downarrow}. \quad (4.2)$$

Eq. (4.2) neglects the effects of atmospheric scattering. Figure 4.1 shows the box plot of the contributions to the MIR signal due to atmospheric scattering, surface reflection, surface emission and atmospheric emission for TRO atmospheric profile (see Section 3.3), considering all simulations performed. The lower and upper lines of the "box" are the 25th and 75th percentiles of the sample. The distance between the top and bottom of the box is the interquartile range. The line in the middle of the box is the sample median. Assuming no outliers, the maximum of the sample is the top of the upper whisker. The minimum of the

sample is the bottom of the lower whisker. It may be noted from Figure 4.1, that the contribution of atmospheric scattering to the total signal ranges from 0.001 to 0.01% and is orders of magnitude smaller than the other terms. A contribution this small is negligible and will not introduce significant errors in the retrieval of surface reflectance. Similar results were found for MLS and MLW atmospheric profiles, which were briefly described in Section 3.3.

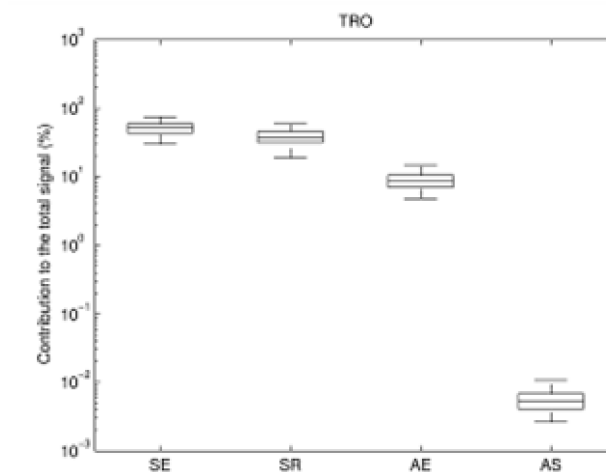


Figure 4.1. Contribution to the MIR signal due to surface emission (SE), surface reflection (SR), atmospheric emission (AE) and atmospheric scattering (AS) for TRO atmospheric profile, considering all simulations.

4.2.2. Retrieval of MIR reflectance

Equation (4.2) lays the grounds for the so-called physically-based methods, which involve a direct evaluation of all constituents of the MIR signal by means of a radiative transfer model, requiring substantial computational means. Operational use of physically-based methods is limited by other factors, namely the need of quantitative information on atmospheric conditions, mainly humidity and temperature profiles, in order to perform the atmospheric corrections.

The above-mentioned limitations led to the development of simpler methods, like the one proposed by KR94, which require neither direct knowledge of atmospheric conditions, nor a radiative transfer model. The approach is based on the studies of Gesell (1989) and Ruff and Gruber (1983), who pointed out the existence of a mutual compensation between attenuation and thermal emission terms, so that both atmospheric transmittances (i.e. t_{MIR} and τ_{MIR}) may be assumed as equal to unity, and both the atmospheric downward and upward thermal emission terms may be neglected. The validity of these assumptions may be assessed by simplifying Eq. (4.2) and then justifying the performed simplifications using typical values of the relevant terms of Eq. (4.2) for surface and atmospheric conditions associated to dense, dark vegetation areas in mid-latitude environments. Typical values are given in Table 4.1 for nadir view and three different values of SZA, respectively 0, 15 and 45°, where a MLW atmospheric profile and a surface temperature T_s of 290 K are assumed. Accordingly, after some algebraic manipulations, Eq. (4.2) may be rewritten as:

$$\rho_{\text{MIR}} = \frac{L_{\text{MIR}} - B(\lambda_{\text{MIR}}, T_s) - \Delta_1}{\left[\frac{E_{0\text{MIR}}}{\pi} \mu_0 - B(\lambda_{\text{MIR}}, T_s) \right] [1 + \Delta_2]} \quad (4.3)$$

where:

$$\Delta_1 = (\tau_{\text{MIR}} - 1)B(\lambda_{\text{MIR}}, T_s) + L_{\text{atm, MIR}} \uparrow \quad (4.4)$$

$$\Delta_2 = \frac{(\tau_{\text{MIR}} - 1) \frac{E_{0\text{MIR}}}{\pi} \mu_0 - (\tau_{\text{MIR}} - 1)B(\lambda_{\text{MIR}}, T_s) + \tau_{\text{MIR}} \bar{L}_{\text{atm, MIR}} \downarrow}{\frac{E_{0\text{MIR}}}{\pi} \mu_0 - B(\lambda_{\text{MIR}}, T_s)} \quad (4.5)$$

Since $\Delta_2 \ll 1$ according to the values in Table 1, the factor $\frac{1}{1+\Delta_2}$ in Eq. (4.4) may be expanded in a Taylor series up to the first order leading to:

$$\rho_{\text{MIR}} = \frac{L_{\text{MIR}} - B(\lambda_{\text{MIR}}, T_S) - \Delta_1}{\left[\frac{E_{\text{OMIR}}}{\pi} \mu_0 - B(\lambda_{\text{MIR}}, T_S) \right]} [1 + \Delta_2] . \quad (4.6)$$

Taking further into account that $\Delta_1 \ll L_{\text{MIR}} - B(\lambda_{\text{MIR}}, T_S)$, terms Δ_1 and Δ_2 may be neglected in Eq. (4.6) leading to the following simplified form:

$$\rho_{\text{MIR}} = \frac{L_{\text{MIR}} - B(\lambda_{\text{MIR}}, T_S)}{\frac{E_{\text{OMIR}}}{\pi} \mu_0 - B(\lambda_{\text{MIR}}, T_S)} . \quad (4.7)$$

Table 4.1. Typical values of the different terms of Eq. (4.2) in the case of nadir view and for three different SZA considering a MLW atmospheric profile and a surface temperature equal to 290 K.

	SZA		
	45°	15°	0°
τ_{MIR}	0.912	0.912	0.912
t_{MIR}	0.794	0.813	0.816
L_{MIR}^1	0.700	0.872	0.899
$B(\lambda_{\text{MIR}}, T_S)^1$	0.315	0.315	0.315
$B(\lambda_{\text{MIR}}, T_{\text{B,TIR}})^1$	0.212	0.212	0.212
$L_{\text{atm,MIR}} \uparrow^1$	0.006	0.006	0.006
$\frac{E_{\text{OMIR}}}{\pi} \mu_0^1$	2.46	3.29	3.42
$\bar{L}_{\text{atm,MIR}} \downarrow^1$	0.011	0.011	0.011

¹[W·m⁻²·μm⁻¹·sr⁻¹]

The above described mathematical procedure may be also viewed from a physical point of view. First, consider the numerator of the second hand term of Eq. (4.2), and suppose the atmospheric upward emission term ($L_{\text{atm,MIR}} \uparrow$) is neglected. Since L_{MIR} is fixed, the only way to compensate the neglected term is by increasing the contribution of the remaining term, $\tau_{\text{MIR}} B(\lambda_{\text{MIR}}, T_S)$. This is only possible by increasing the atmospheric transmittance τ_{MIR} , in particular by setting it equal to unity. Now, taking into consideration the denominator, suppose the atmospheric downward emission term ($\bar{L}_{\text{atm,MIR}} \downarrow$) is neglected. Then, in order to compensate the neglected term, either the contribution of term $\tau_{\text{MIR}} B(\lambda_{\text{MIR}}, T_S)$, or the contribution of term $t_{\text{MIR}} \frac{E_{\text{OMIR}}}{\pi} \mu_0$ have to be increased. However, the first possibility is ruled out by the fact that it was already assumed that $\tau_{\text{MIR}} = 1$. Therefore, the contribution of the $t_{\text{MIR}} \frac{E_{\text{OMIR}}}{\pi} \mu_0$ term has to be raised by increasing t_{MIR} , in particular by setting it equal to unity. Setting both t_{MIR} and τ_{MIR} to unity does lead to the required increase that compensates for neglecting the $\bar{L}_{\text{atm,MIR}} \downarrow$ term. This is due to the fact that, in general, $t < \tau$ and therefore the assumption $t_{\text{MIR}} = \tau_{\text{MIR}} = 1$ leads to a greater increase in the contribution of $t_{\text{MIR}} \frac{E_{\text{OMIR}}}{\pi} \mu_0$ term than in $\tau_{\text{MIR}} B(\lambda_{\text{MIR}}, T_S)$ term.

KR94 introduced another approximation for Eq. (4.7), that consists of using the brightness temperature, $T_{\text{B,TIR}}$, from a TIR band (10 - 12 μm) as a surrogate for the LST, T_S . In fact, as pointed out by Prata et al. (1995), brightness temperature is usually lower than surface temperature, the difference typically ranging from 1 to 5 K in TIR.

Following a procedure similar to the one above-described, Eq. (4.7) may be approximated (up to the first order) as:

$$\rho_{\text{MIR}} = \frac{L_{\text{MIR}} - B(\lambda_{\text{MIR}}, T_{\text{B,TIR}}) - \Delta_3}{\frac{E_{\text{OMIR}}}{\pi} \mu_0 - B(\lambda_{\text{MIR}}, T_{\text{B,TIR}})} \left[1 - \frac{\Delta_3}{\frac{E_{\text{OMIR}}}{\pi} \mu_0 - B(\lambda_{\text{MIR}}, T_{\text{B,TIR}})} \right]. \quad (4.8)$$

Since, according to results in Table 1,

$$\Delta_3 = B(\lambda_{\text{MIR}}, T_S) - B(\lambda_{\text{MIR}}, T_{\text{B,TIR}}) \ll L_{\text{MIR}} - B(\lambda_{\text{MIR}}, T_{\text{B,TIR}}) \quad (4.9)$$

and taking into account that

$$\frac{\Delta_3}{\frac{E_{\text{OMIR}}}{\pi} \mu_0 - B(\lambda_{\text{MIR}}, T_{\text{B,TIR}})} \ll 1. \quad (4.10)$$

Equation (4.2) may be approximated by the following equation, which represents the final form of the KR94 algorithm:

$$\rho_{\text{MIR}} = \frac{L_{\text{MIR}} - B(\lambda_{\text{MIR}}, T_{\text{B,TIR}})}{\frac{E_{\text{OMIR}}}{\pi} \mu_0 - B(\lambda_{\text{MIR}}, T_{\text{B,TIR}})}. \quad (4.11)$$

4.2.3. Radiative transfer simulations

As pointed out in the introduction, the aim of the present Chapter is to perform a systematic assessment of the performance of the KR94 algorithm when applied to burned area discrimination under a wide range of atmospheric, surface and geometry conditions,

paying special attention to those expected when applying the algorithm to the Amazon and Cerrado regions.

For this purpose, estimation of the error associated with MIR reflectance as retrieved using Eq. (4.11) will be performed based on a large number of simulated TOA radiances. These simulations are generated with MODTRAN-4, a widely used radiative transfer model (Berk et al., 2000) which was described in Section 3.3. Encompassing a large set of observation conditions, the simulations are performed in the spectral ranges of 3.62 - 3.97 μm and 10 -12 μm , i.e. covering MODIS channels 20 and 31. Brightness temperature from MODIS channel 31 is also required as input to Eq. (4.11).

The atmospheric contribution is computed for three geographical–seasonal model atmospheres stored in MODTRAN-4, namely MLW, MLS, and TRO (see Chapter 3). Use of mid-latitude profiles (i.e. MLW and MLS) is required to establish a baseline of performance of KR94 when subject to atmospheric, surface and geometric conditions for which the algorithm was specifically designed. Such baseline will then serve to assess the limitations of KR94 when employed beyond specifications, namely in case of tropical environments (e.g. as described by the TRO profile).

The three standard atmospheres cover a wide range of atmospheric conditions, with water vapor content of 0.85, 2.92 and 4.11 $\text{g}\cdot\text{cm}^{-2}$ and 2m-air temperature (T_{atm}) of 272.2, 294.2 and 299.7 K, for MLW, MLS, and TRO respectively. The assigned LST values are based on the 2-m air temperature of each profile, varying from T_{atm} to $T_{\text{atm}} + 30.0$ K in steps of 1.0 K, totalizing 31 different values. The sun-view geometry consists of 31 SZAs, from 0° to 60° in steps of 2° , and of a single VZA of 0° . Although nadir viewing is limited along the tropics when using polar orbiting instruments (such as MODIS), choice of a nadir view corresponds to the most favorable surface observation conditions. If problems arise when simulating nadir viewing (i.e. the most favorable case), then performance is expected to degrade for less favorable observation conditions. In fact, simulations were also performed for off-nadir viewing angles and, as expected, results (not shown) revealed a slight

degradation in performance of the KR94 algorithm with increasing viewing angle, a feature consistent with former studies (França and Setzer, 1998; Jiang et al., 2006) that demonstrate weak dependence of MIR region on view angle variations.

The ranges of SZA and LST are set to be representative of the observed geometric and surface conditions characteristic of regions associated to each atmospheric profile. For instance, Figure 4.2 depicts pixel values of the third quartile (P75) of LST during August 2008, retrieved over Brazil using the Spinning Enhanced Visible and Infra-Red Imager (SEVIRI) on-board METEOSAT-8.

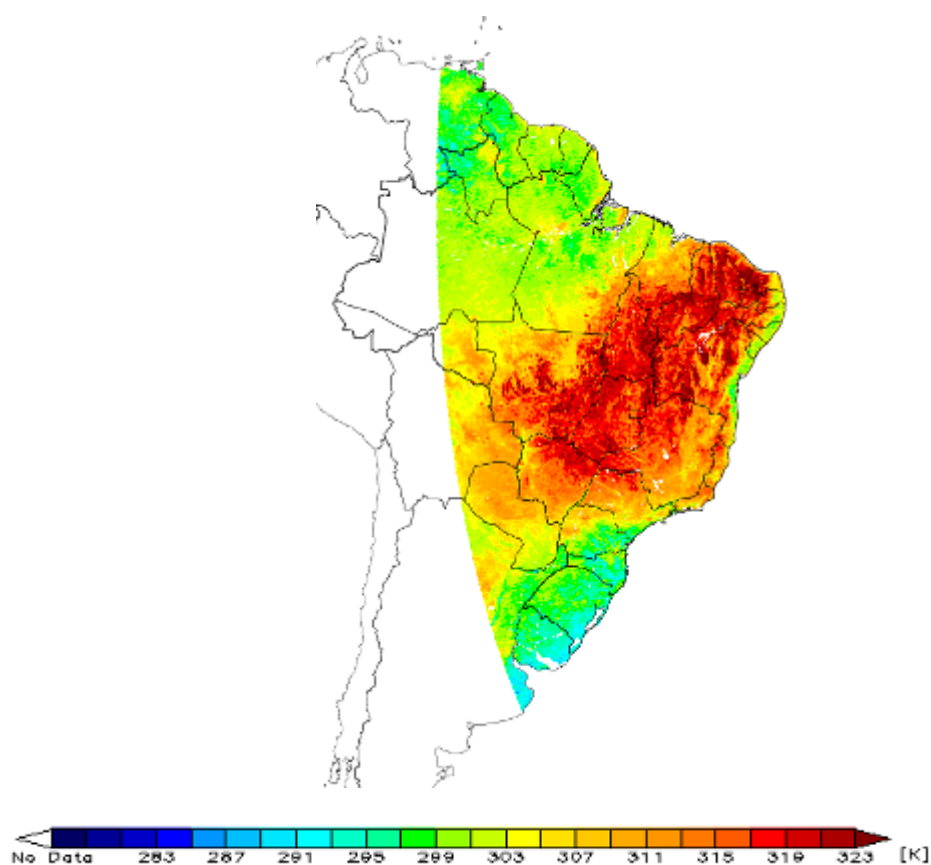


Figure 4.2. Monthly values of P75 of LST during August, 2008 over Brazil. Data were retrieved from METEOSAT-8/SEVIRI data.

Figure 4.3 presents monthly P75 values, throughout the year, of SZA as obtained from a large sample of pixels from MODIS imagery that has been operationally used for

burned area discrimination over Brazil. During the fire season (from June to October) very high values of LST are observed over Amazonia and especially over the adjacent Cerrado, region, where a large area may be found that presents values of P75 larger than 320 K. In addition, more than 25% of the pixels are associated to values of SZA greater than 40° , i.e. to low values of the solar signal.

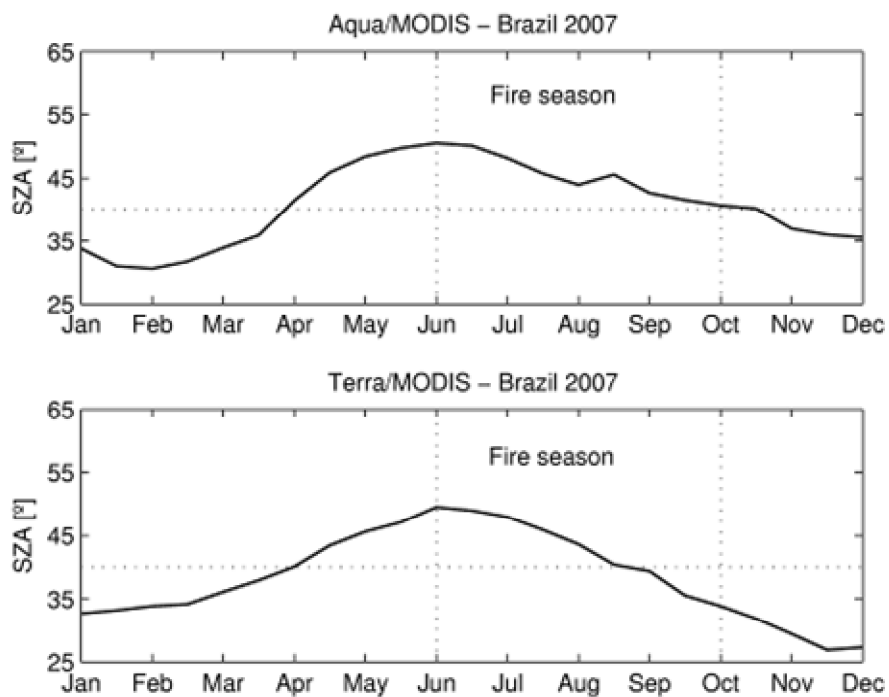


Figure 4.3. Monthly values of P75 of SZA as obtained from samples of Aqua/MODIS and Terra/MODIS imagery along the year of 2007 over Brazil. The threshold of 40° for SZA is highlighted by the dotted horizontal line. Dotted vertical lines delimit the fire season in Amazonia (June to October).

Two types of surface cover were considered, namely burned and unburned. Both surface types were assumed to be homogeneous and Lambertian, the burned and unburned surfaces being characterized respectively by charcoal and vegetation spectra. As discussed in Section 3.2, four fire residue samples were collected at Alta Floresta, state of Mato Grosso, Brazil. Charcoal spectra were measured at the NASA/JPL and may be viewed as

typical of tropical environments. Mean values of the four charcoal spectra were then used to prescribe the surface reflectance of the burned surface as input to MODTRAN-4. Regarding the unburned surface, prescribed reflectance values were obtained from a set of 25 surfaces from the MODIS-UCSB spectral library. The set includes most vegetation types (Salisbury and D'Aria, 1994; Peres and DaCamara, 2004), with reflectance values varying from 0.01 to 0.04, in the MIR region. A value of 0.24 (0.03) was, accordingly, prescribed for MIR reflectance for the burned (unburned) types of surface cover. These values were obtained by averaging the MIR spectral signature for the four (25) considered charcoal (vegetation) types, which were convolved with the MODIS channel 20 normalized response function. Results ought to be applicable to other sensors having spectral windows similar to that used in this work.

4.3. Analysis and results

4.3.1. MODTRAN-4 simulations

As discussed in the previous section, the method developed by KR94 relies on a number of simplifying assumptions regarding atmospheric transmittances and atmospheric downward and upward thermal emission radiances. All these terms are correlated and depend essentially on atmospheric water vapor content. When atmospheric water vapor increases, atmospheric transmittances decrease, whereas the atmospheric downward and upward thermal emission radiances increase. Table 4.2 shows the range of atmospheric terms that may typically be found in the MIR region, in the case of the three geographical-seasonal model atmospheres considered, i.e., when varying from 'dry' to 'moist' conditions. For instance, whereas high transmittances and low path-radiances values characterize the MLW atmospheric profile, the TRO profile is associated to lower transmittances and relatively

high path-radiance values. It is therefore to be expected that use of Eq. (4.11) in retrieving MIR reflectance may introduce systematic deviations, especially in the case of 'moist' atmospheres. For example, in the case of TRO, the relative error associated to the assumption of $\tau_{\text{MIR}} = 1$ (instead of the realistic value $\tau_{\text{MIR}} = 0.79$) is about 27% but drops to 10% in the case of MLW (taking into account that $\tau_{\text{MIR}} = 0.91$). In the case of the two-way atmospheric transmittance, the relative error associated to the assumption of $t_{\text{MIR}} = 1$ (instead of $t_{\text{MIR}} = 0.65$) in the case of TRO is about 54% but drops to 24% in the case of MLW (where $t_{\text{MIR}} = 0.81$). In a similar fashion, neglecting the atmospheric downward emission term leads to a relative error of 17% for the TRO profile, in contrast with MLW where the corresponding error decreases to 3%. Finally, neglecting the atmospheric upward emission term leads to a relative error of 9% for the TRO profile and just to an error of 2% in the case of MLW.

Table 4.2. Effects of water vapor content [$\text{g}\cdot\text{cm}^{-2}$] on atmospheric terms for the three profiles analyzed, considering nadir view and a SZA of 0° .

Profile	Water vapour content [$\text{g}\cdot\text{cm}^{-2}$]	T_{MIR}	t_{MIR}	$L_{\text{atm,MIR}} \uparrow$ [$\text{W}\cdot\text{m}^{-2}\cdot\mu\text{m}^{-1}\cdot\text{sr}^{-1}$]	$\bar{L}_{\text{atm,MIR}} \downarrow$ [$\text{W}\cdot\text{m}^{-2}\cdot\mu\text{m}^{-1}\cdot\text{sr}^{-1}$]
MLW	0.85	0.91	0.81	0.006	0.012
MLS	2.92	0.83	0.70	0.038	0.068
TRO	4.11	0.79	0.65	0.057	0.104

Accuracy of the solutions provided by Eq. (4.11) may be assessed by evaluating the corresponding relative errors, defined as the differences between retrieved values using Eq. (4.2) and the corresponding prescribed values as input to MODTRAN-4, divided by the latter values. Figures 4.4 - 4.6 present the obtained values of relative errors of MIR reflectance as a function of LST and SZA. The curves correspond to nadir-viewing conditions and represent charcoal (left panels) and vegetation (right panels) surfaces for MLW (Figure 4.4), MLS (Figure 4.5) and TRO (Figure 4.6). It is worth stressing that ranges of LST considered are

different for each profile (as discussed in Section 4.2.3) and reflect the surface conditions typically associated to each type of atmosphere.

It is well apparent that relative errors strongly depend on the surface type, for all three atmospheric profiles. In particular, it may be noted that the magnitude of relative errors is considerably larger for vegetation than for charcoal, and increases with moisture content, MLW showing the lowest values and TRO the highest. For instance, the lower values obtained in the case of MLW are in close agreement with results found by KR94, who estimated the accuracy of Eq. (4.11) to lie in the range of 0.01 – 0.02 (absolute errors) for a mid-latitude atmosphere and for the range of reflectance to be expected from a variety of vegetation and soils (0.01 – 0.06). In strong contrast, vegetation surfaces present extremely large relative errors, ranging from 100% – 1,200% for LST values to be expected in tropical regions. Taking the value of 0.03 as reference for reflectance of vegetation, the obtained range corresponds to absolute errors of 0.06 – 0.4. In the case of charcoal, relative errors are one order of magnitude smaller, ranging from -20% – 80%, i.e. from about -0.05 – 0.2 in terms of absolute error, and taking a reference value of 0.24 for charcoal reflectance. Dependence of the relative error on LST is stronger than on SZA, especially for values of SZA lower than 30°, a feature clearly revealed by the low slope of the error curves in Figures 4.4 - 4.6.

Performance of the KR94 algorithm is closely linked to the magnitude of the relative contribution of thermal emitted radiance, L_e , to the total TOA MIR radiance, L_{MIR} , given by Eq. (2.8). It may be noted that L_e is given by the second, third and fourth terms of the right-hand side of Eq. (2.8), i.e.

$$L_e = \tau_{MIR} \varepsilon_{MIR} B(\lambda_{MIR}, T_S) + \tau_{MIR} \rho_{MIR} \overline{L_{atm, MIR} \downarrow} + L_{atm, MIR} \uparrow . \quad (4.12)$$

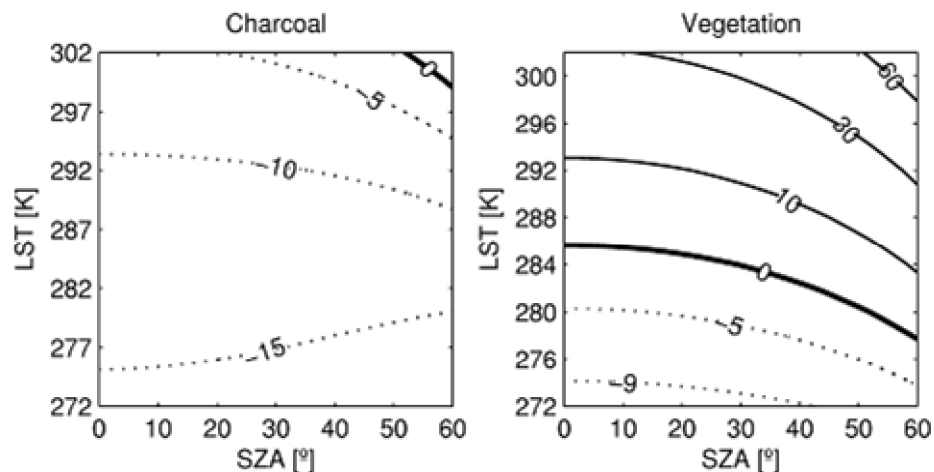


Figure 4.4. Relative error [%] on MIR reflectance in the case of MLW for charcoal (left panel) and vegetation (right panel). Solid (dotted) curves indicate positive (negative) errors and the thick curve highlights the no-error line.

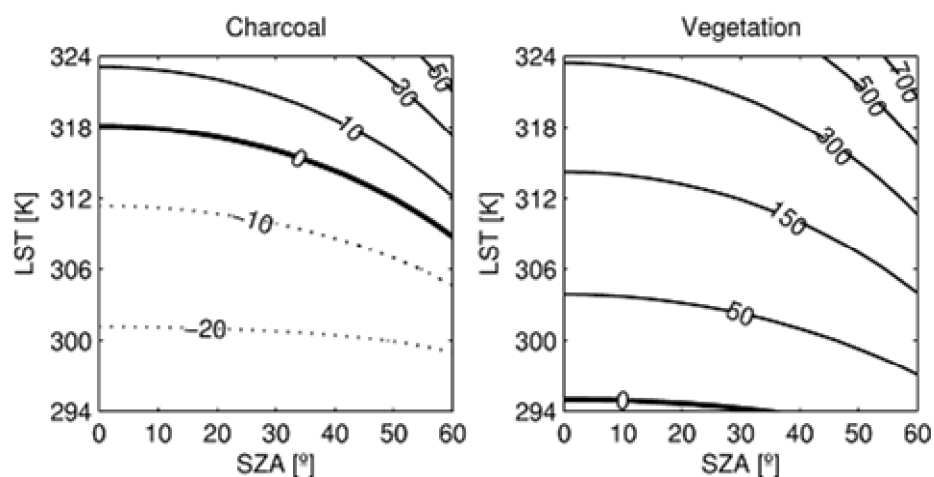


Figure 4.5. As in Figure 4.4 but in the case of MLS.

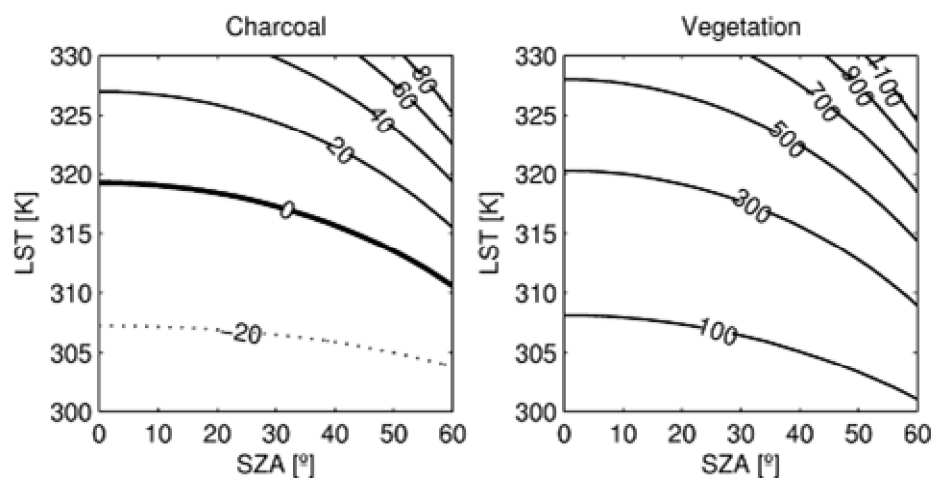


Figure 4.6. As in Figure 4.4 but in the case of TRO.

When the ratio L_e/L_{MIR} exceeds a threshold of about 0.75 the solutions provided by Eq. (4.11) are contaminated by unacceptably large relative errors, on the order of 100%. The magnitude of L_e/L_{MIR} , and therefore the range of validity of Eq. (4.11), mainly depends on the type of the surface considered, as well as on its temperature, atmospheric profile, and sun elevation angle. Figure 4.7 presents the dependence of L_e/L_{MIR} on LST for vegetation (circles) and charcoal (squares) under two extreme illumination angles, respectively an SZA of 0° (open symbols) and of 60° (black symbols), and for the two extreme cases of atmospheric moisture content, respectively MLW (left panel) and TRO (right panel) profiles. The contrasting behavior of charcoal and vegetation is well apparent. In the case of charcoal, high values of MIR reflectance (about 0.24) lead to a major contribution of the reflected component and, therefore, the ratio L_e/L_{MIR} will be below 50% (75%) in the case of MLW (TRO), except for large values of LST, above 289 K (293 K) for MLW (TRO), associated to very low sun elevation angles (SZA= 60°). Acceptable estimates of charcoal reflectance are therefore to be expected from Eq. (4.11), the sole exception being cases of high LST values (larger than 320 K), co-occurring with high SZA values (larger than 50°), which may lead to relative errors in excess of 25%. Because of the very low vegetation reflectance (about 0.03, i.e. eight times lower than that of charcoal), total TOA MIR radiance, L_{MIR} , will be primarily due to the thermal emitted component, and a deeply contrasting behavior is to be expected between charcoal and vegetation. In the latter type of surface, the ratio L_e/L_{MIR} is always larger than 75% in the case of TRO, and in the case of MLW for low solar elevation (SZA= 60°). Even for solar zenith conditions (SZA= 0°) the ratio L_e/L_{MIR} exceeds 75% in the case of MLW, for LST values as low as 288 K. Implications of the solutions provided by Eq. (4.11) on relative errors are well depicted in the left panels of Figs. 4.4 and 4.6; in the case of TRO, relative errors are unacceptably large (exceeding 50%) over the entire domain

considered, whereas in the case of MLW relative errors are larger than 25% for values of LST beyond 290 K, whenever SZA surpasses 50°.

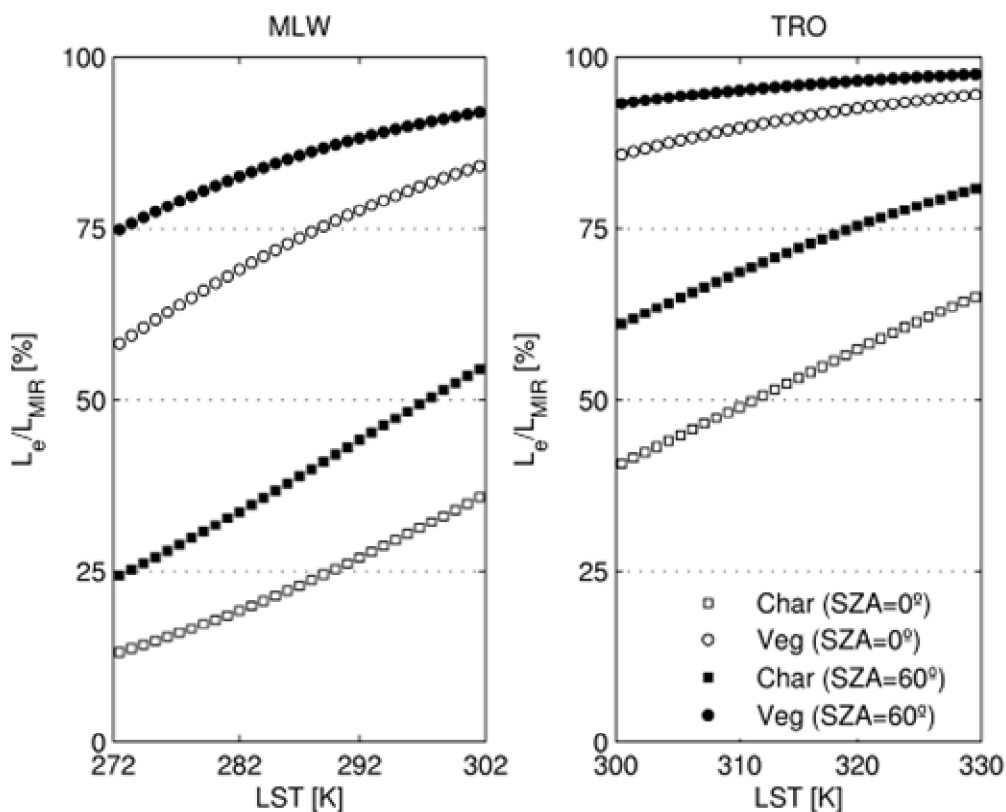


Figure 4.7. Plot of the ratio L_e/L_{MIR} [%] as a function of LST in the case of MLW (left panel) and TRO (right panel). Square (circle) symbols denotes charcoal (vegetation) surface whereas open (black) symbols characterizes SZA of 0° (60°).

The above-discussed limitations of the KR94 algorithm may give rise to serious difficulties when attempting to discriminate between burned and unburned surfaces, in particular in the case of tropical environments. For instance, an absolute error of 0.2 in a typical vegetation reflectance of about 0.03 leads to a retrieved value of about 0.23 which reaches the range characteristic of charcoal. The problem is illustrated in Figure 4.8, which presents results obtained when using Eq. (4.11) to retrieve the reflectance of vegetation (with the prescribed value of 0.03) and of charcoal (with the prescribed value of 0.24) in the three

considered cases of MLW, MLS and TRO, for values of SZA from 0 – 60° and for ranges of typical values of LST for each profile.

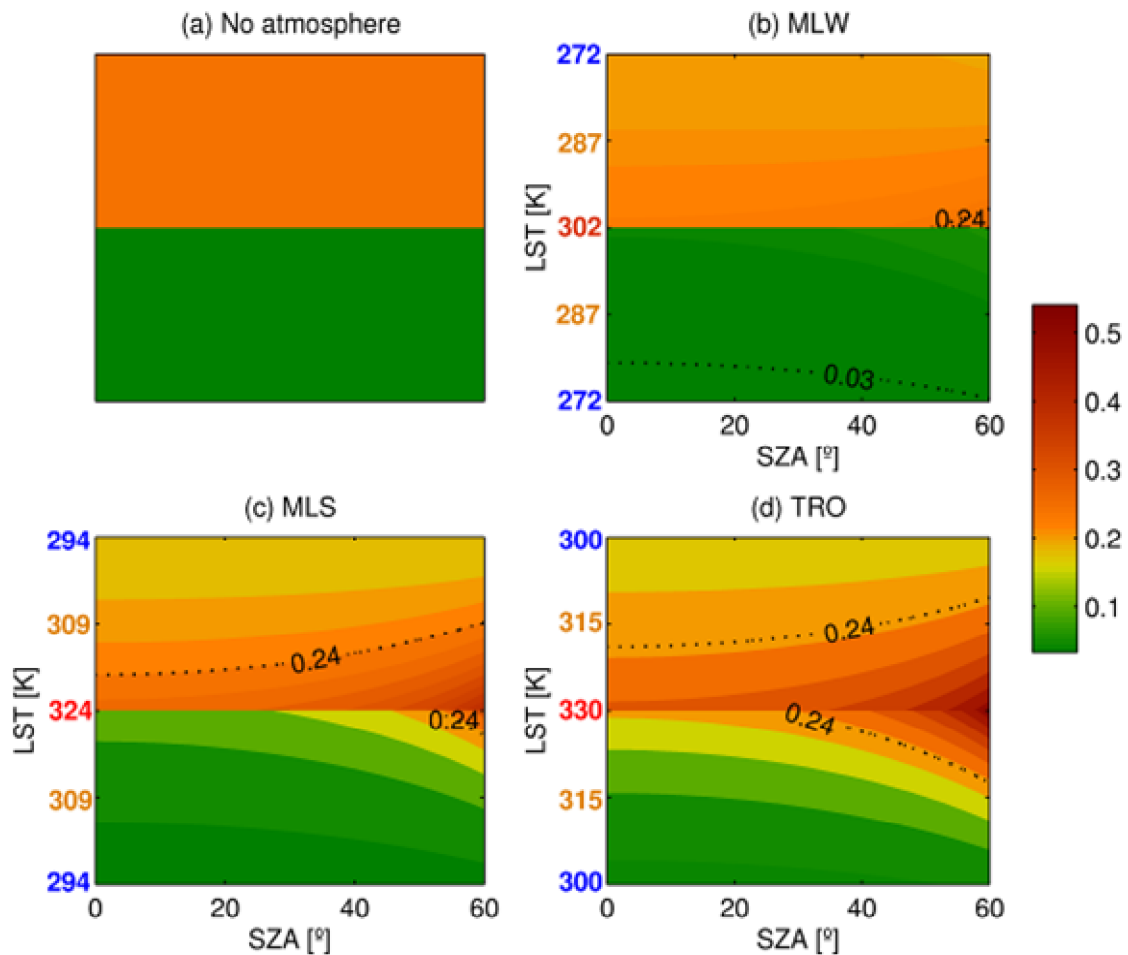


Figure 4.8. Diagram of values of reflectance for vegetation and charcoal surfaces for different atmospheric profiles, LST and SZA; a) the two surfaces with prescribed constant values of 0.03 and 0.24 for vegetation (green) and charcoal (orange); b) to d) retrieved values of reflectance using Eq. (4.11) as a function of SZA and LST for MLW, MLS and TRO profiles.

It is well apparent that the accuracy of retrieved values of reflectance is much more sensitive to LST and SZA in the case of vegetation than for charcoal. For instance, the reference contour line of 0.03 (for vegetation) is displaced out of the considered domain in the case of MLS and TRO and, even for MLW; it is located at the bottom, almost out of the

domain. The displacement of the reference contour line of 0.24 for charcoal is much smaller and is barely noticeable in the case of MLW. However, the robustness of Eq. (4.11) in the case of charcoal is not enough to discriminate burned from unburned surfaces, because values of reflectance for vegetation attain those characteristics of charcoal for sufficiently high values of LST and SZA. As shown in Figure 4.8, in the case of MLS, even if the discontinuities observed along the band separating the two considered surfaces indicate the possibility of discriminating between them, values of the contour lines on both sides are larger than 0.20. Therefore, it is not possible to label either type as the unburned surface. The situation is even worse for TRO where, for values of LST greater than 315 K and SZA larger than 30° , both surfaces reach similar reflectance values, becoming undistinguishable.

4.3.2. Case study

A more realistic assessment of the implications of using Eq. (4.11) for burned area discrimination in tropical environments may be achieved by means of a case study based on satellite imagery. However, as pointed out by Roger and Vermote (1998), any attempt to validate retrieved values of MIR reflectance from satellite data is virtually impaired by the absence of “in-situ” (direct) measurements. This limitation may be circumvented by creating a reference dataset of MIR reflectance based on information from a real satellite image. The adopted approach consists of the following steps: (1) collect information about land surface temperature, land surface emissivity, atmospheric profiles and view/solar angles for the selected scene; (2) use a radiative transfer model (MODTRAN-4 in the present study) to compute the respective values of transmittance and atmospheric parameters; and (3) use Eq. (4.2) with values obtained in the previous steps to retrieve MIR reflectance from the total signal. The generated reference dataset of MIR reflectance may then be used to validate the corresponding MIR reflectance as retrieved by means of KR94.

Taking into account the described procedure, it seems appropriate to select an image where the atmospheric conditions are particularly favorable, e.g. with low values of the water vapor column, and a low amount of aerosols (i.e. with a clear sky surrounding). Since results from simulations (Section 4.3.1) showed that the accuracy of retrieved values of reflectance is very sensitive to high values of LST, it seems also appropriate to select an image with moderate values of LST.

All the above-mentioned favorable characteristics are met in the case of the large fire event that took place from April 30 to May 12, 2006 and affected the entire area of the Ilha Grande National Park, located between the states of Paraná and Mato Grosso do Sul, Brazil. The burned is about 200 km², as estimated by INPE based on information from Landsat TM imagery (Figure 4.9). A total of 413 active fires during the above-mentioned period were also identified by INPE, using data from GOES, NOAA, Aqua and Terra satellites.

Performance of Eq. (4.11) was assessed using TOA values of MIR radiance and TIR brightness temperature as acquired on May 12, 2006 by the MODIS instrument on-board Aqua. Data were obtained from the Aqua/MODIS Level 1B 1km V5 product, MYD021 (MCST, 2006) and correspond to channels 20 and 31. Surface values of MIR reflectance were then retrieved by solving Eq. (4.2) using MODTRAN-4, using information about surface temperature and sun elevation together with data of temperature and humidity for the atmospheric column. As mentioned in Section 3.2.1.1, pixel values of LST and of SZA, varying from 295 to 315 K and from 48.5 to 51°, respectively were obtained from Land Surface Temperature/Emissivity Daily 5-Min L2 Swath 1 km product, MYD11_L2 (Wan, 1999). As also mentioned in Section 3.2.1.1, atmospheric profiles of temperature and humidity were obtained from the Atmosphere Profile Level 2.0 product, MYD07_L2 (Seemann et al., 2006), the water vapor content over the selected area varying from 1.3 to 2.3 g·cm⁻², a quite low amount when compared with the value of 4.11 g·cm⁻² of the TRO profile stored in MODTRAN-4. Figure 4.10 represents the MODIS mean profiles of

temperature and humidity together with the TRO profile that will be used to generate synthetic imagery with characteristics to be expected over tropical environments.

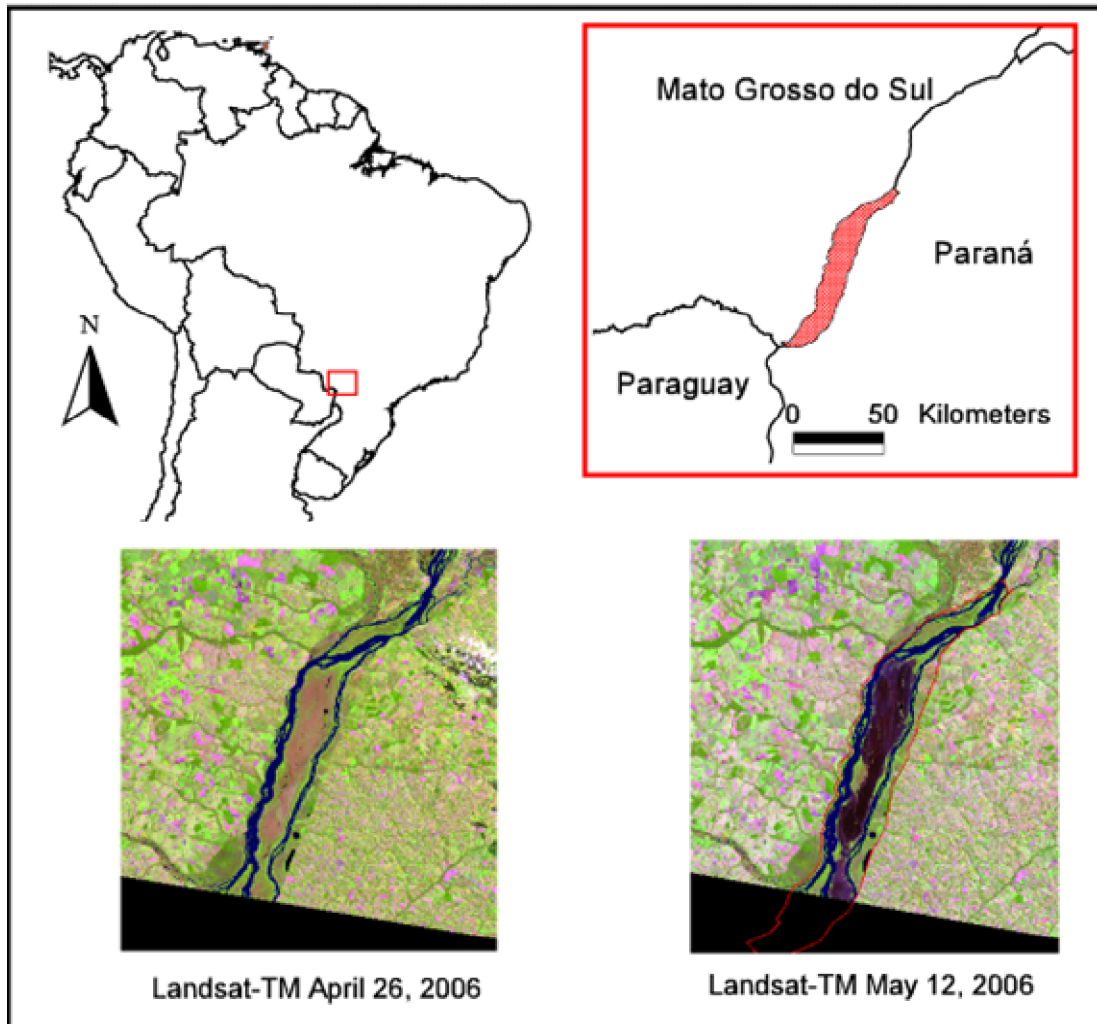


Figure 4.9. Location of the Ilha Grande National Park, between the states of Paraná and Mato Grosso do Sul (upper right panel) in southwestern Brazil (upper left panel) and Landsat TM image (RGB 543) of the National park before the fire episode, on April 26, 2006 (lower left panel) and after the fire episode on May 12, 2006 (lower right panel). The outline of the National Park is shown in red.

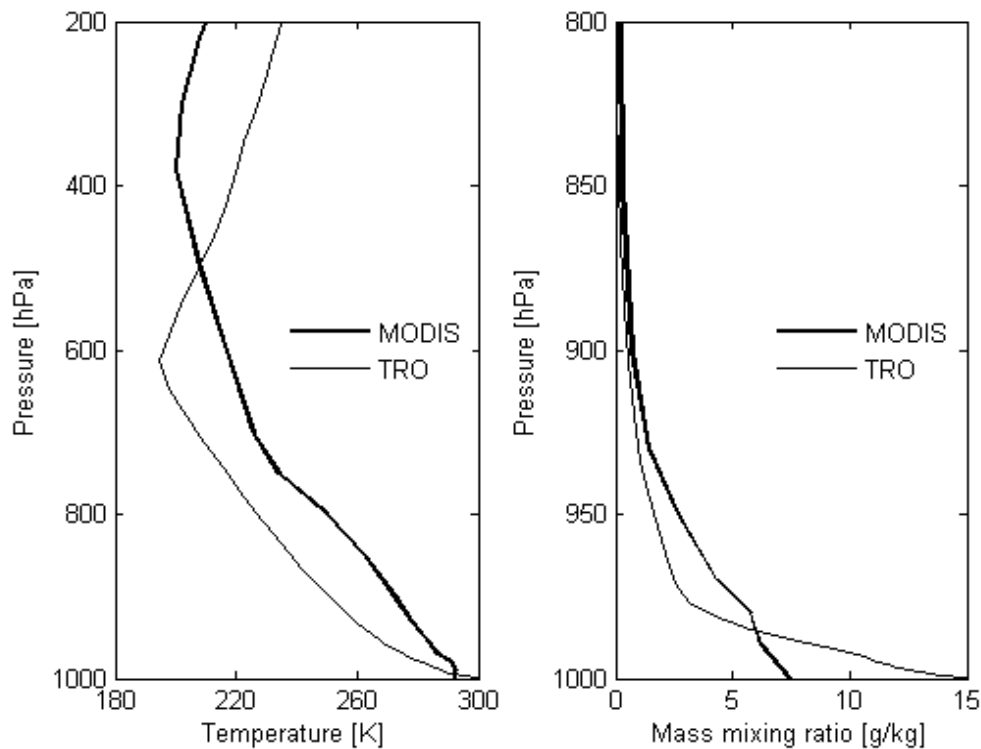


Figure 4.10 MODIS mean profiles (bold curves) of temperature (left panel) and humidity (right panel) over Ilha Grande National Park on May 12, 2006. The TRO profile stored at MODTRAN-4 is also represented (thin curves).

Retrieved values of surface MIR reflectance and values of LST are shown in Figure 4.11. Higher values of MIR reflectance and LST over the burned area are particularly conspicuous, especially because of the contrasting behavior of the surrounding vegetated areas, which present a large spatial variability of reflectance and temperature.

Values of retrieved surface MIR reflectance and of LST (Figure 4.11) were input to MODTRAN-4, to produce synthetic images of TOA MIR radiance and TIR brightness temperature. These images correspond to the following two environments, characterized by atmospheric and surface conditions expected in tropical regions; i) the TRO environment, obtained using the TRO profile and the LST of May 12 ,2006 and ii) the TRO-HOT environment, obtained using the TRO profile and LST+20 K. The KR94 algorithm was then used to retrieve values of surface reflectance from TOA MIR radiance and TIR brightness

temperature of the original images (May-12 environment) and of the synthetic ones (TRO and TRO-HOT environments).

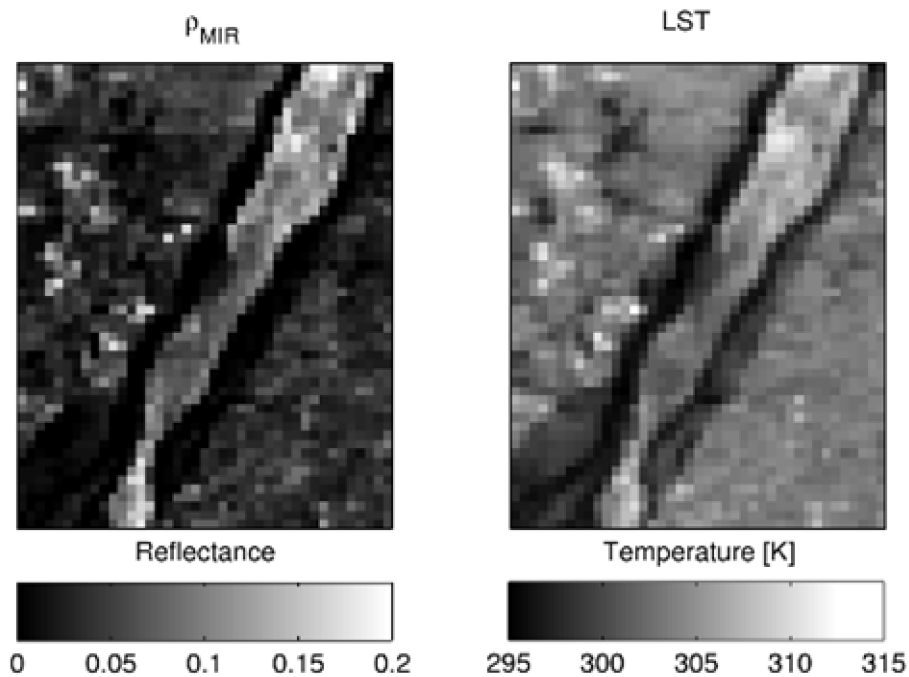


Figure 4.11. Retrieved values of surface MIR reflectance (left panel) and LST (right panel) over the Ilha Grande National Park on May 12, 2006.

The impact of using retrieved values to discriminate between burned and unburned surfaces for the three considered environments was evaluated by comparing the values of reflectance as retrieved by Eq. (4.11) over two sets of pixels representative of the two classes to be discriminated and then checking whether the respective statistical distributions allow distinguishing between the surfaces.

A set of 133 burned pixels, hereafter referred to as the burned class, was therefore selected from the scene, together with a set of 262 pixels that included the remaining land cover types (namely green vegetation, crop fields and water bodies), hereafter referred to as the unburned class. As described in Section 3.2.1.2, choice of pixels was made by visual comparison between two Landsat TM scenes (path/row 224/76) acquired on April 24 and

May 12, 2006. Hot spots detected by INPE (see Section 3.2.3.2) were also used in the process of selecting pixels associated to burned surfaces.

According to Kaufman and Remer (1994), a quantitative assessment of the effectiveness of the KR94 algorithm to discriminate between burned and unburned surfaces may be obtained with the M index, as described in Chapter 2 (Eq. (2.9)). It is worth noting that index M may be viewed as an estimator of signal-to-noise ratio, the absolute difference between the mean values of the two classes representing the signal (associated to between-group variability) and the sum of the standard deviations representing noise (associated to within-group variability). Values of M larger than one indicate good separability, whereas values smaller than one represent a large degree of overlap between the values associated to the two classes.

Results are shown in Figure 4.12 and Table 4.3. In the case of unburned surfaces, and when going from May-12 to TRO-HOT environments, there is a progressive shift of the histograms towards larger values of reflectance, accompanied by an increase of dispersion. Both shift and increase are especially pronounced from TRO to TRO-HOT. In strong contrast, in the case of burned surfaces, histograms of reflectance remain virtually unchanged when comparing May-12 to TRO environments, and there is a moderate shift when going from TRO to TRO-HOT environments.

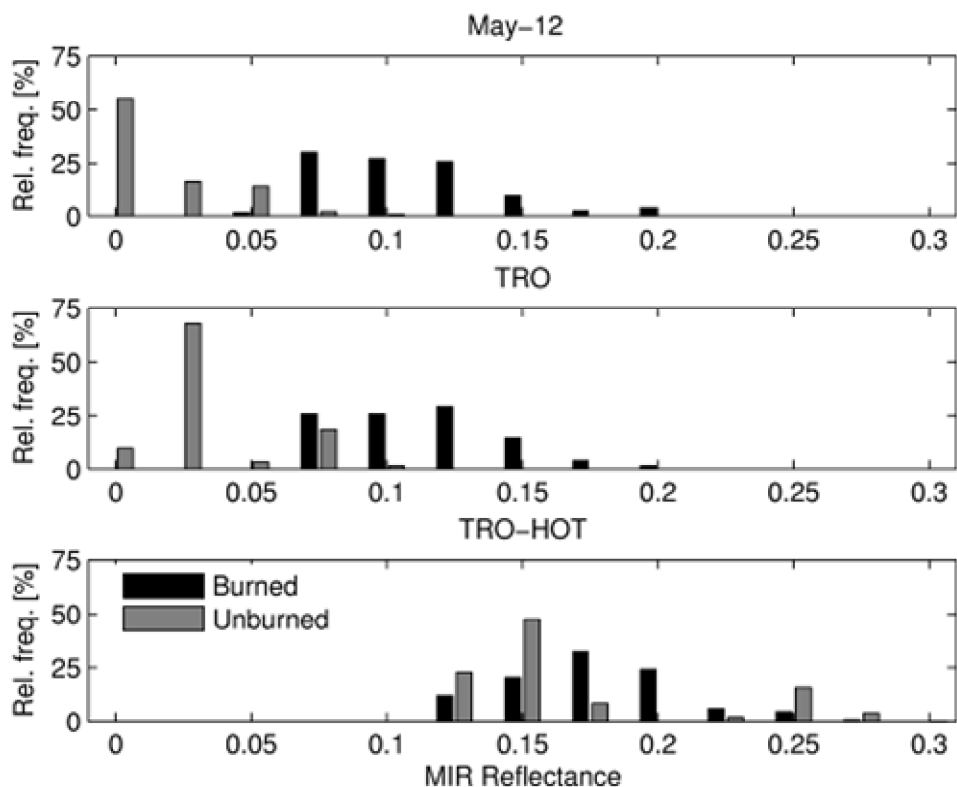


Figure 4.12. Histograms of MIR reflectance for burned (black) and unburned (gray) classes as retrieved by means of Eq. (4.11) for May-12 (upper panel), TRO (middle panel) and TRO-HOT (lower panel) environments.

Moreover, the dispersion is virtually unaffected by injection of water vapor in the atmosphere and by surface temperature increase. The different sensitivity of the two types of surface leads to a progressive overlap of the histograms, which is translated by the decrease of M , from May-12 to TRO-HOT, and especially from TRO to TRO-HOT. In the latter type of environment M reaches a value of 0.53, an indication of very poor discriminant ability.

Results obtained for the fire event at the Ilha Grande National Park confirm those previously obtained with MODTRAN-4 simulations, namely that discrimination between burned and unburned surface based on values of surface reflectance retrieved with the KR94 algorithm is virtually impaired in the case of tropical regions for high values of surface temperature, especially when associated to low sun elevation angles. Since such circumstances are often present when using data from instruments on-board polar-orbiters

(namely MODIS in Aqua and Terra) to identify burned areas over the Amazon and the adjacent Cerrado, special care is required when using the KR94 algorithm.

Table 4.3. Mean values, μ_u (μ_b), and standard deviation, σ_u (σ_b), of unburned (burned) surfaces and discrimination indices, M, for retrieved values of surface reflectance in the case of May-12, TRO and TRO-HOT environments.

	μ_u	σ_u	μ_b	σ_b	M
May-12	0.02	0.021	0.11	0.032	1.76
TRO	0.03	0.024	0.12	0.027	1.58
TRO+HOT	0.17	0.046	0.18	0.033	0.53

4.4. Concluding remarks

Identification of burned areas over the Amazon and Cerrado regions is a challenging task because of the ephemeral character of the radiative signal and the presence of aerosols that prevent using classical approaches e.g. based on red and near-infrared information. MIR presents the advantage of being virtually unaffected by the presence of most types of aerosols, in particular those associated to biomass burning. In this respect the reflected component of MIR has proven to be especially adequate to discriminate between burned and unburned surfaces in mid-latitude regions (e.g. Pereira, 1999).

Kaufman and Remer (1994) proposed a methodology that presents the advantage of enabling for the retrieval of MIR reflectance with no need for auxiliary datasets or major computational means. The so-called KR94 algorithm, given by Eq. (4.11), has been specifically designed to retrieve MIR reflectance over dense dark forests in the middle latitudes. It has been also successfully applied to other types of surfaces and atmospheric environments, in particular for burned area discrimination (e.g. Barbosa et al., 1999; Roy et al., 1999). However, the quality of the retrieved values of MIR reflectance by means of KR94

methodology may significantly degrade when the relative contribution of the thermal emitted component to the total signal exceeds a threshold of about 75%. In the case of surfaces, such as vegetation, characterized by low values of MIR reflectance, the relative contribution of the solar component to the total MIR signal tends to be small, especially when the surface is hot (i.e. in case of relatively high values of LST). This contribution may be further reduced when the solar signal is weak due to low sun elevation angles (i.e. in case of high values of SZA). The above-mentioned aspects are especially relevant in tropical environments, where high land surface temperatures naturally dominate the scenes and pixels illuminated by low sun elevation angles are often present when using data from sensors on-board polar orbiters, in particular MODIS on-board Aqua and Terra.

Use of Eq. (4.11) in tropical environments to retrieve vegetation reflectance may lead to errors that are at least of the same order of magnitude of the reflectance to be retrieved and considerably higher for large values of LST and SZA. Under such conditions, retrieved values of reflectance for vegetation may attain those characteristic of charcoal making the two types of surface undistinguishable. Use of the KR94 algorithm becomes severely impaired and the complete radiative transfer equation, i.e. Eq. (4.2), may be an alternative, provided the required auxiliary information is available about the surface (LST) and the atmospheric column (temperature and humidity profiles). This aspect will be addressed in Chapter 5.

Chapter 5

Retrieval of middle-infrared reflectance using the Radiative Transfer Equation

5.1. Introduction

Retrieval of middle infrared reflectance may be undertaken by means of approximate methods, like that proposed by KR94, which are fast and easy to implement, but may be insufficiently accurate under specific surface and atmospheric conditions. For instance, in the previous chapter, an assessment was made on the quality and limitations of retrieved MIR reflectance by means of KR94's method when applied to discriminate burned areas in tropical environments, in particular in the Amazon and Cerrado regions. It was shown that

the quality of retrieved values may significantly degrade when the relative contribution of the thermal emitted component to the total signal exceeds a threshold of about 75%. In the case of surfaces, such as vegetation, characterized by low values of MIR reflectance, the relative contribution of the solar component to the total MIR signal tends to be small, especially when the surface is hot (i.e. in case of relatively high values of LST). This contribution may be further reduced when the solar signal is weak due to low sun elevation angles (i.e. in case of high values of SZA).

The two above-mentioned limitations are especially relevant in tropical environments, where high land surface temperatures naturally dominate the scenes and pixels illuminated by low sun elevation angles are often present when using data from sensors on-board polar orbiters, in particular MODIS on-board Aqua and Terra. Libonati et al. (2010) have concluded that using the KR94 algorithm in tropical environments to retrieve vegetation reflectance may lead to errors that are at least of the same order of magnitude of the reflectance to be retrieved and considerably higher for large values of LST and SZA. In fact, there is a critical region in the LST vs. SZA space where the MIR reflectance retrieval is severely impaired. Under such conditions, retrieved values of reflectance for vegetation may attain those characteristic of charcoal making the two types of surface undistinguishable. Provided auxiliary information about the surface (LST) and the atmospheric column (temperature and humidity profiles) is available, use of the RTE appears, in this context, as a possible way to circumvent the problem or, at least, as a means to improve the estimates provided by KR94 in the domain where this algorithm is applicable.

Accordingly, the main purpose of this study is to carry out a systematic comparison between the RTE and KR94 approaches taking into account the performance and the need for auxiliary data, as well as the required computing resources. The added value that is expected from using the complete radiative transfer equation will be assessed, both inside and beyond the region where the KR94 produces usable estimates of MIR reflectance and paying special attention to their use for discriminating burned areas in tropical environments,

namely in the Amazon and Cerrado regions of Brazil. The adequacy of using the RTE will be assessed by considering the background error covariance matrix used in the assimilation schemes of the Global Circulation Model operated at ECMWF, the radiometric noise in the MODIS instrument and the errors associated to the MODIS LST product (MOD11_L2). It may be noted that use of the ECMWF background error covariance matrix instead of the uncertainties on the MODIS Atmospheric Profile product (MOD07) was justified in Chapter 3.

5.2. Method and data

5.2.1. Radiative Transfer Simulations

Retrieval of MIR reflectance using Eq. (4.2) involves a direct evaluation of all components of the MIR signal by means of a radiative transfer model. Besides requiring substantial computational means, the operational use of the RTE is limited by other factors, namely the need of quantitative information on 1) atmospheric conditions, mainly humidity and temperature profiles, which are required to perform the atmospheric corrections, and 2) on LST which is required as a boundary condition. The above-mentioned limitations led to the development of simpler methods, like the one proposed by KR94, which require neither direct knowledge of atmospheric conditions and LST, nor a radiative transfer model.

The estimation of the error associated with MIR reflectance as retrieved when using either RTE, i.e. Eq. (4.2) or the KR94 method, i.e. Eq. (4.7), will be performed based on a large number of simulated TOA radiances. These simulations will be generated by means of MODTRAN-4 (see Section 3.3), encompassing a large set of observation conditions. The simulations will be performed in the spectral ranges of 3.62 – 3.97 μm and 10 – 12 μm , i.e. covering MODIS channels 20 and 31.

The following cases will be considered:

1. *Atmospheric Temperature and Humidity Profiles*: The database relies upon temperature and humidity profiles from three geographical–seasonal model atmospheres stored in MODTRAN-4, namely MLW, MLS, and TRO, as discussed in Chapter 3. The minimum air temperature at 2-meter is 272.2 K (MLW) and the maximum value is 299.7 K (TRO). The water vapor contents ranges from 0.85 to 4.11 g·cm⁻²;
2. *LST*: The assigned LST values are based on the 2-m air temperature of each profile, varying from T_{atm} to $T_{\text{atm}}+30.0$ K in steps of 1.0 K, totalizing 31 different values;
3. *LSE/reflectance*: Two types of surface cover are considered, namely burned and unburned. Both surface types were assumed to be homogeneous and Lambertian, the burned and unburned surfaces being characterized respectively by charcoal and vegetation spectra, as discussed in Chapter 3. A value of 0.24 (0.03) was, accordingly, prescribed for MIR reflectance for the burned (unburned) types of surface cover. These values were obtained by averaging the MIR spectral signature for the four (25) considered charcoal (vegetation) types, which were convolved with the MODIS channel 20 normalized response function;
4. *SZA and VZA*: The sun-view geometry consists of 31 solar zenith angles, from 0° to 60° in steps of 2°, and of view zenith angles of 0°, 30° and 60°.

5.2.2. Sources of errors in the retrieval of MIR reflectance

Besides the errors inherent to the inversion procedure and those introduced by the adopted approximations, the accuracy of Eq. (4.2) will depend essentially on three sources of error, namely, i) the uncertainties on the atmospheric profile, which are usually due to the errors in temperature and humidity profiles, ii) the error due to instrument performance, which

is quantified by the radiometric noise and iii) the error due to uncertainties in the retrieval of the LST. Contribution of each source of error will be analyzed separately in the followings sections.

5.2.2.1. Radiometric Noise of MODIS channel 20

The radiance measured by a sensor onboard a satellite is affected by an inherent uncertainty due to electronic devices involved in the construction of the sensor (Jiménez-Muñoz and Sobrino, 2006). Levels of noise to be introduced into the MODIS channel were based on the noise equivalent temperature (NE Δ T) at 300 K of channel 20 (0.05 K) that were converted to the respective noise equivalent radiance (NE Δ L). The radiance sensitivity of channel 20 to small changes in temperature is shown in Figure 5.1.

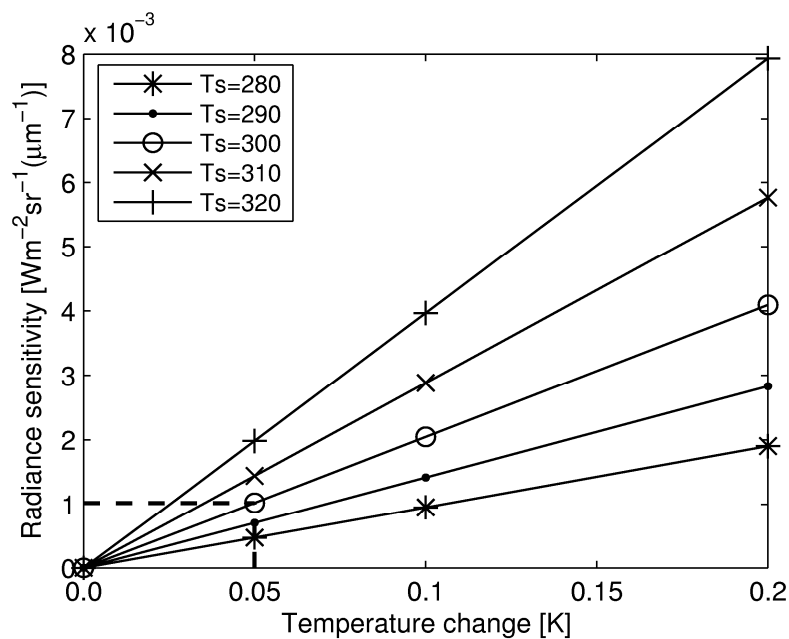


Figure 5.1. Sensitivity of MODIS channel 20 to small changes in temperature. The dashed line indicates the values of NE Δ T and NE Δ L.

Randomly generated perturbations were then added to the simulated TOA radiances. Added perturbations are normally distributed around zero mean and with standard deviations equal to the respective MODIS channel NE Δ L (see Figure 5.2). In order to get a statistical significantly result, we have generated 1,000 random perturbations.

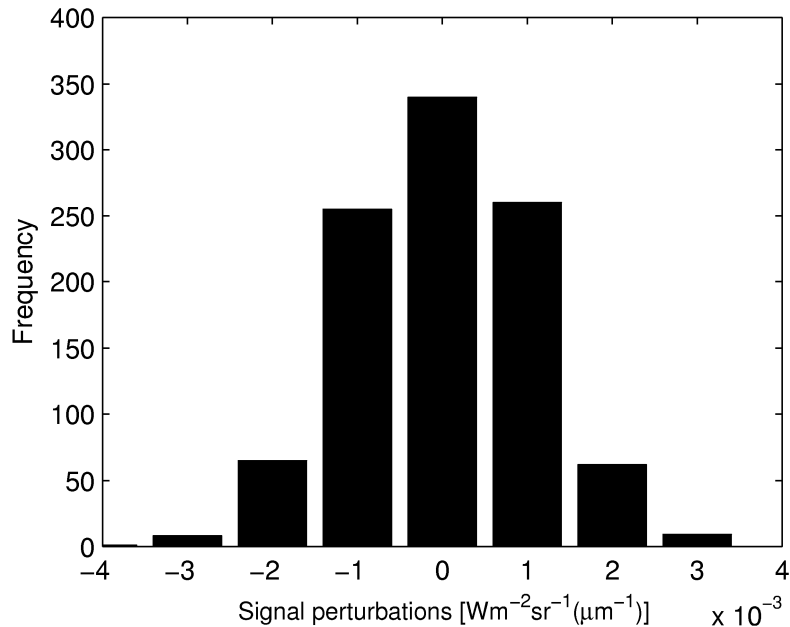


Figure 5.2. Frequency histogram of the satellite radiance perturbations for MODIS channel 20.

5.2.2.2. Atmospheric Profiles

The effects of uncertainties on the humidity and temperature profiles may be analyzed by comparing the radiation at the top of the atmosphere for a given perturbed profile with the radiance for the reference profile. Because the results will depend on the reference (non-perturbed) profile, the experiment adopts the three standard atmospheres stored at MODTRAN-4, namely, TRO, MLS and MLW.

A possible way to take into account the errors in the atmospheric profiles might consist in perturbing each atmospheric profile level with values randomly taken from a

normal distribution of zero mean and a standard deviation characteristic of the uncertainty. In this case, perturbations on temperature and water vapor are assumed to be independent from each other and values of both quantities at a given level are also taken as independent from those at the other levels. An extreme opposite procedure would be considering the perturbations to be perfectly correlated, e.g., by using perturbed profiles that are offset by given amounts (Tjemkes and Schmetz, 1998). Since in our case, we intend to perform a sensitivity study reflecting more realistic situations we have followed Peres and DaCamara (2004) and have adopted the procedure described in Section 3.3. Figure 5.3 allows making a visual comparison between the perturbed profiles and the respective reference profile of water vapor mass mixing ratio and of temperature.

The imposed perturbations on the atmospheric profiles translate into uncertainties on the atmospheric parameters in Eq. (4.2), namely, τ_{MIR} (one-way total atmospheric transmittance), t_{MIR} (two-way total atmospheric transmittance), $L_{\text{atm,MIR}} \uparrow$ (upward atmospheric radiance) and $L_{\text{atm,MIR}} \downarrow$ (downward atmospheric radiance). Statistical distributions of the uncertainties are shown respectively in Figures 5.4, 5.5 and 5.6.

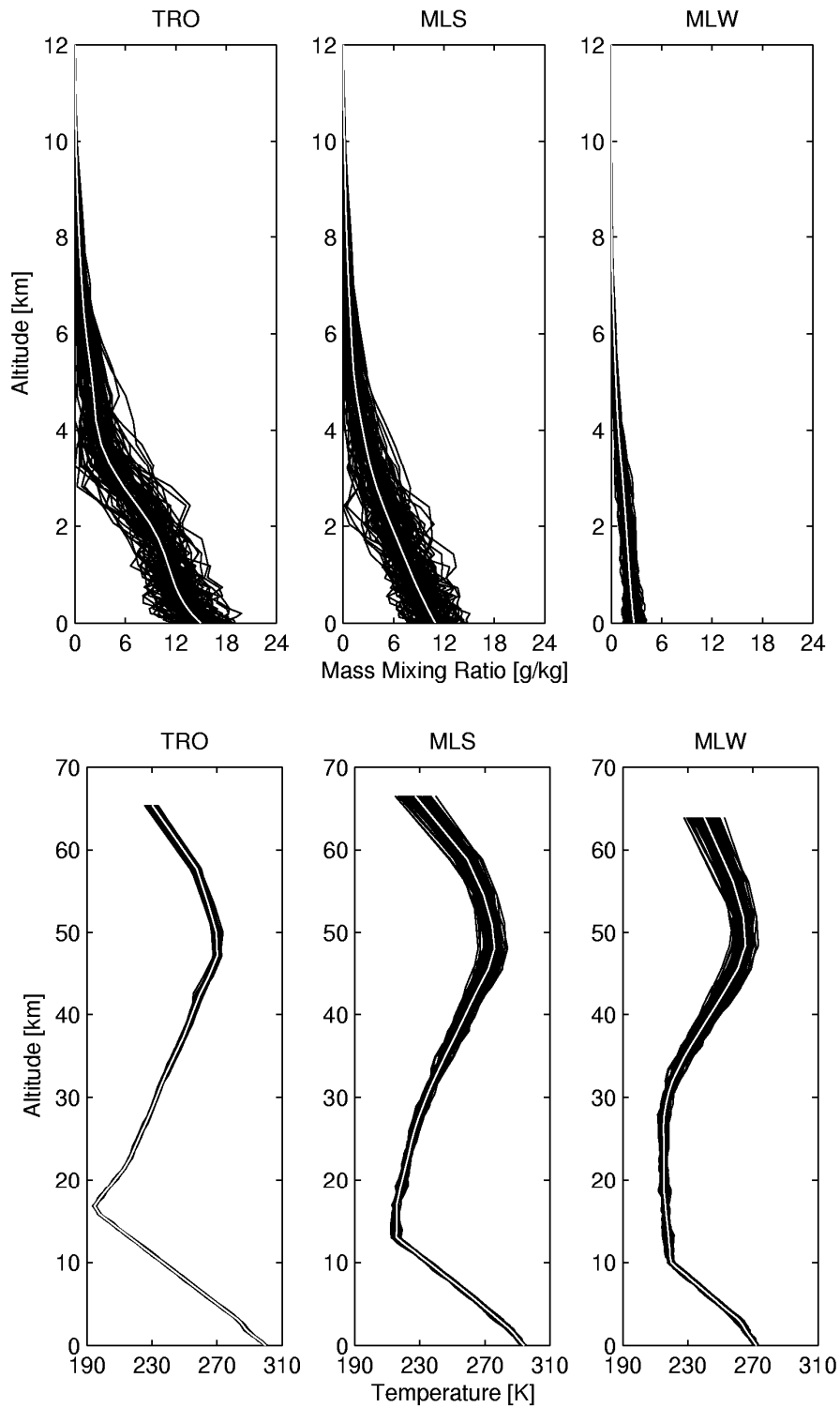


Figure 5.3. Comparison between the perturbed profiles (black curves) and respective reference profile (white curve) of water vapor mass mixing ratio (upper panel) and temperature (lower panel). Adapted from Peres and DaCamara (2004).

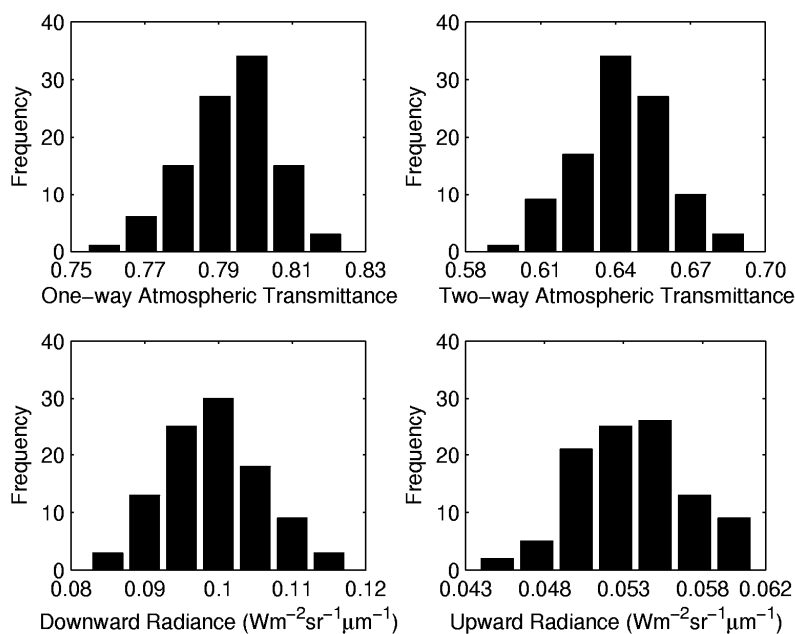


Figure 5.4. Distributions of the perturbed atmospheric parameters, namely one-way total atmospheric transmittance, two-way total atmospheric transmittance, atmospheric upward radiance and atmospheric downward radiance, respecting to MODIS channel 20 for TRO standard atmosphere.

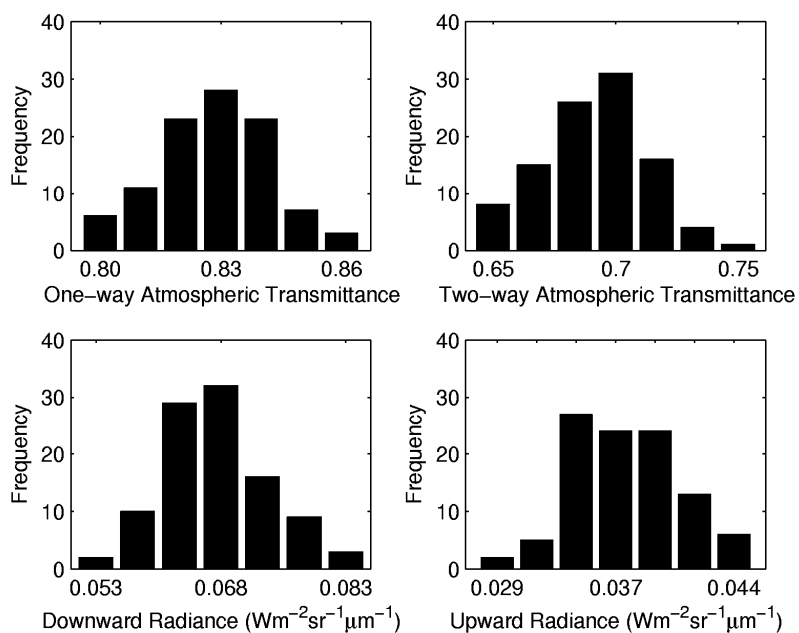


Figure 5.5. As in Figure 5.4 but for MLS standard atmosphere.

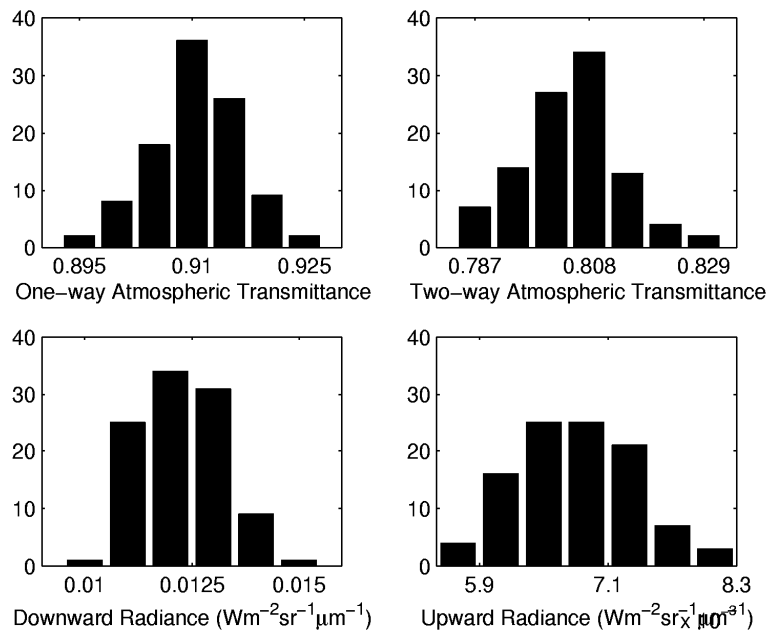


Figure 5.6. As in Figure 5.4 but for MLW standard atmosphere.

5.2.2.3. Uncertainty in Surface Temperature

In order to take into account the sensitivity of the MIR reflectance retrieval due to the land surface temperature, radiative transfer calculations are performed for the standard profiles, and then errors associated to the inaccuracies in LST are introduced into Eq. (4.2). The errors are generated based on the accuracy specification for MODIS LST (1 K) at 1 km resolution under clear-sky conditions (Wan, 1999). The generated errors are normally distributed around zero mean and with standard deviations equal to the respective accuracy specification for MODIS LST (Figure 5.7). A set of 1,000 random perturbations was again generated in order to guarantee a statistically significant result.

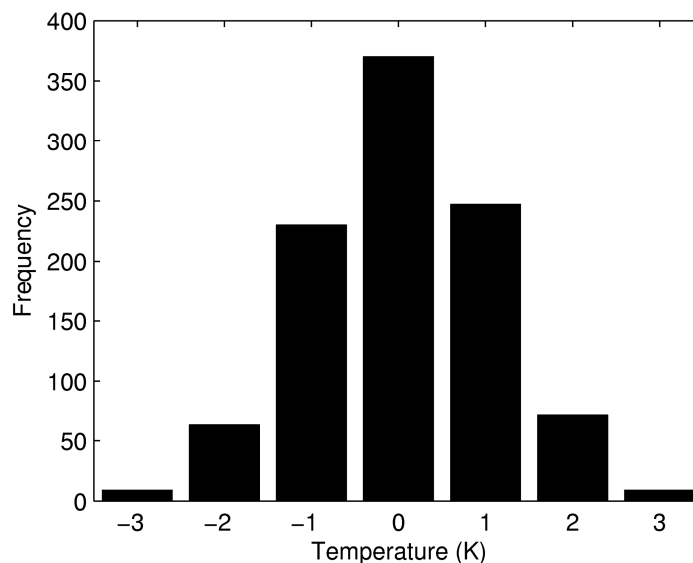


Figure 5.7. Frequency histogram of the errors in LST.

5.3. Analysis and Results

5.3.1. Error-free case

The accuracy of the solutions to the inverse problem was assessed by evaluating the retrieval errors, defined as the absolute differences between retrieved values of MIR reflectance by means of Eq. (4.2) and the corresponding values prescribed as input to MODTRAN-4. Although actual retrieved values of MIR reflectance are affected by measurement uncertainties, the assessment was initially carried out assuming error-free input data, implying that the errors in the MIR reflectance are entirely due to the model uncertainty. The reason for first choosing this assumption is because it allows identifying the problems that are exclusively due to the inversion procedure under conditions typical of tropical environments. Moreover, such approach, usually referred to in the literature as inverse method parameter sensitivity (Rodgers, 2000), is particularly adequate in our study, not only because it allows evaluating the contribution to the retrieval error due to the inverse

method, but especially because it helps establishing a baseline that reveals pitfalls likely to occur when retrieving MIR reflectance from real data.

Figure 5.8 exhibits the accuracy in the retrieval of MIR reflectance using Eq. (4.2), for TRO, MLS and MLW, three view angles, three solar zenith angles and for charcoal (full lines) and pine tree (dashed lines). The VZA and SZA dependence may be analyzed in Figure 5.8. As expected, the VZA dependence reveals a slight degradation in the MIR reflectance retrieval with increasing viewing angle, indicating a weak dependence of MIR region on view angle variations, both for bright and dark surfaces. These results are in agreement with the studies of França and Setzer (1998) and Jiang et al. (2006). The deviation in MIR reflectance with solar zenith angle (from 0° to 45°) is weak for low values of LST, and, as the LST increases the angular deviations with SZA become more prominent. Figure 5.9, which shows the obtained MIR reflectance retrieval errors as a function of LST and SZA, allows performing a visual analysis of the dependency of the errors on both LST and SZA. It may be noted that in order to enhance the error variation, the retrieval errors are represented in a logarithmic scale.

Large and abrupt fluctuations in the retrieval error may be observed for different combinations of SZA and LST along a curved stripe at the upper right corner of Figure 5.9. For instance, the logarithm of the retrieval error reaches the value of -0.74, which corresponds to the pair SZA= 46° and LST=337 K. This value of retrieval error is equivalent to a relative error around 25% and it may be observed that, for the same value of LST but with SZA= 24° , the relative error is as low as 0.38%. The obtained pattern along the curved stripe strongly suggests that the solution does not depend continuously on the data and is typical of ill-conditioning (Peres and DaCamara, 2006).

In order to put into evidence the ill-conditioning behavior, Figure 5.10 illustrates the dependency on surface temperature of errors in the retrieval of MIR reflectance from charcoal for TRO (left panel), MLS (middle panel) and MLW (right panel) for nadir, but for four solar zenith angles, including SZA equal to 60° . It may be noted that critical regions

where the problem is ill-posed also occur for other types of atmosphere in case of sufficiently high values of LST. Nevertheless, for mid-latitude winter atmospheres, it may be found that the critical region is located well beyond the range of observed/physical LST values in temperate regions. In the case of mid-latitudes, and excepting the case of very low sun elevations, large retrieval errors of reflectance are also not to be expected.

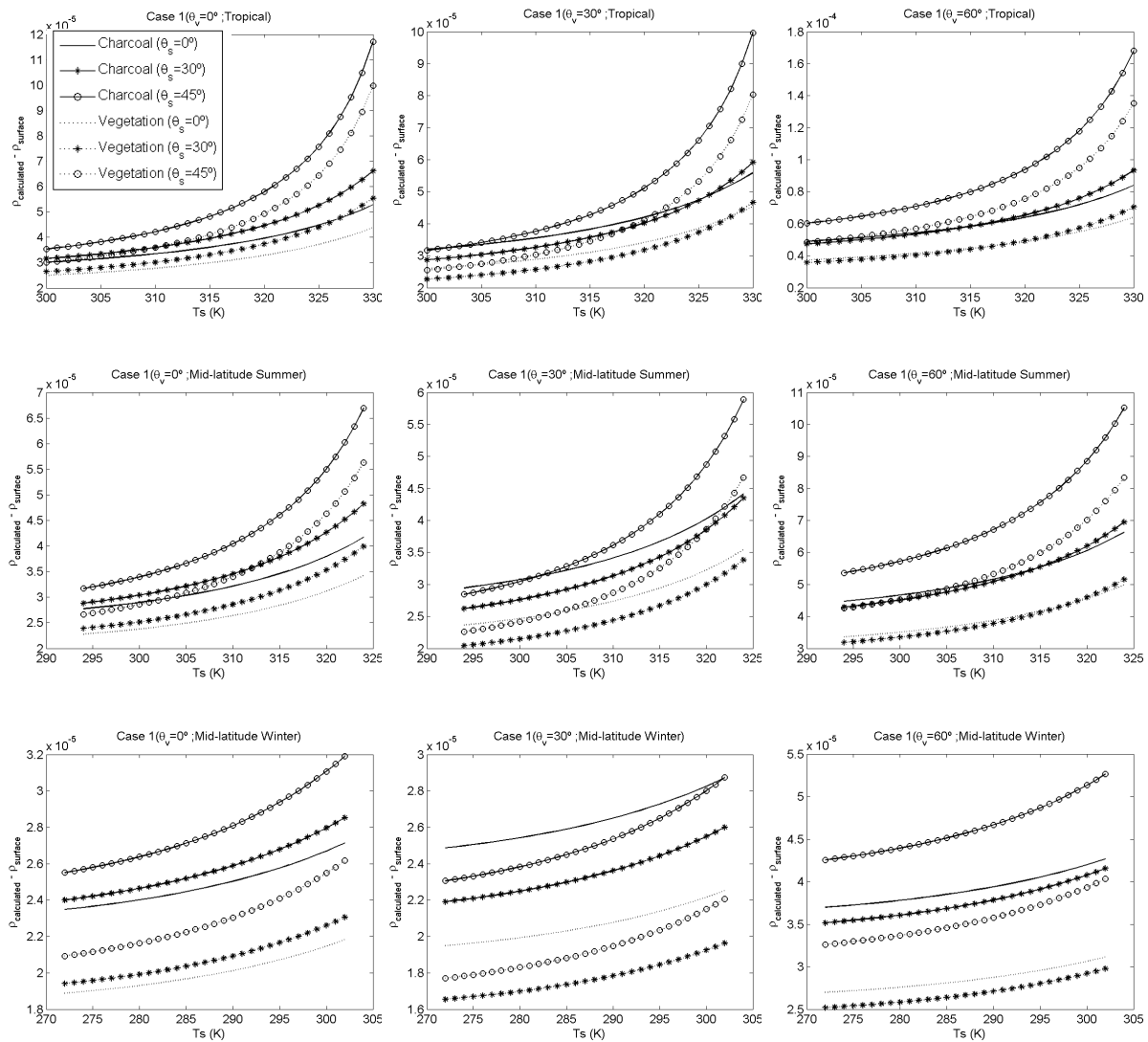


Figure 5.8. Accuracy in the retrieval of MIR reflectance using Eq. (4.2), for TRO, MLS and MLW, three view angles, three solar zenith angles and for charcoal (full lines) and pine tree (dashed lines).

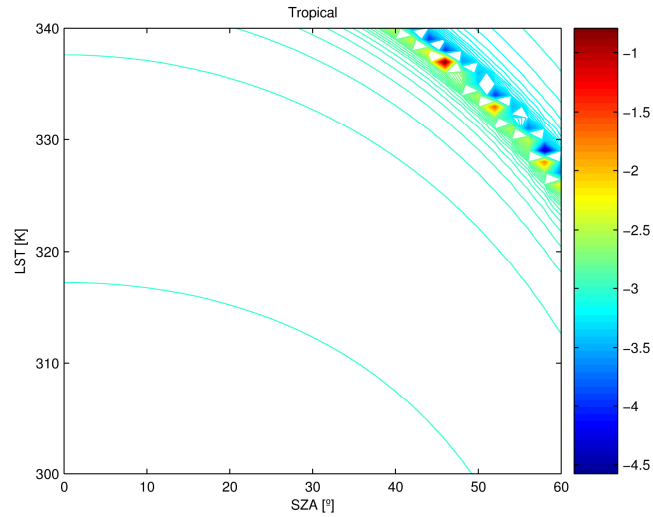


Figure 5.9. Dependence of the logarithm of retrieval error on LST and SZA for TRO profile.

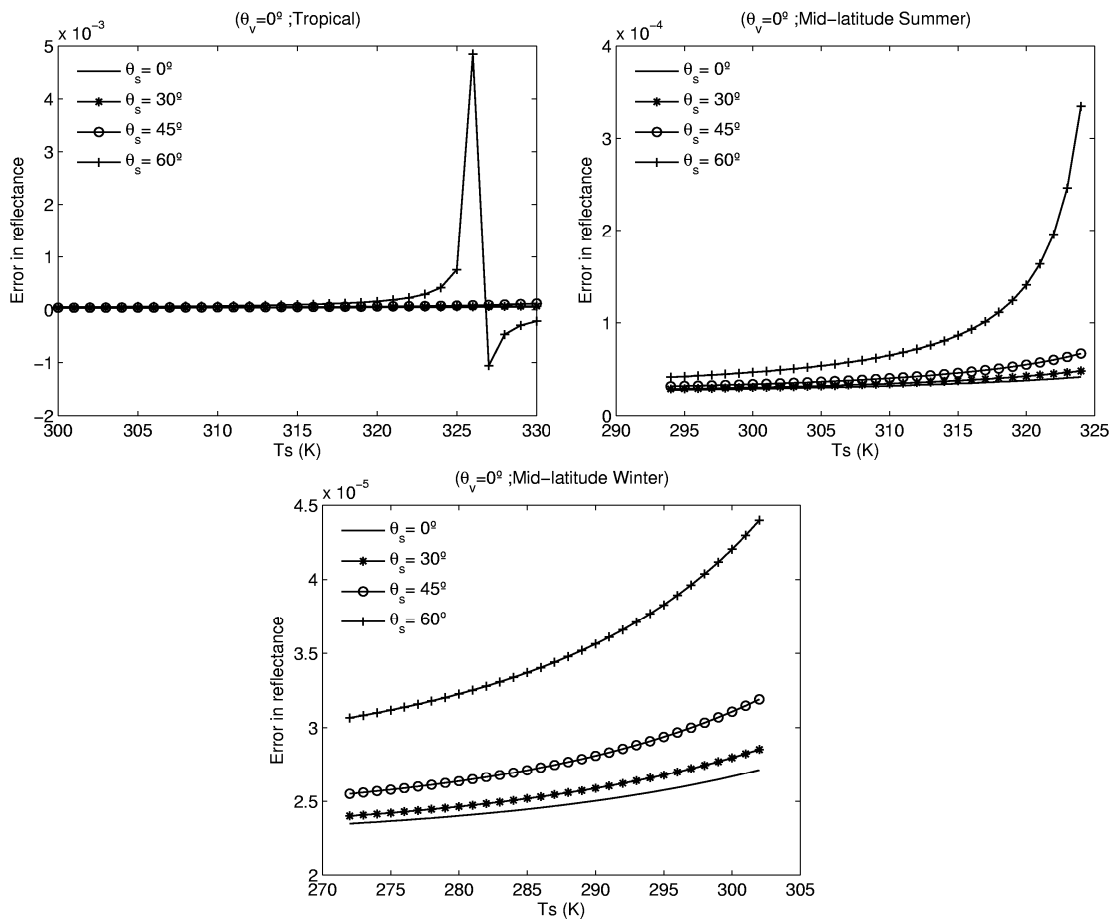


Figure 5.10. Dependence of land surface temperature of errors in the retrieval of MIR reflectance of charcoal for TRO, MLS and MLW for nadir view and four solar zenith angles.

It may therefore be concluded that the problem of MIR reflectance retrieval is ill-conditioned for ranges of LST and SZA that may be observed over tropical regions. Figure 5.11 depicts the behavior of each term of Eq. (4.2), with the exception of the one concerning the total radiance, L_{MIR} for four values of SZA, namely 0, 20, 40 and 60°. For instance, considering SZA between 40° and 60°, the curve corresponding to the term $\tau_{\text{MIR}} B(\lambda_{\text{MIR}}, T_s)$ crosses that corresponding to the term $t_{\text{MIR}} \frac{E_{\text{OMIR}}}{\pi} \mu_0$ around 325 K. As temperature rises, the former term increases up to the magnitude of the latter term (which decreases with the increase of SZA) and the denominator of Eq. (4.2) tends to zero, inducing large variations in the solution. However it is worth stressing that the problem will not restrict to the single point where the curves cross each other and will still be ill-conditioned for all regions where the curves are close enough. In addition (and as shown in Figure 5.11 for SZA = 0, 20, 40, 60°), the curve representing the term $\tau_{\text{MIR}} B(\lambda_{\text{MIR}}, T_s)$ will cross an infinite number of curves $t_{\text{MIR}} \frac{E_{\text{OMIR}}}{\pi} \mu_0$ resulting in peaks of error (positive and negative), as those presented in Figures 5.9 and 5.10.

At first sight, it may be argued that the obtained magnitude of retrieval errors is not large enough to prevent discriminating between charcoal and vegetation (see Figure 2.2). However performed analysis refers to the error-free input data case and therefore the other sources of error were not taken into account. In fact, when using real data, the inversion problem will certainly become more difficult to solve because the errors related to both sensor performance and the meteorological parameters are usually much larger than the error due to model uncertainties.

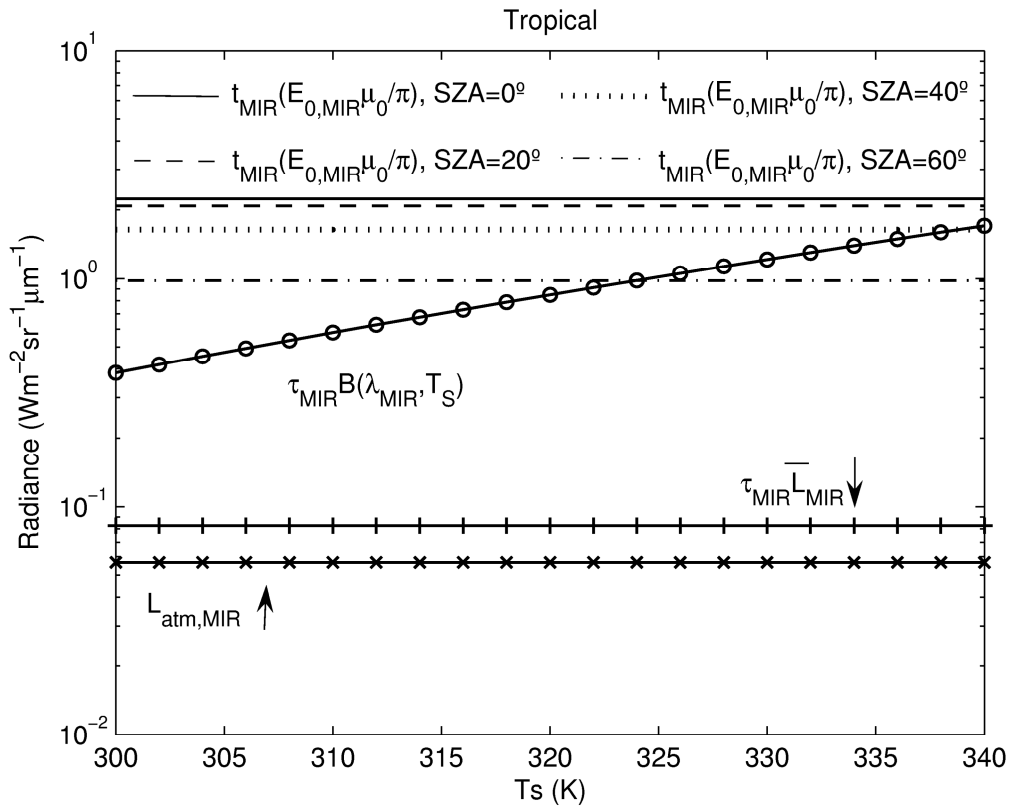


Figure 5.11. Dependence on LST of the different terms of Eq. (4.2).

5.3.2. Error case

In this section the performance of the radiative transfer equation is evaluated based on the solution to the inversion problem (Rodgers, 2000), which is given by Eq. (4.2). Simulations of TOA radiance at MODIS channel 20, as well as the imposed perturbations (i.e. noise in the satellite radiances and measurement errors in the atmospheric profiles as well as in LST) were generated as described in the previous section.

Figures 5.12 to 5.17 depict the error in MIR reflectance using Eq. (4.2) as obtained from each set of imposed perturbations on TRO, MLS and MLW profiles as a function of four solar zenith angles (0°, 30°, 45° and 60°) and three view zenith angles (0°, 30° and 60°), and for a charcoal surface (Figures 5.12, 5.14 and 5.16) and for a vegetated surface (Figures 5.13, 5.15 and 5.17). It may be noted that, for all atmospheres, the instrumental error is weak

compared to the others sources of error and may be neglected. The KR94 algorithm was also analyzed in terms of the instrumental noise and, although not shown, the results are analogous to those obtained with the RTE. The negligible impact of instrumental noise is justified (Figure 5.1) by the low sensitivity of MODIS channel 20 radiance to changes in temperature.

It may be observed that, in general, for charcoal surfaces, the measurement errors in LST and the inaccuracies in atmospheric profiles have comparable magnitude. In the case of vegetation, the measurement errors in LST are the most important source of errors. The errors are more pronounced in TRO profile. For instance, in the case of TRO and charcoal, for SZA between 0° and 45° the maximum error due to measurement errors in the atmospheric profiles is around 0.04, whereas the maximum error due to measurement errors in LST s is around 0.035, with mean values around 0.02. In this case of TRO and vegetation, the maximum error due to measurement errors in the atmospheric profiles is around 0.035, while the maximum error due to measurement errors in LST s is around 0.05.

In the case of low sun elevations (SZA equal to 60°) the ill-conditioned behavior may be observed again such as obtained in the previous chapter for KR94 and it may be noted that the measurement errors in LST become the most important source of error.

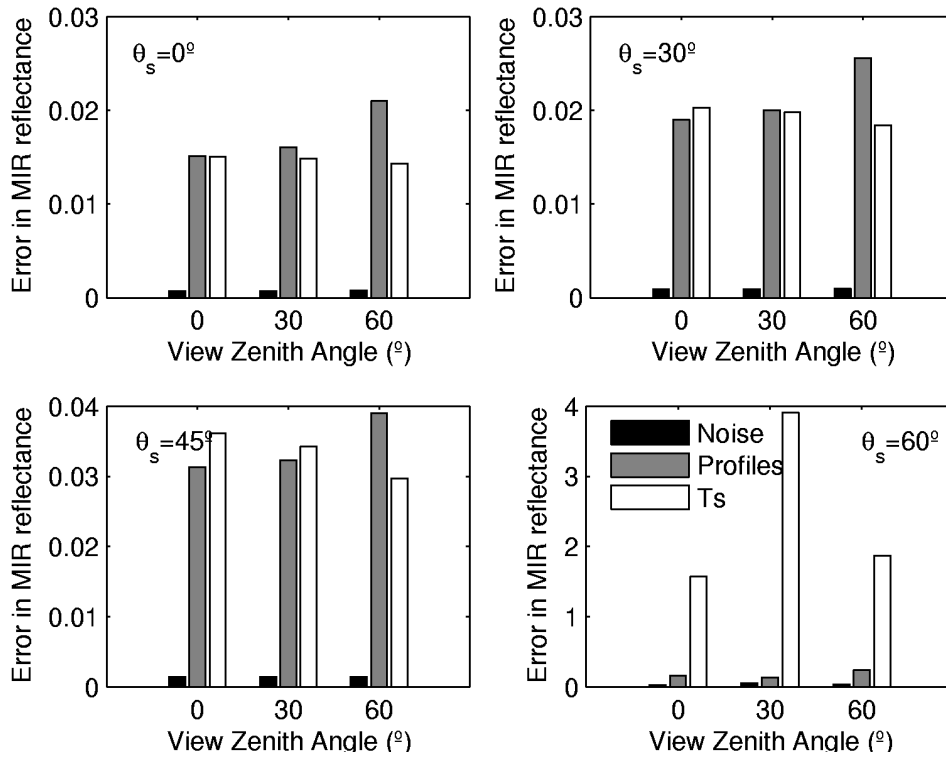


Figure 5.12. Error in MIR reflectance using Eq. (4.2) as obtained from each set of imposed perturbations on TRO profile as a function of four solar zenith angles (0° , 30° , 45° and 60°) and three view zenith angles (0° , 30° and 60°) in the case of a charcoal surface.

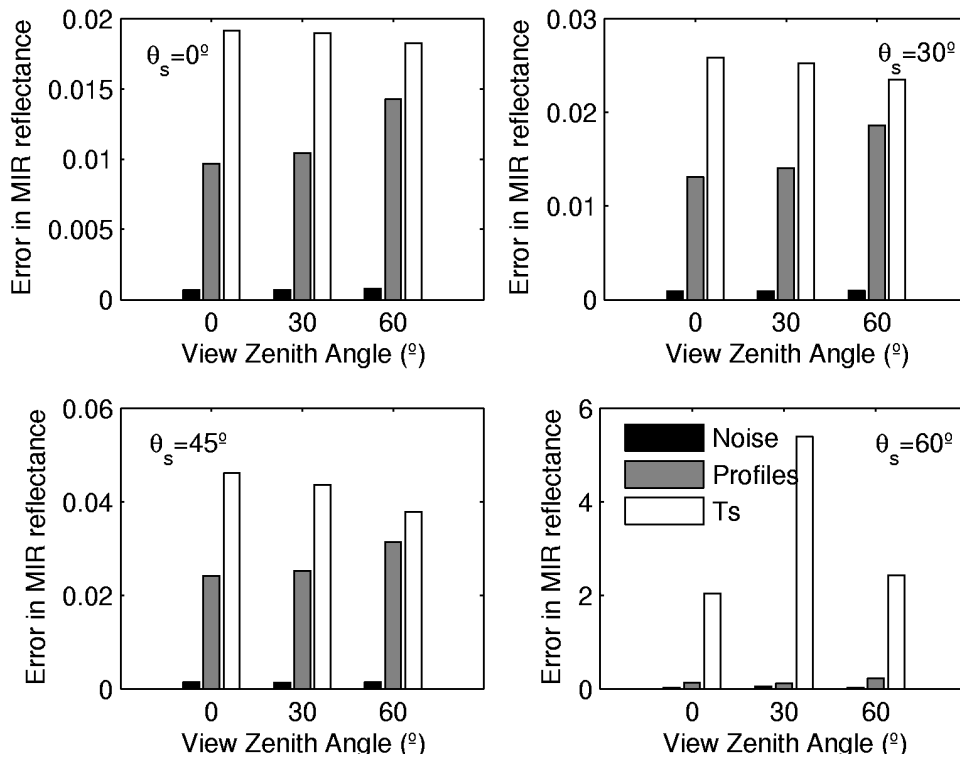


Figure 5.13. As in Figure 5.12 but for a vegetated surface.

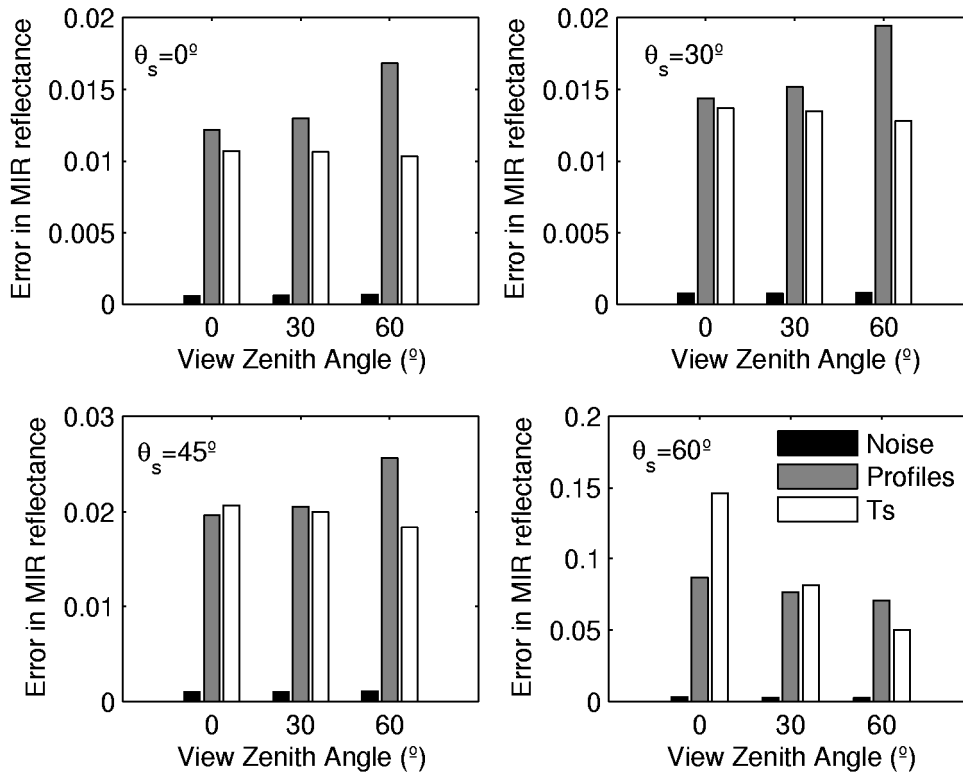


Figure 5.14. As in Figure 5.12 but for the MLS profile.

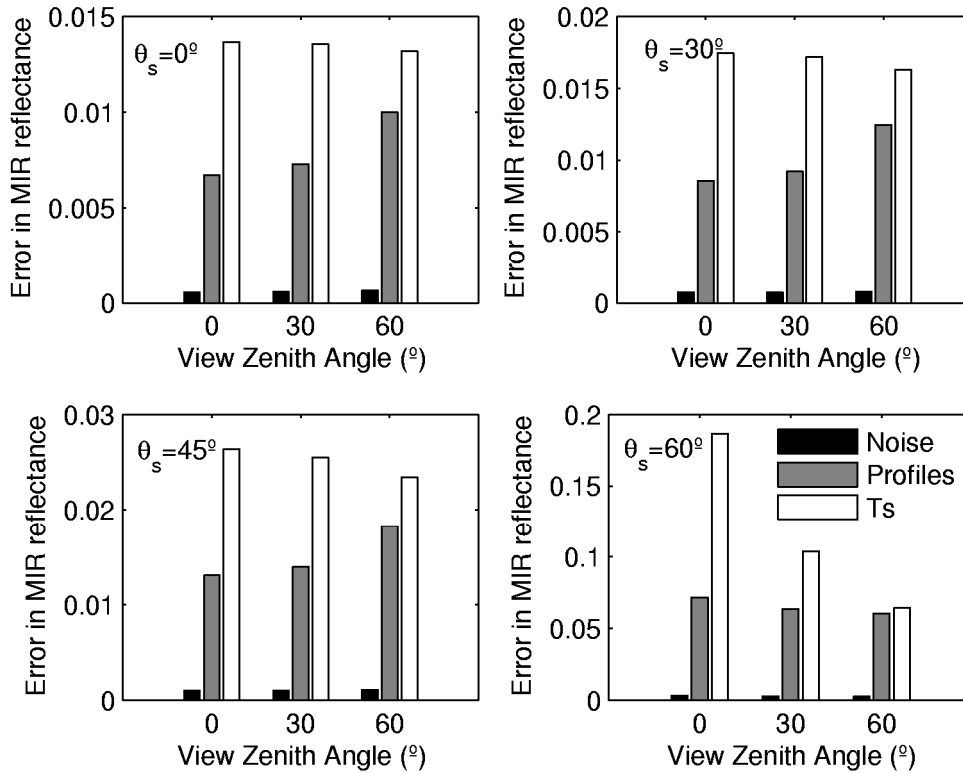


Figure 5.15. As in Figure 5.13 but for the MLS profile.

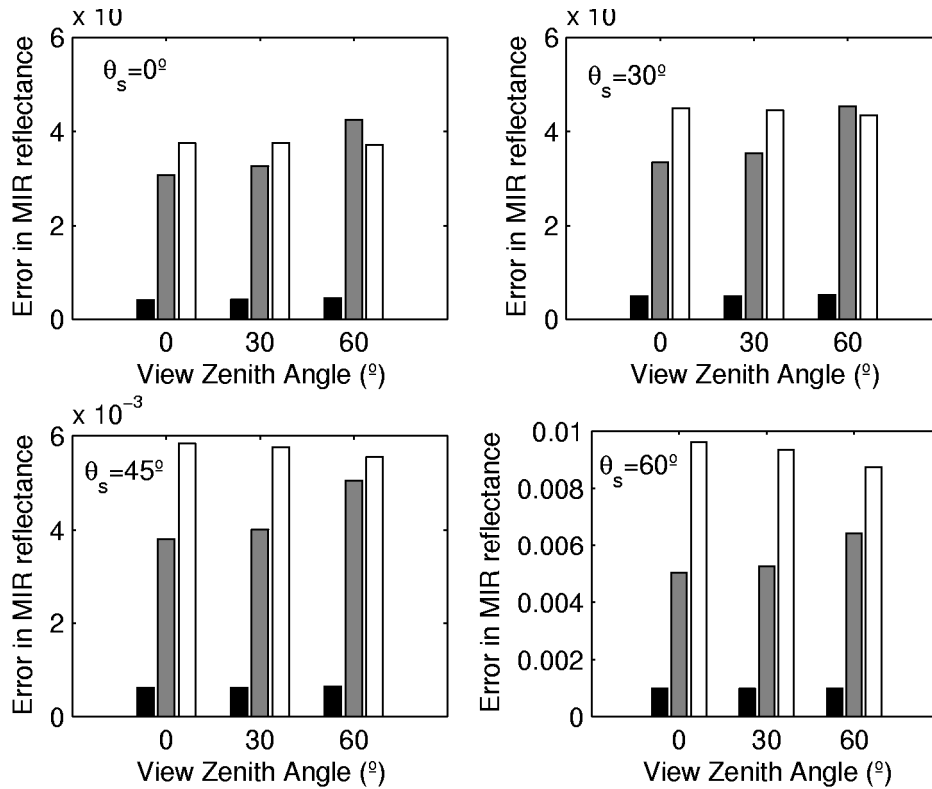


Figure 5.16. As in Figure 5.12 but for the MLW profile.

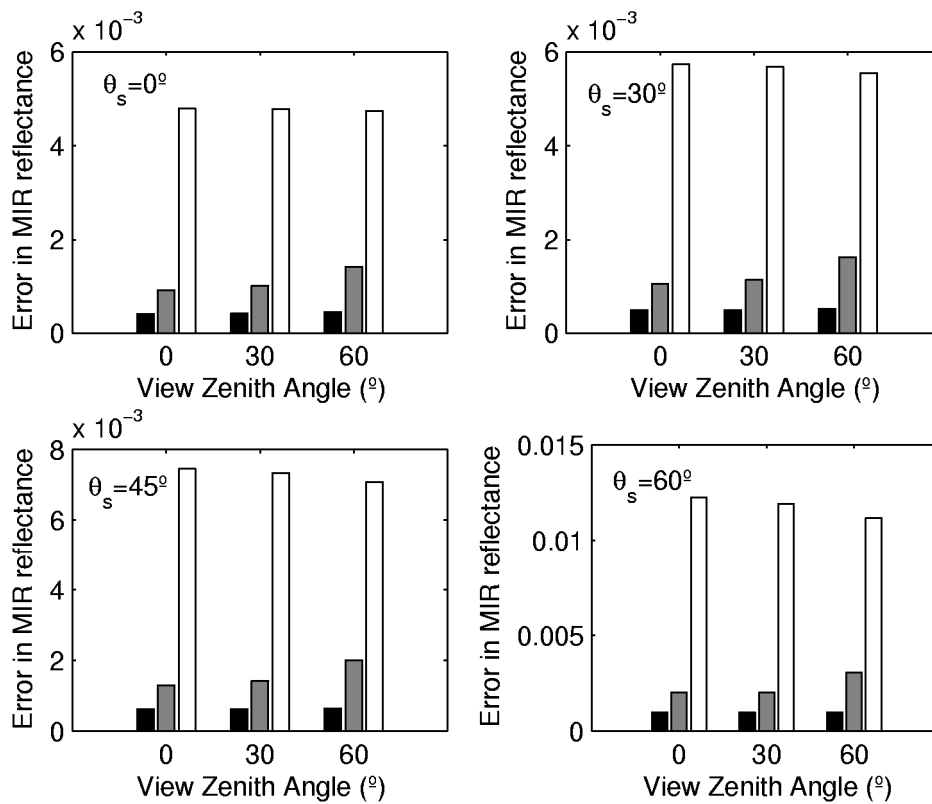


Figure 5.17. As in Figure 5.13 but for the MLW profile.

Figure 5.18 presents the obtained dependency of retrieval errors on LST and SZA for an offset of +1 K in LST. This value of the offset was chosen based on the goal that was set for the accuracy of the MODIS LST algorithm (Wan, 1999). The ill-conditioning behavior that is present in Figures 5.13 to 5.17 for SZA equal to 60° may now be observed in a continuous way. As expected, retrieval errors present similar fluctuations to those previously obtained with the sensitivity experiment respecting to the error-free input data case (Figure 5.9). When compared to Figure 5.9, the offset of +1 K in LST greatly amplifies the retrieval errors (as indicated by the statistics derived from Figures 5.13 to 5.17), leading to unrealistic physical solutions in some of the simulations. For instance, relative errors may reach $7.0 \times 10^4 \%$ for SZA= 46° and LST=336 K. It is worth stressing that Figure 5.18 may be useful to defining a critical region in the space SZA vs. LST where the solution does not depend continuously on the data and therefore where the retrieval of MIR reflectance is severely impaired.

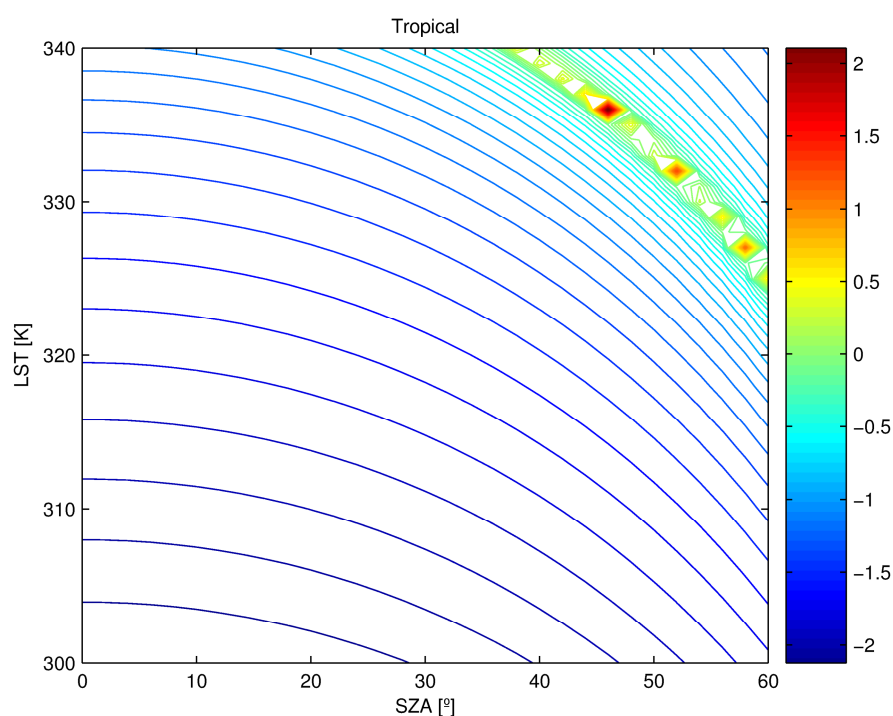


Figure 5.18. As in Figure 5.9, but for an offset of +1 K in LST.

It may be finally noted that critical regions where the problem is ill-posed also occur

for other types of atmosphere in case of sufficiently high values of LST. Nevertheless, and as already found in the free error case, for mid-latitude winter atmospheres (Figure 5.14) the critical region is located well beyond the range of observed/physical LST values in temperate regions and, excepting for very low sun elevations, large retrieval errors of reflectance are not to be expected.

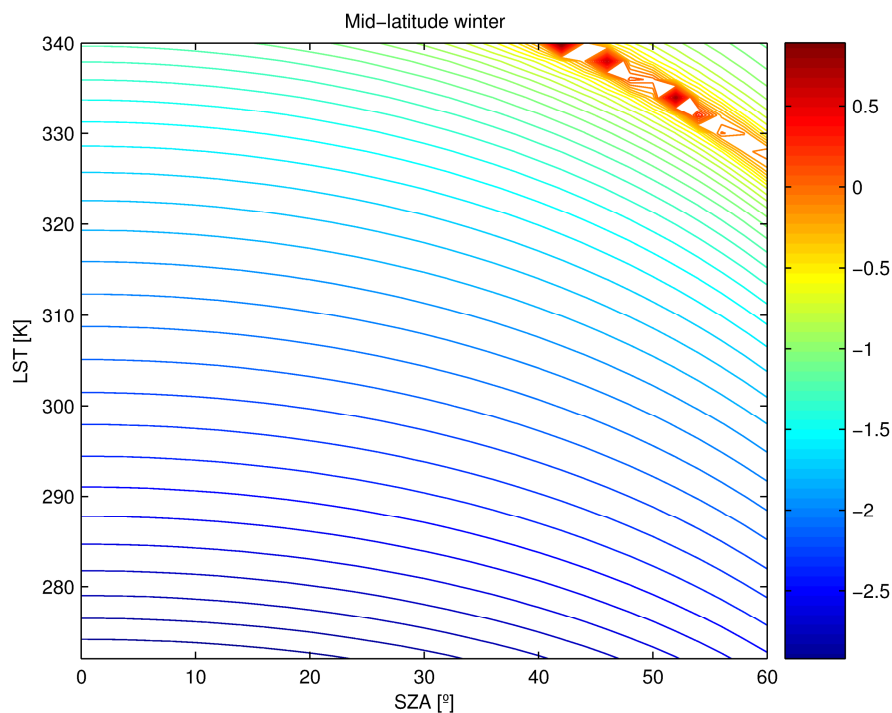


Figure 5.19. As in Figure 5.18, but for the MLW atmosphere.

5.3.3. Total MIR Reflectance Error

Assuming the three sources of errors as independent, the total error in MIR reflectance using the RTE (Eq. 4.2) is given by:

$$\delta\rho = \left[(\delta\rho_a)^2 + (\delta\rho_T)^2 + (\delta\rho_n)^2 \right]^{1/2} \quad (5.1)$$

where $\delta\rho_a$, $\delta\rho_T$ and $\delta\rho_n$ are the errors due to the atmospheric correction, the LST uncertainty and the radiometric noise, respectively as obtained in the previous section. Figures 5.20-5.22 show the total error in MIR reflectance obtained throughout RTE and the respective total error when using KR94 (labeled in the Figures as KFE) for each angle considered in this study, in the case of TRO, MLS and MLW profiles and for vegetation (MIR reflectance around 0.03) and charcoal (MIR reflectance around 0.24).

As found in Chapter 4, MIR reflectance errors for charcoal are generally lower than reflectance errors for vegetation and the same kind of qualitative remark remains for dry and moist atmospheres. Since the MLW profile presents much lower values of moisture together with colder temperatures compared to those from TRO profile, in the case of MLW the atmosphere will not perturb enough the retrieval of MIR reflectance, when using either KR94 or RTE, namely when comparing against the case of the tropical atmosphere (TRO). Restricting to results when the solar zenith angle lies between 0° and 45° , the maximum values of the relative errors varies from 750% (KF94 - vegetation) to 30% (KF94 - charcoal) and from 250% (RTE - vegetation) to 18% (RTE- charcoal) in the case of TRO atmosphere and from 38% (KF94 - vegetation) to 16% (KF94 - charcoal) and from 38% (RTE - vegetation) to 5% (RTE- charcoal) in the case of MLW atmosphere. Results obtained are a clear indication that, besides the important role played by moisture (MLW versus TRO), RTE works better than KF94 for virtually all atmospheric conditions and geometries. Nevertheless an accurate characterization of atmospheric conditions is crucial to ensure appropriate estimates of MIR reflectance.

The retrieval of MIR reflectance is severely contaminated by errors in the case of low sun elevations (SZA around 60°), especially for TRO and MLS atmospheres and it may be noted that the impact of ill-conditioning is more severe in the case of RTE than when KR94 is used. In fact, even if the retrieved values using KR94 are still unusable for high values of SZA, it is worth stressing that the errors in MIR reflectance are smaller than the corresponding errors when using RTE meaning that the approximations made in the

simplified algorithm (i.e. in KR94) tend to smooth the effects of ill-conditioning. This feature may reveal to be useful when attempting to develop an algorithm able to produce usable estimates of MIR reflectance for high values of SZA.

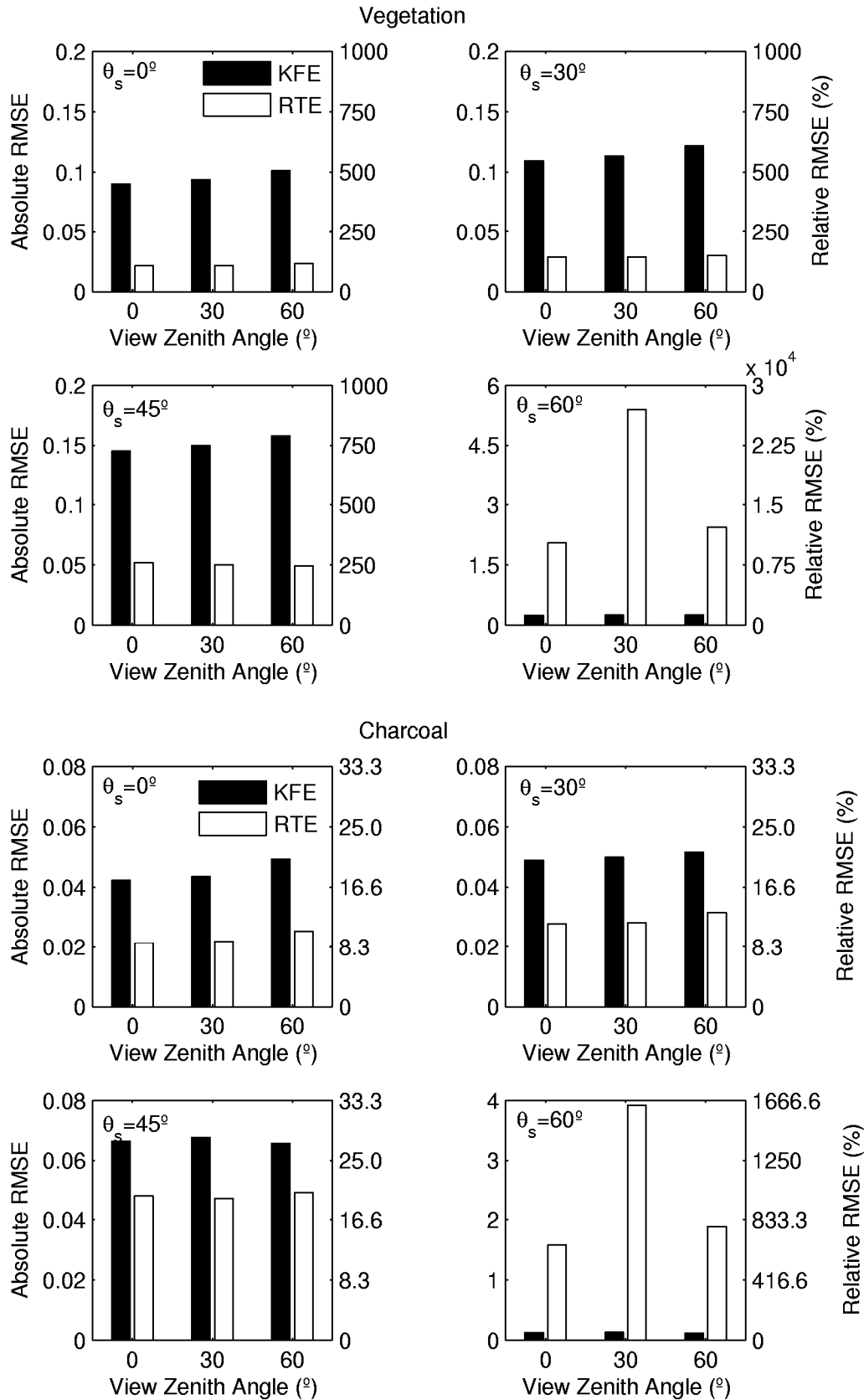


Figure 5.20. Comparison between the total errors when using KR94 (labeled as KFE) and RTE in the case of TRO.

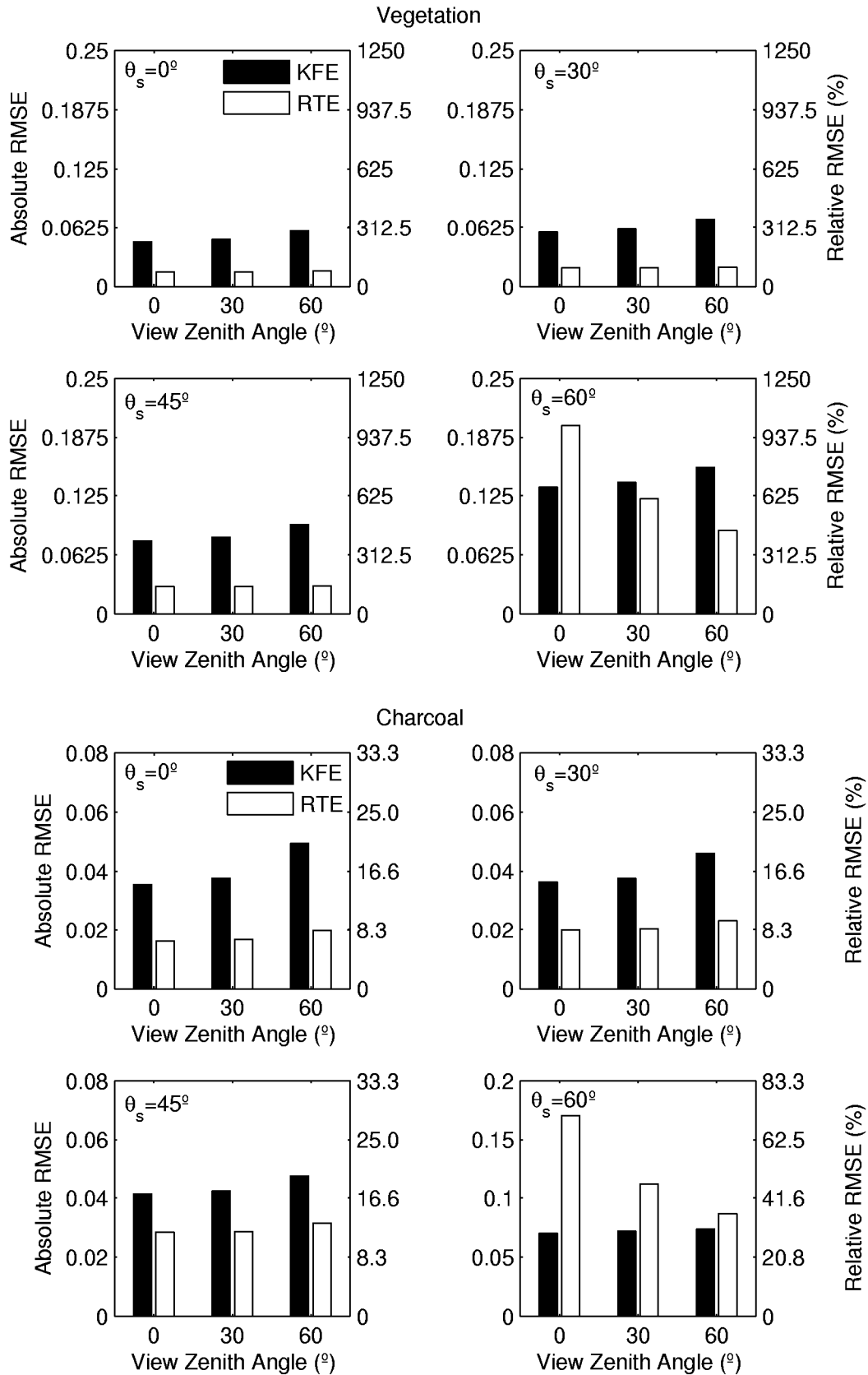


Figure 5.21. As in Figure 5.20 but in the case of MLS.

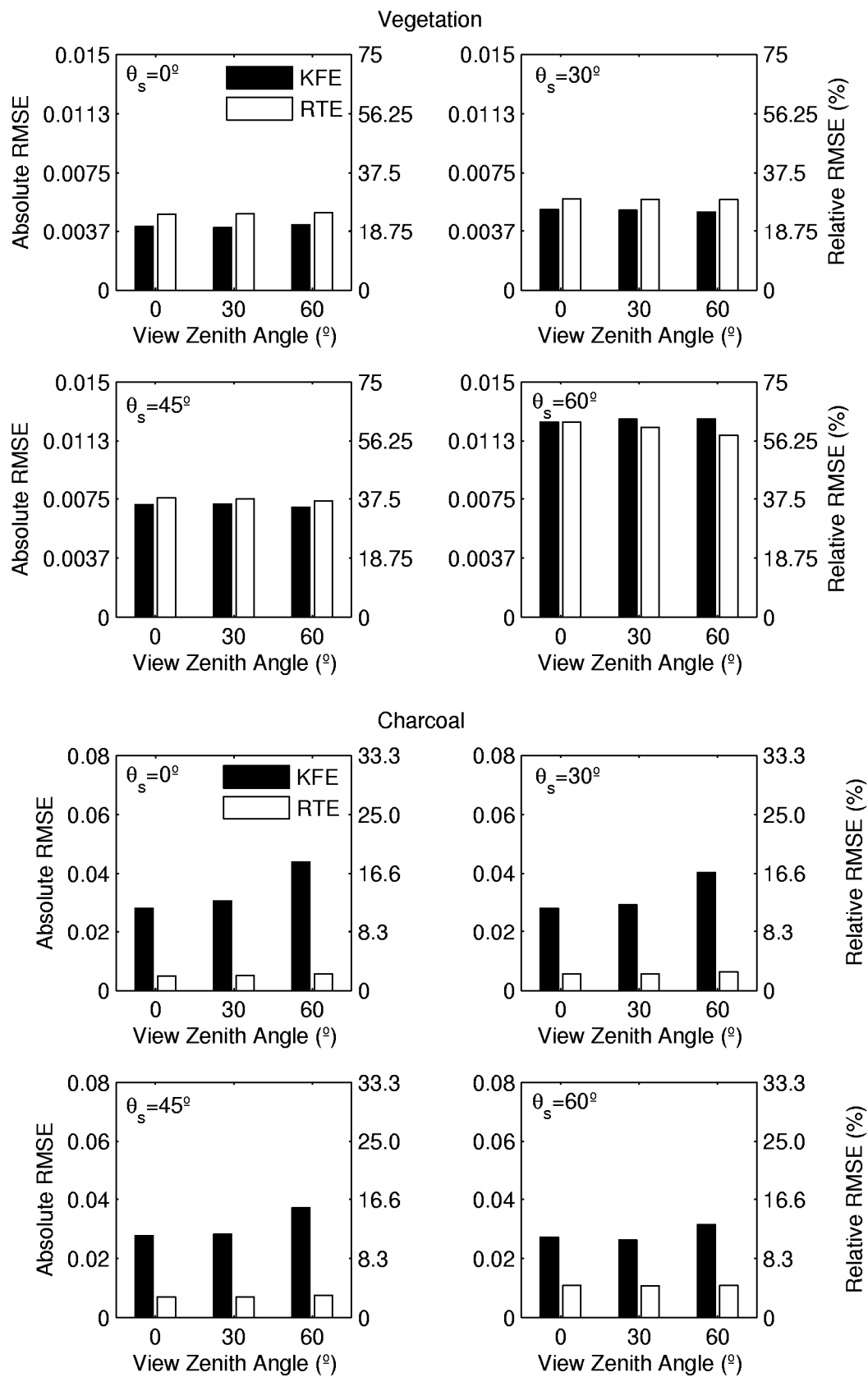


Figure 5.22. As in Figure 5.20 but in the case of MLW.

5.4. Concluding remarks

The purpose of this Chapter was to investigate the problem of retrieving MIR reflectance in MODIS channel 20, namely when obtained using the full radiative transfer equation (given by Eq. (4.2)) or the algorithm proposed by Kaufman and Remer (1994).

For this purpose the measurement errors that may affect the accuracy of the estimated MIR reflectance were characterized, namely those associated to the noise in MODIS channels, the errors in the atmospheric profile and the uncertainties in LST. A sensitivity study was then performed imposing conditions as close as possible to an operational environment. Imposed errors on atmospheric profiles and LST were accordingly generated with the aim of reflecting realistic situations. The effect of the atmospheric profile source of error was evaluated by perturbing the profiles with values based on the current ECWMF background error covariance matrix, whereas errors associated to LST were based on the errors from the MODIS LST product (MOD11_L2).

We have then verified that, for certain atmospheric and geometric conditions, the retrieval of MIR reflectance from radiance measurements based on RTE is an ill-posed problem because the solution does not depend continuously on the data, i.e. small perturbations in measurements (due to e.g. sensor noise, uncertainties in atmospheric profiles and in LST) may induce large errors in the solution. We have also verified that this occurs for the same combinations of pairs of LST and SZA where KF94 does not lead to a proper retrieval of MIR reflectance (as described in the previous Chapter).

Although in the case of dry and cold atmospheres (e.g. MLW), the increase in performance when using the RTE instead of KR94 is not significant, deviations are more pronounced for moist and hot atmospheres, like TRO. However, the estimated values of the total error when using RTE, point out the need of having accurate atmospheric and LST data, the total error being almost completely driven by the uncertainty on these two parameters.

Results from this Chapter, together with those from Chapter 4, clearly suggest that there are no advantages in using RTE as a surrogate for KR94 when geometric and atmospheric conditions turn the inversion into an ill-posed problem. However, the RTE approach leads to better estimates than KR94 in virtually all cases, the exception consisting of low sun elevations and high LST, where results from KR94 are also not usable.

Despite the better performance of RTE when compared to KR94, the atmospheric correction and the LST estimation are time consuming and there is the additional problem of atmospheric and LST data which are not always operationally available and/or accurate. Using the method developed by Kaufman and Remer (1994) presents the advantage of not requiring any auxiliary datasets (e.g. atmospheric profiles) and major computational means (e.g. radiative transfer computations). Besides, as shown in Chapter 4, the errors obtained using KR94 are acceptable when the aim is the discrimination of burned and unburned areas. In this case, even considering the errors of KR94 (with the exception of low sun elevations and high LST values), the discrimination between both surfaces may be achieved on reasonably good grounds. There are some cases however (e.g. in the case of LST and surface emissivity retrieval), where a precise quantitative value of MIR reflectance is required, and in such cases the more accurate estimates provided by RTE should be used instead.

It may be finally noted that the use of the RTE equation in order to retrieve MIR reflectance aiming at burned area discrimination is further impaired by a drawback found in the MODIS LST product, in particular in the MODIS/Aqua LST/E 5-Minute L2 Swath 1 km data set (MYD11_L2). As already mentioned, LST is a required parameter in order to solve RTE and retrieve MIR reflectances. We have found, however, that burned areas are flagged as "Not a Number" (NaN) in the MODIS LST product, and the lack of LST data over such areas naturally prevents using the RTE for burned area discrimination.

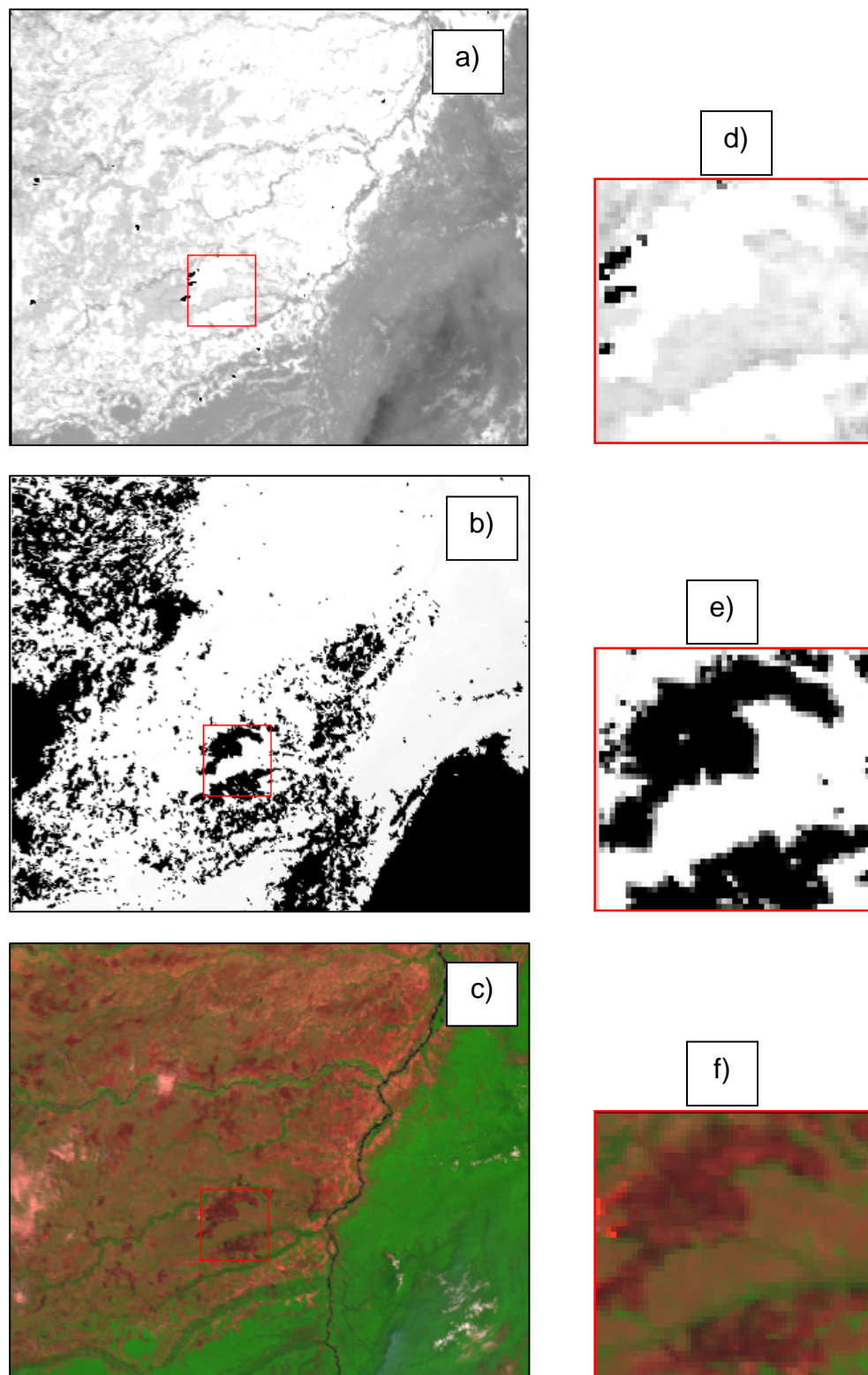


Figure 5.23. MODIS images (02/28/2001) over Los llanos, Venezuela/Colombia, South America: a) MODIS channel 20 radiance; b) MODIS LST product cloud mask; c) RGB from MODIS channels 7, 2 and 1; d), e) and f) zooms of a burned scar (red square) of a), b) and c), respectively. Black pixels denote NaN.

An example of the drawback, which seems to be related to the cloud mask algorithm used in MODIS LST product, is given in Figure 5.23 that shows MODIS images from the region of Los llanos, Venezuela/Colombia in 02/28/2001. It may be observed that, although there are no clouds around the burned scar, the MODIS LST product masks the scar as NaN. The same problem may be identified over other burned scars present in the scene.

We have therefore decided to use the KR94 algorithm (instead of RTE) when retrieving MIR reflectance from MODIS in order to validate with real imagery the indices that will be derived in Chapter 6.

Chapter 6

On a new coordinate system for optimal discrimination of vegetation and burned areas using MIR/NIR information

6.1. Introduction

As mentioned in the previous Chapters, several studies have demonstrated the effectiveness of the reflectance of MIR for discriminating among different types of vegetation (Holben and Shimabukuro, 1993; Shimabukuro et al., 1994; Kaufman and Remer, 1994; Goita et al., 1997); estimating total and leaf biomass of several forest ecosystems (Boyd et

al., 1999; 2000); and monitoring intra- and inter-annual climate-induced changes in vegetation (Boyd and Duane, 2001; Boyd et al., 2002). MIR reflectance has also proven to be useful when applied to burned area discrimination (e.g. Roy et al., 1999; Barbosa et al., 1999; Pereira, 1999). It may be nevertheless noted that, when used to identify vegetation and detect its changes, the MIR band is commonly used together with the NIR, given the strong contrast between the two bands, green vegetation displaying high reflectance in the latter and low reflectance in the former (Pereira et al., 1997). In fact, vegetation reflectance in the NIR, around 0.8 μm , is affected primarily by leaf structure (Slaton et al., 2001); green vegetation exhibits high reflectance values but, after the leaf matures, the cells enlarge, crowd together, reducing the intercellular space and leading to a decrease in reflectance (Gates et al., 1965). On the other hand, MIR is often employed as a surrogate of the traditional R band (around 0.6 μm), based on the fact that MIR reflectance is well correlated to the R one, but is not sensitive to most aerosols, namely to those associated with smoke from biomass burning events (Libonati et al., 2010). Kaufman and Remer (1994) showed that the correlation between MIR and R is due to the simultaneous occurrence of processes that darken the surface in these two bands. Whereas in the visible wavelengths, the pigmentation of leaves, especially by active chlorophyll, absorbs the solar radiation, reducing the reflectivity, in the MIR domain (around 3.7 - 3.9 μm) the cellular water content, present in green vegetation, causes a strong absorption, reducing the reflectance at these wavelengths (Gates et al., 1965; Salisbury and D'Aria, 1994). As green leaves become senescent due to the decrease of the levels of chlorophyll and water content, the absorption of solar radiation drops off in both R and MIR regions, increasing reflectance at the two bands.

Within the framework of the above described context, substantial efforts have been spent by the research community in the development of vegetation indices (Verstraete and Pinty, 1996). For instance, the development of optimal vegetation indices in the R/NIR spectral domain has greatly benefited from the so-called soil line concept (Rondeaux et al., 1996). Introduced by Richardson and Wiegand (1977), the soil line concept is a linear

relationship between NIR and R reflectances of bare soil, where changes in soil reflectance are associated to moisture and organic matter (Baret, et al., 1993), and departures from the soil line are in turn strongly related to biophysical parameters such as the Fraction of Green Vegetation, FGV, or the Fraction of Absorbed Photosynthetically Active Radiation, FAPAR (Pinty and Verstraete, 1992). The soil line is therefore a constraint in the R/NIR spectral space that greatly contributes to the design of new vegetation indices that are insensitive to the soil background while remaining responsive to vegetation. Examples of improved alternatives to the traditional NDVI (Rouse et al., 1973) are the Perpendicular Vegetation Index, PVI (Richardson and Wiegand, 1977), the Soil-Adjusted Vegetation Index, SAVI (Huete, 1988) and the GEMI (Pinty and Verstraete, 1992).

However, to the best of our knowledge, no similar constraint has been found in the MIR/NIR space, a circumstance that may have impaired the design of optimal vegetation indices, which have been heuristically derived from indices already developed in the R/NIR domain. This is the case of VI3 (Kaufman and Remer, 1994), a modification of NDVI, as well as of GEMI3 (Pereira, 1999) that directly resulted from GEMI. As pointed out by the developers of VI3 and GEMI3, the derivation of the indices was primarily based on the fact that MIR and R reflectance are strongly correlated. On the other hand, as also stressed by the authors, the processes that govern reflectance in R and MIR are not expected to lead to similar results and the existence of other processes that may change reflectance in the two channels cannot be ignored.

The aim of the present Chapter is to investigate the possibility of defining a transformation in the MIR/NIR space that leads to an enhancement of the spectral information about vegetation. For this purpose, and taking into account the methodology suggested by Verstraete and Pinty (1996) to design optimal indices, a new space is proposed and an appropriate coordinate system is then defined that is appropriate to discriminate vegetation and is sensitive to its water stress. The rationale adopted may be viewed as comparable to that followed to derive the tasseled cap transformation (Crist and

Cicone, 1984; Kauth and Thomas, 1976; Cohen et al., 1995), where a new coordinate system is introduced in order to optimize data for vegetation studies. Using satellite imagery, it will be then shown that the proposed coordinate system is particularly appropriate to operationally monitor vegetation stress and to detect vegetation changes, in particular those caused by droughts and fire events.

6.2. Data

The present Chapter relies on data from remotely-sensed observations, as well as from laboratory measurements. Remotely-sensed observations were gathered over two main Brazilian biomes, namely the Amazon Forest and the Cerrado region (see Figure 3.3 and Table 3.3) as covered by 16 Landsat ETM+ images. Data consist of TOA values of MIR radiance, NIR reflectance and TIR brightness temperature, acquired by the MODIS instrument on-board Terra satellite during the year of 2002, together with the respective SZA. Data were obtained from the Terra/MODIS Level 1B 1 km V5 product, MOD021 (MCST, 2006) and correspond to channels 2 (centered at 0.858 μm), 20 (centered at 3.785 μm), and 31 (centered at 11.017 μm). Surface values of MIR reflectance were then retrieved by applying the methodology developed by Kaufman and Remer (1994), paying special attention to the possible drawbacks previously pointed out by Libonati et al. (2010).

Validation of results from the analysis performed on MODIS images was mainly carried out based on ETM+ imagery. Direct validation of results in the MIR domain is, however, a difficult task because of the lack of “in-situ” (direct) measurements of MIR reflectance. This limitation may be partially circumvented by laboratory measurements of MIR reflectance. In this respect, spectral libraries are currently available that may provide useful information about the spectral features and ranges of the reflectance for natural and manmade materials. Spectral libraries are, in fact, commonly used as reference sources for the identification of surfaces in remote sensing imagery, but the spectral range currently

covered differs from library to library. For instance, the MODIS-UCSB spectral library provides information in thermal infrared domain (from 3 to 14 μm), whereas the ASTER spectral library (Baldrige et al., 2009) makes available spectral reflectance data from the visible to the thermal infrared domain (from 0.4 to 15.4 μm). We restricted the analysis to materials belonging to vegetation, water, and soil classes from the ASTER spectral library because of data accessibility constraints in both NIR and MIR regions (see Chapter 3, Section 3.2.2.1).

For each laboratory spectral data described above, the MODIS channel equivalent reflectance was computed by convolving the laboratory spectral reflectance signatures with the MODIS channels normalized response function (see Chapter 3, Figure 3.10). Finally, for the sake of simplicity, MODIS channels 1, 2 and 20 will be hereafter referred to as R, NIR and MIR, respectively.

6.3. Methods

6.3.1. Rationale

It is well apparent from Figure 3.10 that the different materials tend to form clusters on the MIR/NIR space and that there is an overall displacement from vegetation (top left corner), to burned materials (bottom right corner) across the soil surfaces located along the diagonal of the graph. Both features provide an indication that radiative signature of natural surfaces may be characterized in MIR/NIR space by means of appropriate spectral indices.

Aiming at the identification of dark, dense vegetation, Kaufman and Remer (1994) proposed a new vegetation index, the so-called VI3, which is a modified version of the traditional NDVI, the red reflectance being simply replaced by the reflective part of the middle-infrared signal (channel 3 from AVHRR sensor). VI3 was heuristically derived from

NDVI taking into account the fact that MIR reflectance tends to correlated well with red reflectance. Accordingly, the index is defined as follows:

$$VI3 = \begin{cases} \frac{(\rho_{NIR} - \rho_{MIR})}{(\rho_{NIR} + \rho_{MIR})}, & \text{for } \rho_{NIR} \geq \rho_{RED} \\ 0, & \text{for } \rho_{NIR} < \rho_{RED} \end{cases} \quad (6.1)$$

where ρ_{MIR} and ρ_{RED} are the MIR and red reflectance, respectively. The restriction $\rho_{NIR} \geq \rho_{RED}$ prevents the index from being erroneously applied to water surfaces where it is ill defined (Kaufman and Remer, 1994).

Adopting a similar strategy for burned area identification, Pereira (1999) proposed GEMI3 for mapping fire-affected areas, by replacing AVHRR channel 1 (red) by channel 3 in GEMI, an optimized index in the R/NIR space, originally proposed by Pinty and Verstraete (1992) and designed to minimize contamination of the vegetation signal by extraneous factors, such as the atmosphere and the soil background. A similar procedure may be applied to the so-called Burned Area Index (BAI) (Martín, 1998), which was specifically designed for burned area discrimination in AVHRR R/NIR imagery over Mediterranean environments. The index is defined as the inverse spectral distance to a previously fixed convergence point, given by the minimum (maximum) reflectance of burned vegetation in the NIR (R) bands. Therefore, the corresponding index in the MIR/NIR space may be heuristically defined as:

$$BAI3 = \frac{1}{(\rho_{NIR} - \rho_{CNIR})^2 + (\rho_{MIR} - \rho_{CMIR})^2} \quad (6.2)$$

where ρ_{CNIR} and ρ_{CMIR} are the coordinates of the above-mentioned convergence point, given by the NIR minimum and MIR maximum values of reflectance for burned vegetation.

Using the same rationale for MODIS, the two following indices will be adopted here:

$$\eta = \sqrt{(x - x_0)^2 + (y - y_0)^2} \quad (6.3a)$$

$$\xi = x - y \quad (6.3b)$$

where x and y are the reflectance of MODIS NIR and MIR channels, and x_0 and y_0 are the respective reflectances of the convergence point. It may be noted that indices η and ξ contain the relevant characteristics of BA13 and VI3, namely, the distance to a pre-defined convergence point and the difference between MIR and NIR reflectances. Figure 6.1 is a plot of values obtained from samples of recently burned pixels as extracted from 12 burned scars in MODIS images, six of them over the Amazon and the remaining six over Cerrado. The identification of recent burned pixels in MODIS images was based on burned area polygons, as derived from visual classification of Landsat ETM+ images (Table 3.3).

Taking into account that burned areas correspond to the upper (lower) range of values of MIR (NIR) reflectance that are observed in natural surfaces, the values of 0.24 and 0.05 were assigned to x_0 and y_0 . Moreover, both NIR and MIR reflectance of charcoal, as obtained from laboratory measurements present lower (higher) values than x_0 (y_0) (Figure 3.10) and are therefore in very good agreement with the prescribed values for the upper and lower bounds in MIR and NIR.

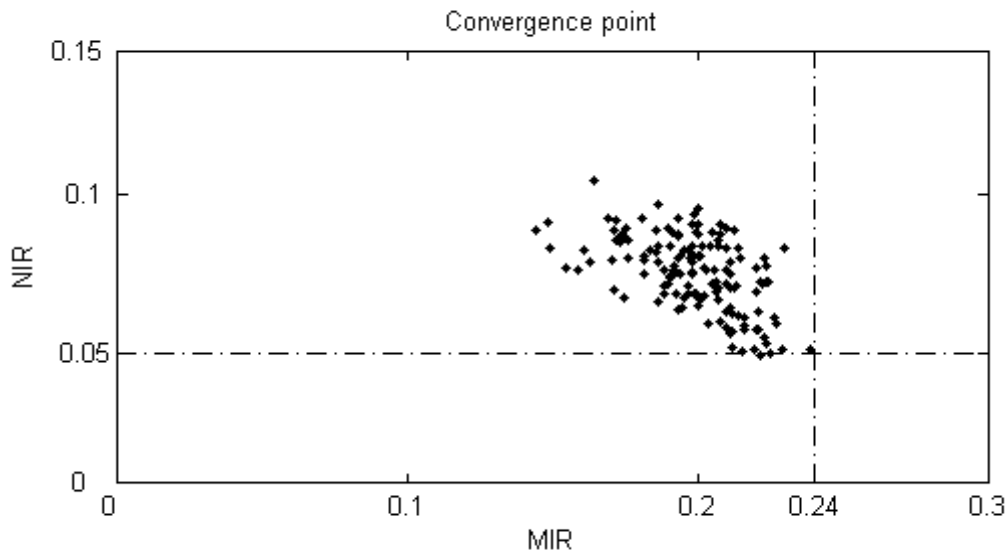


Figure 6.1. MIR and NIR reflectance bi-spectral space showing the reflectance convergence point of recently burned areas samples extracted from MODIS imagery covering the north, northwest and midwest of Brazil. Dashed-dot lines delimit the upper and lower bounds in MIR and NIR and their intersection is the convergence point.

Figure 6.2 shows the location of the pre- and post-fire mean values of MIR and NIR reflectance corresponding to the selected 12 scars. Changes of reflectance from pre- to post-fire are indicated by line segments and it may be noted that those corresponding to forests are almost normal to the contour lines of ξ , whereas those associated to Cerrado are almost normal to the contour lines of η . As pointed out by Verstraete and Pinty (1996), the more perpendicular a displacement vector is to the contour lines of a given index, the better the sensitivity of the index to the observed change at the surface. Despite the small sample size, it seems that $\eta(\xi)$ is especially sensitive to burning events in the Amazon forest (Cerrado). Following Liang (2004), it may, therefore, be useful to compare the two indices in a single plot, in an analysis of the η/ξ space

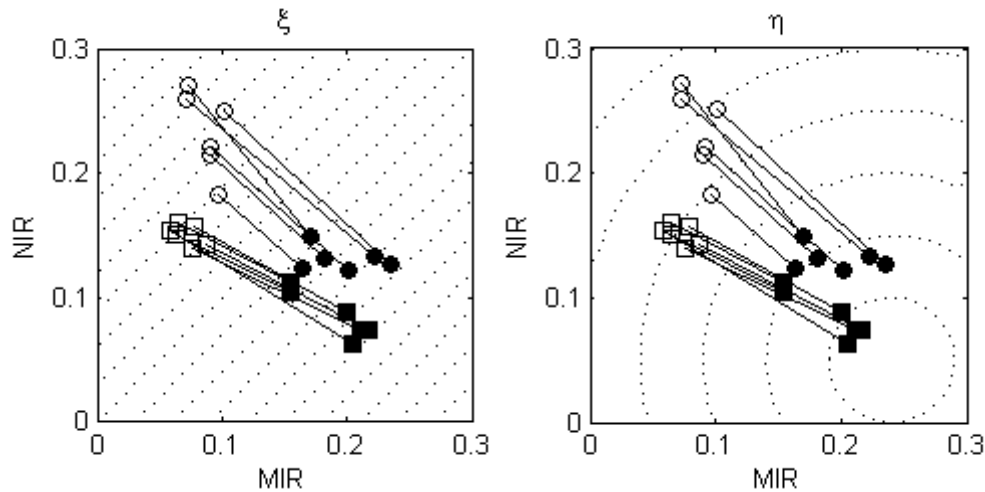


Figure 6.2. Pre- (open symbols) and post-fire (black symbols) mean values of MIR and NIR over 12 selected scars in the Amazon (circles) and Cerrado (squares). Displacement vectors and contour lines of ξ (left panel) and η (right panel) are represented by solid and dotted lines, respectively.

6.3.2. The η/ξ space

Let U be the unit square in the MIR/NIR space and let U' be the corresponding image in the η/ξ space by means of the transformation defined by Eq. (6.3a) and Eq. (6.3b). The domains U and U' are shown in Figure 6.3, together with a set of points in U and the respective images in U' . Because of its shape, the domain U' will be hereafter referred to as the kite domain.

Let $A(x_0, y_0)$ be the convergence point so that $A'(0, x_0 - y_0)$ is the corresponding image according to the transformation given by Eq. (6.3a) and Eq. (6.3b). The curve $[A' B' C']$ ($[A' F' E']$) that defines the upper (lower) limit of U' will be the set of points that, for each value of $\xi \geq x_0 - y_0$ ($\xi \leq x_0 - y_0$), have the minimum value of η . The respective equations of the

curves may accordingly be obtained by replacing Eq. (6.3b) into Eq. (6.3a) and then

computing $\left(\frac{\partial \eta}{\partial x}\right)_{\xi} = 0$, leading to:

$$2x - (x_0 + y_0 + \xi) = 0. \quad (6.4)$$

Replacing Eq. (6.3b) into Eq. (6.4) leads to:

$$y = -x + (x_0 + y_0). \quad (6.5)$$

Given the limits of U, the straight line defined by Eq. (6.5) will go from point B($x_0 + y_0$, 0) to point F(0, $x_0 + y_0$). The image of segment \overline{BF} may therefore be obtained by replacing Eq. (6.5) into Eq. (6.3b) leading to

$$\eta = \frac{|\xi - (x_0 - y_0)|}{\sqrt{2}} \quad (6.6)$$

i.e., to:

$$\eta = \begin{cases} -\frac{\xi - (x_0 - y_0)}{\sqrt{2}}, & \xi \in [-(x_0 + y_0), x_0 - y_0] \\ \frac{\xi - (x_0 - y_0)}{\sqrt{2}}, & \xi \in [x_0 - y_0, x_0 + y_0] \end{cases}. \quad (6.7)$$

It may be noted that the straight line with positive slope goes from A'(0, $x_0 - y_0$) to B'($\sqrt{2} y_0$, $x_0 + y_0$), whereas the straight line with negative slope goes from F'($\sqrt{2} x_0$, $-(x_0 + y_0)$) to A'(0, $x_0 - y_0$). Beyond point B (point F), the minimum distances to point A, for a

given value of ξ , will be located along segment \overline{BC} (segment \overline{FE}). Since $\overline{BC} = \{(x,0), x \in [x_0 + y_0, 1]\}$, then $\xi = x$ along the respective image and, taking Eq. (6.3a) into account, η will be given by:

$$\eta = \sqrt{(\xi - x_0)^2 + y_0^2}, \quad \xi \in [x_0 + y_0, 1]. \quad (6.8)$$

In an analogous way, $\xi = -y$ along the image of $\overline{FE} = \{(0, y), y \in [x_0 + y_0, 1]\}$ and therefore:

$$\eta = \sqrt{x_0^2 + (\xi + y_0)^2}, \quad \xi \in [-1, -(x_0 + y_0)]. \quad (6.9)$$

Point $D(1,1)$ is the point in domain U with maximum value of ξ and its image, $D'(\sqrt{(1-x_0)^2 + (1-y_0)^2}, 0)$, is readily obtained by means of Eq. (6.3a) and Eq. (6.3b).

The right limits of the kite domain U' are defined by the images of segments $\overline{ED} = \{(x,1), x \in [0,1]\}$ and $\overline{CD} = \{(1, y), y \in [0,1]\}$. Taking into account that $x = 1 + \xi$ along \overline{ED} , the respective image will be given by:

$$\eta = \sqrt{(1 + \xi - x_0)^2 + (1 - y_0)^2}, \quad \xi \in [-1, 0]. \quad (6.10a)$$

The image of \overline{CD} may be finally obtained in a similar way by noting that $y = 1 - \xi$ along the segment, leading to:

$$\eta = \sqrt{(1 - x_0)^2 + (1 - \xi - y_0)^2}, \quad \xi \in [0, 1]. \quad (6.10b)$$

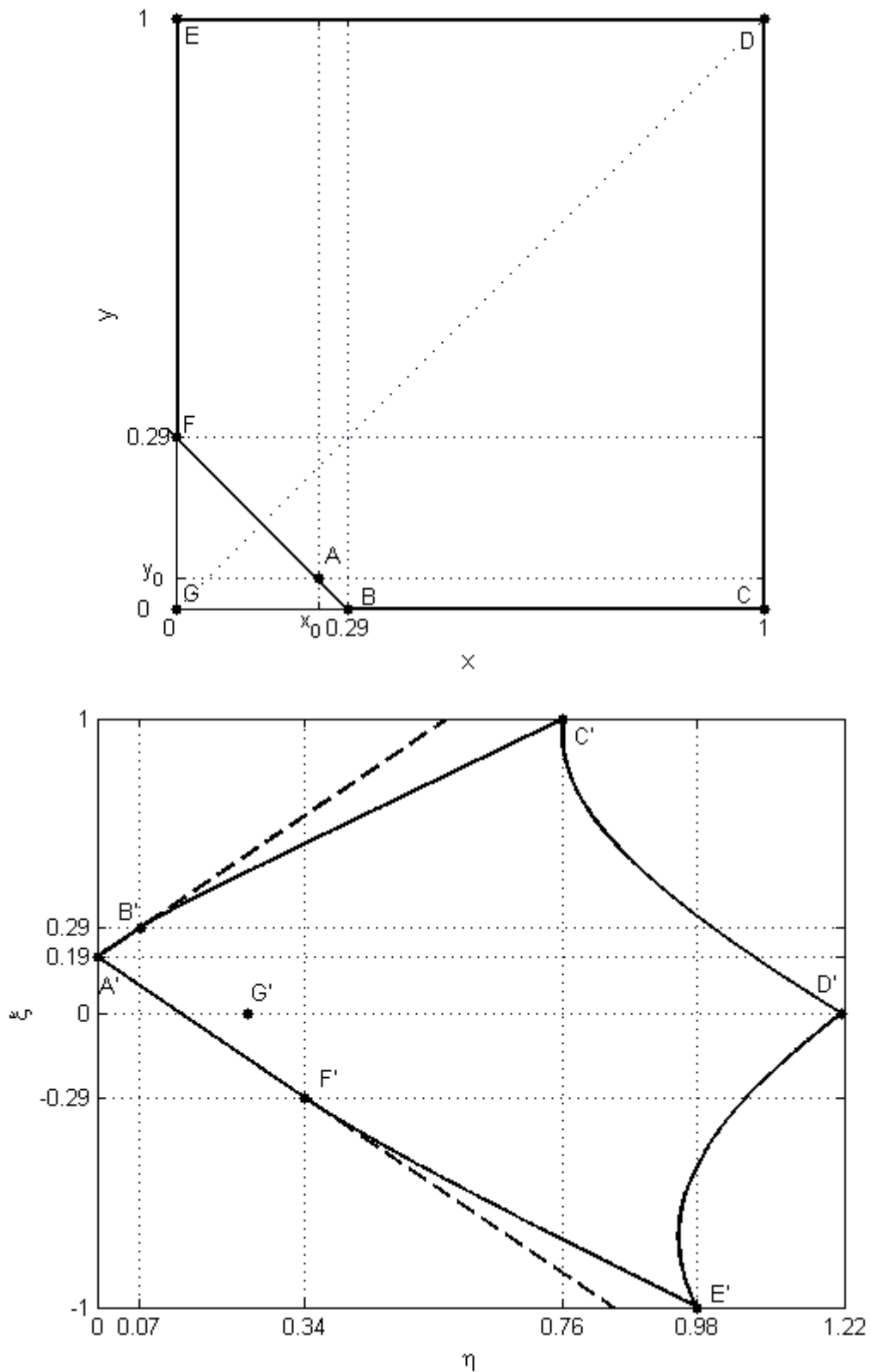


Figure 6.3. The unit square U in the x - y space and the kite domain U' in the η/ξ space, together with a set of points in U and the respective images in U' .

Table 6.1 presents the coordinates (x,y) of all above considered points as well as the coordinates (η, ξ) of the respective images. For further reference, the inverse forms of Equations (6.7) - (6.9) are given below.

Top boundary [A'B'C']

$$\xi = \begin{cases} \sqrt{2}\eta + (x_0 - y_0), & 0 \leq \eta \leq \sqrt{2}y_0 \\ \sqrt{\eta^2 - y_0^2} + x_0, & \sqrt{2}y_0 \leq \eta \leq \sqrt{(1-x_0)^2 + y_0^2} \end{cases} . \quad (6.11)$$

Bottom boundary [A'F'E']

$$\xi = \begin{cases} -\sqrt{2}\eta + (x_0 - y_0), & 0 \leq \eta \leq \sqrt{2}x_0 \\ -\sqrt{\eta^2 - x_0^2} - y_0, & \sqrt{2}x_0 \leq \eta \leq \sqrt{x_0^2 + (1-y_0)^2} \end{cases} . \quad (6.12)$$

Table 6.1. Coordinates (x,y) of the considered points in Figure 6.3 (upper panel) and coordinates (η, ξ) of the respective images (lower panel).

	U domain			U' domain	
	x	y		η	ξ
A	x_0	y_0	A'	0	$x_0 - y_0$
B	$x_0 + y_0$	0	B'	$\sqrt{2}y_0$	$x_0 + y_0$
C	1	0	C'	$\sqrt{(1-x_0)^2 + y_0^2}$	1
D	1	1	D'	$\sqrt{(1-x_0)^2 + (1-y_0)^2}$	0
E	0	1	E'	$\sqrt{x_0^2 + (1-y_0)^2}$	-1
F	0	$x_0 + y_0$	F'	$\sqrt{2}x_0$	$-(x_0 + y_0)$
G	0	0	G'	$\sqrt{x_0^2 + y_0^2}$	0

Figure 6.4 is a plot in space η/ξ of the points shown in Figure 3.10. It may be noted that the materials corresponding to vegetation and charcoal, as well as part of the samples corresponding to soil tend to lie along the bottom boundary line, as given by Eq. (6.12). On the other hand, three samples of charcoal lie along the top boundary line, as defined by Eq. (6.11).

As shown in Figure 6.5, a similar behavior may be observed with the pixels of mean pre- and post-fire reflectance values from the 12 selected scars (Figure 6.2), which all lie along the bottom boundary line of the kite domain. This consistent behavior strongly suggests defining an adequate coordinate system in space η/ξ .

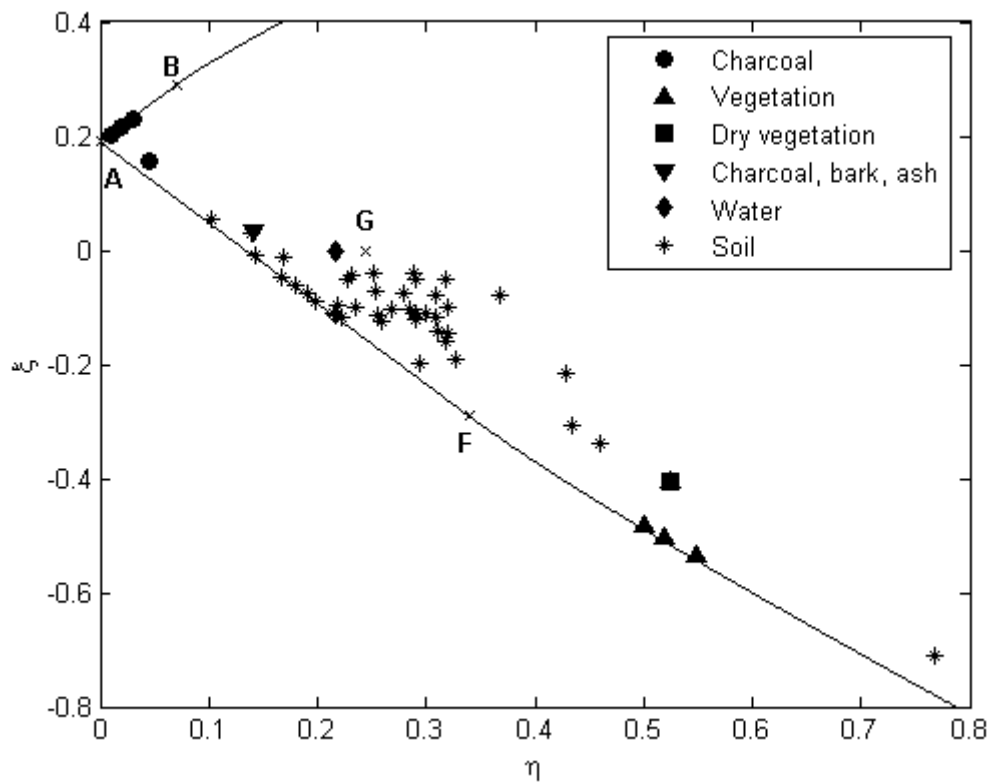


Figure 6.4. Location in the η/ξ space of laboratory measurements respecting to five types of materials.

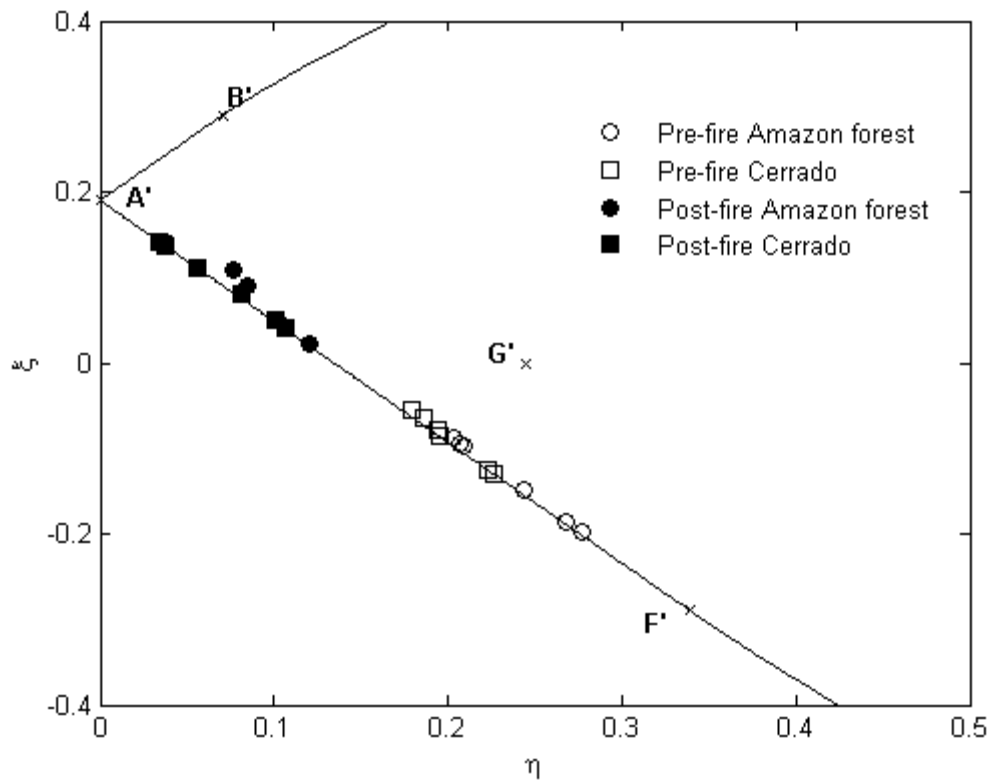


Figure 6.5. Images in the space η/ξ of the points shown in Figure 6.2.

6.3.3. The V-W coordinate system

The kite domain U' being limited, and taking into account the fact that vegetated and burned surfaces tend to lie along the top and bottom boundaries of U' , it will be advantageous to define a system of coordinates (V, W) such that the boundaries of the domain (Figure 6.3) are coordinate curves, e.g. V remaining constant along $[A'B'C']$ as well as along $[A'F'E']$, and W being constant along $[C'D'E']$.

The coordinate V will accordingly be defined such that $V \equiv -1$ along $[A'B'C']$ and $V \equiv +1$ along $[A'F'E']$, i.e.

$$\xi = f(V, \eta) = \begin{cases} f_1(V, \eta), & 0 \leq \eta \leq p(V) \\ f_2(V, \eta), & p(V) \leq \eta \leq q(V) \end{cases}, \text{ for } -1 \leq V \leq +1 \quad (6.13)$$

where $f_1(V, \eta)$, $f_2(V, \eta)$, $p(V)$ and $q(V)$ will have to fulfill the boundary conditions as defined by Eq. (6.11) and Eq. (6.12), respectively for $V = -1$ and for $V = +1$. In the case of f_1 and p this may be easily achieved by defining the coordinate curves f_1 as straight lines with slope proportional to V and by assuming that $p(V)$ is the straight line $\eta = mV + b$ such that $\eta = \sqrt{2}y_0$ for $V = -1$ and $\eta = \sqrt{2}x_0$ for $V = +1$. Accordingly:

$$\xi = f_1(V, \eta) = -\sqrt{2}\eta V + (x_0 - y_0) \quad (6.14)$$

and

$$\eta = p(V) = \frac{\sqrt{2}}{2} [(x_0 - y_0) V + (x_0 + y_0)] \quad (6.15)$$

A similar approach may be used in the case of f_2 leading to:

$$\xi = f_2(V, \eta) = - \left[\sqrt{\eta^2 - \frac{[p(V)]^2}{2}} + \frac{p(V)}{\sqrt{2}} \right] V + x_0 - y_0, \quad (6.16)$$

which fulfills the boundary conditions given by Eq. (6.11) and Eq. (6.12), respectively for $V = -1$ and for $V = +1$. Besides, since by construction $f_1[p(V)] = f_2[p(V)]$, the condition of continuity of f at each point $p(V)$ is also fulfilled.

Finally, $q(V)$ may be obtained by solving for η the system formed by Eq. (6.10a,b) and Eq. (6.16), i.e. by computing the coordinate η_{\max} of the point of intersection of the coordinate curve V with the right boundary curve [E'D'C']. This system may be solved numerically in a straightforward manner by successively halving the interval of solutions.

Finally, Eq. (6.13) may be inverted leading to:

$$V = F(\eta, \xi) = \begin{cases} F_1(\eta, \xi) = -\frac{\xi - (x_0 + y_0)}{\sqrt{2}}, & 0 \leq \eta \leq p(V) \\ F_2(\eta, \xi), & p(V) \leq \eta \leq q(V) \end{cases} \quad (6.17)$$

where $F_2(\eta, \xi)$ may be again evaluated by successive halving.

The second coordinate, W , will now be defined in such a way that $W \equiv 0$ at point $A'(0, x_0 - y_0)$ and $W \equiv 1$ along the curve [C' D' E']. Let P' be a generic point within the kite domain U' and let V_* be the coordinate curve V that contains P' and intersects the right boundary curve [E'D'C'] at point R' . Coordinate W of point P' will be accordingly given by:

$$W = \frac{\Lambda(V_*, A' \rightarrow P')}{\Lambda(V_*, A' \rightarrow R')} \quad (6.18)$$

where $\Lambda(V_*, X' \rightarrow Y')$ is the arc length, along coordinate curve V_* , from point X' to point Y' .

Taking into account Equations (6.13), (6.14) and (6.16), Eq. (6.17) may be written as follows:

$$W = \begin{cases} \frac{\sqrt{1+2V_*^2} \eta_{p'}}{\sqrt{1+2V_*^2} p(V) + \Psi[p(V), \eta_{R'}]}, \eta_{p'} \leq p(V) \\ \frac{\sqrt{1+2V_*^2} \eta_{p'} + \Psi[p(V), \eta_{p'}]}{\sqrt{1+2V_*^2} p(V) + \Psi[p(V), \eta_{R'}]}, \eta_{p'} \geq p(V) \end{cases} \quad (6.19)$$

where the integral given by:

$$\Psi[\alpha, \beta] = \int_{\alpha}^{\beta} \sqrt{1 + \frac{V_*^2 [p(V)]^2}{\eta^2 - \frac{[p(V)]^2}{\sqrt{2}}}} d\eta \quad (6.20)$$

may be evaluated by gaussian quadrature.

Figure 6.6 presents the coordinate curves (V, W) as obtained by applying Eq. (6.17) and Eq. (6.19) over the kite domain U'. Finally, Figure 6.7 presents the system of coordinates (V, W) as defined in the original domain U in the MIR/NIR space. The "spider web" was obtained by successively applying Eq. (6.3a) and Eq. (6.3b) to the original unit square U in the MIR/NIR space and then by applying Eq. (6.17) and Eq. (6.19).

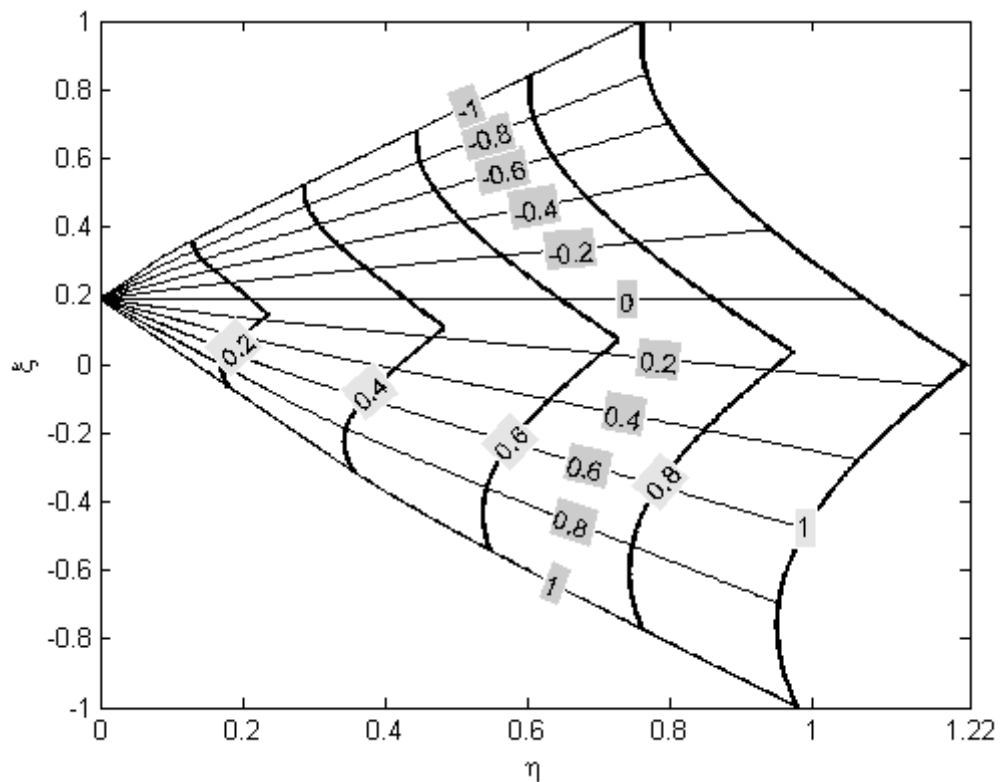


Figure 6.6. Coordinate lines $V=\text{const}$ (from -1 to 1 with intervals of 0.2) and $W=\text{const}$ (from 0 to 1 with intervals of 0.2) over the kite domain U' .

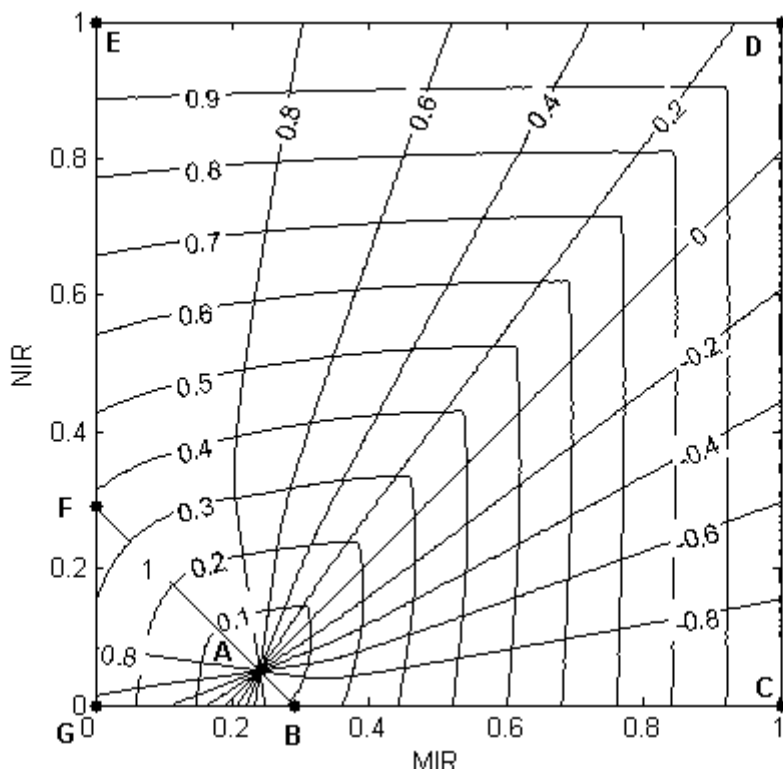


Figure 6.7. The spider web (V, W) in the MIR/NIR space. Contour lines of V from -1 to 1 (with intervals of 0.2) and contour lines of W from 0 to 1 (with intervals of 0.1).

Figure 6.8 (left panel) presents the coordinates V and W of the laboratory measurements shown in Figure 6.4, but with discrimination among the different types of soil. It is worth noting that vegetation samples and some soil types containing organic matter (e.g. Inceptisol, Mollisol, Entisol and Alfisol) are in close alignment with the coordinate curve $V = 1$. On the other hand, dry vegetation, water, charcoal and the remaining soil types, in particular Aridisol, do not lie near $V = 1$. It should be noted that Aridisols, which never fall close to $V = 1$, are the dominant soil types in deserts and xeric shrublands, and have a very low concentration of organic matter. The other soil types nevertheless present a less stable behavior; for instance Mollisols, which tend to have high organic matter content, fall close to $V = 1$ in the case of the Cryoboroll sub-class but the same does not happen with the other sub-classes. This may be attributed to the fact that the overall soil reflectance is controlled by carbonate and quartz rather than by organic matter (Salisbury and D'Aria, 1994). It is also worth pointing out that, besides tending to lie along the contour line $V = 1$, vegetated and burned surfaces as well as soils containing organic matter tend to organize themselves according to water stress, with green vegetation, soils and burned vegetation being respectively associated to large (~ 0.6), moderate ($\sim 0.2-0.4$) and low values (~ 0) of W . Figure 6.8 (right panel) presents the corresponding distribution of points and V - W coordinates in the more familiar MIR/NIR space, allowing for a better understanding of the role of the proposed system of coordinates. The spider web is in fact able to delimit a sector in the MIR/NIR space associated to organic matter, which is then subdivided in subsectors according to their water content. The sector associated to organic matter may be viewed as roughly defined by the coordinate line $V=0.8$ and the efficacy of coordinate V to qualitatively define the sector is mainly due to the steep increase of the gradient of V for larger values. On the other hand, the rather uniform gradient of W allows an effective quantification of the water contents of surfaces with organic matter.

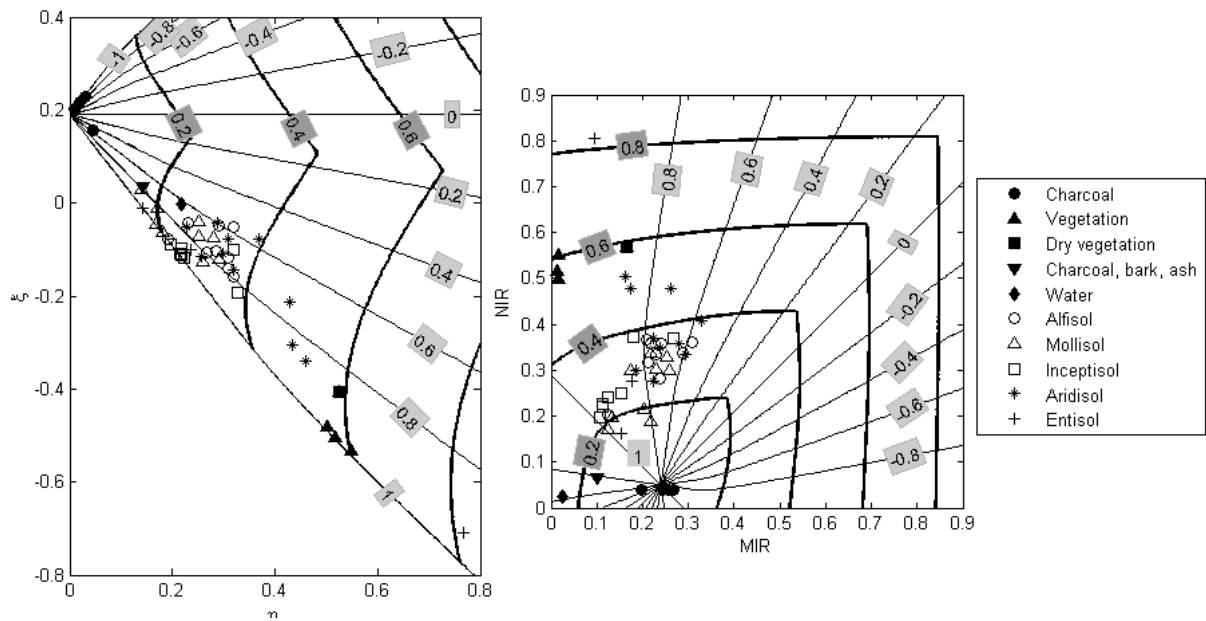


Figure 6.8. As in Figure 6.4 (left panel) and in Figure 3.10 (right panel) but with representation of coordinate curves of V (thin lines) and of W (thick lines) on spaces η/ξ and MIR/NIR, respectively. Laboratory measurements include discrimination among soil types.

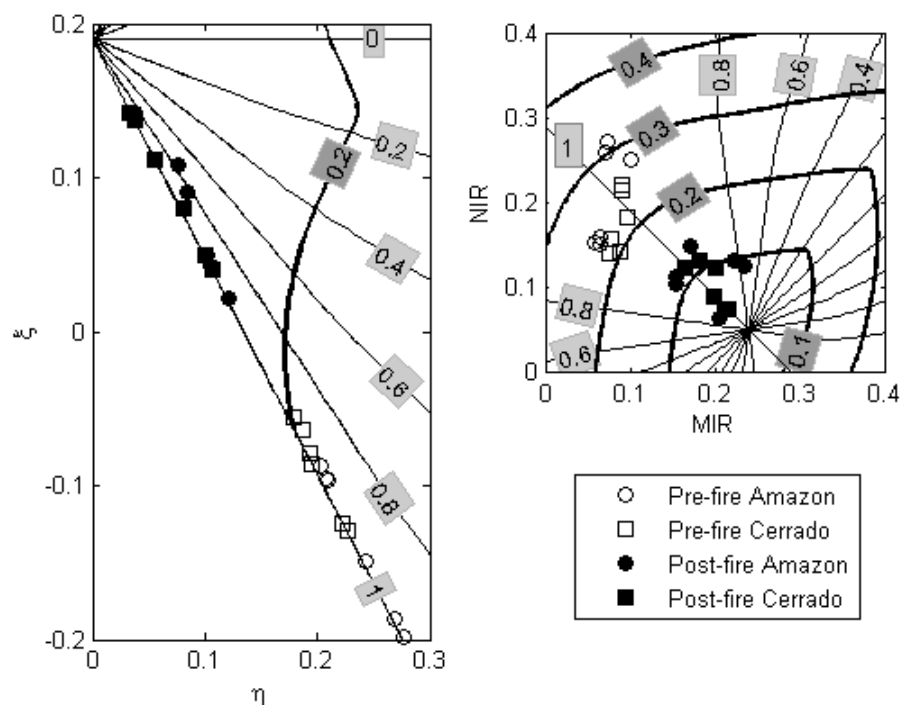


Figure 6.9. As in Figure 6.8 but respecting to pre- and post-fire pixels as shown in Figure 6.5 (left panel) and in Figure 6.2 (right panel).

The above-described behavior of vegetated surfaces according to water stress is confirmed by the results shown in Figure 6.9 corresponding to the V and W coordinates of the pre- and post-fire samples shown in Figures 6.2 and 6.5. All vegetated and burned surfaces are accordingly located along coordinate curve $V = 1$, pre-fire (post-fire) pixels, with green, dry and burned vegetation being associated to decreasing values of W .

An application to real data is given in Figure 6.10, which shows a comparison of an RGB (721) image from MODIS sensor and corresponding to scene number 3 (Table 3.3) with two false color images respectively representing V and W coordinates as derived from the corresponding MIR and NIR MODIS images. The ability of coordinate V to discriminate between green vegetation, stressed and dry vegetation, soil, and burned surfaces, on the one hand, and other types of surfaces (e.g. clouds), on the other, is well apparent. The sensitivity of coordinate W to water stress is also conspicuous, green vegetation presenting the higher values which progressively decrease to drier surfaces and finally to burnt areas.

V and W have different properties regarding the scatter of values; whereas the former coordinate has a very small scatter for pixels associated with surfaces containing organic matter (values concentrating between 0.8 and 1), coordinate W has a much wider range of values (between 0 for burned surfaces up to 0.8 for very green vegetated surfaces). As pointed out by Verstraete and Pinty (1996), the complementary character of coordinates V and W is especially appropriate for application purposes since the strict scale character of V makes it a good classifier (of biomass) and the large scale character of W makes it a good quantifier (of water content or water stress).

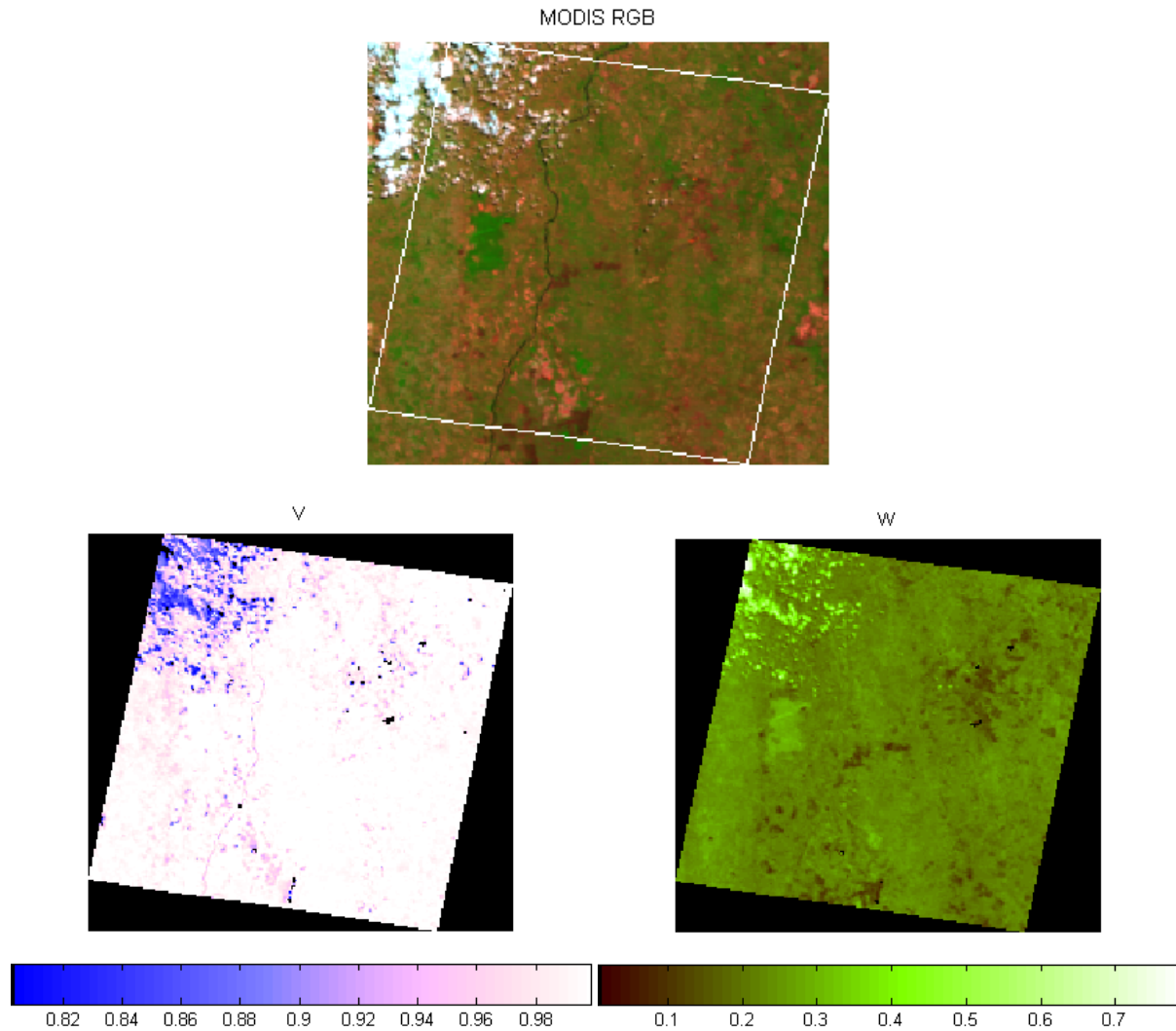


Figure 6.10. Comparison between RGB (721) from MODIS showing scene number 3 and two false color images respectively from V and W coordinates.

6.4. Results and discussion

An assessment on the potential of coordinates V and W to discriminate vegetated surfaces and to ascribe their water stress will be performed by analyzing the set of 16 images that was described in Chapter 3 (Section 3.2.3.1, Table 3.3). For that purpose a supervised validation of results will be first undertaken by choosing several types of surfaces and by then comparing the respective representations in the η/ξ space with those in the

traditional MIR/NIR and R/NIR spaces. This study is then followed by an unsupervised validation that will help evaluating the discriminating ability of V and the sensitivity of W , i.e. the usefulness of V as a classifier and of W as a quantifier.

6.4.1. Supervised validation

As shown in Figures 6.11-6.13 corresponding to scenes 3, 4, 6 and 8, respectively (see Table 3.3), different classes of surfaces (namely dense vegetation, sparse vegetation, soil, burned vegetation, water, clouds and cloud shadows) were selected by visual inspection of the respective high resolution Landsat ETM+ images. The corresponding MODIS data were then used to represent the chosen surfaces in the R/NIR, MIR/NIR and η/ξ spaces. As expected, the representation of the different surfaces in the three spaces are topologically equivalent in the sense that each representation may be continuously transformed into the other by means of translations, rotations and deformations. The advantages of the η/ξ space together with the associated system of coordinates (V , W) are nevertheless conspicuous. Whereas vegetation, soil and burned pixels tend to lie along the coordinate curve $V = 1$, the position of the remaining pixels is always displaced off the curve. In fact, the trend for surfaces with (without) organic matter to lie close to (away from) $V = 1$ was found in all 16 scenes analyzed, with no exception for any surface. On the other hand, the two extreme values of W are associated with opposite characteristics of vegetated surfaces; whereas burned surfaces tend to have values of W close to zero, especially shortly after the fire event; green vegetation tends to be characterized by high values (~ 0.8) of W . Intermediate values of W generally correspond to a decreased density of vegetation and/or to the emergence of the soil background.

It may be finally noted that the alignment of vegetated surfaces with the coordinate curve $V = 1$ is mainly due to the already mentioned strict scale character of that coordinate,

whereas the large scale character of W allows estimating the water content of vegetated surfaces. It is therefore to be expected that such characteristics will enable the use of coordinates (V, W) to discriminate vegetated surfaces and to estimate the water content. This will be investigated in the next subsection.

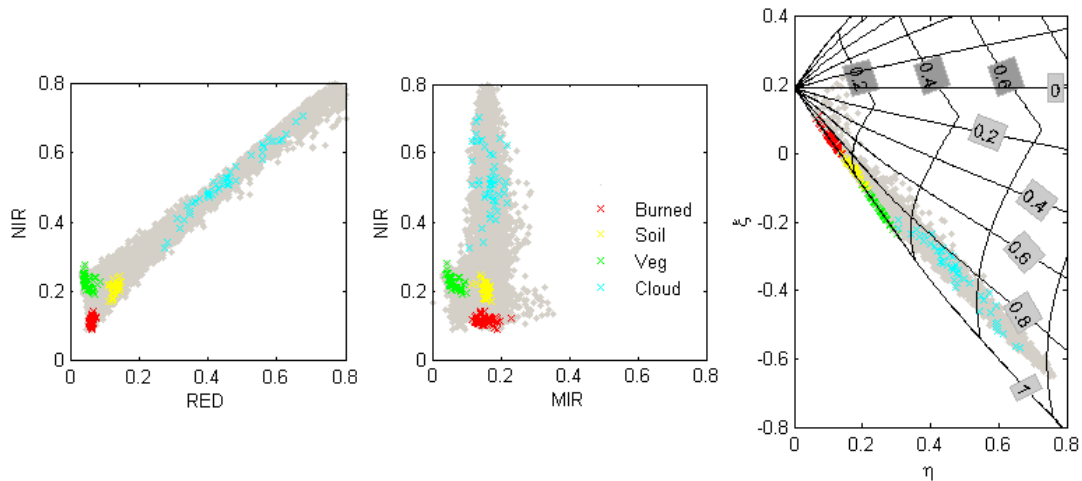


Figure 6.11. Scatter plot (gray points) of MODIS pixels corresponding to scene 3 in the R/NIR space (left panel), in the MIR/NIR space (middle panel) and in the η/ξ space and respective coordinate lines of V and W (right panel). Selected pixels corresponding to burned surfaces, soil, vegetation and clouds are respectively represented by red, yellow, green and cyan crosses.

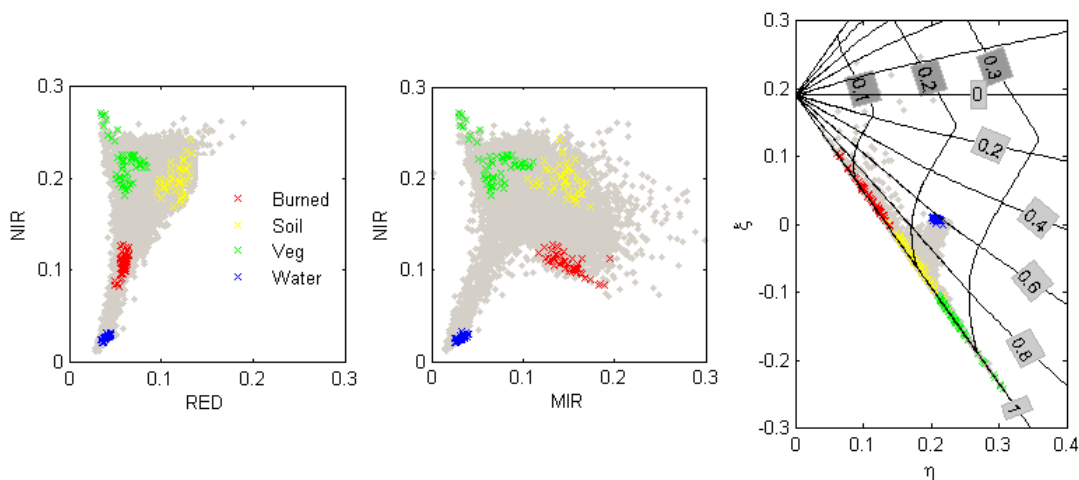


Figure 6.12. As in Figure 6.11 but corresponding to scene 4. Selected pixels representative

of burned surfaces, soil, vegetation and water are respectively represented by red yellow, green and blue crosses.

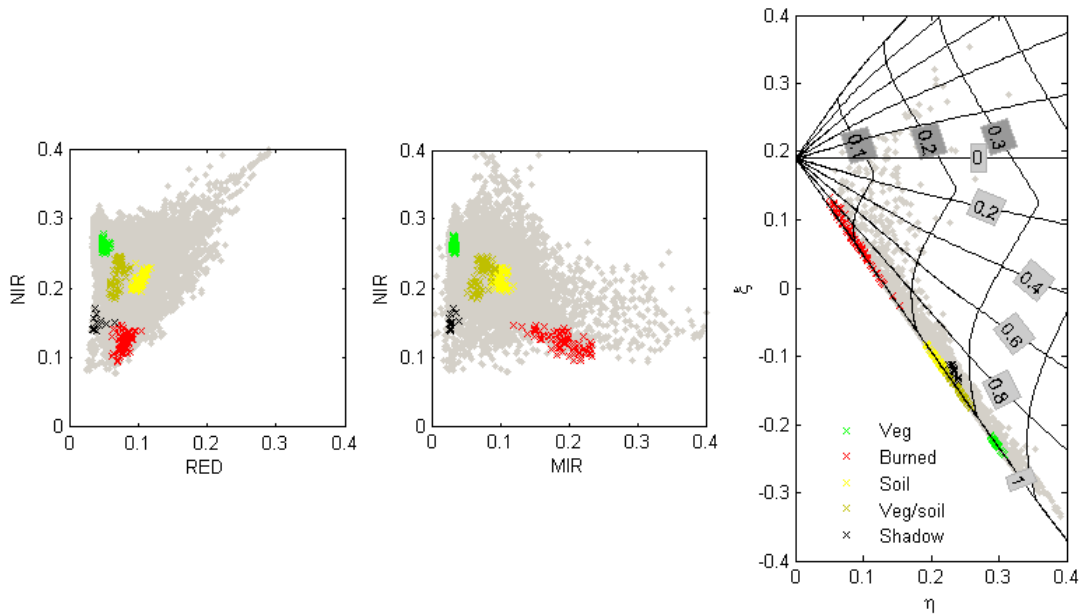


Figure 6.13. As in Figure 6.11 but respecting to scene 6. Selected pixels corresponding to burned surfaces, soil, vegetation, sparse vegetation and cloud shadows are respectively represented by red yellow, green brown and black crosses.

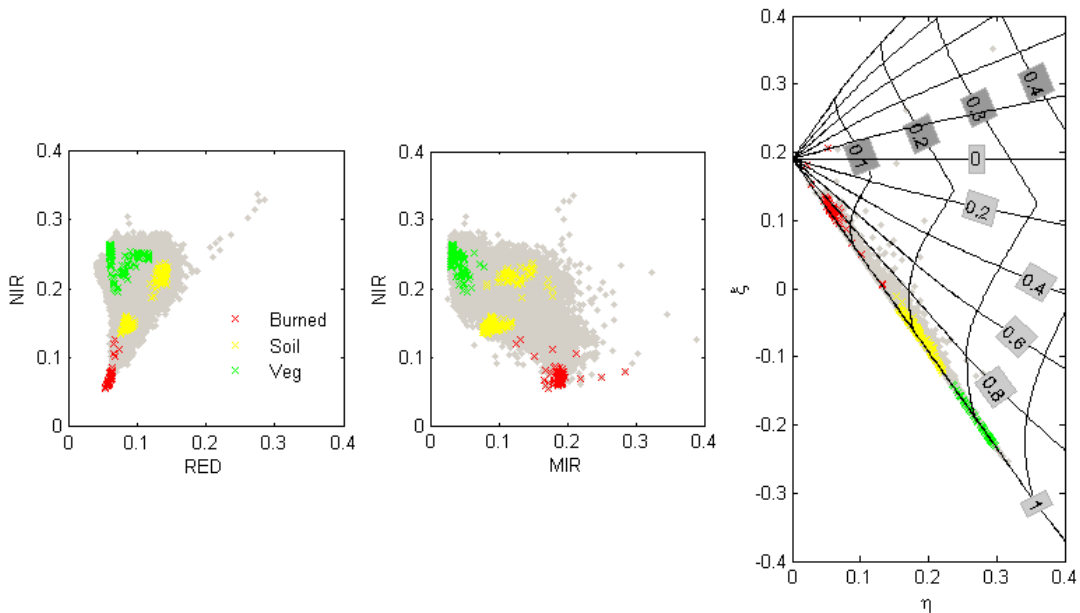


Figure 6.14. As in Figure 6.11 but corresponding to scene 8. Selected pixels representative of burned surfaces, soil and vegetation are respectively represented by red, yellow, and green crosses.

6.4.2. Unsupervised validation

The performance of coordinates V and W respectively as a classifier of vegetated surfaces and as a quantifier of water stress may be assessed by means of an unsupervised approach, which as pointed out e.g. by Lillesand and Kiefer (1994) allows distinguishing among classes according to their own characteristics, even if there is the need to subsequently interpret the information in order to make use of it. Because of its simplicity and wide use the k-means algorithm was successively applied to coordinates V and W of several MODIS images; first, two cluster centers were estimated from the V sample and then four clusters were derived from the W sample restricted to those pixels belonging to the centre with higher V . Results obtained from the unsupervised classification of each image were finally compared against the respective Landsat ETM+ high resolution image (see Table 3.3).

Figures 6.15 and 6.16 present the results obtained after applying k-means to scenes 3 and 4, respectively. Regarding to the η/ξ space (left panel), gray points correspond to the first of the two clusters obtained applying k-means to V whereas colored points represent the second cluster. This second cluster was then used as input to k-means regarding to W . Thus each colored cluster denotes the clusters derived from the k-means from W , and the isolines values denote the limits between these clusters. It is worth noting that colors in the left and central panels correspond to the same clusters. Taking for reference the RGB (543) of the high resolution images (Figures 6.15 and 6.16, right panels), it is well apparent that, when applied to the V samples, the k-means algorithm is able to discriminate between pixels associated to green vegetation, stressed vegetation, and burned surfaces, on the one hand and to the other types (e.g. water bodies and clouds), on the other, whose centroids respectively present a high and a low value of V . The two clusters will be hereafter referred to as the “biomass” and the “non-biomass”, respectively and it may be noted that the latter cluster corresponds to the gray points in the left panels of Figures 6.15 and 6.16, whereas the remaining colors identify the “biomass” cluster. When k-means is further applied to the

latter pixels (i.e. to those belonging to “biomass”), the obtained four clusters in W appear to be related respectively to one class of green vegetation (represented in green), two classes of soil or stressed vegetation or sparsely vegetated areas (represented in dark green and dark brown) and one class of burned surfaces (represented in black). A close agreement is well apparent between the spatial patterns of the above-referred five classes (central panels) and the spatial distribution of RGB (543) pixels (right panels). For instance, the “non-biomass” cluster corresponds to clouds in case of scene number 3 (Figure 6.15) and to water in case of scene 4 (Figure 6.16); the green vegetation class corresponds to the greener patches in both scenes, the soil-stressed/sparse vegetation may be identified as the pinkish and purple areas; finally, the burned surfaces are readily identifiable as the very dark or black pixels of the ETM+ images. As expected, in the η/ξ space, pixels belonging to the “non-biomass” cluster (grey pixels) do not stand close to coordinate curve $V = 1$, as opposed to the “biomass” cluster, whose pixels lie along that coordinate curve.

A summary of results of k-means for all 16 scenes is presented in Table 6.2 and the obtained overall consistency is evident.

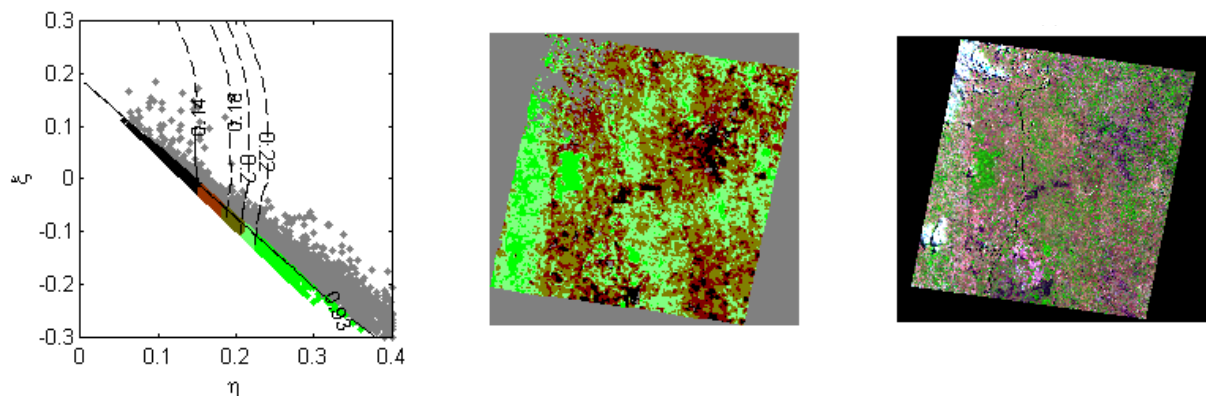


Figure 6.15. Comparison of results of k-means corresponding to scene 3 in the η/ξ (left panel) and the geographical (central panel) spaces with the RGB (543) of the corresponding high resolution ETM+ image (right panel). See main text for color codes of clusters.

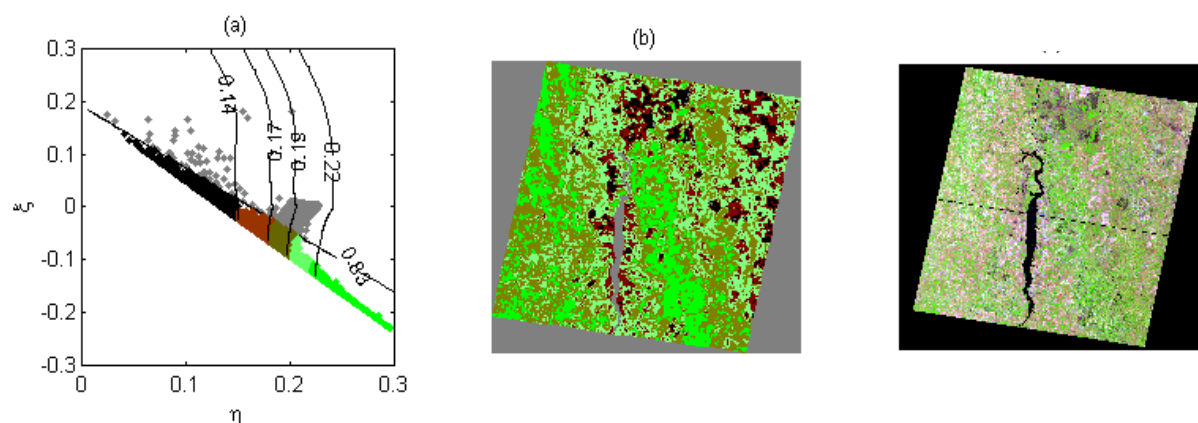


Figure 6.16. As in Figure 6.15, but corresponding to scene 4.

In fact, in all 16 scenes analyzed the V cluster with centroid around 0.97 to 0.99 is associated with surfaces containing organic matter. As expected, the other V cluster is less stable, since it considerably depends upon the type of “non-biomass” surface (e.g. clouds or water bodies) that is present in the image. The centroids of the W clusters also depend on the types of landcover in each scene and, for this reason; results have to be compared against the respective high resolution image. Accordingly, scenes 1, 2, 3, 4, 5, 6, 7, 10 and 14, that contain burned areas always have the cluster with lowest centroid with values close to 0.1. On the other hand, scenes mostly covered by vegetation, usually have the cluster with the highest centroid with values about 0.23. Finally, soil and sparsely vegetated areas are associated to clusters with centroids between 0.15 and 0.22.

Table 6.2. Centroids of clusters as obtained from applying k-means to coordinates V and W of the 16 scenes described in Table 3.3.

Scene number	V Cluster centre 1	V Cluster centre 2	W Cluster centre 1	W Cluster centre 2	W Cluster centre 3	W Cluster centre 4
1	0.99	0.77	0.11	0.15	0.17	0.19
2	0.99	0.72	0.14	0.17	0.19	0.20
3	0.99	0.87	0.12	0.16	0.18	0.20
4	0.99	0.66	0.12	0.16	0.18	0.20
5	0.98	0.66	0.14	0.21	0.22	0.24
6	0.99	0.42	0.13	0.20	0.23	0.27

7	0.99	0.49	0.10	0.16	0.20	0.24
8	0.99	0.90	0.16	0.20	0.23	0.27
9	0.99	0.57	0.22	0.25	0.28	0.30
10	0.99	0.51	0.13	0.20	0.24	0.28
11	0.97	0.87	0.23	0.27	0.29	0.31
12	0.99	0.98	0.23	0.28	0.30	0.31
13	0.99	0.97	0.25	0.28	0.31	0.32
14	0.99	0.93	0.14	0.18	0.22	0.26
15	0.99	0.89	0.22	0.24	0.26	0.28
16	0.99	0.84	0.21	0.26	0.29	0.46

6.5. Concluding remarks

A transformation was defined on the MIR/NIR space of reflectances with the aim of enhancing the spectral information in such a way that vegetated surfaces may be effectively discriminated and that its water stress of vegetation may be adequately estimated, leading to the distinction among green vegetation, stressed and dry vegetation, and burned surfaces. The transformation was in fact designed to make a synergic use of advantages of indices, like BAI, that rely on the concept of distances to a fixed point and of indices, like NDVI and VI, which incorporate differences between channels.

When the defined transformation was applied to the unit square of reflectance in the MIR/NIR space, the resulting “kite” domain revealed the property that laboratory materials and land surfaces corresponding to green vegetation, stressed vegetation and burned vegetation tended to lie along the bottom boundary line. A coordinate system was therefore defined in the “kite” domain in such a way that the boundaries of the domain were coordinate curves. The proposed coordinate system presented the two following properties; 1) one of the coordinates, the so-called V coordinate, had a very small dispersion for pixels associated to surfaces containing organic matter (e.g. green vegetation, sparse vegetation, some types of organic soil and incompletely burned surfaces), whereas 2) the other coordinate, the so-called W coordinate, covered a wide range of values according to the water content of vegetated surfaces. These two properties are extremely convenient for application purposes

since, as pointed out by Verstraete and Pinty (1996), the strict scale character of V makes it a good classifier (of biomass) whereas the large scale character of W makes it a good quantifier of water stress. The new coordinate revealed therefore the ability to provide more information than ratio or modified ratio indices (like most vegetation indices), which also rely on a pair of spectral bands.

A validation exercise was performed with the aim of assessing the potential of coordinate V to discriminate vegetated surfaces and of coordinate W to ascribe their water stress. For that purpose a set of 16 scenes were used covering the two main Brazilian biomes, namely the Amazon Forest and the Cerrado region during the year of 2002. Data consisted of information from Landsat ETM+ and of MIR radiance, NIR reflectance and TIR brightness temperature as acquired by the MODIS instrument.

A supervised validation was first carried out by selecting, in the scenes, different classes of surfaces (namely vegetation, sparsely vegetated, soil, burned vegetation, water, clouds and cloud shadows). Results obtained allowed understanding the two properties of the (V, W) coordinate system. In fact, the representation of the surfaces in the space η/ξ may be viewed as resulting from the MIR/NIR space by means of translations, rotations and deformations leading to a compression in V and a dilation in W that determine the above-mentioned strict scale character of V and large character of W . Surfaces containing any kind of biomass tended to lie close to and along the coordinate line $V = 1$, whereas “non-biomass” surfaces, such as clouds, water bodies, mineral soil and completely burned surfaces (i.e. charcoal only) were mainly located away from that contour line. Nevertheless, burned surfaces in MODIS imagery always fell close to $V = 1$ because it is virtually impossible to find a MODIS pixel completely covered by charcoal and without any trace of biomass. On the other hand, values of W from low to high values were associated with different levels of water content, from full coverage of green vegetation, going across sparsely or senescent vegetation up to burned areas, which are very dry.

The robustness of the coordinate system was then tested by using an unsupervised validation approach, where no a priori knowledge was assumed about V and W data. For instance, it was shown that even when using a simple unsupervised clustering algorithm, such as k-means, appropriate and consistent clusters could be found in all the 16 scenes in what regards to the biomass/non-biomass character of the surfaces and their water content. It seems reasonable to conclude that the (V, W) coordinate system is optimal to discriminate biomass (by means of V) and to assess biomass water content interclass variability (by means of W).

The concept behind the (V, W) coordinate system presents some similarities with the tasseled cap transformation, where a new coordinate system is used in order to emphasize vegetation properties. On the other hand, the properties of the η/ξ space and of the associated (V, W) coordinate system open interesting perspectives for applications like drought monitoring and burned area discrimination using remotely-sensed information. Finally, it is worth emphasizing that, although tested with the MODIS sensor, the proposed transformation may be straightforwardly adapted to other sensors, such as the AVHRR, working in the MIR and NIR bands. The approach may be further extended to other combination of bands, e.g. SWIR/NIR according to the purpose of study and to the availability of remotely-sensed information.

Chapter 7

Concluding remarks

A strategy was presented that allows deriving a new index aiming at burned area discrimination. The index relies on information provided by the NIR and MIR channels of the MODIS sensor and was especially developed for the Amazon and Cerrado regions of Brazil.

In order to develop the new index, and taking into account the characteristics of the MIR signal, a thorough review was undertaken of existing methods for retrieving MIR reflectance. Particular attention was devoted to assess the performance of the method based on, the complete radiative transfer equation and a comparison was made against the mostly used procedure in the context of burned area studies, namely the KR94 methodology.

Our results show that the quality of the retrieved values of MIR reflectance by means of KR94 may significantly degrade when the relative contribution of the thermal emitted

component to the total signal exceeds a threshold of about 75%. Use of KR94 algorithm in tropical environments to retrieve vegetation reflectance may lead to errors that are at least of the same order of magnitude of the reflectance to be retrieved and considerably higher for large values of LST and SZA. In fact, there is a critical region in the LST vs. SZA space where the MIR reflectance retrieval is severely impaired. Under such conditions, retrieved values of reflectance for vegetation may attain those characteristic of charcoal making the two types of surface undistinguishable. We have also shown that use of the complete radiative transfer equation does not bring any significant advantages (as compared to using KR94) when geometric and atmospheric conditions turn the inversion into an ill-posed problem. However, the RTE approach leads to better estimates than KR94 in virtually all cases, the exception consisting of low sun elevations and high LST, where results from KR94 are nevertheless also not usable.

Another drawback, of an operational nature, was also found in what respects to using RTE with MODIS data. As already mentioned, LST is a required parameter in order to solve RTE and retrieve MIR reflectance. We have found, however, that burned areas are flagged as Not a Number (NaN) in MODIS LST product, which completely impaired the use of RTE for MIR reflectance retrieval aiming burned area discrimination.

Obtained results, even when based on synthetic data, allowed establishing a baseline that may help avoiding pitfalls when retrieving MIR reflectance from real data. This is an especially relevant issue when relying on algorithms based on MIR reflectance (as retrieved from the total signal) in order to perform a continuous monitoring of burned areas. A proper delineation of regions of ill-conditioning is also critical when attempting to derive indices (based on the reflective part of MIR radiance) aiming to discriminate burned areas in tropical environments.

In order to design a spectral index aiming at specifically discriminating burned areas we have defined a transformation in the MIR/NIR space that leads to an enhancement of the spectral information about vegetation. The transformation consisted of 1) the distance, η , of

each point in MIR/NIR to a pre-defined convergence point, representative of a given target (e.g. a totally burned surface), and 2) the difference, ξ , between the respective MIR and NIR reflectance of each point. A coordinate system was then defined which presented the two following properties; 1) one of the coordinates, the so-called V coordinate, had a very small dispersion for pixels associated to surfaces containing organic matter, whereas 2) the other coordinate, the so-called W coordinate, covered a wide range of values according to the water content of vegetated surfaces.

The developed new pair of indices (V,W) open interesting perspectives for applications e.g. drought monitoring and burned area discrimination using remotely-sensed information. The potential of the new pair of indices to be operationally used to discriminate burned areas in the Amazon and Cerrado regions of Brazil is currently being assessed with very encouraging preliminary results. Some of these results are presented in Table 7.1, which shows a comparison of the ability in discriminating burned and unburned surfaces when using traditional indices and the new proposed (V,W) index for three regions over Amazon and Cerrado (as defined in Table 3.3). The discriminating ability is assessed by means of the M index, as defined in Eq. (2.11)). Values of M larger than one indicate good separability, whereas values smaller than one represent large degrees of histogram overlap between the two classes. The new proposed (V,W) index works better than the traditional indices in all three cases analyzed, with the advantage of not requiring either cloud or land/water masks, which is not true for the remaining traditional indices shown in Table 7.1. Besides the (V,W) index has the advantage of not having been heuristically derived as opposed to VI20 (or more precisely VI3, suggested by Kaufman and Remer, 1994) and GEMI20 (or more precisely GEMI3, suggested by Pereira, 1999). Moreover by exploiting the temporal and spatial characteristics of the (V,W) index will certainly improve the discrimination performance of the new index among burned and unburned surfaces.

Table 7.1. Comparison of the discriminating ability between burned and unburned surfaces (M index) by means of traditional indices and using the new proposed (V,W) index for three regions over Amazon and Cerrado (see Table 3.3).

	M index		
	Cerrado (scene 3)	Cerrado (scene 4)	Amazon Forest (scene 6)
(V,W)	2.08	2.40	2.72
NDVI	0.20	0.65	1.27
VI20	0.96	1.65	2.65
BAI20	1.73	1.68	2.09
GEMI	0.24	1.55	1.90
GEMI20	0.75	1.80	2.70

The main contribution and the originality of the work developed with respect to the use of MIR reflectance data for burned area identification in tropical regions may be summarized as follows:

- Performance of a quality assessment of MIR reflectance when retrieved using the algorithm proposed by KR94, for a wide range of atmospheric, geometric and surface conditions when applied to burned area discrimination, in particular in the Amazon and Cerrado regions using MODIS data;
- Collection of samples of charcoal from tropical regions and measurement of its spectral signatures in the vicinity of 3.9 μm , being currently the only available information in literature about the behavior of burned materials in this spectral domain;
- A systematic comparison between RTE and KR94 approaches taking into account the performance and the need for auxiliary data, as well as the required computing resources aiming burned area studies;

- Evaluation of the effect of the atmospheric profile, LST and instrument noise sources of error on the retrieval of MIR reflectance by means of the radiative transfer equation;
- A proper delineation of regions of ill-conditioning when retrieving MIR reflectance from MODIS sensor in tropical environments.
- Definition of a transformation on the MIR/NIR space of reflectances leading to an enhancement of the spectral information about vegetation;
- Development of a new set of indices based on the above mentioned transformation, providing more information than traditional ratio or modified ratio indices, and revealing to be appropriate to operationally monitor vegetation stress and to detect vegetation changes, in particular those caused by fire events.

It is expected that the improvements in burned area quantification that may be achieved using the results from this thesis, may contribute to a better understanding of biomass emissions, and therefore to an improvement in climate changes studies. Results are also expected to reveal useful to assess the economic value of the damage area by fires, namely in the Amazon and Cerrado regions of Brazil, an issue that is becoming more and more relevant nowadays.

References

Ahern, F. J., Goldammer, J. G., and Justice, C. O. (2001). Global and regional vegetation fire monitoring from space: Planning a coordinated international effort. The Hague, The Netherlands: SPA Academic Publishing.

Amaral, S. (1992). Imagens do sistema sensor AVHRR/NOAA na detecção e avaliação de desmatamentos na floresta amazônica - relações com dados do sistema TM/Landsat. MSc thesis, Instituto Nacional de Pesquisas Espaciais - INPE, S. J. Campos (INPE-5501-TDI/516).

Andreae, M. (1991). Biomass Burning in the Tropics: Impact on Environmental Quality and Global Climate. *Resources, Environment, and Population: Present Knowledge, Future Options*, 268-291.

Arino, O., Piccolini, I., Siegert, F., Eva, H., Chuvieco, E., Martin, P., Li, Z., Frsaer, R. H., Kasischke, E., Roy, D., Pereira, J. M. C., and Stroppiana, D. (2000). Burn scar mapping methods. In Ahern, F., Grégoire, J. M., Justice, C., Ed. *Forest Fire Monitoring and Mapping: a component of global observation of forest cover*. Joint Research Centre Ispra, Italy.

Baldrige, A. M., Hook, S. J., Grove, C. I., and Rivera, G. (2009). The ASTER spectral library version 2.0. *Remote Sensing of Environment*, 113, 711-715.

Barbosa, P. M., Gregoire, J. -M., and Pereira, J. M. C. (1999). An algorithm for extracting burned areas from time series of AVHRR GAC data applied at a continental scale. *Remote Sensing of Environment*, 69, 253-263.

Baret, F., Jacquemoud, S., and Hanocq, J. F. (1993). About the soil line concept in remote sensing. *Remote Sens. Rev.*, 5, 281-284.

Becker, F., and Li, Z. -L. (1990). Temperature-independent spectral indices in thermal infrared bands. *Remote Sensing of Environment*, 32, 17-33.

Berk, A., Anderson, G. P., Acharya, P. K., Chetwynd, J. H., Bernstein, L. S., Shettle, E. P., Matthew, M. W., and Alder-Golden, S. M. (2000). MODTRAN4 version 2 user's manual. Air Force Research Laboratory, Space Vehicles Directorate, Air Force Material Command, Hanscom AFB, MA 01731-3010.

Bird, R. E. (1984). A simple, solar spectral model for direct-normal and diffuse horizontal irradiance. *Solar Energy*, 32, 461-471.

Boyd, D. S. (1999). The relationship between the biomass of Cameroonian tropical forests and radiation reflected in middle infrared wavelengths (3.0-5.0 μm). *International Journal of Remote Sensing*, 20, 1017-1023

Boyd, D. S., and Duane, W. J. (2001). Exploring spatial and temporal variation in middle infrared reflectance (at 3.75 μm) measured from the tropical forests of West Africa. *International Journal of Remote Sensing*, 22, 1861–1878.

Boyd, D. S., Foody, G. M., and Curran, P. J. (1999). The relationship between the biomass of Cameroonian tropical forests and radiation reflected in middle infrared wavelengths (3.0–5.0 mm). *International Journal of Remote Sensing*, 20, 1017–1023.

Boyd, D.S., and Petitcolin, F. (2004). Remote sensing of the terrestrial environment using middle infrared radiation 3.0–5.0 μm . *International Journal of Remote Sensing*, 22, 1861–1878.

Boyd, D. S., Phipps, P. C., Foody, G. M., and Walsh, R. P. D. (2002). Exploring the utility of NOAA AVHRR middle infrared reflectance to monitor the impacts of ENSO induced drought stress on Sabah rainforests. *International Journal of Remote Sensing*, 23, 5141–5147.

Boyd, D. S., Wicks, T. E., and Curran, P. J. (2000). Use of middle infrared radiation to estimate leaf area index of a boreal forest. *Tree Physiology*, 20, 755–760.

Caetano, M., Mertes, L., Cadete, L., and Pereira, J. M. C. (1996). Assessment of AVHRR data for characterising burned areas and post-fire vegetation recovery. *EARSEL Advances in Remote Sensing*, 4, 124–134.

Chase, T. N., Pielke, R. A., Kittel, T. G. F., Nemani, R. R., and Running, S. W. (2000). Simulated impacts of historical land cover changes on global climate in northern winter. *Climate Dynamics*, 16, 93–10.

Chuvieco, E., Opazo, S., Sione, W., Valle, H., Anaya, J., Bella, C., Cruz, I., Manzo, L., Lopez, G., Mari, N., Gonzalez-Alonso, F., Morelli, F., Setzer, A., Csiszar, I., Kanpandegi, J. A., Bastarrika, A., and Libonati, R. (2008). Global Burned Land Estimation in Latin America using MODIS Composite Data. *Ecological Applications*, 18, 64-79.

Chuvieco, E., Ventura, G., Martín, M. P., and Gómez, I. (2005). Assessment of multitemporal compositing techniques of MODIS and AVHRR images for burned land mapping. *Remote Sensing of Environment*, 94, 450-462.

Cohen, W. B., Spies, T. A., and Fiorella, M. (1995). Estimating the age and structure of forests in a multi-ownership landscape of western Oregon, U.S.A. *International Journal of Remote Sensing*, 16, 721-746.

Cox, C., and Munk, W. (1954). Measurements of the roughness of the sea surface from photographs of the Sun's glitter. *Journal of Optical Society of America*, 44, 838–850.

Crist, E. P. and Cicone, R. C. (1984). A physically-based transformation of Thematic Mapper data -- the TM Tasseled Cap. *IEEE Transactions on Geoscience and Remote Sensing*, 22, 256-263.

Crutzen, P. J., and Andreae, M. O. (1990). Biomass burning in the tropics: Impact on atmospheric chemistry and biogeochemical cycles. *Science*, 250, 1669–1678.

Di Maio-Mantovani, A., and Setzer, A. W. (1996). A change detection methodology for the amazon forest using multitemporal NOAA/AVHRR data and GIS: preliminary results. *ASTM publication*, 1279, 43-46.

Di Maio-Mantovani, A., and Setzer, A. W. (1996). Deforestation detection in the Amazon with an AVHRR-based system. *International Journal of Remote Sensing*, 18, 273-286.

Eck, T. F., Holben, B. N., Slutsker, I., and Setzer, A. W. (1998). Measurements of irradiance attenuation 30 and estimation of aerosol single scattering albedo for biomass burning aerosols in Amazonia. *Journal of Geophysical Research*, 103, 31865–31878.

Esaias, W., Abbott, M., Barton, I., Brown, O., Campbell, J., Carder, K., Clark, D., Evans, R., Hoge, F., Gordon, H., Balch, W., Letelier, R., and Minnett, P. (1998). An overview of MODIS capabilities for ocean science observations. *IEEE Transactions on Geoscience and Remote Sensing*, 36, 1250–1265.

Eva, H., and Lambin, E. F. (1998). Burnt area mapping in Central Africa using ATSR data. *International Journal of Remote Sensing*, 19, 3473–3497.

Evangelista, H., Maldonado, J., Godoi, R. H. M., Pereira, E. B., Koch, D., Tanizaki-Fonseca, K., Van Grieken, R., Sampaio, M., Setzer, A., Alencar, A., and Gonçalves, S. C. (2007). Sources and transport of urban and biomass burning aerosol black carbon at the South-west atlantic coast. *Journal of Atmospheric Chemistry*, 56, 225–238.

Fillion, L., and Mahfouf, J.-F. (2000). Coupling of moist-convective and stratiform precipitation processes for variational data assimilation. *Monthly Weather Review*, 128, 109-124.

Florinsky, I. V., Kulagina, T. B., and Meshalkina, J. L. (1994). Influence of topography on landscape radiation temperature distribution. *International Journal of Remote Sensing*, 15, 3147–3153.

França, H., and Setzer, A. W. (1998). AVHRR temporal analysis of a savanna site in Brazil. *International Journal of Remote Sensing*, 19, 3127–3140

França, H., and Setzer, A. W. (2001). AVHRR analysis of savanna site through a fire season in Brazil. *International Journal of Remote Sensing*, 22, 2449–2461.

Fraser, R. H., Li, Z., and Cihlar, J. (2000). Hotspot and NDVI differencing synergy (HANDS): A new technique for burned area mapping over boreal forest. *Remote Sensing of Environment*, 74, 362–376.

Fraser, R. S., and Kaufman, Y. J. (1985). The relative importance of scattering and absorption in remote sensing. *IEEE Transactions on Geoscience and Remote Sensing*, 23: 625-633.

Frederiksen P., Langaas, S., and Mbaye, M. (1990). NOAA-AVHRR and GISbased monitoring of fire activity in Senegal — A provisional methodology and potential applications. Fire in the Tropical Biota. *Ecological Studies*, 84, 400–417.

Gates, D.M., Keegan, H. J., Schleiter, J. C., and Weidner, V. R. (1965). Spectral properties of plants. *Applied Optics*, 4, 11–20.

Gedney, N., and Valdes, P. J. (2000). The effect of Amazonian deforestation on the northern hemisphere circulation and climate. *Geophysical Research Letters*, 27, 3053-3056.

Gesell, G. (1989). An algorithm for snow and ice detection using AVHRR data: An extension to the APOLLO software package. *International Journal of Remote Sensing*, 10, 897–905.

Gillespie, A. R., Rokugawa, S., Hook, S. J., Matsunaga, T., and Kahle, A. B. (1999). Temperature/emissivity separation algorithm theoretical basis document. Version 2.4. Prepared under NASA Contract NAS5-31372.

Goita, K., and Royer, A. (1997). Surface temperature and emissivity separability over land surface from combined TIR and SWIR AVHRR data. *IEEE Transactions on Geoscience and Remote Sensing*, 35, 718–733.

Goita, K., Royer, A., and Bussiere, N. (1997). Characterization of land surface thermal structure from NOAA-AVHRR data over a Northern ecosystem. *Remote Sensing of Environment*, 60, 282–298.

Goody, R. M. (1964). Atmospheric radiation: Theoretical basis. Oxford: Clarendon Press.

Gregoire, J. -M., Tansey, K., and Silva, J. M. N. (2003). The GBA2000 initiative: Developing a global burned area database from SPOTVEGETATION imagery. *International Journal of Remote Sensing*, 24, 1369–1376.

Holben, B. N., Eck, T. F., Slutsker, I., Tanre, D., Buis, J. P., Setzer, A., Vermote, E., Reagan, J. A., Kaufman, Y., Nakajima, T., Lavenue, F., Jankowiak, I., and Smirnov, A. (1998). AERONET – A federated instrument network and data archive for aerosol characterization, *Remote Sensing of Environment*, 66(1), 1–16.

Holben, B. N., Kimes, D., and Fraser, R.S. (1986). Directional reflectance response in AVHRR red and near-IR bands for three cover types and varying atmospheric conditions. *Remote Sensing of Environment*, 19, 213-236.

Holben, B. N., and Shimabukuro, Y. E. (1993). Linear mixture model applied to coarse spatial resolution data from multispectral satellite sensors. *International Journal of Remote Sensing*, 14, 2231–2240.

Houghton, R. A. (2000). Interannual variability in the global carbon cycle. *Journal of Geophysical Research*, 105, 20121-20130.

Houghton, R. A., Skole, D. L., Nobre, C. A., Hackler, J. L., Lawrence, K. T., and Chomentowski, W. H. (2000). Annual fluxes of carbon from deforestation and regrowth in the Brazilian Amazon. *Nature*, 403, 301-304.

Huete, A. R. (1988). A soil-adjusted vegetation index (SAVI). *Remote Sensing of Environment*, 25, 53-70.

Jiang, G. -M., and Li, Z.-L- (2008). Intercomparison of Two BRDF Models in the Estimation of the Directional Emissivity in MIR Channel From MSG1-SEVIRI Data. *Optics Express*, 16(23), 19310-19321.

Jiang, G. -M., Li, Z. -L., and Nerry, F. (2006). Land surface emissivity retrieval from combined mid-infrared and thermal infrared data of MSG-SEVIRI. *Remote Sensing of Environment*, 105, 326– 340.

Jiménez-Muñoz, J. C., and Sobrino, J. A. (2006). Error sources on the land surface temperature retrieval from thermal infrared single channel remote sensing data. *International Journal of Remote Sensing*, 27, 999-1014.

Jin, Y., and Roy, D. P. (2005). Fire-induced albedo change and its radiative forcing at the surface in northern Australia. *Geophysical Research Letters*, 32, L13401.

Justice, C., Vermote, E., Townshend, J., Defries, R., Roy, D., Hall, D., Salomonson, V., Privette, J., Riggs, G., Strahler, A., Lucht, W., Myneni, R., Lewis, P., and Barnsley, M. (1998). The Moderate Resolution Imaging Spectroradiometer (MODIS): land remote sensing for global change research. *IEEE Transactions on Geoscience and Remote Sensing*, 36, 1228–1249.

Kasischke, E. S., and French, N. H. F. (1995). Locating and estimating the areal extent of wildfires in Alaskan boreal forests using multiple-season AVHRR NDVI composite data. *Remote Sensing of Environment*, 51, 263–275.

Kasischke E. S., French, N. H. F., Harrel, P., Christensen, N. L. , Ustin, S. L., and Barry, D. (1993). Monitoring wildfires in boreal forests using large area AVHRR NDVI composite image data. *Remote Sensing of Environment*, 45, 61–71.

Kaufman, Y. J. (1995). Remote sensing of direct and indirect aerosol forcing. In R. J. Charlson, and J. Heintzenberg (Eds.), *Aerosol forcing of climate* (pp. 298–332). London: Wiley.

Kaufman, Y. J., and Remer, L. (1994). Detection of forests using mid-IR reflectance: An application for aerosol studies. *IEEE Transactions on Geoscience and Remote Sensing*, 32(3), 672–683.

Kauth, R. J., and Thomas, G. S. (1976). The tasseled cap --a graphic description of the spectral-temporal development of agricultural crops as seen in Landsat. In *Proceedings on the Symposium on Machine Processing of Remotely Sensed Data*.

Kerber, A. G., and Schutt, J. B. (1986). Utility of AVHRR channels 3 and 4 in land-cover mapping. *Photogrammetric Engineering and Remote Sensing*, 52, 1877–1883.

King, M., Menzel, M., Kaufman, Y., Tanre, D., Gao, B., Platnick, S., Ackerman, S., Remer, L., Pincus, R., and Hubanks, P. (1998). Cloud and aerosol properties, precipitable water, and profiles of temperature and water vapor from MODIS. *IEEE Transactions on Geoscience and Remote Sensing*, 41, 442–458.

Koren, I., Kaufman, Y. J., Remer, L. A., and Martins, J. V. (2004). Measurement of the effect of Amazon smoke on inhibition of cloud formation. *Science*, 303, 1342–1345.

Lambin, E. F., and Geist, J. (2006). Land-use and land-cover change — Local processes and global impacts. Series: Global Change — The IGBP Series.

Lean, A. (1991). Variations in the sun's radiative output. *Reviews of Geophysics*, 29, 505–535.

Levine, J. S., Cofer, W. R., III, Cahoon, D. R., Jr., and Winstead, E. L. (1995). Biomass burning: a driver for global change. *Environmental Science and Technology*, 29, 120-125.

Li, Z.-L., and Becker, F. (1993). Feasibility of land surface temperature and emissivity determination from NOAA/AVHRR data. *Remote Sensing of Environment*, 43, 1–20.

Liang, S. (2004). *Quantitative Remote Sensing of Land Surfaces*. John Wiley and Sons, Inc.

Libonati, R., DaCamara, C.C., Pereira, J.M.C., and Peres, L.F. (2010). Retrieving middle-infrared reflectance for burned area mapping in tropical environments using MODIS. *Remote Sensing of Environment*, 114, 831–843.

Libonati, R., DaCamara, C. C., Pereira, J. M. C., Setzer, A. W., and Morelli, F. (2007). A new optimal index for burnt area discrimination in satellite imagery. In the Proceedings of the 2007 EUMETSAT Meteorological Satellite Conference and the 15th Satellite Meteorology & Oceanography Conference of the American Meteorological Society.

Libonati, R., Morelli, F., Setzer, A. W., DaCamara, C. C., and Pereira, J. M. C. (2006). Assinatura espectral de áreas queimadas em produtos MODIS. In the Proceedings of the XIV Congresso Brasileiro de Meteorologia.

Lillesand, T. M., and Kiefer, R. W. (1994). *Remote Sensing and Photo Interpretation*. New York: John Wiley and Sons.

Liou, K. N. (1980). *An introduction to atmospheric radiation*. London: Academic Press.

Loboda T., O'Neal, K.J., and Csiszar, I. (2007). Regionally adaptable dNBR-based algorithm for burned area mapping from MODIS data. *Remote Sensing of Environment*, 109, 429–442.

Lopez, M. J., and Caselles, V. (1991) Mapping burns and natural reforestation using thematic mapper data. *Geocarto Int.*, 1, 31–37.

Lucas R. M., Curran, P. J., Honzak, M., Foody, G. M., Milne, R., Brown, T., and Amaral, S. (2000). Mapping the regional extent of tropical forest regeneration stages in the Brazilian Legal Amazon using NOAA AVHRR data. *International Journal of Remote Sensing*, 21, 2855-2881.

Lucht, W., Schaaf, C. B., and Strahler, A. H. (2000). An algorithm for the retrieval of albedo from space using semiempirical BRDF model. *IEEE Transactions on Geoscience and Remote Sensing*, 38, 977–998.

Luvall, J. C., and Holbo, H. R. (1991). Thermal remote sensing methods in landscape ecology. In *Quantitative Methods in Landscape Ecology*, J. C. Luvall, New York: Springer-Verlag, Ecological Studies 82, pp. 127–152.

Luvall, J. C., Lieberman, D., Lieberman, M., Hartshorn, G. S., and Peralta, R. (1990). Estimation of tropical forest canopy temperature, thermal response number, and evapotranspiration using an aircraft-based thermal sensor. *Photogrammetric Engineering and Remote Sensing*, 56, 1393–1401.

Malingreau J. P. (1990). The contribution of remote sensing to the global monitoring of fires in tropical and subtropical ecosystems. In *Fire in the Tropical Biota, Ecosystem Processes and Global Challenges*, J. G. Goldammer, Germany: Springer-Verlag, Ecological Studies 84, pp. 333–370.

Martín, M. P. (1998). Cartografía e inventario de incendios forestales en la Península Ibérica a partir de imágenes NOAA–AVHRR. Departamento de Geografía, Universidad de Alcalá.

Martín, M. P., and Chuvieco, E. (1993). Mapping and evaluation of burned land from multitemporal analysis of AVHRR NDVI images. In Proc. Int. Workshop Satellite Technol. GIS Mediterranean Forest Mapping Fire Manage.

Martín, M. P., and Chuvieco, E. (1995). Mapping and evaluation of burned land from multitemporal analysis of AVHRR NDVI images. *EARSel Advances in Remote Sensing*, 4(3), 7–13.

Martín, M. P., Gomez, I., and Chuvieco, E. (2006). Burnt Area Index (BAIM) for burned area discrimination at regional scale using MODIS data. *Forest Ecology and Management*, 234S, S221.

Menon, S., Hansen, J., Nazarenko, L., and Luo, Y. (2002). Climate effects of black carbon in China and India. *Science*, 297, 2250–2253.

MODIS Characterization Support Team – MCST (2006). MODIS Level 1B Product User's Guide. NASA/Goddard Space Flight Center. (available at <http://www.mcst.ssa.gov/mcstweb/documents/M1054.pdf>)

Nemani, R., Pierce, L., Running, S., and Goward, S. (1993). Developing satellite-derived estimates of surface moisture status. *Journal of Applied Meteorology*, 32, 548–557.

Nerry, F., Petitcolin, F., and Stoll, M.-P. (1998). Bidirectional reflectivity in AVHRR channel 3: application to a region in northern Africa. *Remote Sensing of Environment*, 66, 298–316.

Nichol, J. E. (1995). Monitoring tropical rain forest microclimate. *Photogrammetric Engineering and Remote Sensing*, 61, 1159–1165.

Nobre, C. A., Mattos, L. F., Dereczynski, C. P., Tarasova, T. A., and Trosnikov, I. V. (1998). Overview of atmospheric conditions during the Smoke, Clouds, and Radiation-Brazil (SCAR-B) field experiment. *Journal of Geophysical Research*, 103, 31809–31820.

Nobre, C. A., Sellers, P. J., and Shukla, J. (1991). Amazonian deforestation and regional climate change. *Journal of Climate*, 4(10), 957.

O'Brien, K. L. (1996). Tropical deforestation and climate change. *Progress in Physical Geography*, 20(3), 311-332.

Penner, J. E., Dickinson, R. E., and O'Neill, C. A. (1992). Effects of aerosol from biomass burning on the global radiation budget. *Science*, 256, 1432–1433.

Pereira, J. M. C. (1999). A comparative evaluation of NOAA/AVHRR vegetation indexes for burned surface detection and mapping. *IEEE Transactions on Geoscience and Remote Sensing*, 37(1), 217-226.

Pereira, J. M. C. (2003). Remote sensing of burned areas in tropical savannas. *International Journal of Wildland Fire*, 12, 259–270.

Pereira, J. M. C., Cadete, L. and Vasconcelos, M.J.P. (1994). An assessment of the potential of NOAA/AVHRR HRPT imagery for burned area mapping in Portugal. In Proceedings of 2nd International Conference on Forest Fire Research.

Pereira, J. M. C., Chuvieco, E., Beaudoin, A., and Desbois, N. (1997). Remote sensing of burned areas: a review. In: Chuvieco, E.; Ed. A review of remote sensing methods for the study of large wildland fires. Alcalá de Henares, 127-183.

Pereira J. M. C., and Setzer, A. W. (1993). Spectral characteristics of fire scars in Landsat-5 TM images of Amazonia. *International Journal of Remote Sensing*, 14, 2061–2078.

Peres, L. F., and DaCamara, C. C. (2004). LST and emissivity estimation based on the two-temperature method: sensitivity analysis using simulated MSG/SEVIRI data. *Remote Sensing of Environment*, 91, 377-389.

Peres, L. F., and DaCamara, C. C. (2005). Emissivity Maps to Retrieve Land-Surface Temperature from MSG/SEVIRI. *IEEE Transactions on Geoscience and Remote Sensing*, 43, 1834-1844.

Peres, L. F., and DaCamara, C. C. (2006). Improving Two-temperature method retrievals based on a nonlinear optimization approach. *IEEE Geoscience and Remote Sensing Letters*, 3(2), 232-236.

Petitcolin, F., Nerry, F., and Stoll, M.-P. (2002). Mapping temperature independent spectral indice of emissivity and directional emissivity in AVHRR channels 4 and 5. *International Journal of Remote Sensing*, 23, 3473–3492.

Petitcolin F., and Vermote E. F. (2002). Land Surface Reflectance, Emisivity and Temperature from MODIS Middle and Thermal Infrared data. *Remote Sensing of Environment*, 83(1-2), 112-134.

Pielke, R. A., Marland, G., Betts, R. A., Chase, T. N., Eastman, J. L., Niles, J. O., Niyogi, D. D. S., and Running, S.W. (2002). The influence of land-use change and landscape dynamics on the climate system — Relevance to climate change policy beyond the radiative effect of

greenhouse gases. *Philosophical Transactions of the Royal Society of London*, 360, 1705–1719.

Pinty, B., and Verstraete, M. M. (1992). GEMI A nonlinear index to monitor global vegetation from satellites. *Vegetatio*, 101, 15-20.

Prata, A. J., Caselles, V., Coll, C., Sobrino, J. A., and Otle, C. (1995). Thermal remote sensing of LST from satellites: Current status and future prospects. *Remote Sensing Reviews*, 12, 175–224.

Price, J. C. (1989). Quantitative aspects of remote sensing in the thermal infrared. In *Theory and Applications of Optical Remote Sensing*, G. Asrar, New York: John Wiley and Sons, pp. 578–603.

Prins, E. M., Feltz, J. M., Menzel, W. P., and Ward, D. E. (1998). An overview of GOES-8 diurnal fire and smoke results for SCAR-B and 1995 fire season in South America. *Journal of Geophysical Research*, 103, 31 821–31 835.

Procopio, A. S., Artaxo, P., Kaufman, Y. J., Remer, L. A., Schafer, J. S., and Holben, B. N. (2004). Multiyear analysis of amazonian biomass burning smoke radiative forcing of climate, *Geophysical Research Letters*, 31, L03108.

Razafimpanilo, H., Frouin, R., Iacobellis, S.F., and Somerville, R. C. J. (1995). Methodology for estimating burned area from AVHRR reflectance data. *Remote Sensing of Environment*, 54, 273–289.

Reinhardt, T. E., Ottmar, R. D., and Castilla, C. (2001). Smoke impacts from agricultural burning in rural Brazilian Town. *Journal of the Air and Waste Management*, 51, 443–450.

Richardson, A. J., and Wiegand, C. L. (1977). Distinguishing vegetation from soil background information. *Photogramm. Eng. Remote Sens.*, 43, 1541-1552.

Robinson, J.M. (1991). Problems in global fire evaluation: is remote sensing the solution? *Global Biomass Burning: Atmospheric, Climatic, and Biospheric Implications*, J.S. Levine, Cambridge: MIT Press, pp. 67-73.

Rodgers, C. D. (2000). *Inverse Methods for Atmospheric Sounding: Theory and Practice*. Singapore: World Scientific, vol. 2, Series on Atmospheric, Oceanic and Planetary Physics, pp. 1–11.

Roger, J. C., and Vermote, E. F. (1998). A method to retrieve the reflectivity signature at 3.75 mm from AVHRR data. *Remote Sensing of Environment*, 64, 103–114.

Rondeaux, G., Steven, M., and Baret, F. (1996). Optimization of soil-adjusted vegetation indices. *Remote Sensing of Environment*, 55, 95–107.

Rosenfeld, D. (1999). TRMM observed first direct evidence of smoke from forest fires inhibiting rainfall. *Geophysical Research Letters*, 26, 3105–3108.

Rouse, J. W., Haas, R. H., Schell, J. A., and Deering, D. W. (1973). Monitoring vegetation systems in the Great Plains with ERTS. Third ERTS Symposium, NASA SP-351 I.

Roy, D. P., Giglio, L., Kendall, J. D., and Justice, C. O. (1999). Multi-temporal active-fire based burn scar detection algorithm. *International Journal of Remote Sensing*, 20, 1031–1038.

Roy, D.P., Lewis, P.E., and Justice, C.O. (2002). Burned area mapping using multi-temporal moderate spatial resolution data—a bi-directional reflectance model-based expectation approach. *Remote Sensing of Environment*, 83, 263–286.

Ruff, I., and Gruber, A. (1983). Multispectral identification of clouds and earth surfaces using AVHRR data. In *Proceedings of the 5th Conference on Atmospheric Radiation*.

Salisbury, J. W., and D'Aria, D. M. (1994). Emissivity of terrestrial materials in the 3-5 μm atmospheric window. *Remote Sensing of Environment*, 47, 345-361.

Salomonson, V., Barnes, W., Xiong, X., Kempler, S., and Masuoka, E. (2002). An overview of the Earth Observing System MODIS instrument and associated data systems performance. In *Proceedings of IGARSS 2002*.

Schafer, J. S., Eck, T. F., Holben, B. N., Artaxo P., Yamasoe, M. A., and Procopio, A. S. (2002). Observed reductions of total solar irradiance by bio-mass burning aerosols in the Brazilian Amazon and Zambian Savanna. *Geophysical Research Letters*, 29(17), 1823.

Scholes, R. J. (1995). Greenhouse gas emissions from vegetation fires in Southern Africa. *Environmental Monitoring and Assessment*, 38, 169-179.

Schutt, J. B., and Holben, B. N. (1991), Estimation of emittances and surface temperatures from AVHRR data. In *Proceedings IGARSS 91*.

Seemann, S. W., Borbas, E., Li, J., Menzel, W. P., and Gumley, L. M. (2006). MODIS atmospheric profile retrieval algorithm theoretical basis document. University of Wisconsin-Madison, Madison, (available at http://modis-atmos.gsfc.nasa.gov/_docs/MOD07:MYD07_ATBD_C005.pdf)

Sellers, P. J., Bounoua, L., Collatz, G. J., Randall, D. A., Dazlich, D. A., Los, S. O., Berry, J. A., Fung, I., Tucker, C. J., Field, C. B., and Jensen, T. G. (1996). Comparison of radiative and physiological effects of doubled atmospheric CO₂ on climate. *Science*, 271, 1402–1406.

Sellers, P. J., Hall, F. G., Margolls, H., Kelly, B., Baldocchi, D., den Hartog, J., Cihlar, J., Ryan, M., Goodison, B., Crill, P., Ranson, J., Lettermaier, D., and Wickland, D. E. (1995). The Boreal Ecosystem – Atmosphere Study (BOREAS): an overview and early results from 1994 field year. *Bulletin of the American Meteorological Society*, 76, 1549-1577.

Shimabukuro, Y. E., Holben, B. N., and Tucker, C. J. (1994). Fraction images derived from NOAA AVHRR data for studying the deforestation in the Brazilian Amazon. *International Journal of Remote Sensing*, 15, 517–520.

Slaton, M. R., Hunt Jr., E. R., and William, K. S. (2001). Estimating near-infrared leaf reflectance from leaf structural characteristics. *American Journal of Botany*. 88, 278-284.

Stocks, B. J., Cahoon, D. R., Cofer III, J. R., and Levine, J. S. (1996). Monitoring large-scale forest-fire behavior in northeastern Siberia using NOAA-AVHRR satellite imagery. *Biomass Burning and Global Change*, 2, 802– 807.

Strahler, A. H., Muller, J.-P., Lucht, C. B., Tsang, T., Gao, F., Li, X., Lewis, P., and Barnsley, M. J. (1999). MODIS BRDF/Albedo product: Algorithm theoretical basis document, version 5.0, MODIS documentation.

Stroppiana, D., Pinnock, S., Pereira, J. M. C., and Gregoire, J. M. (2002). Radiometric analysis of SPOT-VEGETATION images for burnt area detection in Northern Australia. *Remote Sensing of Environment*, 82, 21–37.

Tjemkes, S.A., and Schmetz J. (1998). Radiative Transfer Simulations for the Thermal Channels of METEOSAT Second Generation. EUMETSAT Technical Memorandum No. 1

Tobin, D. C., Revercomb, H. E., Knuteson, R. O., Lesht, B. M., Strow, L. L., Hannon, S. E., Feltz, W. F., Moy, L. A., Fetzer, E. J., and Cress, T. S. (2006). Atmospheric Radiation Measurement site atmospheric state best estimates for Atmospheric Infrared Sounder temperature and water vapor retrieval validation. *Journal of Geophysical Research*, 111, D09S14.

Trigg, S., and Flasse, S. (2000). Characterising the spectral-temporal response of burned savannah using in situ spectroradiometry and infrared thermometry. *International Journal of Remote Sensing*, 21, 3161–3168.

Trigg, S., and Flasse, S. (2001). An evaluation of different bi-spectral spaces for discriminating burned shrub-savannah. *International Journal of Remote Sensing*, 22, 2641–2647.

Verstraete M. M., and Pinty, B. (1996). Designing optimal spectral indexes for remote sensing applications. *IEEE Transactions on Geoscience and Remote Sensing*, 34(5), 1254–1265.

Wan, Z. (1999). MODIS land-surface temperature algorithm theoretical basis document (LST ATBD): version 3.3. University of California, Santa Barbara, (available at <http://www.icesb.ucsb.edu/modis/atbd-mod-11.pdf>).

Wan, Z., and Dozier, J. (1996). A generalized split-window algorithm for retrieving land-surface temperature from space. *IEEE Transactions on Geoscience and Remote Sensing*, 34, 892-905.

Wan, Z., and Li, Z.-L. (1997). A physical-based algorithm for land-surface emissivity and temperature from EOS/MODIS data. *IEEE Transactions on Geoscience and Remote Sensing*, 35, 980-996.

Wong, Y. K. (1993). The forests and tree populations. Report of the Nature Reserves Survey, Phase 1, Singapore National Parks Board.

Xue, Y. (1996). The impact of desertification in the Mongolian and the Inner Mongolian Grassland on the regional climate. *Journal of Climate*, 9, 2173-2189.

Zhan, X., Sohlberg, R. A., Townshend, J. R. G., Dimiceli, C., Carrol, M. L., Eastman, J. C., Hansen, M. C., and Defries, R. S. (2002). Detection of land cover changes using MODIS 250m data. *Remote Sensing of Environment*, 83, 336-350.

Zhao, M., Pitman, A., and Chase, T. N. (2001). The impacts of land cover change on the atmospheric circulation. *Climate Dynamics*, 17, 467–477.

Annex

Papers in Refereed Journals



Retrieving middle-infrared reflectance for burned area mapping in tropical environments using MODIS

Renata Libonati^{a,c,*}, Carlos C. DaCamara^a, José Miguel C. Pereira^b, Leonardo F. Peres^c

^a University of Lisbon, IDL/CGUL, Lisbon, Portugal

^b School of Agronomy, Technical University of Lisbon, Lisbon, Portugal

^c Center for Weather Forecast and Climate Studies, Brazilian National Institute for Space Research, Cachoeira Paulista, Brazil

ARTICLE INFO

Article history:

Received 10 July 2009

Received in revised form 23 November 2009

Accepted 28 November 2009

Keywords:

Reflectance retrieval

Middle-infrared

Tropics

Burned area

Remote sensing

ABSTRACT

The ephemeral character of the radiative signal together with the presence of aerosols imposes severe limitations on the use of classical approaches, e.g. based on red and near-infrared, to discriminate between burned and unburned surfaces in tropical environments. Surface reflectance in the middle-infrared (MIR) has been used to circumvent these difficulties because the signal is virtually unaffected by the presence of aerosols associated to biomass burning. Retrieval of the MIR reflected component from the total signal is, however, a difficult problem because of the presence of a diversity of radiance sources, namely the surface reflected solar irradiance and the surface emitted radiance that may reach comparable magnitude during daytime. The method proposed by Kaufman and Remer (1994) to retrieve surface MIR reflectance presents the advantage of not requiring auxiliary datasets (e.g. atmospheric profiles) nor major computational means (e.g. for solving radiative transfer models). Nevertheless, the method was specifically designed to retrieve MIR reflectance over dense dark forests in the middle latitudes and, as shown in the present study, severe problems may arise when applying it beyond the range of validity, namely for burned area mapping in tropical environments. The present study consists of an assessment of the performance of the method for a wide range of atmospheric, geometric and surface conditions and of the usefulness of extracted surface reflectances for burned area discrimination. Results show that, in the case of tropical environments, there is a significant decrease in performance of the method for high values of land surface temperature, especially when associated with low sun elevation angles. Burned area discrimination is virtually impaired in such conditions, which are often present when using data from instruments on-board polar orbiters, namely MODIS in Aqua and Terra, to map burned surfaces over the Amazon forest and “cerrado” savanna regions.

© 2009 Elsevier Inc. All rights reserved.

1. Introduction

Over the last decade continuous monitoring of vegetation fires from space has greatly contributed to an increased recognition of the major role played by biomass burning in climate change. In fact, biomass burning is a global source of greenhouse gases (e.g. CO₂ and CH₄) as well as of CO, NO₂, NO_x, CH₃Br and hydrocarbons involved in the formation of acid rain, in the photochemical production of tropospheric ozone and in the destruction of stratospheric ozone (e.g. Crutzen & Andreae, 1990; Penner et al., 1992). At the regional level, biomass burning may induce changes in atmospheric stability and associated vertical motions, leading to alterations of the hydrologic cycle with significant impacts on regional climate (e.g. Rosenfeld, 1999; Menon et al., 2002; Koren et al., 2004). Teleconnection processes may also take place, inducing changes e.g. of rainfall and surface temperature patterns across distant parts of the world (Chase

et al., 2000; Zhao et al., 2001; Pielke et al., 2002). In particular, the study by Evangelista et al. (2007) suggests that almost half of the aerosol black carbon in the South-West Atlantic may derive from South American biomass burning. In addition, vegetation fires are one of the most important causes of land use/cover dynamics (Lambin & Geist, 2006), destroying and altering vegetation structure and depositing charcoal and ash on the surface. Such changes may, in turn, lead to modifications in the physical properties of the surface such as the ratio of latent to sensible heat flux, the transfer of momentum from the atmosphere and the flux of moisture through evaporation and transpiration (Sellers et al., 1996; Jin & Roy, 2005).

Accordingly, a considerable number of environmental studies and Earth resources management activities require an accurate identification of burned areas. However, due to the very broad spatial extent and the limited accessibility of some of the largest areas affected by fire, instruments on-board satellites are currently the only available operational systems capable to collect cost-effective burned area information at adequate spatial and temporal resolutions (Pereira, 1999). This is especially true in the tropics, where most burning take place every year (Le Page et al., 2007). For instance, the Amazon

* Corresponding author. University of Lisbon, IDL/CGUL, Lisbon, Portugal.
E-mail address: rlsantos@fc.ul.pt (R. Libonati).

region together with the adjacent savanna (“cerrado”) presents one of the highest numbers of occurrences of fire events (Prins et al., 1998).

Over the Amazon region the traditional use of red (R) and near-infrared (NIR) channels for detecting burned areas is severely impaired by the presence of heavy smoke layers due to biomass burning, since both channels are very sensitive to aerosol scattering and absorption in the atmosphere (Fraser & Kaufman, 1985; Holben et al., 1992; França & Setzer, 1998). A possible way to mitigate the aerosol effects associated to biomass burning on Earth observation from space is by using the middle-infrared (MIR) region (between 3.5 and 4.1 μm), since this part of the spectrum is also sensitive to vegetation changes but is virtually unaffected by the presence of most aerosols. However, Boyd and Duane (2001) pointed out that the use of MIR for studying the Earth’s surface properties at and beyond the regional scale may be unreliable. They further suggest that, in the case of tropical forests at regional to global scales, it may be preferable to only rely on the reflected component of MIR, since the emitted component of the signal may be subject to additional confounding variables, rather than representing intrinsic surface properties (Kaufman & Remer, 1994). Though related to tropical forest canopy properties, emitted radiation may also be influenced by a wide range of factors that include; i) localized atmospheric conditions such as wind speed and water vapor conductance (Price, 1989), ii) site-specific factors such as topography (Florinsky et al., 1994) and iii) soil moisture conditions (Luvall & Holbo, 1991; Nemani et al., 1993).

A large number of studies have shown that use of MIR reflectance is promising for a variety of applications such as discriminating among different vegetation types (Holben & Shimabukuro, 1993; Shimabukuro et al., 1994; Goita & Royer, 1997); estimating the total biomass and leaf biomass of several forest ecosystems (Boyd, 1999; Boyd et al., 2000); and monitoring the intra- and inter-annual changes in vegetation induced by climatic factors (Boyd & Duane, 2001). In particular, the work of Pereira (1999) showed that spectral vegetation indices using the R and NIR allow for improved burned/unburned area discrimination when the R channel is replaced by the reflected component of the MIR channel. Although use of the reflected component of MIR appears very attractive, its retrieval poses several challenging problems due to the presence, in a single measurement, of a diversity of radiance sources, namely linked to the thermal emission and the solar reflection from the atmosphere and by the surface. For instance, during daytime, the MIR surface reflected solar irradiance and the surface emitted radiance in MIR have comparable magnitude (Li & Becker, 1993).

Several methods have been proposed to solve the difficult problem of retrieving MIR reflectance from the total signal measured by a remote sensing instrument (e.g. Schutt & Holben, 1991; Li & Becker, 1993; Goita & Royer, 1997; Nerry et al., 1998; Roger & Vermote, 1998; Petitcolin & Vermote, 2002). All mentioned methods allow for the retrieval of MIR reflectance with acceptable accuracy, but most are time consuming, and normally require auxiliary datasets (e.g. atmospheric profiles) as well as intensive computational means (e.g. for solving radiative transfer computations). Kaufman and Remer (1994) proposed a different approach for retrieving MIR reflectance without direct knowledge of the atmospheric state and with no need for a radiative transfer model. Their method was originally designed to identify dense, dark vegetation areas in mid-latitude environments and the authors specifically stressed the need for further studies under different atmospheric conditions, as well as for other types of surface. The method has been applied in a number of studies involving both temperate and tropical conditions (e.g. Holben & Shimabukuro, 1993; Boyd, 1999; Boyd & Duane, 2001; Cihlar et al., 2004).

In particular, the approach proposed by Kaufman and Remer (1994), hereafter referred to as KR94, has been applied for burned area discrimination, since the MIR spectral domain may contribute to solving certain ambiguities between burned and unburned surfaces. These occur, for example, when using information from other parts of

the electromagnetic spectrum, namely the short-wave infrared (SWIR), especially between 2.0 and 2.5 μm (França & Setzer, 2001). As shown in Fig. (1), the increase in reflectance over burned surfaces is higher in MIR than in SWIR, allowing a better discrimination between both surfaces. For instance, Pereira (1999) showed the added value of the method developed by KR94 in a pioneering study aiming to assess the ability of various vegetation indices to discriminate between burned and unburned surfaces in Portugal. The same methodology was used by Barbosa et al. (1999) and by Roy et al. (1999) to extract the reflective part of Advanced Very High Resolution Radiometer (AVHRR) channel 3, for input to algorithms aiming to map burned areas in Africa.

Results from the above-mentioned studies are certainly relevant, useful and promising; nevertheless, to the best of our knowledge, no assessment has discussed in depth the accuracy of the methodology proposed by KR94 when used to discriminate burned areas in tropical environments. Approximate solutions, like that proposed by KR94, are fast and easy to implement, but may be insufficiently accurate under specific surface and atmospheric conditions. The aim of the present study is to assess the quality and limitations of the retrieved MIR reflectance by means of KR94’s method when applied to discriminate burned areas in tropical environments.

Accordingly, the main objectives of the analysis are twofold:

1. To perform a quality assessment of MIR reflectance when retrieved using the algorithm proposed by KR94, for a wide range of atmospheric, geometric and surface conditions;
2. To assess the adequacy and limitations of the above-mentioned algorithm when applied to burned area discrimination, in particular in the Amazon and “cerrado” regions. Special attention will be devoted to the Moderate Resolution Imaging Spectrometer (MODIS) sensor, because of its widespread use in operational applications at the Brazilian National Institute for Space Research (INPE).

2. Rationale

One of the major difficulties encountered in the tropics when discriminating burned areas relates to the ephemeral character of

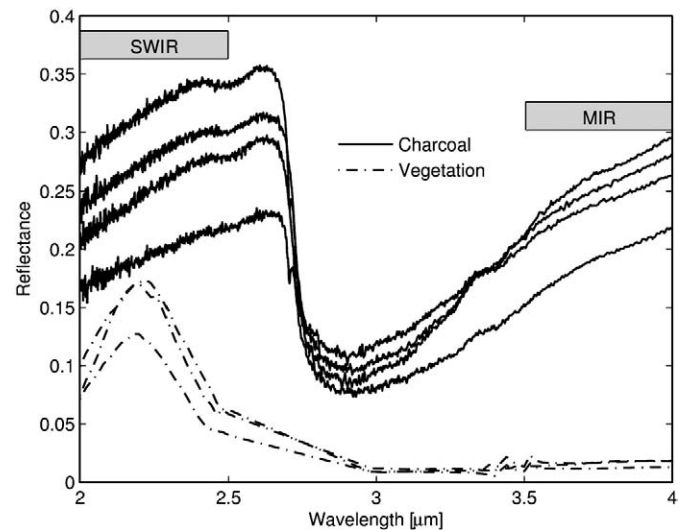


Fig. 1. Spectral signatures of four charcoal samples (solid curves) and of three vegetation samples (dot-dashed curves). Gray boxes delimit the SWIR (between 2.0 and 2.5 μm) and MIR (between 3.5 and 4 μm) spectral regions in order to emphasize their contrast. Charcoal and vegetation signatures were respectively obtained from samples of fire residues from Alta Floresta, state of Mato Grosso, Brazil and from the Advanced Spaceborne Thermal Emission and Reflection Radiometer (ASTER) spectral library (Baldrige et al., 2009).

spectral signatures, in contrast with temperate and boreal regions, where one may wait until the end of the fire season to map scars from previous months (Pereira, 2003). This procedure is not feasible in tropical savannas, where combustion products are easily scattered by wind, and the charcoal spectral signal quickly fades out. Burning of converted tropical forest produces a short-lived signal, since fire in this region is closely related to pasture and agriculture practices, which disturb the soil surface. In tropical regions, mapping burned areas with remote sensing data has, therefore, to be performed during the dry season, i.e. simultaneously with the fire episodes. Results will be, in general, largely affected by smoke aerosols, which contaminate surface observation and reduce the spectral contrast between distinct land cover types. According to Kaufman (1995), most of these particles may remain in the atmosphere for around a week. In addition, from July to October, i.e. during the Amazon fire season, a large high pressure system tends to dominate the region, inhibiting precipitation and reducing relative humidity due to the subsidence of dry air from the upper levels of the atmosphere (Nobre et al., 1998). The associated atmospheric circulation favors the retention over a large horizontal area of smoke emitted by fires, reducing visibility to the point of closing airports during, even up to two or three weeks after the end of the fire season (Reinhardt et al., 2001).

Under such circumstances, the MIR spectral band appears especially adequate for monitoring the land surface during fire episodes, because it is largely unaffected by the presence of most aerosols. This feature of MIR becomes well apparent when atmospheric transmittance attenuation is computed over the visible (VIS) to MIR bands, for different levels of smoke contamination due to biomass burning. Transmittance attenuation is defined here as the difference between the transmittance from an aerosol-free atmosphere and that from an atmosphere with a given level of smoke contamination. Fig. (2) shows the impact on MODIS VIS to MIR channels resulting from increasing the aerosol optical depth (AOD) associated to biomass burning. Values of transmittance attenuation were obtained from radiative transfer simulations performed with MODTRAN-4 (see Section 3.3). The model was run using a Tropical atmospheric profile (see Table 2) perturbed with aerosols associated to biomass burning, based on cloud-screened level 2.0 AOD at 440 nm ($\tau_a(0.44)$) data from the Abracos Hill station. The station is located in Rondonia, Brazil, an area with high fire activity and is part of the

Aerosol Robotic Network (AERONET), a global sun/sky radiometer network for aerosol monitoring (Holben et al., 1998).

During the dry season, in an atmosphere heavily contaminated by smoke (e.g. with an AOD at 0.44 μm for about 2.73), the VIS and NIR channels (0.4–1.0 μm) are inadequate for surface observation. Even at lower levels of contamination by smoke (with an AOD at 0.44 μm lower than 0.72) VIS channels remain strongly affected. Although less sensitive to smoke aerosol, atmospheric transmittance in the SWIR (1.2–2.5 μm) spectral region is still markedly attenuated. In striking contrast, the MIR domain is practically unaffected by smoke, allowing for almost undisturbed surface observation. The atmospheric transmittance attenuation displays almost constantly low values of atmospheric contamination by smoke in all three cases analyzed, including under extreme AOD conditions. This is a major reason to favor the MIR spectral domain for monitoring and mapping burned areas.

3. Data and methods

3.1. Theoretical background

Top of the atmosphere (TOA) radiance measured by a sensor in the MIR region results from the contribution of the reflective and thermal emissive components. In case of clear sky conditions, radiation balance is translated by the so-called radiative transfer equation (RTE):

$$L_{\text{MIR}} = t_{\text{MIR}} \rho_{\text{MIR}} \frac{E_{\text{OMIR}}}{\pi} \mu_0 + \tau_{\text{MIR}} \varepsilon_{\text{MIR}} B(\lambda_{\text{MIR}}, T_s) + \tau_{\text{MIR}} \rho_{\text{MIR}} \bar{L}_{\text{atm}, \text{MIR} \downarrow} + L_{\text{atm}, \text{MIR} \uparrow} + L_s \quad (1)$$

In the previous equation t_{MIR} is the two-way atmospheric transmittance (sun–surface–sensor); ρ_{MIR} is the surface reflectance; E_{OMIR} is the exo-atmospheric irradiance; μ_0 is the cosine of the solar zenith angle (SZA); τ_{MIR} is the one-way atmospheric transmittance (surface–sensor); ε_{MIR} is the surface emissivity; $B(\lambda_{\text{MIR}}, T_s)$ is the emitted radiance given by Planck’s function for surface temperature T_s and central wavelength λ_{MIR} ; $\bar{L}_{\text{atm}, \text{MIR} \downarrow}$ is the hemispherical average of the atmospheric downward emission; and $L_{\text{atm}, \text{MIR} \uparrow}$ is the atmospheric upward emission; and L_s is the term associated with atmospheric scattering.

The first term on the right-hand side of Eq. (1) represents the solar radiance that is attenuated by the atmosphere in its downward path, then reflected by the surface and again attenuated in its upward path to the sensor. The second term represents the radiance emitted by the surface that is attenuated by the atmosphere. The third term denotes the downward atmospheric radiance that is reflected by the surface and then attenuated in its upward path to the sensor. The fourth term represents the radiance emitted by the atmosphere towards the sensor. The last term is associated with atmospheric scattering.

Since the Earth surface is opaque and assuming it behaves as a Lambertian emitter–reflector, surface reflectance and emissivity are related as:

$$\rho_{\text{MIR}} = 1 - \varepsilon_{\text{MIR}} \quad (2)$$

Using Eq. (2) and neglecting the atmospheric scattering term, L_s , the solution to Eq. (1) is given by:

$$\rho_{\text{MIR}} = \frac{L_{\text{MIR}} - \tau_{\text{MIR}} \varepsilon_{\text{MIR}} B(\lambda_{\text{MIR}}, T_s) - L_{\text{atm}, \text{MIR} \uparrow}}{t_{\text{MIR}} \frac{E_{\text{OMIR}}}{\pi} \mu_0 - \tau_{\text{MIR}} \varepsilon_{\text{MIR}} B(\lambda_{\text{MIR}}, T_s) + \tau_{\text{MIR}} \bar{L}_{\text{atm}, \text{MIR} \downarrow}} \quad (3)$$

3.2. Retrieval of MIR reflectance

Eq. (3) lays the grounds for the so-called physically-based methods, which involve a direct evaluation of all constituents of the MIR signal by means of a radiative transfer model, requiring

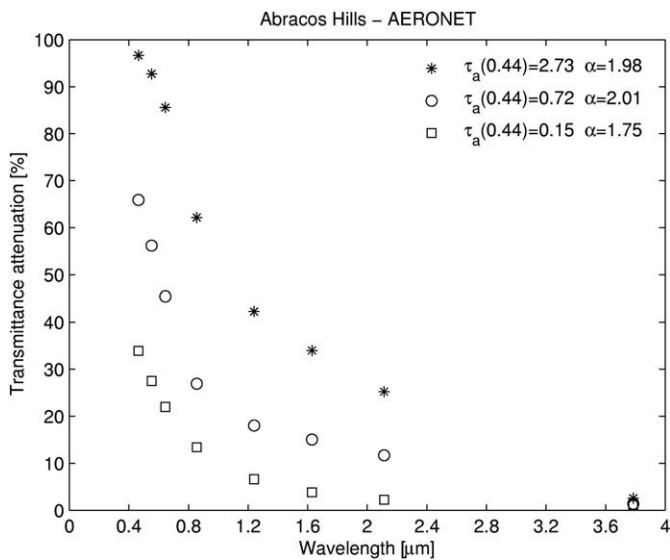


Fig. 2. Atmospheric transmittance attenuation [%] on MODIS VIS to MIR channels for three different levels of smoke contamination due to biomass burning. $\tau_a(0.44)$ indicates the AOD at 0.44 μm and α denotes the Ångstrom parameter, which characterizes aerosol particle size distribution.

substantial computational means. Operational use of physically-based methods is limited by other factors, namely the need of quantitative information on atmospheric conditions, mainly humidity and temperature profiles, in order to perform the atmospheric corrections.

The above-mentioned limitations led to the development of simpler methods, like the one proposed by KR94, which require neither direct knowledge of atmospheric conditions, nor a radiative transfer model. The approach is based on the studies of Gesell (1989) and Ruff and Gruber (1983), who pointed out the existence of a mutual compensation between attenuation and thermal emission terms, so that both atmospheric transmittances (i.e. t_{MIR} and τ_{MIR}) may be assumed as equal to unity, and both the atmospheric downward and upward thermal emission terms may be neglected. The validity of these assumptions may be assessed by simplifying Eq. (3) and then justifying the performed simplifications using typical values of the relevant terms of Eq. (3) for surface and atmospheric conditions associated to dense, dark vegetation areas in mid-latitude environments. Typical values are given in Table 1 for nadir view and three different values of SZA, respectively 0, 15 and 45°, where a Mid-Latitude Winter atmospheric profile (see Table 2) and a surface temperature T_s of 290 K are assumed. Accordingly, after some algebraic manipulations, Eq. (3) may be rewritten as:

$$\rho_{\text{MIR}} = \frac{L_{\text{MIR}} - B(\lambda_{\text{MIR}}, T_s) - \Delta_1}{\left[\frac{E_{\text{OMIR}}}{\pi} \mu_0 - B(\lambda_{\text{MIR}}, T_s) \right] [1 + \Delta_2]} \quad (4)$$

where:

$$\Delta_1 = (\tau_{\text{MIR}} - 1)B(\lambda_{\text{MIR}}, T_s) + L_{\text{atm,MIR}} \uparrow \quad (5)$$

$$\Delta_2 = \frac{(\tau_{\text{MIR}} - 1) \frac{E_{\text{OMIR}}}{\pi} \mu_0 - (\tau_{\text{MIR}} - 1)B(\lambda_{\text{MIR}}, T_s) + \tau_{\text{MIR}} \bar{L}_{\text{atm,MIR}} \downarrow}{\frac{E_{\text{OMIR}}}{\pi} \mu_0 - B(\lambda_{\text{MIR}}, T_s)} \quad (6)$$

Since $\Delta_2 \ll 1$ according to the values in Table 1, the factor $1/1 + \Delta_2$ in Eq. (4) may be expanded in a Taylor series up to the first order leading to:

$$\rho_{\text{MIR}} = \frac{L_{\text{MIR}} - B(\lambda_{\text{MIR}}, T_s) - \Delta_1}{\left[\frac{E_{\text{OMIR}}}{\pi} \mu_0 - B(\lambda_{\text{MIR}}, T_s) \right]} [1 + \Delta_2]. \quad (7)$$

Taking further into account that $\Delta_1 \ll L_{\text{MIR}} - B(\lambda_{\text{MIR}}, T_s)$, terms Δ_1 and Δ_2 may be neglected in Eq. (7) leading to the following simplified form:

$$\rho_{\text{MIR}} = \frac{L_{\text{MIR}} - B(\lambda_{\text{MIR}}, T_s)}{\frac{E_{\text{OMIR}}}{\pi} \mu_0 - B(\lambda_{\text{MIR}}, T_s)}. \quad (8)$$

The above described mathematical procedure may be also viewed from a physical point of view. First, consider the numerator of the second hand term of Eq. (3), and suppose the atmospheric upward emission term ($L_{\text{atm,MIR}} \uparrow$) is neglected. Since L_{MIR} is fixed, the only way to compensate the neglected term is by increasing the contribution of the remaining term, $\tau_{\text{MIR}}B(\lambda_{\text{MIR}}, T_s)$. This is only possible by increasing the atmospheric transmittance τ_{MIR} , in particular by setting it equal to unity. Now, taking into consideration

Table 2

Effects of water vapor content [g cm^{-2}] on atmospheric terms for the three profiles analyzed, considering nadir view and a SZA of 0°.

Profile	Water vapour content [g cm^{-2}]	τ_{MIR}	t_{MIR}	$L_{\text{atm,MIR}} \uparrow$ [$\text{W m}^{-2} \mu\text{m}^{-1} \text{sr}^{-1}$]	$\bar{L}_{\text{atm,MIR}} \downarrow$ [$\text{W m}^{-2} \mu\text{m}^{-1} \text{sr}^{-1}$]
MLW	0.85	0.91	0.81	0.006	0.012
MLS	2.92	0.83	0.70	0.038	0.068
TRO	4.11	0.79	0.65	0.057	0.104

the denominator, suppose the atmospheric downward emission term ($\bar{L}_{\text{atm,MIR}} \downarrow$) is neglected. Then, in order to compensate the neglected term, either the contribution of term $\tau_{\text{MIR}}B(\lambda_{\text{MIR}}, T_s)$, or the contribution of term $t_{\text{MIR}} \frac{E_{\text{OMIR}}}{\pi} \mu_0$ have to be increased. However, the first possibility is ruled out by the fact that it was already assumed that $\tau_{\text{MIR}} = 1$. Therefore, the contribution of the $t_{\text{MIR}} \frac{E_{\text{OMIR}}}{\pi} \mu_0$ term has to be raised by increasing t_{MIR} , in particular by setting it equal to unity. Setting both t_{MIR} and τ_{MIR} to unity does lead to the required increase that compensates for neglecting the $\bar{L}_{\text{atm,MIR}} \downarrow$ term. This is due to the fact that, in general, $t < \tau$ and therefore the assumption $t_{\text{MIR}} = \tau_{\text{MIR}} = 1$ leads to a greater increase in the contribution of $t_{\text{MIR}} \frac{E_{\text{OMIR}}}{\pi} \mu_0$ term than in $\tau_{\text{MIR}}B(\lambda_{\text{MIR}}, T_s)$ term.

KR94 introduced another approximation for Eq. (8), that consists of using the brightness temperature, $T_{\text{B,TIR}}$, from a thermal infrared (TIR) band (10–12 μm) as a surrogate for the land surface temperature (LST), T_s . In fact, as pointed out by Prata et al. (1995), brightness temperature is usually lower than surface temperature, the difference typically ranging from 1 to 5 K in TIR.

Following a procedure similar to the one above-described, Eq. (8) may be approximated (up to the first order) as:

$$\rho_{\text{MIR}} = \frac{L_{\text{MIR}} - B(\lambda_{\text{MIR}}, T_{\text{B,TIR}}) - \Delta_3}{\frac{E_{\text{OMIR}}}{\pi} \mu_0 - B(\lambda_{\text{MIR}}, T_{\text{B,TIR}})} \left[1 - \frac{\Delta_3}{\frac{E_{\text{OMIR}}}{\pi} \mu_0 - B(\lambda_{\text{MIR}}, T_{\text{B,TIR}})} \right]. \quad (9)$$

Since, according to results in Table 1, $\Delta_3 = B(\lambda_{\text{MIR}}, T_s) - B(\lambda_{\text{MIR}}, T_{\text{B,TIR}}) \ll L_{\text{MIR}} - B(\lambda_{\text{MIR}}, T_{\text{B,TIR}})$ and $\frac{\Delta_3}{\frac{E_{\text{OMIR}}}{\pi} \mu_0 - B(\lambda_{\text{MIR}}, T_{\text{B,TIR}})} \ll 1$, Eq. (3) may be approximated by the following equation, that represents the final form of the KR94 algorithm:

$$\rho_{\text{MIR}} = \frac{L_{\text{MIR}} - B(\lambda_{\text{MIR}}, T_{\text{B,TIR}})}{\frac{E_{\text{OMIR}}}{\pi} \mu_0 - B(\lambda_{\text{MIR}}, T_{\text{B,TIR}})}. \quad (10)$$

3.3. Radiative transfer simulations

As pointed out in the Introduction, the aim of the present paper is to perform a systematic assessment of the performance of the KR94 algorithm when applied to burned area discrimination under a wide range of atmospheric, surface and geometry conditions, paying special attention to those expected when applying the algorithm to the Amazon and “cerrado” regions.

For this purpose, estimation of the error associated with MIR reflectance as retrieved using Eq. (10) will be performed based on a

Table 1

Typical values of the different terms of Eq. (3) in the case of nadir view and for three different SZA considering a Mid-Latitude Winter atmospheric profile and a surface temperature, T_s , equal to 290 K.

SZA	τ_{MIR}	t_{MIR}	L_{MIR}^a	$B(\lambda_{\text{MIR}}, T_s)^a$	$B(\lambda_{\text{MIR}}, T_{\text{B,TIR}})^a$	$L_{\text{atm,MIR}} \uparrow^a$	$\frac{E_{\text{OMIR}}}{\pi} \mu_0^a$	$\bar{L}_{\text{atm,MIR}} \downarrow^a$
45°	0.912	0.794	0.700	0.315	0.212	0.006	2.46	0.011
15°	0.912	0.813	0.872	0.315	0.212	0.006	3.29	0.011
0°	0.912	0.816	0.899	0.315	0.212	0.006	3.42	0.011

^a [$\text{W m}^{-2} \mu\text{m}^{-1} \text{sr}^{-1}$].

large number of simulated top of atmosphere (TOA) radiances. These simulations are generated with MODTRAN-4, a widely used radiative transfer model (Berk et al., 2000) encompassing a large set of observation conditions. The simulations are performed in the spectral ranges of $3.62\ \mu\text{m}$ – $3.97\ \mu\text{m}$ and $10\ \mu\text{m}$ – $12\ \mu\text{m}$, i.e. covering MODIS channels 20 and 31. Brightness temperature from MODIS channel 31 is also required as input to Eq. (10).

The atmospheric contribution is computed for three geographical-seasonal model atmospheres stored in MODTRAN-4, namely Mid-Latitude Winter (MLW), Mid-Latitude Summer (MLS), and Tropical (TRO). Use of mid-latitude profiles (i.e. MLW and MLS) is required to establish a baseline of performance of KR94 when subject to atmospheric, surface and geometric conditions for which the algorithm was specifically designed. Such baseline will then serve to assess the limitations of KR94 when employed beyond specifications, namely in case of tropical environments (e.g. as described by the TRO profile).

The three standard atmospheres cover a wide range of atmospheric conditions, with water vapor content of 0.85, 2.92 and $4.11\ \text{g cm}^{-2}$ and 2-m air temperature (T_{atm}) of 272.2, 294.2 and 299.7 K, for MLW, MLS, and TRO respectively. The assigned LST values are based on the 2-m air temperature of each profile, varying from T_{atm} to $T_{\text{atm}} + 30.0\ \text{K}$ in steps of 1.0 K, totalizing 31 different values. The sun-view geometry consists of 31 solar zenith angles, from 0° to 60° in steps of 2° , and of a single view zenith angle of 0° . Although nadir viewing is limited along the tropics when using polar orbiting instruments (such as MODIS), choice of a nadir view corresponds to the most favorable surface observation conditions. If problems arise when simulating nadir viewing (i.e. the most favorable case), then performance is expected to degrade for less favorable observation conditions. In fact, simulations were also performed for off-nadir viewing angles and, as expected, results (not shown) revealed a slight degradation in performance of the KR94 algorithm with increasing viewing angle, a feature consistent with former studies (França &

Setzer, 1998; Jiang et al., 2006) that demonstrate weak dependence of MIR region on view angle variations.

The ranges of SZA and LST are set to be representative of the observed geometric and surface conditions characteristic of regions associated to each atmospheric profile. For instance, Fig. 3 depicts pixel values of the third quartile (P75) of LST during August 2008, retrieved over Brazil using the Spinning Enhanced Visible and Infra-Red Imager (SEVIRI) on-board METEOSAT-8. Fig. 4 presents monthly P75 values, throughout the year, of SZA as obtained from a large sample of pixels from MODIS imagery that has been operationally used for burned area discrimination over Brazil. During the fire season (from June to October) very high values of LST are observed over Amazonia and especially over the adjacent “cerrado”, region, where a large area may be found that presents values of P75 larger than 320 K. In addition, more than 25% of the pixels are associated to values of SZA greater than 40° , i.e. to low values of the solar signal.

Two types of surface cover were considered, namely burned and unburned. Both surface types were assumed to be homogeneous and Lambertian, the burned and unburned surfaces being characterized respectively by charcoal and vegetation spectra. Spectral libraries like ASTER and MODIS-UCSB supply reliable reflectance data for different types of materials, such as vegetation, water, soil, rocks and man-made. However, to the best of our knowledge, no reflectance measurements are currently available for charcoal, ash or any burned plant material, in the spectral region accounted for in this study. Therefore, four fire residue samples were collected at Alta Floresta, state of Mato Grosso, Brazil. Charcoal spectra were measured at the NASA Jet Propulsion Laboratory and may be viewed as typical of tropical environments. Mean values of the four charcoal spectra were then used to prescribe the surface reflectance of the burned surface as input to MODTRAN-4. Regarding the unburned surface, prescribed reflectance values were obtained from a set of 25 surfaces from the MODIS-UCSB spectral library. The set includes most vegetation types

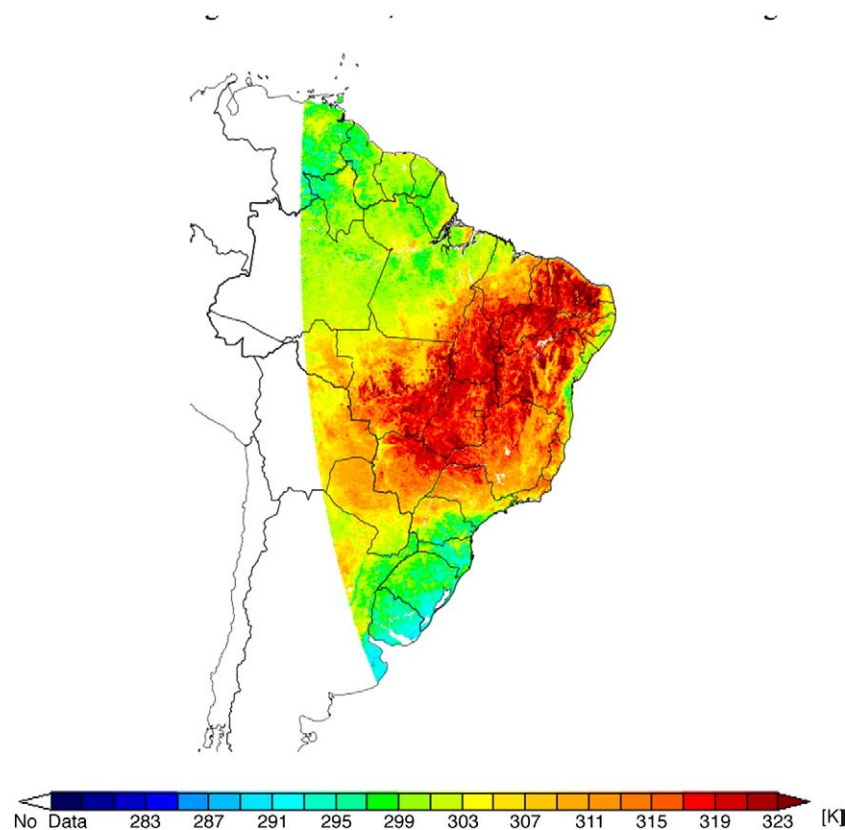


Fig. 3. Monthly values of P75 of LST during August, 2008 over Brazil. Data were retrieved from METEOSAT-8/SEVIRI data.

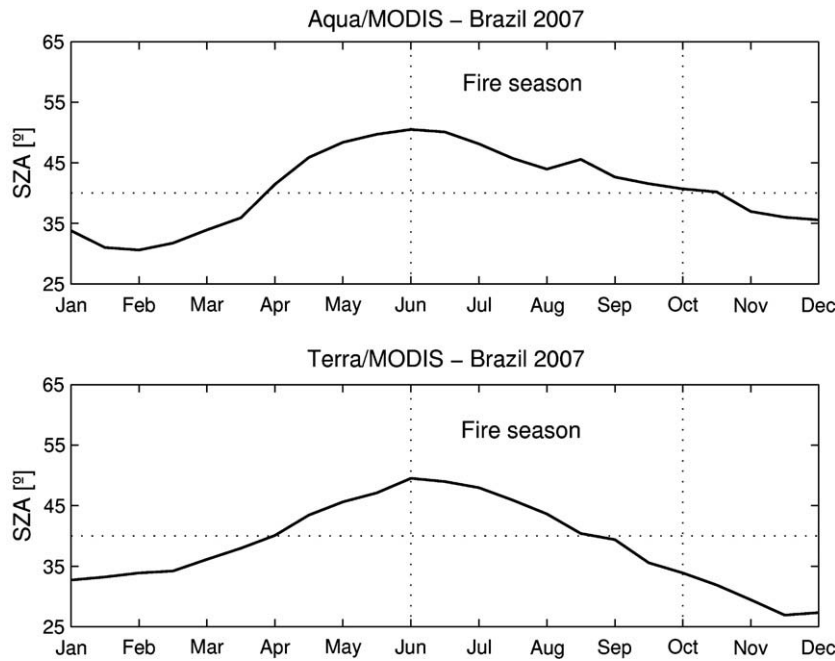


Fig. 4. Monthly values of P75 of SZA as obtained from samples of AQUA/MODIS and TERRA/MODIS imagery along the year of 2007 over Brazil. The threshold of 40° for SZA is highlighted by the dotted horizontal line. Dotted vertical lines delimit the fire season in Amazonia (June to October).

(Salisbury & D'Aria, 1994; Peres & DaCamara, 2004), with reflectance values varying from 0.01 to 0.04, in the MIR region. A value of 0.24 (0.03) was, accordingly, prescribed for MIR reflectance for the burned (unburned) types of surface cover. These values were obtained by averaging the MIR spectral signature for the four (25) considered charcoal (vegetation) types, which were convolved with the MODIS channel 20 normalized response function. Results ought to be applicable to other sensors having spectral windows similar to that used in this work.

4. Analysis and results

4.1. MODTRAN-4 simulations

As discussed in the previous section, the method developed by KR94 relies on a number of simplifying assumptions regarding atmospheric transmittances and atmospheric downward and upward thermal emission radiances. All these terms are correlated and depend essentially on atmospheric water vapor content. When atmospheric water vapor increases, atmospheric transmittances decrease, whereas the atmospheric downward and upward thermal emission radiances increase. Table 2 shows the range of atmospheric terms that may typically be found in the MIR region, in the case of the three geographical–seasonal model atmospheres considered, i.e., when varying from 'dry' to 'moist' conditions. For instance, whereas high transmittances and low path–radiance values characterize the MLW atmospheric profile, the TRO profile is associated to lower transmittances and relatively high path–radiance values. It is therefore to be expected that use of Eq. (10) in retrieving MIR reflectance may introduce systematic deviations, especially in the case of 'moist' atmospheres. For example, in the case of TRO, the relative error associated to the assumption of $\tau_{\text{MIR}} = 1$ (instead of the realistic value $\tau_{\text{MIR}} = 0.79$) is about 27% but drops to 10% in the case of MLW (taking into account that $\tau_{\text{MIR}} = 0.91$). In the case of the two-way atmospheric transmittance, the relative error associated to the assumption of $t_{\text{MIR}} = 1$ (instead of $t_{\text{MIR}} = 0.65$) in the case of TRO is about 54% but drops to 24% in the case of MLW (where $t_{\text{MIR}} = 0.81$). In a similar fashion, neglecting the atmospheric downward emission term leads

to a relative error of 17% for the TRO profile, in contrast with MLW where the corresponding error decreases to 3%. Finally, neglecting the atmospheric upward emission term leads to a relative error of 9% for the TRO profile and just to an error of 2% in the case of MLW.

Accuracy of the solutions provided by Eq. (10) may be assessed by evaluating the corresponding relative errors, defined as the differences between retrieved values using Eq. (3) and the corresponding prescribed values as input to MODTRAN-4, divided by the latter values. Figs. 5–7 present the obtained values of relative errors of MIR reflectance as a function of LST and SZA. The curves correspond to nadir viewing conditions and represent charcoal (left panels) and vegetation (right panels) surfaces for MLW (Fig. 5), MLS (Fig. 6) and TRO (Fig. 7). It is worth stressing that ranges of LST considered are different for each profile (as discussed in Section 3.3) and reflect the surface conditions typically associated to each type of atmosphere.

It is well apparent that relative errors strongly depend on the surface type, for all three atmospheric profiles. In particular, it may be noted that the magnitude of relative errors is considerably larger for vegetation than for charcoal, and increases with moisture content, MLW showing the lowest values and TRO the highest. For instance, the lower values obtained in the case of MLW are in close agreement with results found by KR94, who estimated the accuracy of Eq. (10) to lie in the range of 0.01–0.02 (absolute errors) for a mid-latitude atmosphere and for the range of reflectance to be expected from a variety of vegetation and soils (0.01–0.06). In strong contrast, vegetation surfaces present extremely large relative errors, ranging from 100% to 1200% for LST values to be expected in tropical regions. Taking the value of 0.03 as reference for reflectance of vegetation, the obtained range corresponds to absolute errors of 0.06–0.4. In the case of charcoal, relative errors are one order of magnitude smaller, ranging from –20%–80%, i.e. from about –0.05–0.2 in terms of absolute error, and taking a reference value of 0.24 for charcoal reflectance. Dependence of the relative error on LST is stronger than on SZA, especially for values of SZA lower than 30°, a feature clearly revealed by the low slope of the error curves in Figs. 5–7.

Performance of the KR94 algorithm is closely linked to the magnitude of the relative contribution of thermal emitted radiance, L_e , to the total TOA MIR radiance, L_{MIR} , given by Eq. (1). It may be

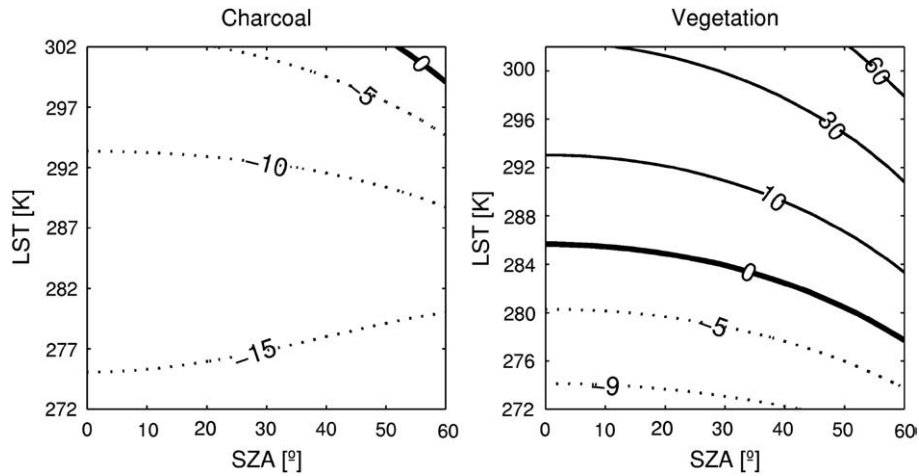


Fig. 5. Relative error [%] on MIR reflectance (retrieved minus prescribed values) as a function of LST and SZA in the case of MLW profile for charcoal (left panel) and vegetation (right panel) surfaces. Solid (dotted) curves indicate positive (negative) errors and the thick curve highlights the no-error line.

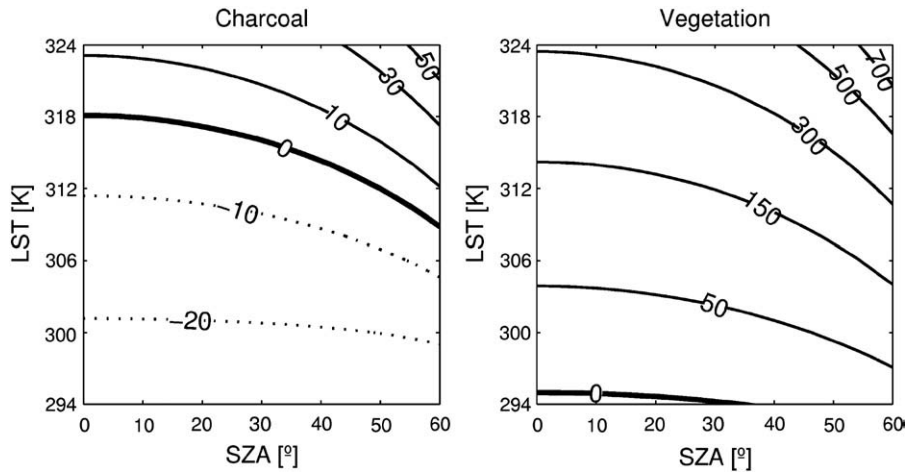


Fig. 6. As in Fig. 5 but in the case of MLS.

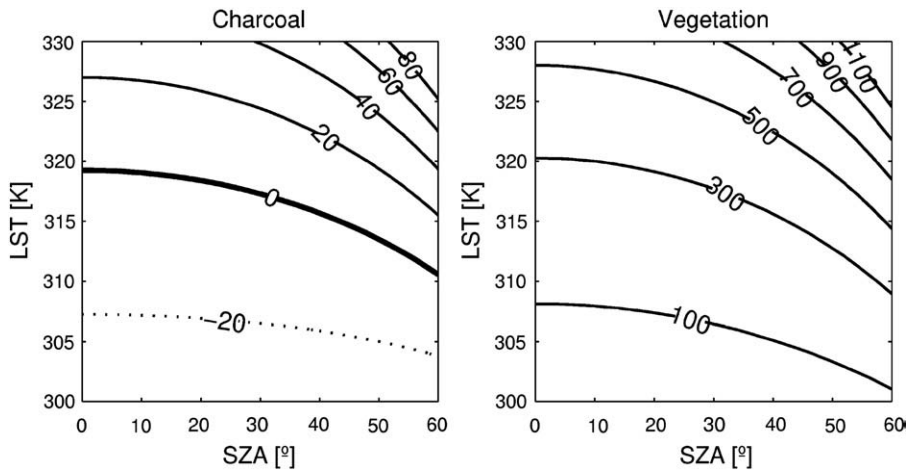


Fig. 7. As in Fig. 5 but in the case of TRO.

noted that L_e is given by the second, third and fourth terms of the right-hand side of Eq. (1), i.e.

$$L_e = \tau_{MIR} \epsilon_{MIR} B(\lambda_{MIR}, T_S) + \tau_{MIR} \rho_{MIR} \bar{L}_{atm, MIR \downarrow} + L_{atm, MIR \uparrow} \quad (11)$$

When the ratio L_e/L_{MIR} exceeds a threshold of about 0.75 the solutions provided by Eq. (10) are contaminated by unacceptably large relative errors, on the order of 100%. The magnitude of L_e/L_{MIR} , and therefore the range of validity of Eq. (10), mainly depends on the type of the surface considered, as well as on its temperature,

atmospheric profile, and sun elevation angle. Fig. 8 presents the dependence of L_e/L_{MIR} on LST for vegetation (circles) and charcoal (squares) under two extreme illumination angles, respectively an SZA of 0° (open symbols) and of 60° (black symbols), and for the two extreme cases of atmospheric moisture content, respectively MLW (left panel) and TRO (right panel) profiles. The contrasting behavior of charcoal and vegetation is well apparent. In the case of charcoal, high values of MIR reflectance (about 0.24) lead to a major contribution of the reflected component and, therefore, the ratio L_e/L_{MIR} will be below 50% (75%) in the case of MLW (TRO), except for large values of LST, above 289 K (293 K) for MLW (TRO), associated to very low sun elevation angles ($SZA=60^\circ$). Acceptable estimates of charcoal reflectance are therefore to be expected from Eq. (10), the sole exception being cases of high LST values (larger than 320 K), co-occurring with high SZA values (larger than 50°), which may lead to relative errors in excess of 25%. Because of the very low vegetation reflectance (about 0.03, i.e. eight times lower than that of charcoal), total TOA MIR radiance, L_{MIR} , will be primarily due to the thermal emitted component, and a deeply contrasting behavior is to be expected between charcoal and vegetation. In the latter type of surface, the ratio L_e/L_{MIR} is always larger than 75% in the case of TRO, and in the case of MLW for low solar elevation ($SZA=60^\circ$). Even for solar zenith conditions ($SZA=0^\circ$) the ratio L_e/L_{MIR} exceeds 75% in the case of MLW, for LST values as low as 288 K. Implications of the solutions provided by Eq. (10) on relative errors are well depicted in the left panels of Figs. 5 and 7; in the case of TRO, relative errors are unacceptably large (exceeding 50%) over the entire domain considered, whereas in the case of MLW relative errors are larger than 25% for values of LST beyond 290 K, whenever SZA surpasses 50° .

The above-discussed limitations of the KR94 algorithm may give rise to serious difficulties when attempting to discriminate between burned and unburned surfaces, in particular in the case of tropical environments. For instance, an absolute error of 0.2 in a typical vegetation reflectance of about 0.03 leads to a retrieved value of about

0.23 which reaches the range characteristic of charcoal. The problem is illustrated in Fig. 9, which presents results obtained when using Eq. (10) to retrieve the reflectance of vegetation (with the prescribed value of 0.03) and of charcoal (with the prescribed value of 0.24) in the three considered cases of MLW, MLS and TRO, for values of SZA from 0 to 60° and for ranges of typical values of LST for each profile. It is well apparent that the accuracy of retrieved values of reflectance is much more sensitive to LST and SZA in the case of vegetation than for charcoal. For instance, the reference contour line of 0.03 (for vegetation) is displaced out of the considered domain in the case of MLS and TRO and, even for MLW, it is located at the bottom, almost out of the domain. The displacement of the reference contour line of 0.24 for charcoal is much smaller and is barely noticeable in the case of MLW. However, the robustness of Eq. (10) in the case of charcoal is not enough to discriminate burned from unburned surfaces, because values of reflectance for vegetation attain those characteristics of charcoal for sufficiently high values of LST and SZA. As shown in Fig. 9, in the case of MLS, even if the discontinuities observed along the band separating the two considered surfaces indicate the possibility of discriminating between them, values of the contour lines on both sides are larger than 0.20. Therefore, it is not possible to label either type as the unburned surface. The situation is even worse for TRO where, for values of LST greater than 315 K and SZA larger than 30° , both surfaces reach similar reflectance values, becoming undistinguishable.

4.2. Case study

A more realistic assessment of the implications of using Eq. (10) for burned area discrimination in tropical environments may be achieved by means of a case study based on satellite imagery. However, as pointed out by Roger and Vermote (1998), any attempt to validate retrieved values of MIR reflectance from satellite data is virtually impaired by the absence of “in-situ” (direct) measurements. This limitation may be circumvented by creating a reference dataset of

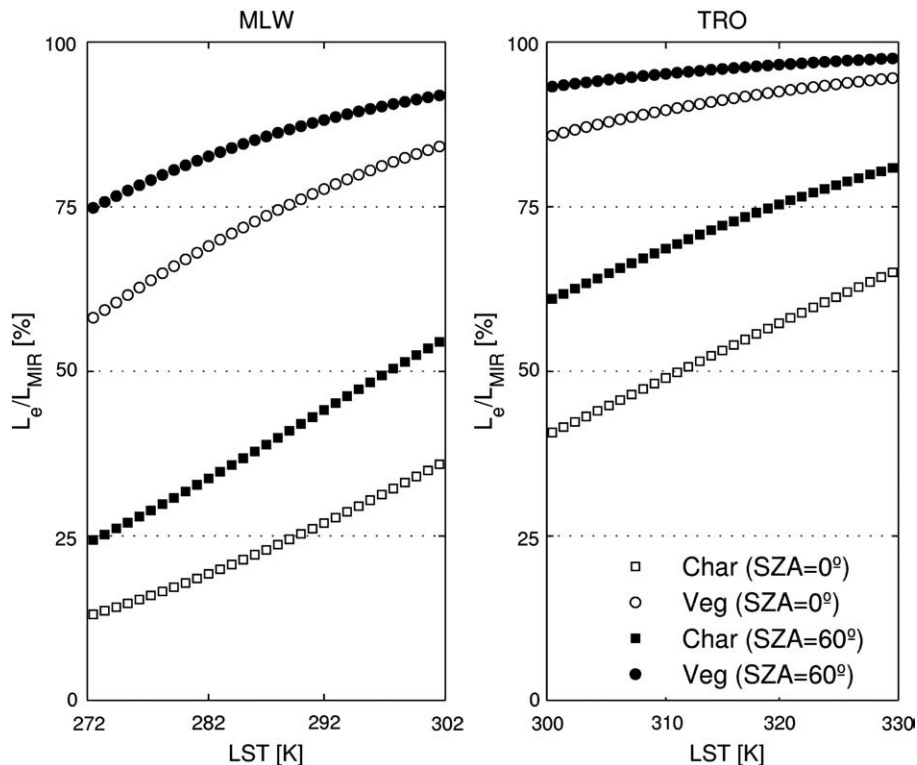


Fig. 8. Plot of the ratio L_e/L_{MIR} [%] as a function of LST in the case of MLW (left panel) and TRO (right panel). Square (circle) symbols denotes charcoal (vegetation) surface whereas open (black) symbols characterizes SZA of 0° (60°).

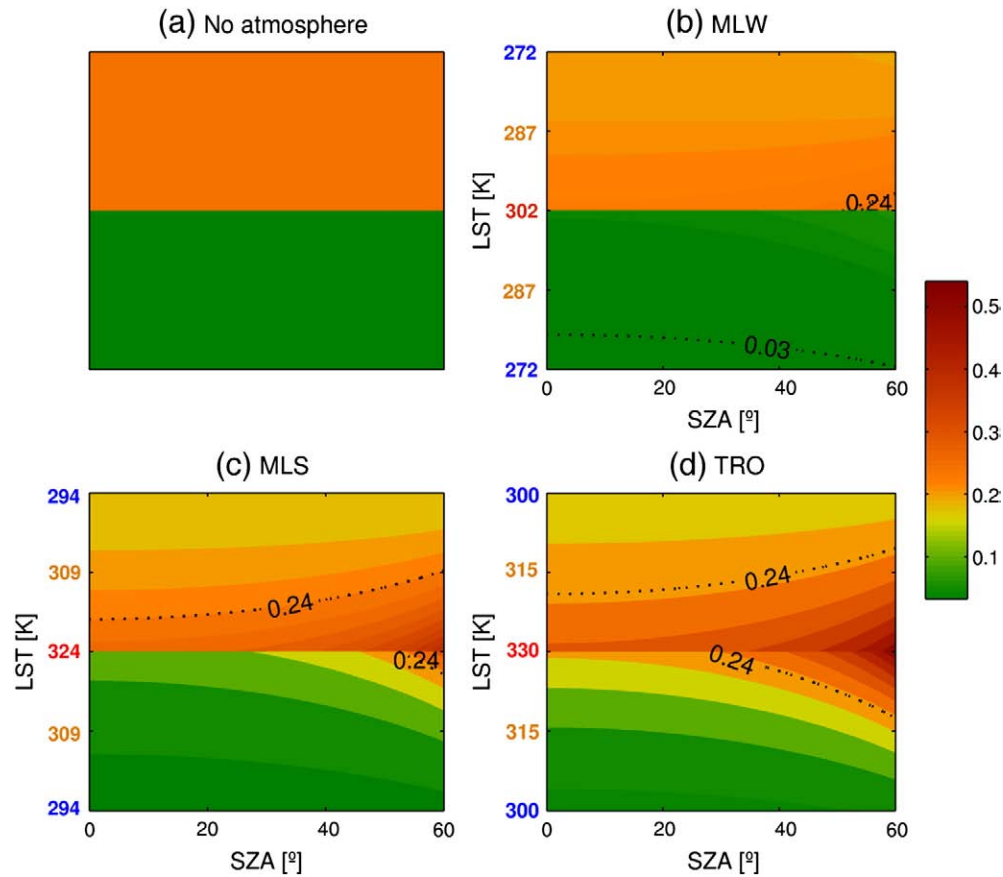


Fig. 9. Diagram of values of reflectance for vegetation and charcoal surfaces for different atmospheric profiles, LST and SZA; a) the two surfaces with prescribed constant values of 0.03 and 0.24 for vegetation (green) and charcoal (orange); b) to d) retrieved values of reflectance using Eq. (10) as a function of SZA and LST for MLW, MLS and TRO profiles.

MIR reflectance based on information from a real satellite image. The adopted approach consists of the following steps: (1) collect information about land surface temperature, land surface emissivity, atmospheric profiles and view/solar angles for the selected scene; (2) use a radiative transfer model (MODTRAN-4 in the present study) to compute the respective values of transmittance and atmospheric parameters; and (3) use Eq. (3) with values obtained in the previous steps to retrieve MIR reflectance from the total signal. The generated reference dataset of MIR reflectance may then be used to validate the corresponding MIR reflectance as retrieved by means of KR94.

Taking into account the described procedure, it seems appropriate to select an image where the atmospheric conditions are particularly favorable, e.g. with low values of the water vapor column, and a low amount of aerosols (i.e. with a clear sky surrounding). Since results from simulations (Section 4.1) showed that the accuracy of retrieved values of reflectance is very sensitive to high values of LST, it seems also appropriate to select an image with moderate values of LST.

All the above-mentioned favorable characteristics are met in the case of the large fire event that took place from April 30 to May 12, 2006 and affected the entire area of the Ilha Grande National Park, located between the states of Paraná and Mato Grosso do Sul, Brazil. The burned is about 200 km², as estimated by INPE based on information from LANDSAT TM imagery (Fig. 10). A total of 413 active fires during the above-mentioned period were also identified by INPE, using data from GOES, NOAA, Aqua and Terra satellites.

Performance of Eq. (10) was assessed using TOA values of MIR radiance and TIR brightness temperature as acquired on May 12, 2006 by the MODIS instrument on-board Aqua. Data were obtained from the Aqua/MODIS Level 1B 1 km V5 product, MYD021 (MCST, 2006) and

correspond to channels 20 (centered at 3.785 μm) and 31 (centered at 11.017 μm). Surface values of MIR reflectance were then retrieved by solving Eq. (3) using MODTRAN-4, using information about surface temperature and sun elevation together with data of temperature and humidity for the atmospheric column. Pixels values of LST and of SZA, varying from 295 to 315 K and from 48.5 to 51°, respectively were obtained from Land Surface Temperature/Emissivity Daily 5-Min L2 Swath 1 km product, MYD11_L2 (Wang, 1999). Atmospheric profiles of temperature and humidity were obtained from the Atmosphere Profile Level 2.0 product, MYD07_L2 (Seemann et al., 2006), the water vapor content over the selected area varying from 1.3 to 2.3 g cm⁻², a quite low amount when compared with the value of 4.11 g cm⁻² of the TRO profile stored in MODTRAN-4. Fig. 11 represents the MODIS mean profiles of temperature and humidity together with the TRO profile that will be used to generate synthetic imagery with characteristics to be expected over tropical environments.

Retrieved values of surface MIR reflectance and values of LST are shown in Fig. 12. Higher values of MIR reflectance and LST over the burned area are particularly conspicuous, especially because of the contrasting behavior of the surrounding vegetated areas, which present a large spatial variability of reflectance and temperature.

Values of retrieved surface MIR reflectance and of LST (Fig. 12) were input to MODTRAN-4, to produce synthetic images of TOA MIR radiance and TIR brightness temperature. These images correspond to the following two environments, characterized by atmospheric and surface conditions expected in tropical regions; i) the TRO environment, obtained using the TRO profile and the LST of May 12, 2006 and ii) the TRO-HOT environment, obtained using the TRO profile and LST + 20 K. The KR94 algorithm was then used to retrieve values of surface

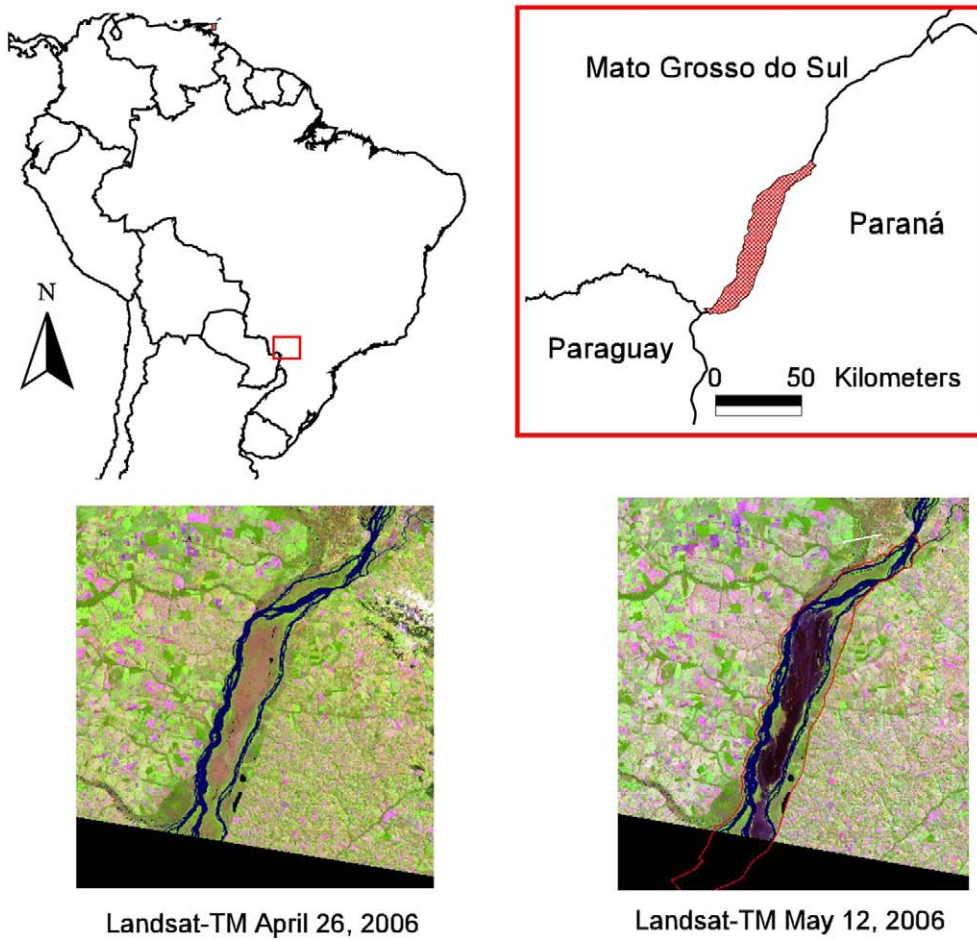


Fig. 10. Location of the Ilha Grande National Park, between the states of Paraná and Mato Grosso do Sul (upper right panel) in southwestern Brazil (upper left panel) and LANDSAT TM image (RGB 543) of the National park before the fire episode, on April 26, 2006 (lower left panel) and after the fire episode on May 12, 2006 (lower right panel). The outline of the National Park is shown in red.

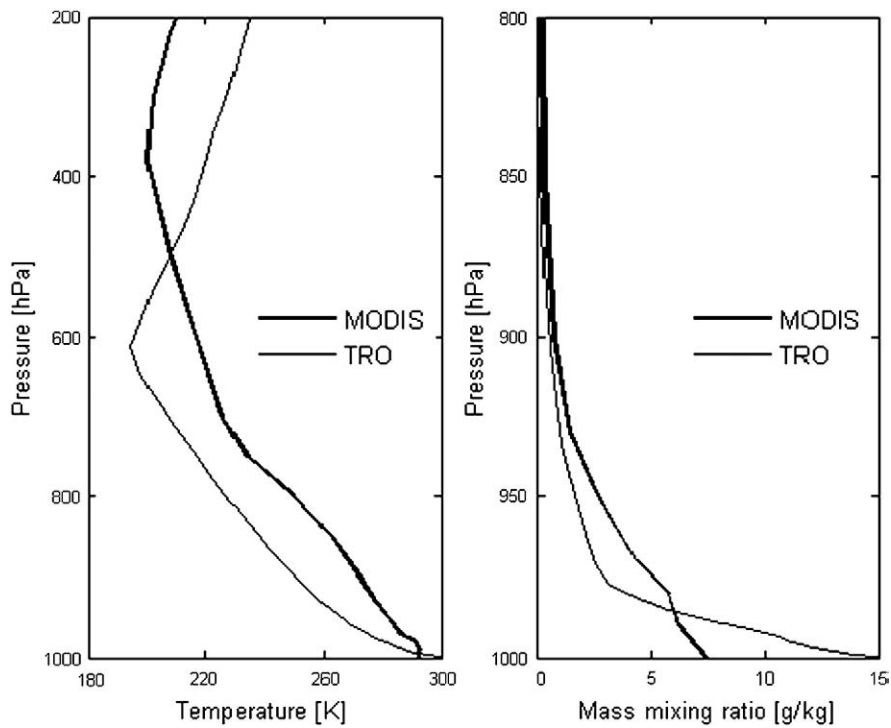


Fig. 11. MODIS mean profiles (bold curves) of temperature (left panel) and humidity (right panel) over Ilha Grande National Park on May 12, 2006. The TRO profile stored at MODTRAN-4 is also represented (thin curves).

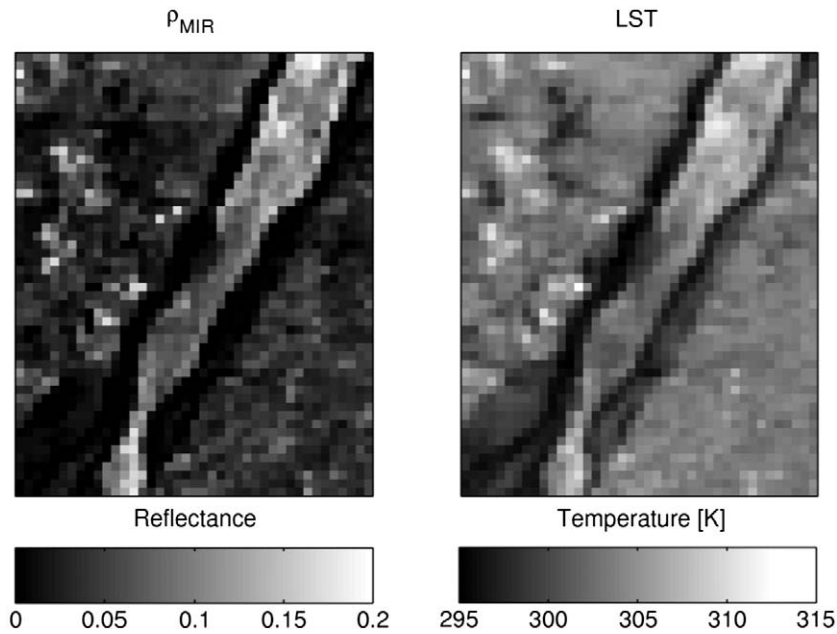


Fig. 12. Retrieved values of surface MIR reflectance (left panel) and LST (right panel) over the Ilha Grande National Park on May 12, 2006.

reflectance from TOA MIR radiance and TIR brightness temperature of the original images (May-12 environment) and of the synthetic ones (TRO and TRO-HOT environments).

The impact of using retrieved values to discriminate between burned and unburned surfaces for the three considered environments was evaluated by comparing the values of reflectance as retrieved by Eq. (10) over two sets of pixels representative of the two classes to be discriminated and then checking whether the respective statistical distributions allow distinguishing between the surfaces.

A set of 133 burned pixels, hereafter referred to as the burned class, was therefore selected from the scene, together with a set of 262 pixels that included the remaining land cover types (namely green vegetation, crop fields and water bodies), hereafter referred to as the

unburned class. Choice of pixels was made by visual comparison between two LANDSAT TM scenes (path/row 224/76) acquired on April 24 and May 12, 2006. Hot spots detected by INPE were also used in the process of selecting pixels associated to burned surfaces.

According to Kaufman and Remer (1994), a quantitative assessment of the effectiveness of the KR94 algorithm to discriminate between burned and unburned surfaces may be obtained with the following index:

$$M = \frac{|\mu_u - \mu_b|}{\sigma_u + \sigma_b} \quad (12)$$

where $\mu_u(\mu_b)$ is the mean value and $\sigma_u(\sigma_b)$ is the standard deviation for the unburned (burned) class. It is worth noting that index M may

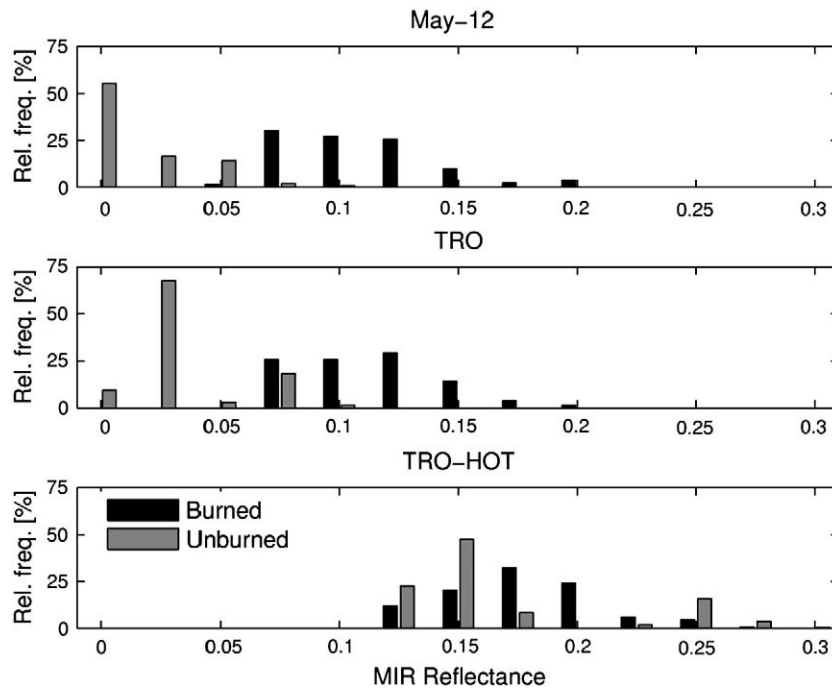


Fig. 13. Histograms of MIR reflectance for burned (black) and unburned (gray) classes as retrieved by means of Eq. (10) for May-12 (upper panel), TRO (middle panel) and TRO-HOT (lower panel) environments.

Table 3

Mean values, $\mu_u(\mu_b)$, and standard deviation, $\sigma_u(\sigma_b)$, of unburned (burned) surfaces and discrimination indices, M , for retrieved values of surface reflectance in the case of May-12, TRO and TRO-HOT environments.

	μ_u	σ_u	μ_b	σ_b	M
May-12	0.02	0.021	0.11	0.032	1.76
TRO	0.03	0.024	0.12	0.027	1.58
TRO-HOT	0.17	0.046	0.18	0.033	0.53

be viewed as an estimator of signal-to-noise ratio, the absolute difference between the mean values of the two classes representing the signal (associated to between-group variability) and the sum of the standard deviations representing noise (associated to within-group variability). Values of M larger than one indicate good separability, whereas values smaller than one represent a large degree of overlap between the values associated to the two classes.

Results are shown in Fig. 13 and Table 3. In the case of unburned surfaces, and when going from May-12 to TRO-HOT environments, there is a progressive shift of the histograms towards larger values of reflectance, accompanied by an increase of dispersion. Both shift and increase are especially pronounced from TRO to TRO-HOT. In strong contrast, in the case of burned surfaces, histograms of reflectance remain virtually unchanged when comparing May-12 to TRO environments, and there is a moderate shift when going from TRO to TRO-HOT environments. Moreover, the dispersion is virtually unaffected by injection of water vapor in the atmosphere and by surface temperature increase. The different sensitivity of the two types of surface leads to a progressive overlap of the histograms, which is translated by the decrease of M , from May-12 to TRO-HOT, and especially from TRO to TRO-HOT. In the latter type of environment M reaches a value of 0.53, an indication of very poor discriminant ability.

Results obtained for the fire event at the Ilha Grande National Park confirm those previously obtained with MODTRAN-4 simulations, namely that discrimination between burned and unburned surface based on values of surface reflectance retrieved with the KR94 algorithm is virtually impaired in the case of tropical regions for high values of surface temperature, especially when associated to low sun elevation angles. Since such circumstances are often present when using data from instruments on-board polar-orbiters (namely MODIS in Aqua and Terra) to identify burned areas over the Amazon and the adjacent "cerrado", special care is required when using the KR94 algorithm.

5. Concluding remarks

Identification of burned areas over the Amazon and "cerrado" regions is a challenging task because of the ephemeral character of the radiative signal and the presence of aerosols that prevent using classical approaches e.g. based on red and near-infrared information. Middle-infrared (MIR) presents the advantage of being virtually unaffected by the presence of most types of aerosols, in particular those associated to biomass burning. In this respect the reflected component of MIR has proven to be especially adequate to discriminate between burned and unburned surfaces in mid-latitude regions (e.g. Pereira, 1999).

Kaufman and Remer (1994) proposed a methodology that presents the advantage of enabling for the retrieval of MIR reflectance with no need for auxiliary datasets or major computational means. The so-called KR94 algorithm, given by Eq. (10), has been specifically designed to retrieve MIR reflectance over dense dark forests in the middle latitudes. It has been also successfully applied to other types of surfaces and atmospheric environments, in particular for burned area discrimination (e.g. Barbosa et al., 1999; Roy et al., 1999). However, the quality of the retrieved values of MIR reflectance by Eq. (10) may significantly degrade when the relative contribution of the thermal emitted component to the total signal exceeds a threshold of about

75%. In the case of surfaces, such as vegetation, characterized by low values of MIR reflectance, the relative contribution of the solar component to the total MIR signal tends to be small, especially when the surface is hot (i.e. in case of relatively high values of LST). This contribution may be further reduced when the solar signal is weak due to low sun elevation angles (i.e. in case of high values of SZA). The above-mentioned aspects are especially relevant in tropical environments, where high land surface temperatures naturally dominate the scenes and pixels illuminated by low sun elevation angles are often present when using data from sensors on-board polar orbiters, in particular MODIS on-board Aqua and Terra.

Use of Eq. (10) in tropical environments to retrieve vegetation reflectance may lead to errors that are at least of the same order of magnitude of the reflectance to be retrieved and considerably higher for large values of LST and SZA. Under such conditions, retrieved values of reflectance for vegetation may attain those characteristic of charcoal making the two types of surface undistinguishable. Use of the KR94 algorithm becomes severely impaired and the complete radiative transfer equation, i.e. Eq. (3), should be used instead, provided the required auxiliary information is available about the surface (LST) and the atmospheric column (temperature and humidity profiles).

Acknowledgments

This work was supported by the Portuguese Foundation of Science and Technology (FCT) (Grant No. SFRH/BD/21650/2005). R. Libonati's work was partially developed at the Satellite Division from the Brazilian National Institute for Space Research (DSA/INPE). We are grateful to Dr. Alberto Setzer (DSA/INPE) for valuable discussions and suggestions, to Dr. Fabiano Morelli and Jurandir Ventura (DSA/INPE) for making available LANDSAT and MODIS data, to José Carlos dos Santos (LCP/INPE) for collecting the samples of charcoal, and to Dr. Simon Hook (JPL/NASA) for performing the charcoal emissivity measurements. The authors also thank Dr. Brent Holben and his staff for their effort in establishing and maintaining Abracos Hill AERONET site. The vegetation spectral emissivity data were made available courtesy of the MODIS UCSB and ASTER Emissivity Libraries.

References

- Baldrige, A. M., Hook, S. J., Grove, C. I., & Rivera, G. (2009). The ASTER Spectral Library Version 2.0. *Remote Sensing of Environment*, 113, 711–715.
- Barbosa, P. M., Gregoire, J. -M., & Pereira, J. M. C. (1999). An algorithm for extracting burned areas from time series of AVHRR GAC data applied at a continental scale. *Remote Sensing of Environment*, 69, 253–263.
- Berk, A., Anderson, G. P., Acharya, P. K., Chetwynd, J. H., Bernstein, L. S., Shettle, E. P., Matthew, M. W., & Alder-Golden, S. M. (2000). MODTRAN4 Version 2 User's Manual. *Air Force Research Laboratory, Space Vehicles Directorate, Air Force Material Command, Hanscom AFB, MA* (pp. 01731–03010).
- Boyd, D. S. (1999). The relationship between the biomass of Cameroonian tropical forests and radiation reflected in middle infrared wavelengths (3.0–5.0 μm). *International Journal of Remote Sensing*, 20, 1017–1023.
- Boyd, D. S., & Duane, W. J. (2001). Exploring spatial and temporal variation in middle infrared reflectance (at 3.75 μm) measured from the tropical forests of West Africa. *International Journal of Remote Sensing*, 22, 1861–1878.
- Boyd, D. S., Wicks, T. E., & Curran, P. J. (2000). Use of middle infrared radiation to estimate the leaf area index of a boreal forest. *Tree Physiology*, 20, 755–760.
- Chase, T. N., Pielke, R. A., Kittel, T. G. F., Nemani, R. R., & Running, S. W. (2000). Simulated impacts of historical land cover changes on global climate in northern winter. *Climate Dynamics*, 16, 93–105.
- Cihlar, J., Latifovic, R., Chena, J., Trishchenko, A., Duc, Y., Fedosejevs, G., & Guindona, B. (2004). Systematic corrections of AVHRR image composites for temporal studies. *Remote Sensing of Environment*, 89, 217–233.
- Crutzen, P. J., & Andreae, M. O. (1990). Biomass burning in the tropics: Impact on atmospheric chemistry and biogeochemical cycles. *Science*, 250, 1669–1678.
- Evangelista, H., Maldonado, J., Godoi, R. H. M., Pereira, E. B., Koch, D., Tanizaki-Fonseca, K., Van Grieken, R., Sampaio, M., Setzer, A., Alencar, A., & Gonçalves, S. C. (2007). Sources and transport of urban and biomass burning aerosol black carbon at the South-west Atlantic coast. *Journal of Atmospheric Chemistry*, 56, 225–238.
- Florinsky, I. V., Kulagina, T. B., & Meshalkina, J. L. (1994). Influence of topography on landscape radiation temperature distribution. *International Journal of Remote Sensing*, 15, 3147–3153.
- França, H., & Setzer, A. W. (1998). AVHRR temporal analysis of a savanna site in Brazil. *International Journal of Remote Sensing*, 19, 3127–3140.

- França, H., & Setzer, A. W. (2001). AVHRR analysis of savanna site through a fire season in Brazil. *International Journal of Remote Sensing*, 22, 2449–2461.
- Fraser, R. S., & Kaufman, Y. J. (1985). The relative importance of aerosol scattering and absorption in remote sensing. *IEEE Transactions on Geoscience and Remote Sensing*, 23, 525–633.
- Gesell, G. (1989). An algorithm for snow and ice detection using AVHRR data: An extension to the APOLLO software package. *International Journal of Remote Sensing*, 10, 897–905.
- Goita, K., & Royer, A. (1997). Surface temperature and emissivity separability over land surface from combined TIR and SWIR AVHRR data. *IEEE Transactions on Geoscience and Remote Sensing*, 35, 718–733.
- Holben, B. N., & Shimabukuro, Y. E. (1993). Linear mixing model applied to coarse spatial resolution data from multi-spectral satellite sensors. *International Journal of Remote Sensing*, 14, 2231–2240.
- Holben, B. N., Vermote, E., Kaufman, Y. J., Tanre, D., & Kalb, V. (1992). Aerosol retrieval over land from AVHRR data – Application for atmospheric correction. *IEEE Transactions on Geoscience and Remote Sensing*, 30, 212–222.
- Holben, B. N., Eck, T. F., Slutsker, I., Tanre, D., Buis, J. P., Setzer, A., Vermote, E., Reagan, J. A., Kaufman, Y. J., Nakajima, T., Lavenu, F., Jankowiak, I., & Smirnov, A. (1998). AERONET a federated instrument network and data archive for aerosol characterization – An overview. *Remote Sensing of Environment*, 66, 1–16.
- Jiang, G., Li, Z., & Nerry, F. (2006). Land surface emissivity retrieval from combined mid-infrared and thermal infrared data of MSG-SEVIRI. *Remote Sensing of Environment*, 105, 326–340.
- Jin, Y., & Roy, D. P. (2005). Fire-induced albedo change and its radiative forcing at the surface in northern Australia. *Geophysical Research Letters*, 32, L13401. doi:10.1029/2005GL022822.
- Kaufman, Y. J. (1995). Remote sensing of direct and indirect aerosol forcing. In R. J. Charlson, & J. Heintzenberg (Eds.), *Aerosol forcing of climate* (pp. 298–332). London: Wiley.
- Kaufman, Y. J., & Remer, L. (1994). Detection of forests using mid-IR reflectance: An application for aerosol studies. *IEEE Transactions on Geoscience and Remote Sensing*, 32(3), 672–683.
- Koren, I., Kaufman, Y. J., Remer, L. A., & Martins, J. V. (2004). Measurement of the effect of Amazon smoke on inhibition of cloud formation. *Science*, 303, 1342–1345.
- Lambin, E. F., & Geist, J. (2006). *Land-use and land-cover change – Local processes and global impacts, Series: Global Change – The IGBP Series*.
- Le Page, Y., Pereira, J. M. C., Trigo, R. M., DaCamara, C. C., Oom, D., & Mota, B. (2007). Global fire activity patterns (1996–2006) and climatic influence: An analysis using the World Fire Atlas. *Atmospheric Chemistry and Physics*, 8, 1911–1924.
- Li, Z., & Becker, F. (1993). Feasibility of LST and emissivity determination from NOAA/AVHRR data. *Remote Sensing of Environment*, 43, 1–20.
- Luvall, J. C., & Holbo, H. R. (1991). Thermal remote sensing methods in landscape ecology. *Quantitative methods in landscape ecology, ecological studies* (pp. 127–152). New York: Springer-Verlag.
- Menon, S., Hansen, J., Nazarenko, L., & Luo, Y. (2002). Climate effects of black carbon in China and India. *Science*, 297, 2250–2253.
- MODIS Characterization Support Team – MCST (2006). *MODIS Level 1B Product User's Guide*: NASA/Goddard Space Flight Center available at <http://www.mcst.ssaai.biz/mcstweb/documents/M1054.pdf>.
- Nemani, R., Pierce, L., Running, S., & Goward, S. (1993). Developing satellite-derived estimates of surface moisture status. *Journal of Applied Meteorology*, 32, 548–557.
- Nerry, F., Petitcolin, F., & Stoll, M. -P. (1998). Bidirectional reflectivity in AVHRR channel 3: Application to a region in northern Africa. *Remote Sensing of Environment*, 66, 298–316.
- Nobre, C. A., Mattos, L. F., Dereczynski, C. P., Tarasova, T. A., & Trosnikov, I. V. (1998). Overview of atmospheric conditions during the Smoke, Clouds, and Radiation-Brazil (SCAR-B) field experiment. *Journal of Geophysical Research*, 103, 31809–31820.
- Penner, J. E., Dickinson, R. E., & O'Neill, C. A. (1992). Effects of aerosol from biomass burning on the global radiation budget. *Science*, 256, 1432–1433.
- Pereira, J. M. C. (1999). A comparative evaluation of NOAA/AVHRR vegetation indexes for burned surface detection and mapping. *IEEE Transactions on Geoscience and Remote Sensing*, 37(1), 217–226.
- Pereira, J. M. C. (2003). Remote sensing of burned areas in tropical savannas. *International Journal of Wildland Fire*, 12, 259–270.
- Peres, L. F., & DaCamara, C. C. (2004). LST and emissivity estimation based on the two-temperature method: Sensitivity analysis using simulated MSG/SEVIRI data. *Remote Sensing of Environment*, 91, 377–389.
- Petitcolin, F., & Vermote, E. (2002). Land surface reflectance, emissivity and temperature from MODIS middle and thermal infrared data. *Remote Sensing of Environment*, 83, 112–134.
- Pielke, R. A., Sr., Marland, G., Betts, R. A., Chase, T. N., Eastman, J. L., Niles, J. O., Niyogi, D. D. S., & Running, S. W. (2002). The influence of land-use change and landscape dynamics on the climate system – Relevance to climate change policy beyond the radiative effect of greenhouse gases. *Philosophical Transactions of the Royal Society of London*, 360, 1705–1719.
- Prata, A. J., Caselles, V., Coll, C., Sobrino, J. A., & Ottle, C. (1995). Thermal remote sensing of LST from satellites: Current status and future prospects. *Remote Sensing Reviews*, 12, 175–224.
- Price, J. C. (1989). Quantitative aspects of remote sensing in the thermal infrared. *Theory and Applications of Optical Remote Sensing* (pp. 578–603). New York: John Wiley and Sons.
- Prins, E. M., Feltz, J. M., Menzel, W. P., & Ward, D. E. (1998). An overview of GOES-8 diurnal fire and smoke results for SCAR-B and 1995 fire season in South America. *Journal of Geophysical Research*, 103, 31821–31835.
- Reinhardt, T. E., Ottmar, R. D., & Castilla, C. (2001). Smoke impacts from agricultural burning in rural Brazilian Town. *Journal of the Air & Waste Management*, 51, 443–450.
- Roger, J. C., & Vermote, E. F. (1998). A method to retrieve the reflectivity signature at 3.75 μm from AVHRR data. *Remote Sensing of Environment*, 64, 103–114.
- Rosenfeld, D. (1999). TRMM observed first direct evidence of smoke from forest fires inhibiting rainfall. *Geophysical Research Letters*, 26, 3105–3108.
- Roy, D. P., Giglio, L., Kendall, J. D., & Justice, C. O. (1999). Multi-temporal active-fire based burn scar detection algorithm. *International Journal of Remote Sensing*, 20, 1031–1038.
- Ruff, I., & Gruber, A. (1983). Multispectral identification of clouds and earth surfaces using AVHRR data. *Proceedings of the 5th Conference on Atmospheric Radiation, Baltimore, MD, October 31–November 4* (pp. 475–478). Boston, MA: American Meteorological Society.
- Salisbury, J. W., & D'Aria, D. M. (1994). Emissivity of terrestrial materials in the 3–5 μm atmospheric window. *Remote Sensing of Environment*, 47, 345–361.
- Schutt, J. B., & Holben, B. N. (1991). Estimation of emittances and surface temperatures from AVHRR data. *Proceedings IGARSS 91, Helsinki, Finland* (pp. 1179–1181).
- Sellers, P. J., Bounoua, L., Collatz, G. J., Randall, D. A., Dazlich, D. A., Los, S. O., Berry, J. A., Fung, I., Tucker, C. J., Field, C. B., & Jensen, T. G. (1996). Comparison of radiative and physiological effects of doubled atmospheric CO₂ on climate. *Science*, 271, 1402–1406.
- Seemann, S. W., Borbas, E., Li, J., Menzel, W. P., & Gumley, L. M. (2006). *MODIS Atmospheric Profile Retrieval Algorithm Theoretical Basis Document* Madison: University of Wisconsin-Madison available at http://modis-atmos.gsfc.nasa.gov/_docs/MOD07:MYD07_ATBD_C005.pdf.
- Shimabukuro, Y. E., Holben, B. N., & Tucker, C. J. (1994). Fraction images derived from NOAA AVHRR data for studying the deforestation in the Brazilian Amazon. *International Journal of Remote Sensing*, 15, 517–520.
- Wang, Z. (1999). *MODIS Land-Surface Temperature Algorithm Theoretical Basis Document (LST ATBD): Version 3.3* Santa Barbara: University of California available at <http://www.ices.ucsba.edu/modis/atbd-mod-11.pdf>.
- Zhao, M., Pitman, A., & Chase, T. N. (2001). The impacts of land cover change on the atmospheric circulation. *Climate Dynamics*, 17, 467–477.

GLOBAL BURNED-LAND ESTIMATION IN LATIN AMERICA USING MODIS COMPOSITE DATA

EMILIO CHUVIECO,^{1,13} SERGIO OPAZO,² WALTER SIONE,³ HÉCTOR DEL VALLE,⁴ JESÚS ANAYA,⁵ CARLOS DI BELLA,⁶ ISABEL CRUZ,⁷ LILIA MANZO,⁸ GERARDO LÓPEZ,⁷ NICOLAS MARI,⁶ FEDERICO GONZÁLEZ-ALONSO,⁹ FABIANO MORELLI,¹⁰ ALBERTO SETZER,¹⁰ IVAN CSISZAR,¹¹ JON ANDER KANPANDEGI,⁶ AITOR BASTARRIKA,¹² AND RENATA LIBONATI¹⁰

¹Departamento de Geografía, Colegios 2, Universidad de Alcalá, Alcalá de Henares, Spain

²Escuela de Ciencia y Tecnologías Agropecuarias, Universidad de Magallanes, Punta Arenas, Chile

³UNLU (Universidad de Luján), Departamento de Ciencias Básicas, PRODITEL (Programa de Desarrollo e Investigación en Teledetección) y UADER-CEREGeo (Centro Regional de Geomática, Universidad de Entre Ríos), Luján, Argentina

⁴Centro Nacional Patagónico (CENPAT), CONICET (Comisión Nacional de Ciencia y Tecnología), Puerto Madryn, Argentina

⁵Facultad de Ingeniería Ambiental, Universidad de Medellín, Medellín, Colombia

⁶Instituto de Clima y Agua, INTA (Instituto Nacional de Tecnología Agropecuaria–Castelar, Buenos Aires, Argentina)

⁷CONABIO (Comisión Nacional para el Conocimiento y Uso de la Biodiversidad), Mexico City, Mexico

⁸Instituto de Geografía, Universidad Nacional Autónoma de México, Mexico City, Mexico

⁹Centro de Investigación Forestal (CIFOR), Instituto Nacional de Investigación y Tecnología Agraria y Alimentaria (INIA), Madrid, Spain

¹⁰Centro de Previsão de Tempo e estudos Climáticos, Instituto Nacional de Pesquisas Espaciais, Sao Jose dos Campos, Brazil

¹¹University of Maryland, Department of Geography, College Park, Maryland 20742 USA

¹²Departamento de Ingeniería Topográfica, Universidad del País Vasco, Vitoria, Spain

Abstract. This paper presents results of the AQL2004 project, which has been developed within the GOF-C-GOLD Latin American network of remote sensing and forest fires (RedLatif). The project intended to obtain monthly burned-land maps of the entire region, from Mexico to Patagonia, using MODIS (moderate-resolution imaging spectroradiometer) reflectance data. The project has been organized in three different phases: acquisition and preprocessing of satellite data; discrimination of burned pixels; and validation of results. In the first phase, input data consisting of 32-day composites of MODIS 500-m reflectance data generated by the Global Land Cover Facility (GLCF) of the University of Maryland (College Park, Maryland, USA) were collected and processed. The discrimination of burned areas was addressed in two steps: searching for “burned core” pixels using postfire spectral indices and multitemporal change detection and mapping of burned scars using contextual techniques. The validation phase was based on visual analysis of Landsat and CBERS (China–Brazil Earth Resources Satellite) images. Validation of the burned-land category showed an agreement ranging from 30% to 60%, depending on the ecosystem and vegetation species present. The total burned area for the entire year was estimated to be 153 215 km². The most affected countries in relation to their territory were Cuba, Colombia, Bolivia, and Venezuela. Burned areas were found in most land covers; herbaceous vegetation (savannas and grasslands) presented the highest proportions of burned area, while perennial forest had the lowest proportions. The importance of croplands in the total burned area should be taken with reserve, since this cover presented the highest commission errors. The importance of generating systematic products of burned land areas for different ecological processes is emphasized.

Key words: biomass burning; burn area index; burn scars; burned area; forest fires; Latin America; MODIS; normalized burn ratio; remote sensing.

INTRODUCTION

Forest fires have an important role in global ecological and climate systems, being responsible for a significant part of greenhouse gas emissions to the atmosphere (van der Werf et al. 2004) and for land degradation and soil erosion processes (Levine 1996). Additionally, many studies have identified wildland fires

as the most comprehensive tool for forest clearing in the tropical regions (Roberts 2000), and therefore the importance of studying global patterns of fire occurrence increases. According to Lioussé et al. (2004), the amount of CO₂ emissions derived from biomass burning in Latin America is eight times larger than its emissions derived from fossil fuel combustion (see Plate 1). Therefore, it is critical to improve current estimations of burned land areas in the region, from both an ecological and management point of view.

Statistics on wildland fire are generally available in developed countries, while in other areas the estimations

Manuscript received 31 December 2006; revised 24 April 2007; accepted 2 August 2007. Corresponding Editor: E. Cuevas.

¹³ E-mail: emilio.chuvieco@uah.es

are generally poor or not available. According to the latest Food and Agriculture Organization of the United Nations (FAO) statistics (FAO 2006) from 1998 to 2002 more than 3 million ha were burned in Latin America. These estimates are very low compared to other projects based on satellite data for the same region (Boschetti et al. 2004) and could be related to the lack of consistent assessment of burned areas in most countries.

The use of remotely sensed data is a sound alternative to traditional field methods for estimating burned-land areas. Satellite observation data of Earth provide timely, cost effective, and spatially comprehensive views of fire-affected areas and fire occurrence patterns (Di Bella et al. 2006). The use of these data for fire effects assessment has grown notably in the last decades, using both high and low resolution satellite sensors (Ahern et al. 2001). Global approaches to map burn areas were based on NOAA-AVHRR images during the 1990s, and multi-temporal comparisons between spectral vegetation indices was a common technique used (Kasischke and French 1995, Martín and Chuvieco 1995, Barbosa et al. 1999, Pereira 1999), although some combinations of thermal infrared and shortwave channels were also used (Fraser et al. 2000).

More recently, other sensors with greater sensitivity to discriminate burn scars have been used to create a global inventory of burned areas. In 2000, two worldwide projects were developed: the GBA2000 (Tansey et al. 2004) and the GLOBSCAR (Simon et al. 2004). The former was based on SPOT-Vegetation data and it was coordinated by the Joint Research Center of the European Union. The latter was an initiative of the European Space Agency, and it was based on ERS-2 ATSR images. Finally, the MODIS program soon plans to release a standard product on burned land areas at the global scale, which will be based on a multitemporal change detection approach to analyze differences between modeled and actual reflectance, and to take into account bidirectional reflectance distribution function (BRDF) corrections (Roy et al. 2005b). Other authors have used active fire detections derived from thermal channels to obtain global estimates of burned areas (Giglio et al. 2006), but the accuracy of this approach strongly varies in different ecozones.

One of the bottlenecks of these global approaches is the assessment of results, which is very complex and costly. However, proper assessment of global products is becoming increasingly important in order to reduce uncertainties when using them as an input to other estimation models (Boschetti et al. 2004).

The critical need to assess global products has led to the creation of regional networks, which can take advantage of local expertise to fine tune global algorithms and make them more suitable for specific ecosystems. The Global Observation of Forest and Land Cover Dynamics (GOFC-GOLD) program is a coordinated international effort working to provide ongoing space-based and in situ observations of forests and other

vegetation cover for the sustainable management of terrestrial resources and to obtain an accurate, reliable, quantitative understanding of the terrestrial carbon budget (information *available online*).¹⁴ Inside this program, the Fire Implementation Team has encouraged the creation of regional networks, which provide a mechanism for the sharing of resources and expertise. Within this framework, a Latin American GOFC-GOLD network (named RedLatif) was created in 2002. RedLatif intended to foster the relationships between scientists working in remote sensing and fire applications throughout the region. One of the first objectives of this network was the creation of a burned land map of the region, which could be used to assess the spatial and temporal patterns of fire occurrence at the continental scale.

The importance of Latin America in the context of fire occurrence and global deforestation is evident. A recent report from the FAO (2006), which focused on the evolution of forested areas between 2000 and 2005, emphasized the importance of Latin America in global deforestation rates. In fact, this region has the highest rate of annual forest conversion, with almost 5 million ha per year, which accounts for 67% of the world's deforestation. A great amount of this deforestation is caused by wildland fires (Cochrane et al. 1999), and therefore it is critical to better understand fire occurrence patterns in the region. Additionally, Latin American biomass burning is a very important source of global gas emissions, around 16% according to recent studies (van der Werf et al. 2006).

The main goal of this paper is to present methods to generate a monthly map of burned areas in Latin America for 2004 and to analyze the spatial and temporal patterns of fire occurrence derived from this product. This project, developed within the RedLatif network, was named AQL2004 (Area Quemada en Latinoamerica, the Spanish translation of Burned Land Areas in Latin America for 2004). The project was intended to improve current estimations of burned areas in the region, thus providing input to global analysis of ecological impacts of fires, to better understand the relations between fire occurrence and biodiversity, and to improve the assessment of atmospheric emissions derived from wildland fires. The extension of the area should facilitate the creation of a global perspective of spatial and temporal patterns of fire occurrence that may be applicable to other regions. Considering the limitations of the input data available for the project, a burn patch size of 250 hectares was selected as the minimum mapping unit.

The AQL2004 project was proposed on a volunteer basis as part of the RedLatif network activity, and without specific funding. Therefore, input data for generation and validation of the product were restricted

¹⁴ <http://www.fao.org/gtos/gofc-gold/index.html>

TABLE 1. MODIS (moderate-resolution imaging spectroradiometer) spectral bands of the 32-day reflectance composite.

Band number	Wavelength (nm)	Spectral region
1	620–670	red
2	841–876	near infrared
3	459–479	blue
4	545–565	green
5	1230–1250	SWIR
6	1628–1652	SWIR
7	2105–2155	SWIR

Note: SWIR is short-wave infrared reflectance.

to satellite data that was publicly available. As we will comment later, this limitation has impacted the results of the project, but it has also provided a good cooperation scenario that might be useful for other active networks. External funds were limited to coordination activities (three meetings) and were obtained from the NASA-START program (information *available online*).¹⁵

METHODS

Image acquisition and preprocessing

Moderate-resolution imaging spectroradiometer (MODIS) images were selected for the project, since they provided a good spatial, spectral and temporal resolution while being freely downloadable (*available online*).¹⁶ The MODIS program offers a wide range of standard products covering land, atmospheric, and water applications (information *available online*).¹⁷ The standard reflectance product MOD09 is an 8-day composite of atmospherically corrected and calibrated surface reflectances at 500×500 m pixel size, covering the whole Earth in tiles of 1200×1200 km using a Sinusoidal Projection system. Additionally, the MODIS program offers another reflectance product (MOD43) that includes a correction of the observation and illumination effects (BRDF). This product includes the same bands as the MOD09, but with lower spatial (1000×1000 m) and temporal (16-day) resolution. Finally, the University of Maryland's Global Land Cover Facility (GLCF) compiled 32-day composites of the MOD09 product. This is not a standard product of the MODIS program, but it has been used for land cover analysis, and it is also freely available (Townshend et al. 2003). The product has the same spatial and spectral resolution as MOD09 and chooses for each pixel the second lowest albedo value among the four 8-day composites that formed a single 32-day product (*available online*).¹⁸ This criterion is used to reduce clouds and cloud shadows in the final composites. The product includes the seven reflectance bands of MODIS with 500×500 m pixel size

(Table 1). This product is joined together by continents as a mosaic and uses the Goode Interrupted Homolosine projection. After analyzing the advantages and disadvantages of the different products, the 32-day composites produced by GLCF were selected, since they provided an adequate temporal resolution for our project (monthly burn-area estimations) and reduced the effects of cloud and cloud shadow contamination of the 8-day composites. In addition, this product does not require the user to perform geometric transformations to obtain continental mosaics, while the standard MODIS products are offered in 1200×1200 km tiles.

Twelve 32-day composites were downloaded from the GLCF site, covering the period from December 2003 through December 2004. The complete mosaic of North and South America was divided in 12 subregions, which were assigned to each of the participant groups. The aim of each group was to develop a basic discrimination algorithm for the study area that could be later compared with other areas for deriving a burned land algorithm that could be used for the entire region.

In spite of the temporal compositing of daily data, cloud contamination was still observed in the 32-day composites, especially in some tropical regions of the Amazon Basin and Central Venezuela. A cloud screening was performed with three reflectance bands using the following criteria: if (band 2 > 25 AND band 3 > 60 AND band 5/band 3 > 0.7) then label as cloud, where bands 2, 3, and 5 are MODIS reflectance in percentage.

To avoid confusion between burn scars and low reflectance over some non-vegetated areas, such as dark soils or water, a vegetation mask was derived from the Vegetation Continuous Fields (VCF) data set (Hansen et al. 2002). The product was produced by the GLCF at the University of Maryland from the same 32-day MODIS composite data used in our project and it was generated from spectral unmixing analysis (Hansen et al. 2005). The VCF product was downloaded from the GLCF web site and included three data files, with percentage of trees, bare soil, and herbaceous vegetation, covering the period between November 2000 and November 2001 (*available online*).¹⁹ The values are scaled between 1 and 100 and the sum of the three layers estimates 100% of ground cover.

For the AQL2004 project, the “non-burnable” category was defined as pixels that had >80% of bare soil, or alternatively those that met two conditions: <70% herbaceous and <10% trees. Otherwise, they were considered areas that could be burned. Considering the great variety of ecosystems in Latin America, this criterion was not applied at the beginning of the process to avoid potential errors in areas of low vegetation coverage. It was used as a filter at the final stages, but regional thresholds were also applied in the semi-arid regions of Argentina and Chile.

¹⁵ <http://www.start.org/Program/GOFC.html>

¹⁶ <http://modis.gsfc.nasa.gov/about/>

¹⁷ <http://modis.gsfc.nasa.gov/data/dataproduct/index.php>

¹⁸ <http://glcfapp.umiacs.umd.edu:8080/esdi/index/jsp>

¹⁹ <http://glcf.umiacs.umd.edu/data/vcf/>

Burned-land discrimination methods

Mapping of burn scars was based on a two-step approach. The first step was dedicated to selecting the most severely burned pixels in each burn scar. The second step was aimed at improving the mapping of each burned area by including the neighboring pixels of those previously identified. The goal of the first phase was to reduce, as much as possible, the commission errors (pixels labeled as burned areas that were not actually burned), while the objective of the second phase was to reduce the omission error (pixels that were indeed burned and were not classified as such; Chuvieco et al. 2002). This two-step burned-land mapping approach should produce better results than trying to classify all the burn scars in a single algorithm, since it was expected to find a great diversity of spectral signatures in such a large territory.

Discrimination of “core” burned pixels.—The first phase of our discrimination algorithm was based on applying multiple thresholds to the postfire images as well as on multitemporal change detection. From the original 32-day reflectance products, two vegetation indices were computed to improve the separability of burned and unburned areas. The normalized burn ratio (NBR) was proposed in the 1990s to discriminate burned areas (López García and Caselles 1991, Key and Benson 2006) based on the contrast between near-infrared (NIR) and short-wave infrared (SWIR) reflectance:

$$\text{NBR} = \frac{\rho_{\text{SWIR}} - \rho_{\text{NIR}}}{\rho_{\text{NIR}} + \rho_{\text{SWIR}}} \quad (1)$$

where ρ_{SWIR} and ρ_{NIR} are NIR (generally from 700 to 900 nm) and SWIR (from 2100 to 2300 nm), respectively. The index has a range from -1 to 1 , with the largest number being the most severe burn. Recently, this index has been extensively used in the framework of the FIREMON (Fire Effects Monitoring and Inventory System) project (Key and Benson 2006) and will be the basis for mapping burn severity in the United States from Landsat-TM/ETM+ data (*available online*).²⁰ We should clarify that, for this paper, the NBR has been formulated after changing the sign of the numerator ($\rho_{\text{SWIR}} - \rho_{\text{NIR}}$ instead of $\rho_{\text{NIR}} - \rho_{\text{SWIR}}$) to keep the scale consistent with the index definition, since reflectance in the SWIR is higher than in the NIR for most recently burned areas. Since this index is intended to discriminate burn severity, only high values of the index should be of interest for the first phase of the project, leaving the intermediate values to be classified in the second phase.

In addition to the NBR, a burned area index (BAI) was also used in this project to confirm that the pixels selected in the first phase were as close as possible to charcoal signal, thus avoiding false alarms with other potential mixtures of dark reflectance objects. The BAI was developed initially for NOAA-AVHRR images (Martín 1998) and was recently adapted to MODIS data, also

TABLE 2. Thresholds to determine burned-land core pixels in the first phase of the mapping algorithm.

Variable	Threshold value
Postfire image	
BAI MODIS	>99
NBR	>0
Multitemporal change	
BAI MODIS _t – BAI MODIS _{t-1}	>1.74
NBR _t – NBR _{t-1}	>0.35

Note: BAI is burned area index; NBR is the normalized burn ratio, which discriminates burned areas based on the contrast between near-infrared (NIR) and short-wave infrared (SWIR) reflectance.

using the NIR and SWIR bands (Martín et al. 2005). This index is defined as the inverse quadratic distance of every pixel to the convergence point of charcoal:

$$\text{BAI} = \frac{1}{(\text{Pc}_{\text{SWIR}} - \rho_{\text{SWIR}})^2 + (\text{Pc}_{\text{NIR}} - \rho_{\text{NIR}})^2} \quad (2)$$

where ρ_{SWIR} and ρ_{NIR} have the same meaning as in Eq. 1, and Pc_{SWIR} and Pc_{NIR} are the convergence points in the same bands. After an analysis of sampled burned pixels in different types of fires, they were fixed as 0.2 and 0.08, respectively.

The thresholds for discriminating burned pixels were based on NBR and BAI values of the postfire image, as well as the multitemporal comparisons of these indices with previous images. These images were computed by postfire (t) minus prefire ($t - 1$) values. The prefire conditions were taken from the 32-day composite previous to the one that was being analyzed, starting in January 2004, which was the first target composite and was compared to December 2003 and ending in December 2004.

The specific threshold values were obtained from a sample of 485 MODIS pixels extracted from burn scars in Argentina, Colombia, and Brazil and covering different months of the year. As said previously, the main goal of the first phase was to reduce commission errors to a minimum, and therefore the selection of thresholds was based on a low percentile of the total pixels classified as burned areas in the sampling sites. The percentile was changed iteratively to test which value provided consistent classification in all study sites and land-cover types being analyzed. The final values are included in Table 2. With these values, 12% of the sampled pixels were detected as burn areas. This implies a large omission error, but our main goal in this phase was to avoid confusion with other covers.

The final step of the first phase was to eliminate small clusters of pixels. Since the minimum target burn scar was 250 ha, small groups of pixels were not very reasonable and would have created severe noise. Therefore all patches with fewer than five pixels (125 ha) were eliminated. It was expected that the final patches would be greater than this size after the contextual algorithm was applied.

²⁰ (http://burnseverity.cr.usgs.gov/fire_main.asp)

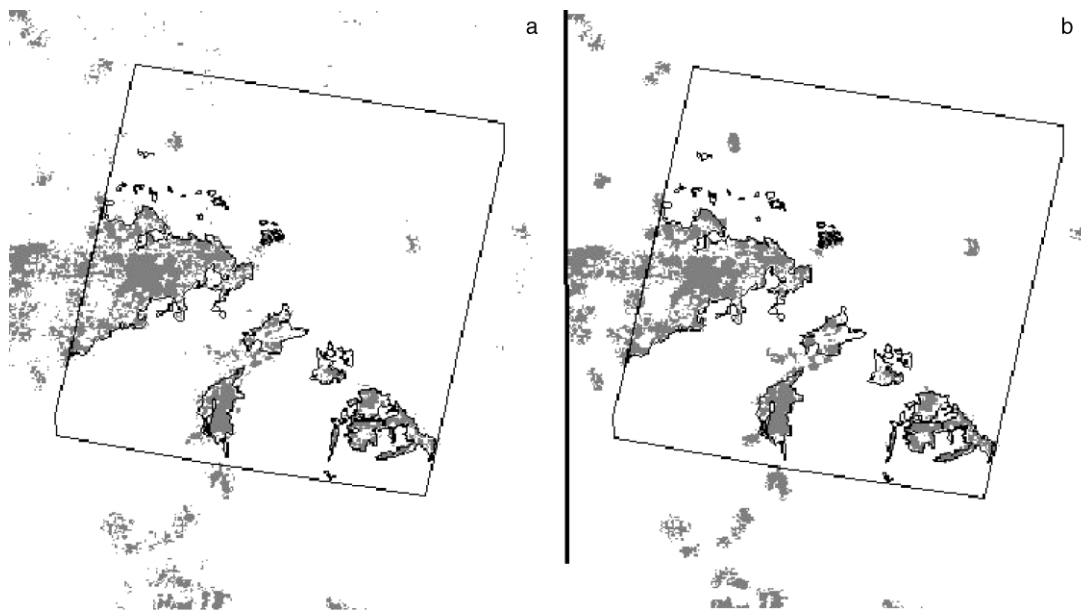


FIG. 1. Effect of changing window size in the regional context algorithm: (a) 3×3 pixels, (b) 21×21 pixels. The area shown covers a MODIS image of central Brazil.

Contextual algorithm.—The second step in our processing method was intended to refine the discrimination of burn scars from those areas previously detected as “core” burned pixels. In order to do this, a contextual algorithm was developed to take into account the similarity of neighboring pixels to those previously labeled as burned areas. In this case, the goal was to reduce omission errors by including those pixels that might be less severely burned or those with a weaker charcoal signal.

The criteria to extend the core pixels to their surroundings were based on the geographical and spectral similarity of targeted pixels with those already identified as burned areas. As a criterion of geographical similarity, a maximum distance for inclusion was established, while the spectral criterion to add a pixel to the burned area was based on comparing the BAI values of that pixel with those in the vicinity. The comparison of pixel values with the local neighborhood has been previously used in burned land mapping (Fernández et al. 1997), and it is routinely used in fire detection algorithms (Martín et al. 1999). For this project, the BAI was used as a measure of charcoal similarity, and the criterion to include a pixel was based on whether that pixel had a BAI value above the mean of the surroundings, as defined by a certain window size centered in that pixel. In summary, a pixel would be added to a burn scar when its distance to any pixel in the burn scar was below a certain threshold and when its BAI value was above the mean BAI of the vicinity. Several maximum distances to the core pixels were analyzed (from 3 to 11 km) studying their performance against sampled burned areas from which burn perim-

eters were available. A similar approach was applied to find out the most convenient window size to extract mean BAI value for estimating the neighborhood patterns. Window sizes from 3×3 pixels to 21×21 pixels were tested (Fig. 1). The effects of different window sizes were not evident, although larger windows tended to be more consistent in patchy areas. Therefore, a window of 21×21 pixels was finally selected.

Analysis

Geographical patterns of the results were based on latitude and longitude fringes on one hand and land cover types on the other. The former was aimed at providing a zoning analysis of fire occurrence, while the latter was intended to offer a global view of the most affected ecosystems. The land cover layer was extracted from the MOD12Q1 (v.4) standard MODIS product, generated by the University of Boston (*available online*).²¹ This product was generated from MODIS data from the period 1 January 2001 to 31 December 2001, and it is based on reflectance data, spectral vegetation indices and surface texture information. The product is offered for different land-cover classification systems. We selected the classification system defined by the International Geosphere Biosphere Program (IGBP) land cover project (Belward 1996), which includes 17 global land cover categories. The product was available in Interrupted Goode Homolosine projection, thus facilitating the comparison with the AQL2004 results. The world mosaic was downloaded, and the Latin

²¹ <http://www-modis.bu.edu/landcover/userguide/Intro.html>

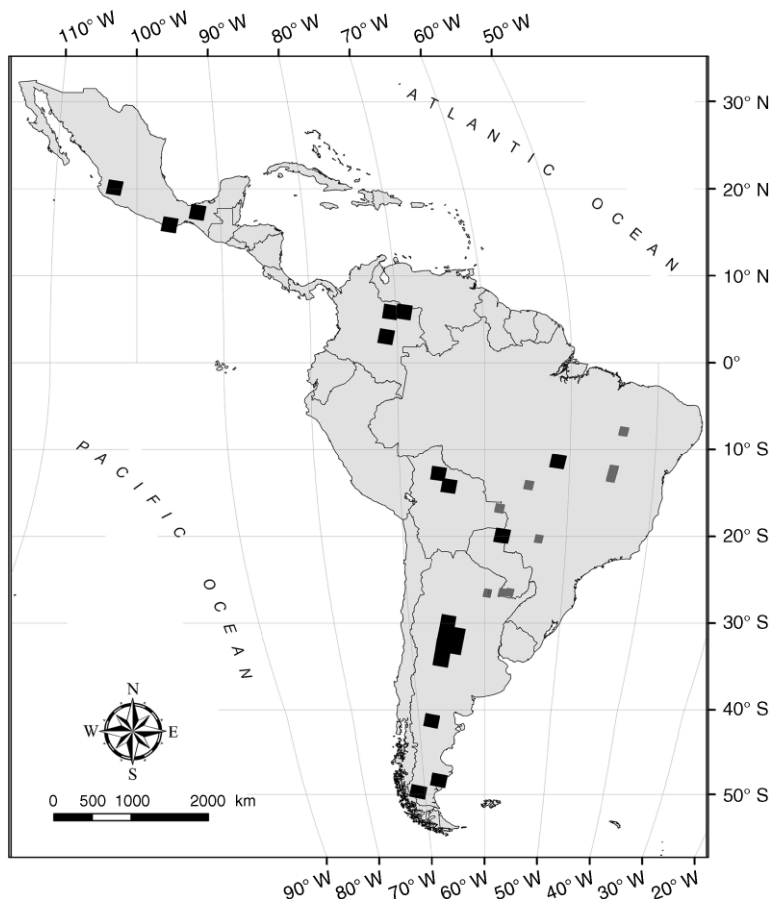


FIG. 2. Validation sites where high-resolution satellite data were processed. Dark boxes refer to Landsat-TM/ETM+ data; gray boxes are CBERS images.

American region was extracted for further analysis (available online).²²

Assessment

Accuracy assessment is a critical component of any method to generate spatial information, but it has been greatly emphasized in studies based on remotely sensed images (Congalton and Green 1999). Most local studies include sound procedures to validate the results, based on field sampling or higher spatial resolution imagery. However, this task is especially complex when generating global products since it involves covering large areas with a wide diversity of potential errors. However, the importance of validating global variables is acknowledged by most global scope projects, and networks of scientists are built upon those projects to ensure accuracy assessment. For instance, the MODIS program has a specific task group dedicated to product validation (Morissette et al. 2002), and the team involved in the MODIS burned-land product has already produced an

extensive validation protocol for some study sites within the SAFARI campaign (Roy et al. 2005a). In burned-land mapping, neither the GBA2000 nor the GLOBSCAR project have undertaken a full validation strategy, although some efforts have been proposed for retrospective validation (Boschetti et al. 2006).

The AQL2004 project was designed by a network of local scientists, therefore product validation was considered a priority from the beginning of the project. Considering the financial constraints of the project, the validation was based on high-resolution satellite images that were donated by regional space agencies. The Argentinean agency CONAE (Comisión Nacional de Actividades Espaciales), the Brazilian agency INPE (Instituto Nacional de Pesquisas Espaciales), and the Mexican agency CONABIO (Comisión Nacional para el Conocimiento y Uso de la Biodiversidad) provided Landsat-TM/ETM+ (30-m pixel size), CBERS (China-Brazil Earth Resources Satellite; 20 m), and SPOT (20 m) images, respectively, for the validation of the burn-scar product. Fig. 2 shows the images that were used for validation of the whole project.

²² (<http://duckwater.bu.edu/lc/mod12q1.html>)

The validation itself was based on visual interpretation of those higher resolution images from which fire perimeters were derived. The images were previously converted to the Goode Homolosine Projection, to match the MODIS input data. Visual analysis has been widely used for discriminating burn scars (Roy et al. 2005a), since burned areas generally have a distinct color and shape pattern. Visual interpretation was digitized on screen, and vector files were extracted to cross tabulate with results from our burned land algorithm to generate confusion matrices (agreement between the results and the high-resolution data). Common measures of accuracy and error (omission and commission errors, and global accuracies; Congalton and Green 1999) were computed.

Considering the great differences in spatial resolution between the two sets of images (MODIS, 500 m and TM/ETM/CBERS 20–30 m), the interpretation of the omission and commission errors from this cross tabulation must be done cautiously, since some of them should in fact be associated to misregistration or differences in spatial coverage of both data sets. To reduce the impact of these problems, other validation techniques were carried out. An alternative to validate our burned area results was to extract the proportion of burned area in both MODIS and high-resolution images for a grid of regular cells (in this case, a 5×5 km grid was selected). This approach has been suggested by other authors (Roy et al. 2005a) and facilitates a spatial statistical assessment that is less affected by registration problems or differences in pixel size. This approach was restricted to those images with a significant proportion of burned area. Otherwise, the comparison is statistically meaningless.

Additionally, to test the effect of fire size on the quality of discrimination, a global comparison between the number of burn patches detected by MODIS and those detected by high-resolution images was performed. In this case, we completed that analysis only for the validation sites that have a great number and diversity of burn scars. Also, we considered that a burn patch was detected when at least 10% of its area was identified in the MODIS images.

Finally, our results were also compared to the active fires detected by the MODIS program. Although they are produced by the same sensor, active-fire products are independent from burned-land products because they are based on a completely different physical principle (Justice et al. 2002). Active fire detection is based on middle infrared bands (3–5 μm wavelength), which are the most sensitive to detect high-temperature targets, and therefore the fires are only detectable when they are active, while burned-land maps are based on postfire conditions. Therefore, since the two products are independent, their agreement indicates a greater likelihood of accuracy (Roy et al. 2005b). For this project, all active fires detected by the MODIS program (Giglio et al. 2003) for 2004 were downloaded and grouped in 25 \times

25 km cell sizes (data *available online*).²³ The number of active fires per month was compared with the total burned area discriminated by our algorithm. A total number of 29 175 cells was obtained for South America and 5174 for Mexico and Central America, after removing those where water covered more than 95% of the cell area.

RESULTS

Geographical analysis of burned areas

Fig. 3 includes the summary of the project results, with the geographical distribution of burned areas discriminated in the different periods of the MODIS 32-day composites. A total number of 14 446 burned land polygons were identified by the AQL2004 algorithm, which covered an area of 153 215 km². The most affected countries were Argentina, Brazil, Colombia, Bolivia, and Venezuela, which make up 90% of the total area burned. In relative terms, the AQL2004 results show that the most affected countries were Cuba, Colombia, Bolivia, Venezuela, and Argentina, all of which had >1.2% of the national territory burned (Table 3). The most continuous areas affected by biomass burnings are the savanna regions of Colombia and Venezuela, the boundaries of the evergreen forest in Brazil and Bolivia, and the Central and Northern provinces of Argentina. Central Cuba and the southern part of Guatemala were also noticeable. Scattered patches were observed in Mexico and Chile.

The burned areas affected a wide variety of land-cover types, but the herbaceous areas presented a much higher impact. In fact, grasslands, woody savannas, and savannas accounted for 63% of the total burned area detected in this project. For these categories the fire affected around 1.5% of the total area they cover in the region. Only croplands represented a higher proportion, with more than 2%.

The evergreen forest showed the higher ratio between the percentage of total area covered in the region and the percentage of total burned area (36%:7.22%), while the lower ratio was found for croplands and grasslands (8.04%:17.21%). This ratio implied that the percentage of burned area in evergreen forest was much lower than the total percentage of area covered by this category, being the opposite in the case of grasslands. In other words, according to our results, biomass burning had much less impact in evergreen forests than in grasslands. However, from a fire-emissions point of view, the importance of evergreen forests is obviously greater because they have much higher biomass loads.

Seasonal trends

Biomass burning followed seasonal dry periods in 2004, as it might be expected. Grasslands and herbaceous areas in the Northern Hemisphere were burned

²³ <http://maps.geog.umd.edu/firms/shapes.htm>

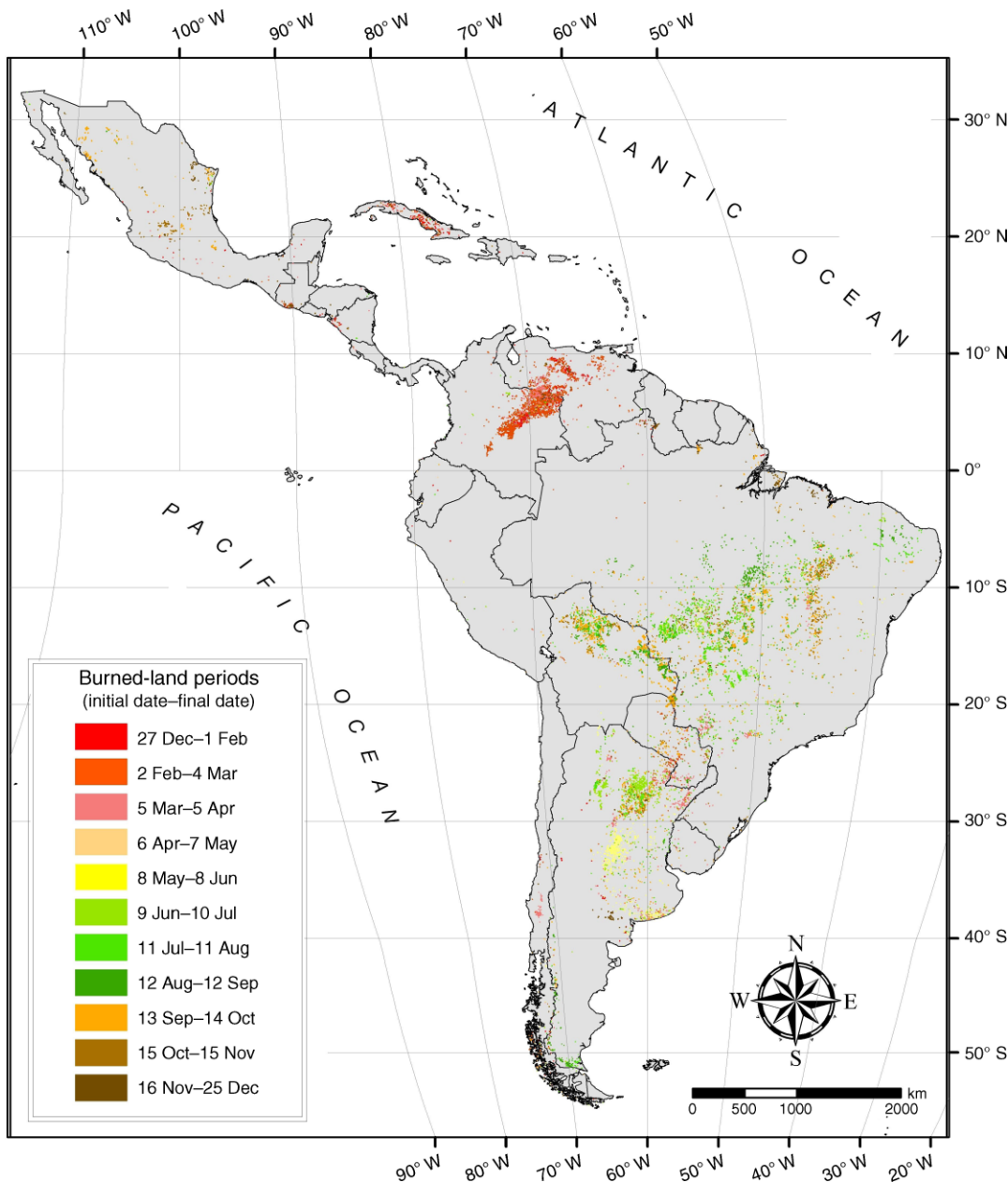


FIG. 3. Geographical distribution of burn scars for the different MODIS 32-day composites, December 2003 through December 2004.

mainly between January and the middle of March, while in the Southern Hemisphere the peak of fire occurrence was observed between July and September (Fig. 3). Seasonal distribution of burned areas for the most affected countries can be observed in Fig. 4. A clear burn-land peak during the dry season was observed for Colombia and Venezuela in the Northern Hemisphere (February), and Brazil and Bolivia in the Southern Hemisphere (September–October). Mexico had low fire occurrence in 2004, and the most affected months do not

clearly match the driest periods. Argentina presented an unexpected pattern, too, since most burned areas were detected between March and June.

The most common land covers in burned areas are shown in Fig. 5 for the different periods of analysis. The impact of fire on herbaceous vegetation was distributed throughout the year, although in the dry season (February in the Northern Hemisphere and August–September in the Southern Hemisphere) it accounted for an even larger percentage. An important percentage of

TABLE 3. Burned areas mapped in the AQL2004 project in the different 32-day periods.

Country	Burned area (km ²)												Total, all periods
	27 Dec– 1 Feb	2 Feb– 4 Mar	5 Mar– 5 Apr	6 Apr– 7 May	8 May– 8 Jun	9 Jun– 10 Jul	11 Jul– 11 Aug	12 Aug– 12 Sep	13 Sep– 14 Oct	15 Oct– 15 Nov	16 Nov– 25 Dec		
Argentina	542	1357	2953	6851	6803	7285	2701	1700	3321	667	1000	35 178	
Belize	0	0	0	0	0	0	0	0	0	11	0	11	
Bolivia	42	156	29	107	98	265	2139	5632	6453	1274	80	16 274	
Brazil	298	332	2135	2012	2010	5233	9744	12 510	12 687	4611	1560	53 131	
Chile	56	256	671	312	109	66	18	80	223	62	69	1921	
Colombia	4532	12 789	1602	0	0	86	32	85	134	10	180	19 449	
Costa Rica	0	15	34	0	0	0	0	0	0	0	0	48	
Cuba	1261	645	1052	54	0	0	19	0	0	120	170	3320	
Dominican Republic	23	0	0	0	0	0	0	0	0	0	0	23	
Ecuador	18	0	13	12	0	0	14	0	31	28	0	116	
El Salvador	30	0	0	0	0	0	0	0	0	0	21	51	
Guatemala	263	159	40	0	0	0	0	0	0	24	182	668	
Guyana	54	26	0	0	0	0	0	11	0	83	159	332	
Haiti	0	0	0	0	0	0	0	0	0	17	0	17	
Honduras	23	0	20	0	0	0	0	24	0	0	42	107	
Mexico	234	89	262	161	19	32	106	62	1907	1295	664	4829	
Nicaragua	223	40	19	0	0	0	26	0	0	9	30	347	
Panama	0	0	0	0	0	13	0	0	0	0	0	13	
Paraguay	46	753	877	24	24	162	57	518	1411	461	0	4333	
Peru	28	12	23	16	15	14	9	20	28	19	5	188	
Suriname	0	12	10	0	0	0	0	0	39	8	14	81	
Trinidad and Tobago	0	8	8	0	0	0	0	0	0	0	0	16	
Uruguay	6	12	67	9	9	7	37	30	34	24	27	260	
Venezuela	3567	6384	2041	0	0	41	0	0	0	55	414	12 501	
Total	11 246	23 041	11 854	9557	9087	13 203	14 901	20 670	26 266	8777	4613	153 215	

Notes: Dates (32-day measured periods) are shown as initial day and month through final day and month, beginning in December 2003 and ending December 2004. AQL2004 is Area Quemada en Latinoamerica (burned land areas in Latin America) for 2004.

the burned land was found in agricultural areas (17%). Shrubs were the dominant land cover in 8% of the burned area and they were distributed evenly throughout the year. The forested areas covered almost 10% of

the burn scars. From those areas, evergreen forests burned more than deciduous forest, although important proportions of deciduous forest were also burned in June/July and September.

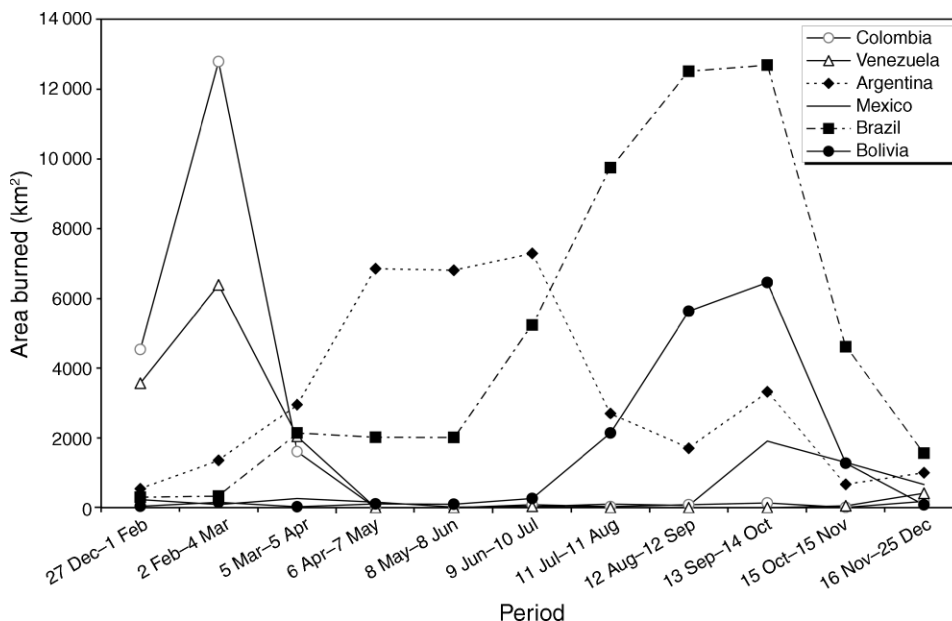


FIG. 4. Seasonal distribution of burned areas for different Latin American countries, December 2003 through December 2004.

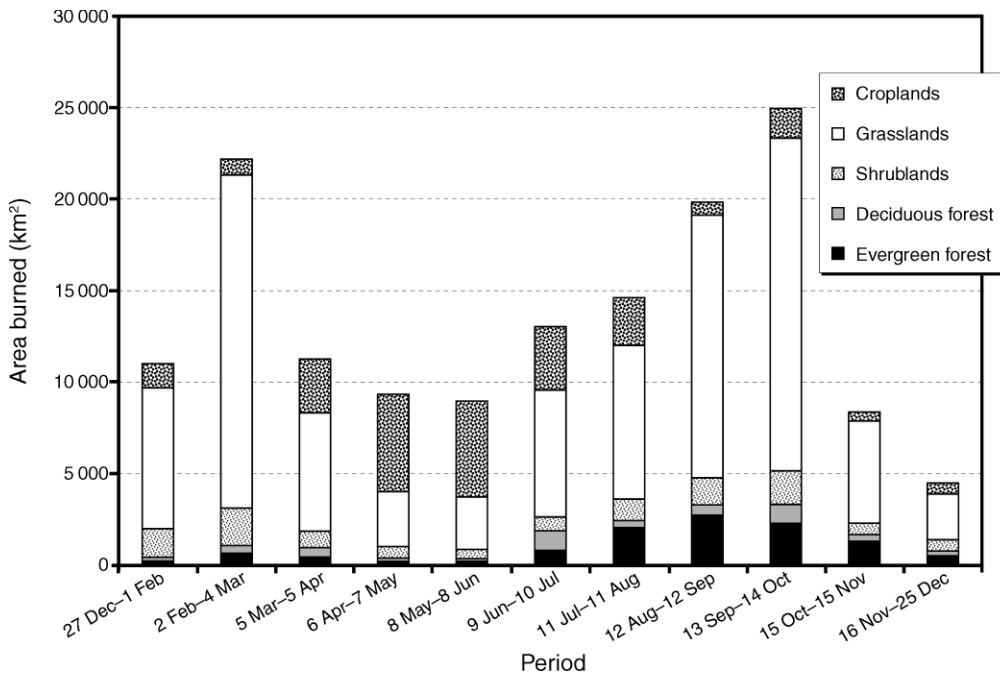


FIG. 5. Monthly burned areas for different land covers, December 2003 through December 2004.

Assessment

Validation of the AQL2004 algorithm results were performed with both higher resolution data and active fires detected by the thermal channels of the MODIS instrument. We have used the term agreement, instead of accuracy, since the disagreements between reference data

(high-resolution images or active fire detections) can not always be considered errors, as it will be explained in the *Discussion* section, although they provided an initial assessment of the project performance.

The first assessment was based on cross-tabulation analysis of MODIS and high-resolution images. Fig. 6

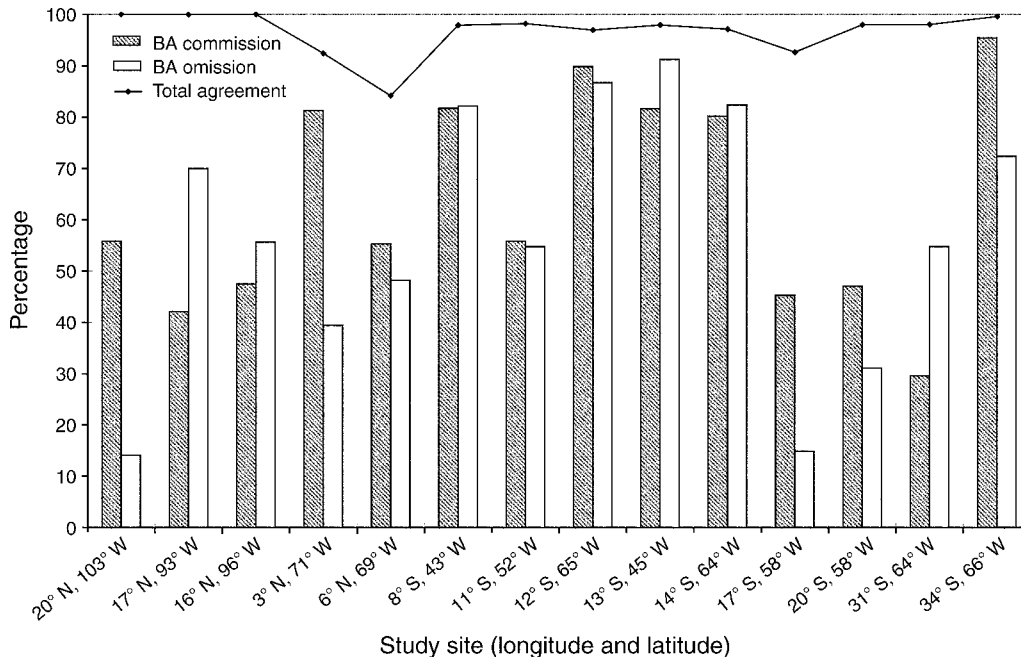


FIG. 6. Validation results by study site. Total percentage agreement (black line) refers to both burned and unburned classes, while bars refer to omission and commission percentage disagreements of the burned area (BA) exclusively.

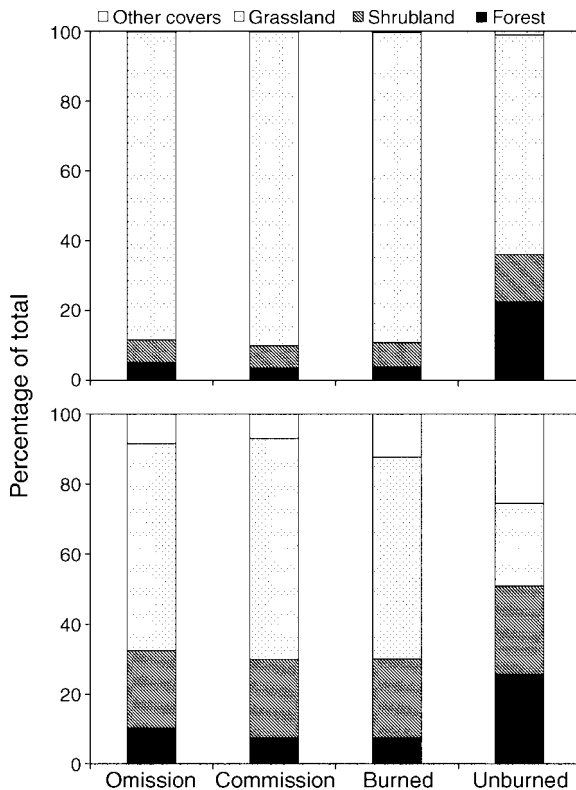


FIG. 7. Validation results by main land covers (upper panel) as a percentage of total area in different agreement conditions and (lower panel) as a percentage of total area of different land covers. Burned and unburned categories refer to areas that were well detected as burned or unburned.

includes total agreement between the two sources, as well as commission and omission disagreements for burned land discrimination as a proportion of areas observed in high resolution images (Landsat or CBERS).

Total agreement, as defined by both the burned and unburned area discrimination, was very high in all study sites, since in most validation sites the vast part was covered by unburned areas that were properly discriminated as such. Values were generally higher than 95%, with a global value of 96% for all validation sites. However, burned-land discrimination showed high omission and commission disagreements in most validation sites, with a total value of 47% commission and 63% of omission with respect to high-resolution burned areas. The disagreements between the two sources were especially high between 8° S and 14° S of the Southern Hemisphere, and central and Southern regions of Argentina (Fig. 6). The lower omission errors were found for Mexico and the border between Brazil and Bolivia. It is important to remark that omission and commission disagreements were generally balanced in the different study areas, which made it possible to obtain more confident area estimations from our results.

Areas covered by herbaceous vegetation offered the lowest agreement across all validation sites, although they were also the most frequent (Fig. 7). We observed 87% of all omission and 89% of commission disagreements in herbaceous covers (grass and crops), mostly associated with croplands in the latter case. Grasslands offered higher agreement in tropical regions of Colombia and Brazil than in temperate areas of Argentina; although the amount of burned area in herbaceous vegetation was also lower in this latter region. Forest showed a higher proportion of well discriminated unburned areas and had a significant, lower ratio of omission and commission errors.

An alternative view of validation can be observed in Fig. 8, which shows two examples of the spatial validation procedure. A cross tabulation between burn scars discriminated in the MODIS and the high-resolution images made it possible to analyze the spatial distribution of agreements and disagreements between the two sources. As it can be observed in Fig. 8a, c, the disagreements are spatially contiguous with the matched pixels, and therefore they should be more related to boundary effects than to an incorrect discrimination. The scatter plots with the proportion of burned areas in both high and low resolution data for different 5 × 5 km cells (Fig. 8b, d) provided a complementary view of the spatial agreements between the two data sources. In both cases, the correlations between the two sources are highly significant, but the slope is closer to 1 in the Brazilian site, mainly covered by forested areas.

Table 4 classifies the performance of burn-scars detection by the AQL algorithm considering fire size. As it could be expected, small patches have a low detection rate. Below 1500 ha, the rate fluctuates from 75% to just 50% of all burn patches. Above that threshold the detections significantly improve, going up to 100% in most cases. The differences in area detected between MODIS and high-resolution images are notable, but it is important to emphasize that the algorithm provides a good spatial assessment of burns in the region, at least for medium-to-large fire sizes.

The final validation exercise was focused on comparing burn scars and active fires. A 25 × 25 km grid cell was used in this case for extracting both sources of fire information. The proportion of pixels within each cell in both sources was correlated for the entire region. Table 5 offers the results for South America and Mexico. The trends show a global tendency of agreement between the two data sources with positive correlations for most periods. The mean correlation between the two sources of data was 0.229 ($P < 0.001$). The peaks of fire occurrence, in January–February and August–September, also offered the highest correlations, especially the former. In Central America, the correlations were generally lower. Differences in agreement values were observed between different land covers. Grasslands presented the highest correlations in the dry periods of both hemispheres, while forested areas and crops offered

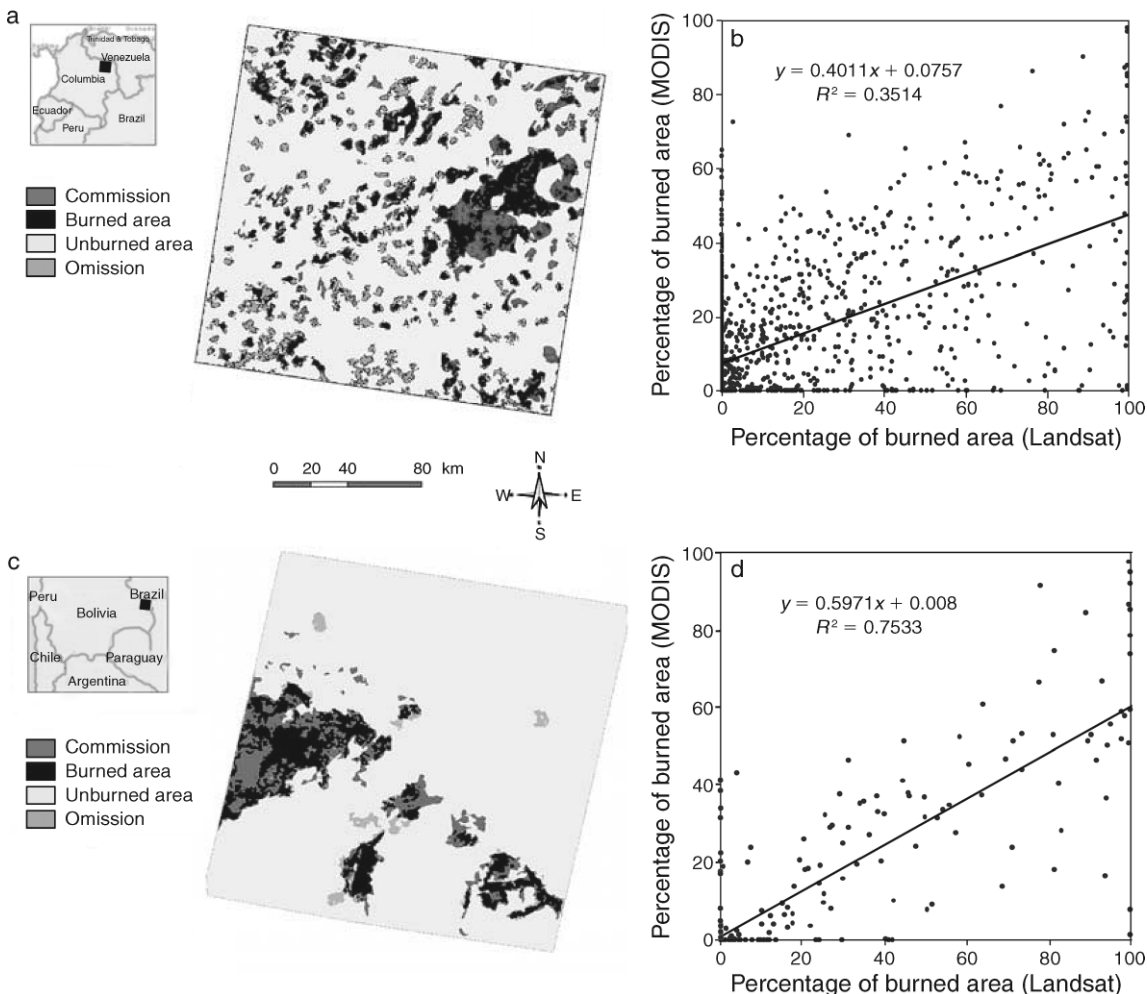


FIG. 8. Two examples of the validation procedure: panels (a) and (c) show cross-tabulated images of burned areas in Landsat and MODIS; panels (b) and (d) are scatter graphs derived from 5×5 km grids with the percentages of burned area identified by both sources. The site in panels (a) and (b) is eastern Colombia; the site for panels (c) and (d) is western Brazil.

low accuracy at the beginning of the year, but the correlations increase from February to August. Shrubs showed better r correlation at the beginning of the time series, but show poor agreement for the months of March–October.

DISCUSSION AND CONCLUSIONS

The AQL2004 project generated a burned land map of Latin America for 32-day periods covering 2004. The total estimation of burned area for the region ($153\,215\text{ km}^2$) was close to that obtained from similar projects for 2000, when the GBA2000 project estimated $137\,000\text{ km}^2$ and GLOBSCAR $162\,774\text{ km}^2$, as well as with the mean burned area calculated for the 1997–2004 period from active fire detections ($200\,000\text{ km}^2$; van der Werf et al. 2006). To obtain similar estimations, in spite of using very different sensors (SPOT/VEGETATION for the GBA2000 project and ATSR for GLOBSCAR) or different data sources (active fires in the van der Werf

et al. [2006] study), confirms the robustness of the burned-area estimations.

At a local scale, the estimations should be taken with more caution, according to the results of our assessment exercise and the work of other authors. For instance, Armenteras et al. (2005) found the burned area to be about one-third of the AQL2004 results in their 2000 and 2001 analysis of the Colombian savannas using Landsat images, although their data do not refer to the whole country, as AQL2004 does. In any case, their study showed a similar temporal pattern to the one found for AQL2004 data. Conversely, according to deforestation rates of Brazil and its close association to burnings, as well as the use of fire for some crops (sugar cane), the estimation of burned areas for the AQL2004 project should be considered very conservative, since some sources estimate the annual burned area in this country up to more than $500\,000\text{ km}^2$ (A. Setzer, *personal observation*).

TABLE 4. Number of burn patches detected by the AQL algorithm vs. those observed in high-resolution (HR) images.

Fire size (ha)	No. burn patches		HR estimation (ha)	AQL estimation (ha)	Detected fires (%)
	Observed	Detected			
250–500	54	27	20 515	6078	50.0
500–750	30	20	17 885	7043	66.7
750–1000	28	23	23 480	12 686	82.1
1000–1250	16	9	17 713	6455	56.3
1250–1500	16	12	21 016	8940	75.0
1500–1750	13	12	20 152	10 994	92.3
1750–2000	8	6	13 892	4505	75.0
2000–2250	11	9	22 061	11 614	81.8
2250–2500	9	8	19 823	5727	88.9
2500–2750	7	7	16 397	7895	100.0
2750–3000	9	8	23 571	9630	88.9
3000–3500	12	10	35 243	14 034	83.3
3500–4000	8	8	26 934	10 748	100.0
4000–10 000	15	14	98 215	36 917	93.3
>10 000	14	14	493 586	252 200	100.0
Total	250	187	870 483	405 466	74.8

The case of Mexico requires a further examination, since it offered a very low percentage of burned areas compared to the size of the country. Although national statistics do not match AQL2004 estimations in absolute numbers, they clearly show a decrease in fire activity for 2004. In fact, that year had the lowest fire occurrence in Mexico in the period 1998–2005 according to the Mexican Forest Service. This was caused by humid conditions, especially at the beginning of the year. The seasonal trends of expected fire occurrence did not agree with the observed trends, since in Mexico the burned land areas were mainly detected during the fall, which is ordinarily wetter than early spring, although the particular weather patterns of 2004 were not available for validation of this hypothesis. Confusion between agricultural crops and wildland fires may explain this temporal trend since many burn scars were located in agricultural areas. However, there is not much information on agricultural burnings in the country.

The validation of the results was done with four different methods that generally agreed, although various uncertainties in the reference data preclude deriving definitive conclusions. On one hand, the

comparison of high resolution data (Landsat or CBERS) with MODIS data implies potential problems caused by misregistration or boundary effects related to the great difference of pixel sizes between the two sources. In this regard, the comparison between burn patches in our results and high-resolution data shows very adequate agreement, especially when fires are larger than 1500 ha.

Another source of discrepancy between MODIS and high-resolution images was associated with the different time periods they refer to. Our input data were 32-day composite periods. Therefore, when using a Landsat image from after the end of the composite period, it was difficult to assess whether, for instance, the burned areas not detected by the AQL algorithm were in fact omission errors or rather fires that occurred between the end of the 32-day composite period and the time of Landsat image acquisition. An opposite situation would occur when the Landsat image was acquired within the 32-day composite period, but in this case it would affect the commission errors.

Finally, the relation between hot spots and burn scars improved the spatial analysis of errors, but it can not be

TABLE 5. Pearson r correlation values between burn scars and active fires for the different 32-day study periods.

Period	South America					Mexico
	Forest	Shrubs	Grasslands	Crops	All covers	All covers
27 Dec–1 Feb	0.045	0.376	0.492	0.035	0.367	0.020
2 Feb–4 Mar	0.265	0.450	0.453	0.423	0.383	0.236
5 Mar–5 Apr	0.071	0.119	0.309	0.096	0.233	0.069
6 Apr–7 May	0.033	–0.002	0.103	–0.042	0.022	0.056
8 May–8 Jun	0.173	0.173	0.131	–0.027	0.042	0.077
9 Jun–10 Jul	0.203	0.137	0.273	0.368	0.195	0.057
11 Jul–11 Aug	0.227	0.062	0.293	0.301	0.170	0.000
12 Aug–12 Sep	0.331	–0.032	0.404	0.083	0.149	0.119
13 Sep–14 Oct	0.190	0.048	0.221	0.054	0.184	0.240
15 Oct–15 Nov	0.130	–0.002	0.062	0.015	0.066	0.160
16 Nov–25 Dec	0.119	0.130	0.069	0.040	0.065	0.237

Note: Study periods are shown as initial day and month through final day and month.

properly considered a reliable validation, as detected active fires refer to the specific time of the satellite overpass, and it may miss those that occurred at other day or night periods.

The agreements between our results and both sets of data can be globally considered as acceptable, considering the project constraints. Global agreement (both burned and unburned areas) was very high, and omission and commission disagreements were generally balanced in the different validation sites. The most spatially comprehensive validation of our results was based on comparing active fire detections and burned area, although these two products are conceptually different (Giglio et al. 2006). The global correlation between these two sources ($r = 0.229$) was very significant, showing common spatial patterns of fire occurrence. This Pearson r correlation is higher than those measured for similar global burned-land products. For instance, Boschetti et al. (2004) computed for the Latin American region a Pearson r value of 0.013 between the results of the GBA2000 burned land areas and the active fires derived from ATSR sensor on board the ERS satellite. The r value was even lower for the relationship between GLOBSCAR and active fires (-0.003), in spite of being derived from the same ATSR sensor.

However, for local regions, our assessment exercise also showed that additional efforts are required to adapt the global algorithm to specific land cover or climatic regions, as well as to explore potential improvements with other standard MODIS products. The main potential sources of errors for the AQL2004 project can be related to the limitations of input data, the global character of the algorithm, and the great ecological diversity of the region.

One of the most important limitations of our input data for burned-land mapping is the length of 32-day MODIS composites. In fact, the herbaceous vegetation showed the lower agreement with high-resolution data, on one hand because commission problems were observed because of changes from green areas to dark soils after harvesting. When referring to omission errors, the postfire char signal of grasslands is the less permanent among land covers, and therefore the use of long compositing periods, such as the 32 days used in this project, may be responsible for lower agreements with observed burn scars in high-resolution images. This effect of image frequency on discrimination of burn scars has been observed in other studies from tropical regions, where the carbon signal has almost disappeared within a few weeks after the fire (Trigg and Flasse 2000, Armenteras et al. 2005). Regarding the angular effects on the 32-day MODIS composite, the use of the MOD43 product, which includes a BRDF correction, may be more advisable as it has already observed by other authors (Roy et al. 2005b).

Development of local algorithms is another line of potential improvement of the AQL2004 project. The results from Mexico and Patagonia, for instance, show



PLATE 1. (Top) Recent fires in the Ecuadorian Andes. Burn areas in wet zones of the tropical Andes region tend to have small sizes and create a patchy mosaic. Photo credit: E. Chuvieco, December 2005. (Bottom) Active fires in the interior sierras of Cordoba Province (Argentina). A mixture of pine plantations and natural forest was affected by this fire, in one of the driest summer seasons on record. Photo credit: E. Chuvieco, November 2003.

promising opportunities for developing thresholds or new spectral indices that may be better adapted to the particular soils or vegetation characteristics of the region. Preliminary analysis in Patagonia and Central Buenos Aires in Argentina with “local tuned” algorithms showed better results than those obtained with the global AQL2004 algorithm, but they could not be easily generalized.

We have already commented on the importance of having a systematic evaluation of burned areas in the region. From a global emission estimation point of view, Latin America during the period of 1997–2004 accounted for 5.81% of the total burned area and 15.77% of the total biomass burning carbon emissions, and it had an emission ratio more than three times higher than Africa for the same period (van der Werf et al. 2006).

On the other hand, wildland fires are still the main factor of land-use change in the region. Fire is used to remove vegetation in the first phase or after logging,

then causing a permanent degradation in many areas previously covered by evergreen forest (Cochrane et al. 1999).

Finally, the ecological impacts of fire need to be addressed at global and local scales by improving current fire history estimates and spatial distribution of burned areas. The effects of fire on biodiversity and soil degradation have been emphasized by several authors (Sieger et al. 2001, van Nieuwstadt et al. 2001), especially when the natural fire regimes are shortened. Fire regimes are a combination of many different aspects (fire frequency, size, length, seasonality, severity, and so on), and burned land products should be considered an important component of their analysis, including monitoring changes to the regimes and developing better understandings of the role of fire in current landscape spatial structure (Vega-Garcia and Chuvieco 2006). The AQL2004 project has shown a great potential to provide input data to undertake this ecological analysis.

ACKNOWLEDGMENTS

The AQL2004 project has been partially funded by the NASA-START program, which covered the costs for the technical meetings. Support from the GOF-C-GOLD program is also acknowledged. The GLCF of the University of Maryland provided the MODIS 32-day composites and the active-fire data. High-resolution images for validation purposes were obtained from INPE, CONAE, and ERMEXS (Estación de recepción México de la Constelación SPOT). All participant institutions have provided support to the participants to share costs of processing the data and validating the results. Some of the Argentinean coauthors were financed from a grant of the Inter-American Institute for Global Change Research (IAI) CRN-203, which is supported by the U.S. National Science Foundation (Grant GEO-0452325). Elizabeth Hoy provided very useful comments and corrections.

LITERATURE CITED

- Ahern, F. J., J. G. Goldammer, and C. O. Justice. 2001. Global and regional vegetation fire monitoring from space: planning a coordinated international effort. SPB Academic Publishing, The Hague, The Netherlands.
- Armenteras, D., M. Romero, and G. Galindo. 2005. Vegetation fire in the savannas of the Llanos Orientales of Colombia. *World Resource Review* 17:628–638.
- Barbosa, P. M., J. M. Grégoire, and J. M. C. Pereira. 1999. An algorithm for extracting burned areas from time series of AVHRR GAC data applied at a continental scale. *Remote Sensing of Environment* 69:253–263.
- Belward, A. S. 1996. The IGBP-DIS global 1 km land cover data set (DISCover)-proposal and implementation plans. IGBP-DIS Working Paper, Toulouse, France.
- Boschetti, L., P. A. Brivio, H. D. Eva, J. Gallego, A. Baraldi, and J. M. Gregoire. 2006. A sampling method for the retrospective validation of Global Burned Area products. *IEEE Transactions on Geoscience and Remote Sensing* 44: 1765–1773.
- Boschetti, L., H. D. Eva, P. A. Brivio, and J. M. Gregoire. 2004. Lessons to be learned from the comparison of three satellite-derived biomass burning products. *Geophysical Research Letters* 31:L21501 [doi:21510.21029/22004GL021229].
- Chuvieco, E., M. P. Martín, and A. Palacios. 2002. Assessment of different spectral indices in the red-near-infrared spectral domain for burned land discrimination. *International Journal of Remote Sensing* 23:5103–5110.
- Cochrane, M. A., A. Alencar, M. D. Schulze, C. M. Souza, D. C. Nepstad, P. Lefebvre, and E. A. Davidson. 1999. Positive feedbacks in the fire dynamic of closed canopy tropical forests. *Science* 284:1832–1835.
- Congalton, R. G., and K. Green. 1999. Assessing the accuracy of remotely sensed data: principles and applications. Lewis Publishers, Boca Raton, Florida, USA.
- Di Bella, C. M., E. G. Jobbágy, J. M. Paruelo, and S. D. Pinnock. 2006. Continental fire density in South America. *Global Ecology and Biogeography* 15:192–199.
- FAO. 2006. Global Forest Resources Assessment 2005. FAO, Rome, Italy.
- Fernández, A., P. Illera, and J. L. Casanova. 1997. Automatic mapping of surfaces affected by forest fires in Spain using AVHRR NDVI composite image data. *Remote Sensing of Environment* 60:153–162.
- Fraser, R. H., Z. Li, and J. Cihlar. 2000. Hotspot and NDVI Differencing Synergy (HANDS): a new technique for burned area mapping over boreal forest. *Remote Sensing of Environment* 74:362–376.
- Giglio, L., J. Descloitres, C. O. Justice, and J. B. Kauffmann. 2003. An enhanced contextual fire detection algorithm for MODIS. *Remote Sensing of Environment* 87:273–282.
- Giglio, L., G. R. van der Werf, J. T. Randerson, G. J. Collatz, and P. S. Kasibhatla. 2006. Global estimation of burned area using MODIS active fire observations. *Atmospheric Chemistry and Physics* 6:957–974.
- Hansen, M. C., R. S. DeFries, J. R. G. Townshend, R. Sohlberg, C. Dimiceli, and M. Carroll. 2002. Towards an operational MODIS continuous field of percent tree cover algorithm: examples using AVHRR and MODIS data. *Remote Sensing of Environment* 83:303–319.
- Hansen, M. C., J. R. G. Townshend, R. S. Defries, and M. Carroll. 2005. Estimation of tree cover using MODIS data at global, continental and regional/local scales. *International Journal of Remote Sensing* 26:4359–4380.
- Justice, C. O., L. Giglio, S. Korontzi, J. Owens, J. T. Morisette, D. Roy, J. Descloitres, S. Alleaume, F. Petitcolin, and Y. Kaufman. 2002. The MODIS fire products. *Remote Sensing of Environment* 83:244–262.
- Kasischke, E., and N. H. French. 1995. Locating and estimating the areal extent of wildfires in Alaskan boreal forest using multiple-season AVHRR NDVI composite data. *Remote Sensing of Environment* 51:263–275.
- Key, C., and N. Benson. 2006. Landscape assessment (LA). Sampling and analysis methods. Pages LA1–LA51 in D. C. Lutes, R. E. Kenane, J. F. Caratti, C. H. Key, N. C. Benson, S. Sutherland, and L. J. Gangi, editors. FIREMON: fire effects monitoring and inventory system. Integration of standardized field data collection techniques and sampling design with remote sensing to assess fire effects. U.S. Forest Service, Rocky Mountain Research Station, Fort Collins, Colorado, USA.
- Levine, J. S. 1996. Biomass burning and global change. MIT Press, Cambridge, Massachusetts, USA.
- Lioussé, C., M. O. Andreae, P. Artaxo, P. Barbosa, H. Cachier, J. M. Grégoire, P. Hobbs, D. Lavoué, F. Mouillot, J. Penner, M. Scholes, and M. G. Schultz. 2004. Deriving global quantitative estimates for spatial and temporal distributions of biomass burning emissions. Pages 77–120 in C. Granier, P. Artaxo, and C. E. Reeves, editors. Emissions of atmospheric trace compounds. Kluwer Academic Publishers, Dordrecht, The Netherlands.
- López García, M. J., and V. Caselles. 1991. Mapping burns and natural reforestation using Thematic Mapper data. *Geocarto International* 1:31–37.
- Martín, M. P. 1998. Cartografía e inventario de incendios forestales en la Península Ibérica a partir de imágenes NOAA-AVHRR. Dissertation. Universidad de Alcalá, Alcalá de Henares, Spain.

- Martín, M. P., P. Ceccato, S. Flasse, and I. Downey. 1999. Fire detection and fire growth monitoring using satellite data. Pages 101–122 in E. Chuvieco, editor. *Remote sensing of large wildfires in the European Mediterranean Basin*. Springer-Verlag, Berlin, Germany.
- Martín, M. P., and E. Chuvieco. 1995. Mapping and evaluation of burned land from multitemporal analysis of AVHRR NDVI images. *EARSeL Advances in Remote Sensing* 4:7–13.
- Martín, M. P., I. Gómez, and E. Chuvieco. 2005. Performance of a burned-area index (BAIM) for mapping Mediterranean burned scars from MODIS data. Pages 193–198 in J. Riva, F. Pérez-Cabello, and E. Chuvieco, editors. *Proceedings of the Fifth International Workshop on Remote Sensing and GIS applications to Forest Fire Management: Fire Effects Assessment*. Universidad de Zaragoza, GOF-C-GOLD, EARSeL, Paris, France.
- Morissette, J. T., J. L. Privette, and C. O. Justice. 2002. A framework for the validation of MODIS Land products. *Remote Sensing of Environment* 83:77–96.
- Pereira, J. M. C. 1999. A comparative evaluation of NOAA/AVHRR vegetation indexes for burned surface detection and mapping. *IEEE Transactions on Geoscience and Remote Sensing* 37:217–226.
- Roberts, S. J. 2000. Tropical fire ecology. *Progress in Physical Geography* 24:281–288.
- Roy, D., et al. 2005a. The Southern Africa Fire Network (SAFNet) regional burned area product validation protocol. *International Journal of Remote Sensing* 26:4265–4292.
- Roy, D., Y. Jin, P. Lewis, and C. Justice. 2005b. Prototyping a global algorithm for systematic fire-affected area mapping using MODIS time series data. *Remote Sensing of Environment* 97:137–162.
- Siegert, F., G. Rücker, A. Hinrichs, and A. Hoffmann. 2001. Increased damage from fires in logged forests during droughts caused by El Niño. *Nature* 414:437–440.
- Simon, M., S. Plummer, F. Fierens, J. J. Hoelzemann, and O. Arino. 2004. Burnt area detection at global scale using ATSR-2: the GLOBSCAR products and their qualification. *Journal of Geophysical Research—Atmospheres* 109:D14S02 [doi:10.1029/2002JD003622:1-16].
- Tansey, K., et al. 2004. Vegetation burning in the year 2000: global burned area estimates from SPOT VEGETATION data. *Journal of Geophysical Research—Atmospheres* 109:D14S03 [doi:10.1029/2002JD003598:2-22].
- Townshend, J. R., R. DeFries, M. Hansen, R. Sohlberg, M. Carroll, and C. DiMiceli. 2003. MODIS 32-day composites. The Global Land Cover Facility, College Park, Maryland, USA.
- Trigg, S., and S. Flasse. 2000. Characterizing the spectral-temporal response of burned savannah using in situ spectroradiometry and infrared thermometry. *International Journal of Remote Sensing* 21:3161–3168.
- van der Werf, G. R., J. Randerson, T. G. J. Collatz, L. Giglio, P. S. Kasibhatla, A. F. Arellano, S. C. Olsen, and E. S. Kasischke. 2004. Continental scale-partitioning of fire emissions during the 1997 to 2001 El Niño/La Niña period. *Science* 303:73–76.
- van der Werf, G. R., J. T. Randerson, L. Giglio, G. J. Collatz, P. S. Kasibhatla, and A. F. Arellano. 2006. Interannual variability in global biomass burning emissions from 1997 to 2004. *Atmospheric Chemistry and Physics* 6:3423–3441.
- van Nieuwstadt, M. G. L., D. Sheil, and K. Kartawinata. 2001. The ecological consequences of logging in the burnt forests of East Kalimantan, Indonesia. *Conservation Biology* 15:1183–1186.
- Vega-Garcia, C., and E. Chuvieco. 2006. Applying local measures of spatial heterogeneity to Landsat-TM images for predicting wildfire occurrence in Mediterranean landscapes. *Landscape Ecology* 21:595–605.

